The metamorphic evolution of the Isua supracrustal belt: Implications for Archean tectonics

Anthony Ramirez Salazar

Submitted in accordance with the requirements for the degree of

Doctor of Philosophy

The University of Leeds

School of Earth and Environment

June 2022

Intellectual property

The candidate confirms that the work submitted is his own, except where work which has formed part of jointly authored publications has been included. The contribution of the candidate and the other authors to this work has been explicitly indicated below. The candidate confirms that appropriate credit has been given within the thesis where reference has been made to the work of others

During the course of my PhD I have published a paper entitled *Tectonics of the Isua Supracrustal Belt 1: P-T-X-d Constraints of a Poly-Metamorphic Terrane* published in *Tectonics* (Ramírez-Salazar et al., 2021) on February 6th 2021. I was the first author of the paper with Thomas Müller, Sandra Piazolo, A. Alexander G. Webb, Christoph Hauzenberger, Jiawei Zuo, Peter Haproff, Jason Harvey, Tsz Kin Wong, and Callum Charlton as co-authors. I was in charge of the conceptualization, manuscript writing, most of data collection, figures, thermodynamic modelling and analysis. Thomas Müller and Sandra Piazolo supervised and were involved in the conceptualization of the work. Sample collection was made by Thomas Müller, A. Alexander G. Webb, Jiawei Zuo and Peter Haproff. Tsz Kin Wong and Callum Charlton obtained microprobe data as part of their undergrad and MSc thesis project. All authors were involved in the editing and reviewing of the work. Furthermore, review comments by Matthijs A. Smit and Hugh Rollinson improved the manuscript. This manuscript forms most of Chapter 2.

I will also submit the paper *Quantitative microstructural and chemical analyses reveal compositional and mineralogical effects on inclusion-rich garnet growth in medium-grade rocks: An example from the Isua supracrustal belt, Greenland* (Ramírez-Salazar et al., submitted) for publication to *Contributions to Mineralogy and Petrology*. I am the first author of this contribution with Sandra Piazolo, Thomas Müller, Dominik Sorger, Jiawei Zuo, Joyjit Dey, A. Alexander G. Webb, and Peter J. Haproff as co-authors. I was responsible for

conceptualization, manuscript writing, most of the data collection (apart where it is indicated below), data processing, figures, and data analysis. Sandra Piazolo and Thomas Müller supervised and were involved in the conceptualization. Sandra Piazolo and Joyjit Dey collected the EBSD data. Dominik Sorger obtained the high-resolution images of the thin sections. Jiawei Zuo obtained the SEM compositional maps. Sample collection was made by Thomas Müller, A. Alexander G. Webb, Jiawei Zuo and Peter Haproff. All authors participated in editing. This manuscript forms most of Chapter 3.

The drafts of two additional manuscript are also part of this work. For the first one, it is planned that the manuscript will be sent for publication shortly after thesis submission. It is entitled *Constraining the prograde metamorphic and tectonic evolution of garnet porphyroblasts in the Isua supracrustal belt, SW Greenland*. I will be the first author of this publication with Thomas Müller, Sandra Piazolo, Dominik Sorger, as co-authors. I was responsible for the original manuscript, figures, data analysis, thermodynamic modelling, data collection and conceptualization. Thomas Müller and Sandra Piazolo supervised and, with Dominik Sorger, were involved in the conceptualization. This manuscript forms most of Chapter 4.

Finally, a preliminary draft of another paper is also included in this work. The manuscript will be sent for publication after thesis submission and will be centred in the geochronology of the samples. I will be the first author of this publication with Thomas Müller, Sandra Piazolo, Dominik Sorger, and, Ian Millar as co-authors. I was responsible for writing the original manuscript draft, figures, data analysis, sample preparation and conceptualization. Thomas Müller and Sandra Piazolo supervised and were involved in the conceptualization and review of the draft manuscript. Dominik Sorger continued with the geochronological data for Sm-Nd garnet analysis, as well as titanite and rutile ages processed at UGoe after the end of my second research visit (Sept-Nov 2021). Additional geochronology data have been

prepared and measured at the British Geological Survey by Ian Millar for which I wrote a small research proposal (NEIF 2247.0420, granted to Jason Harvey) and prepared mineral separates. This manuscript forms most of Chapter 5.

Acknowledgements

This thesis was possible thanks to the countless contributions of many people. First, I would like to thank my supervisors, Thomas Müller, Sandra Piazolo, and Jason Harvey for all the work they did to find the resources needed to complete this project.

I specially would like to thank Sandra and Thomas for their support in all the aspects of my PhD project. I am grateful for all the feedback you provided throughout this process and for always pushing me and encouraging me to be a better scientist. I thank both of you for your support during the pandemic and for always understanding there is human behind the scientist. I am really happy with everything I learned with you. I hope you enjoyed the process of learning about Isua along me and that you are proud of this work.

My project would not have been possible without the support of the Isua group: A. Alex G. Webb, Jiawei Zuo, Dominik Sorger and Peter J. Haproff. Thank you guys for all the discussions on the complexity of Isua and for all the question you threw at me. They definitely enriched this work and my way to approach geological problems.

Abstract

Knowledge on the metamorphic evolution of the Eoarchean Isua supracrustal belt (ISB) remains fragmentary and results presented to date are contradictory. This translates into an ambiguity on the interpretations on the tectonic evolution of the belt as the three main competing tectonic models predict different metamorphic signatures. The distinction between the three possibilities has larger implications for early Archean geodynamics, since two argue for an early onset of plate tectonics while the other proposes a non-uniformitarian alternative. This work presents a detail P-T-X-d-t evolution of the ISB to provide further constraints in its tectonic evolution. Detail characterization and quantification of the metamorphic fabrics reveal a syn-tectonic metamorphic event (M_1) that evolved along a near isothermal burial path followed by an increase in T and decrease in P that culminated in the peak metamorphic conditions 550-600 °C and 0.5-0.7 GPa. M_1 homogeneously affected the entire belt. This also suggested by the detailed garnet study showing the diversity in porphyroblasts is a consequence of (local) chemistry and previous microstructures, and not the product of different tectonometamorphic histories as previously interpreted. Preliminary analysis suggest that M_1 occurred at c. 3.3 Ga or c. 2.9-2.7 Ga. Post-tectonic Neoarchean (c. 2.6 Ga) lower amphibolite facies (540°C, ≤ 0.5 GPa) metamorphism (M_2) later affected the ISB, recorded by the inclusion-poor rims of garnets and the appearance of titanite overgrowing the foliation. Proterozoic (<2220 Ma) low-grade retrogression (M_3) features such as late quartz-calcite veins, garnet pseudomorphs and chloritization overprinted M_1 and M_2. Moreover, pre-M_1 (3.60-3.68 Ga) local contact metamorphism is recorded in the enclaves, while magmatic garnet dating expands the intrusion of the granites from 3.66-6.60 to 3.66-3.55 Ga. The data and analysis provided in this thesis show that non-uniformitarian tectonics are a plausible scenario to explain the tectonic evolution of the ISB during the Archean.

Tables of contents

List of figures and tables

Figure. 1.1 Global map showing the location of Archean cratons and their names.

Figure 1.2 Mantle potential temperatures (T_P) and thickness of the crust as a function of T_P

Figure 1.3 Schematic representation of the different tectonic models proposed for the Archean and some of their characteristics.

Figure 1.4 Geological map of the Nuuk Region.

Figure. 1.5 Proposed models for the evolution of the Isua supracrustal belt and their predicted major structures and metamorphic gradient.

Figure. 2.1 Geological map of the Isua Supracrustal Belt showing the location of samples used in Chapter 1

Figure 2.2 Timeline showing the major geological events interpreted for the ISB and ages int
Figure. 2.3 Tectonic models proposed for the evolution of the ISB.

Figure 2.4 Photomicrographs showing peak mineralogy and micro-structures.

Figure. 2.5 Post-tectonic medium- and low-temperature paragenesis and micro-structures.

Figure 2.6 Geochemical characterization of spiral-like garnet in sample 714-5E.

Figure 2.7 Classical geothermobarometry plots.

Figure. 2.8 Isochemical phase diagrams.

Figure 2.9 Overlap of all the stability fields of the calculated isochemical phase diagrams and their schematic positions in the eastern arm of the ISB

Figure 2.10. Metamorphic evolution of the ISB and schematic representation the characteristics of the three different metamorphic events reported in Chapter 2

Figure 3.1. Geological map of the Isua supracrustal belt, showing the location of the samples studied in chapter 3. AFC ternary diagram showing the compositional groups identified.

Figure 3.2. Characteristics of garnets in Ca-rich metapelitic rocks

Figure 3.3 Maps showing the distribution of different features of the garnets in the ISB

Figure 3.4. Characteristics of Type-I garnet in felsic rocks; sample 802-5.

Figure 3.5 Textural parameter correlations.

Figure 3.6. Quantitative chemical maps and phase maps of Type-I garnets.

Figure. 3.7 Pyrope+Almandine (Py+Alm)-Spessartine (Sps)-Grosssular (Gro) ternary diagrams for garnet composition.

Figure. 3.8 Comparison of GROD maps compared with some chemical maps, stereographic projections of the {001} garnet planes for different grains and ψ-values.

Figure 3.9 Quantitative chemical maps and phase maps for Type-II garnets for meta-mafic rocks

Figure 3.10 Quantitative chemical maps and phase maps for Type-II garnets

Abbreviations, acronyms, and symbols

EBSD = Electron Backscatter Diffraction analysis

EPMA = Electron Probe Micro Analyzer

GROD = Grain Reference Orientation Deviation

IGC = Itsaq Gneiss Complex

ISB = Isua supracrustal belt

LOI = Loss on ignition

P-T-*X*-d-t = Pressure-Temperature-Composition-Deformation-Time

QuiG = Quartz in garnet

SEM = Scanning Electron Microscope

TTG = Tonalite-trondhjemite-Granodiorite

Ti-in-Bt = Ti in Biotite

XRF = X-ray fluorescence

μXRF = micro-X-ray fluorescence

E = Garnet elongation

ψ = normalize orientation spread parameter

φ = skeletalness coefficient

Chapter 1. Introduction

The Eoarchean Isua supracrustal belt (ISB) is one of the oldest and best-preserved pieces of ancient crust (Fig. 1.1), as well as one of the extensively studied early Earth terranes. The rocks and minerals of the ISB record valuable information of the history of our young planet. Isua is thus a window into old surficial and deep-seated geological processes. Understanding its tectono-metamorphic evolution has the potential to provide insights on the nature of Archean geodynamics, which is key to improve our understanding of early Earth evolution.
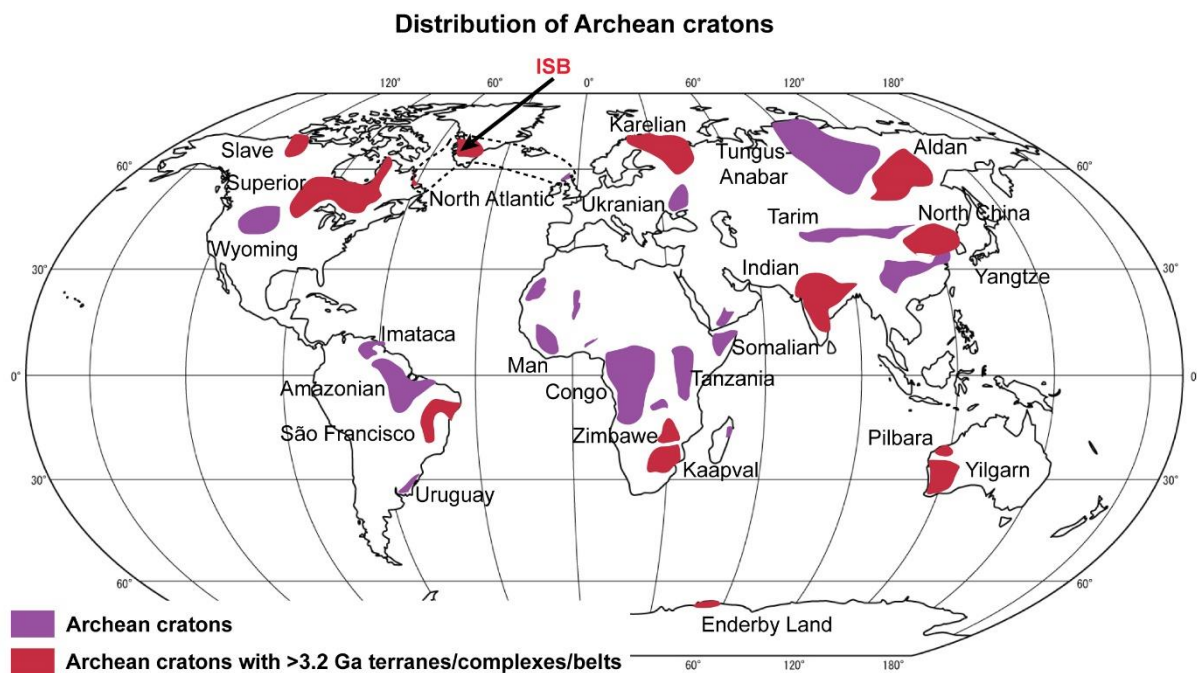
Figure. 1.1 Global map showing the location of Archean cratons and their names. Cratons with >3.2 Ga rocks are highlighted. Modified from (Condie, 2007) with information of (Anhaeusser, 2014). The location of the North Atlantic craton and the location of the Isua supracrustal belt (ISB) are also highlighted.

The ISB and its geological record have typically been interpreted as the product of a convergent boundary, either as an accretionary prism (Komiya et al., 1999) or as a continent-continent collision (Nutman and Friend, 2009; Nutman et al., 2013). Essentially, both of these models argue for the establishment of subduction processes similar to modern settings since 3.8 Ga. Therefore, these models are often cited to support the uniformitarian hypothesis suggesting that plate tectonics operated since the Eoarchean (Komiya et al., 1999; Nutman

and Friend, 2009; Windley et al., 2021). However, this nearly unanimous view of Isua has recently been challenged by Webb et al. (2020) who suggested that the geological record of the belt could be more easily explained in the context of vertical tectonics, such as heat-pipe tectonics (Moore and Webb, 2013). This interpretation is in support of non-uniformitarian tectonic models for the early Earth, that argue that our planet transitioned from a non-plate tectonics to a plate tectonics regime around 3.0 Ga (Dhuime et al., 2012; Sizova et al., 2014; Condie, 2015; Brown and Johnson, 2018; Palin et al., 2020a). In order to discern between the different tectonic interpretations, the tectono-metamorphic evolution of the belt needs to be addressed in detail.

Research related to the metamorphic evolution of Isua is relatively scarce and so far has led to apparent contradictions regarding the interpretations of the metamorphic record and its timing; issues that are generally not discussed in the literature so far. Importantly, the elusive understanding of the P-T-X-t-D evolution of the belt does not represent a minor deficiency in our knowledge of the belt; it marks an important gap since the different tectonic interpretations are predicted to result in contrasting metamorphic signatures. To be able to evaluate the potential geodynamic scenario of Isua and with that the crustal evolution of the early Earth, it is necessary to establish a full P-T-X-t-d path across the Isua supracrustal belt.

1.1 Archean geodynamics: Importance and first order considerations

Mass exchange between the rocky interior and surficial components of planets is largely regulated by recycling, outgassing and crustal processes, of which efficiency and mechanisms are the direct consequence of the dominant tectonic style. Our robust comprehension of plate tectonics as they are active today revealed that tectonic processes play a major role in the feedback mechanisms that drive changes in surficial terrestrial systems both on Earth and other planets, especially through the supercontinent cycle (e.g. Nance et al., 2014). Thus, to achieve a more cohesive and integral understanding of the evolution of the Earth, from its

rocky interior to its gaseous veil, a comprehensive understanding of the nature of Archean geodynamics and the onset of plate tectonics is pivotal.

Looking at the early evolution of the Earth through the uniformitarian lens, assuming plate tectonics has operated from the earliest stages of the planet evolution appears to be a simple and logical conclusion. However, by reading the Precambrian rock record, comparison with other rocky bodies in our solar neighbourhood, as well as running numerical models, scientist have suggested that plate tectonics only became the dominant geodynamic regime later in the evolution of the Earth.

If true, major questions to address are what possibly preceded plate tectonics and when it started. The literature regarding the onset of plate tectonics and the nature of Archean geodynamics is extensive (Brown, 2006; Cawood and Pisarevsky, 2006; Van Kranendonk, 2007, 2010, 2011; Condie and Kröner, 2008; Sizova et al., 2010, 2014, 2015, 2018; Korenaga, 2013, 2018; Gerya, 2014; Rozel et al., 2017; Bédard, 2018; Kemp, 2018; Lenardic, 2018; Maruyama et al., 2018; Moyen and Laurent, 2018; Brown and Johnson, 2018; Stern, 2018; Cawood et al., 2018; Condie, 2018; Hawkesworth and Brown, 2018; Holder et al., 2019; Lourenço et al., 2020; Palin and Santosh, 2020; Palin et al., 2020; Windley et al., 2021). Despite the large number of studies, no consensus exists within the geoscientific community. Alternative tectonic modes are diverse and proposed timings for the initiation of plate tectonics essentially cover most of the history of the planet, varying from the Hadean (Hopkins et al., 2008; Turner et al., 2020) to the Neoproterozoic (Stern, 2005, 2018). In the following sections a brief summary of the tectonic styles, their characteristics and the proposed timings for the initiation of plate tectonics are presented.

1.2 Archean tectonic modes: Characteristics and geological consequences

The possibility of different tectonic modes operating in the young Earth is rooted in observations and data retrieved from the geological record of our planet as well as from other

rocky bodies in our solar neighbourhood. On the one hand, there are convincing arguments supporting the interpretation that the thermomechanical nature of the early Earth was different to the present conditions. For example, the potential temperatures (T_P) of the mantle were higher due to the accretionary heat and higher production of radioactive isotopes (Herzberg et al., 2007, 2010; Korenaga, 2018). Calculations using the record of non-arc basalts and komatiites suggest T_P values up to 250 °C higher compared to present conditions (Fig., 1.2a; Herzberg et al., 2007, 2010; Korenaga, 2018), which also translated in higher surface heat flow (Moore and Webb, 2013). A hotter mantle allowed for more extensive partial melting and thus a thicker (c. 30 km, Fig. 1.2b), more buoyant and weaker oceanic crust (van Hunen and van den Berg, 2008; Sizova et al., 2010; Korenaga, 2018). On the other hand, other rocky bodies like Mars, Venus and the Jupiter's satellite Io, present tectonic modes that are different from plate tectonics. With this in mind, geoscientist have theorized a plethora of alternative tectonic styles for the Archean.

The diversity of observed and hypothesized tectonic models is often categorized in different ways according to different authors. Some of them fall within different categories depending on the author's criteria. For the purpose of this study, a modified classification of Lenardic (2018) is used, where the tectonic styles are grouped in three main categories: active lid, stagnant lid, and sluggish lid tectonic (Fig. 1.3; Table 1.1). Other common terms in the literature are vertical and horizontal tectonics, due to the dominant movements of the lithosphere. Geodynamics in a stagnant lid and, generally, sluggish lid regime would be considered vertical tectonics, while the active lid style is classified as horizontal tectonics. Generally, the models differ in some particular aspects. Thus, broad descriptions of the three main groups and their characteristic features are summarized in the following sections.
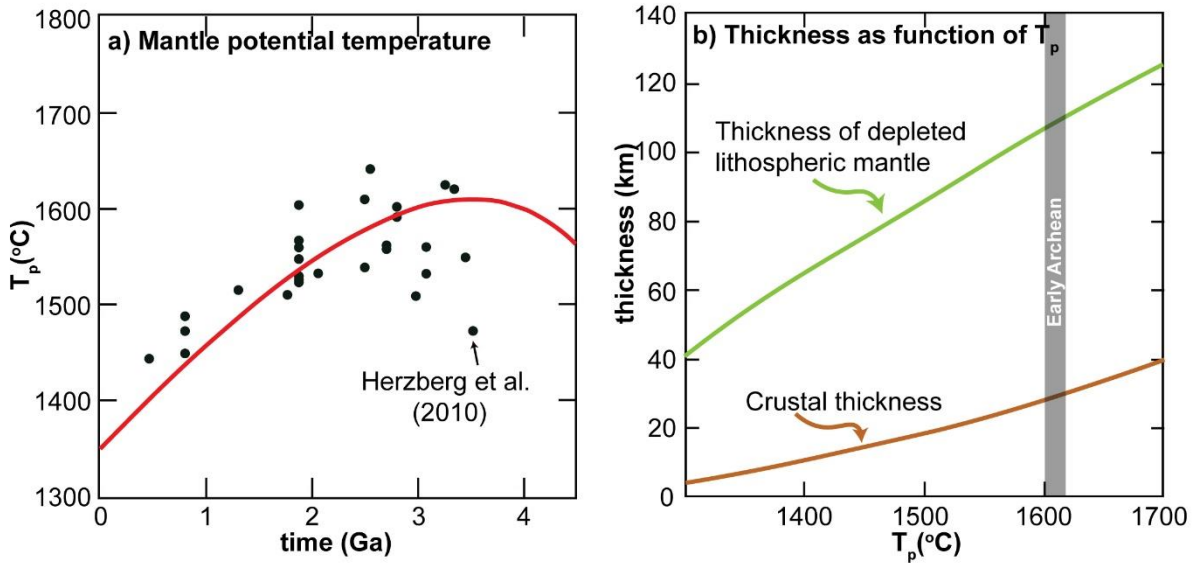
Figure. 1.2 (a) Showing the calculated mantle potential temperatures (T_P) through Earth's history using data from (Herzberg et al., 2010) (after Korenaga, 2013). (b) Predicted thickness of the oceanic crust and depleted mantle as a function of T_P (modified from Korenaga, 2013); thickness according to the predicted T_P in the Early Archean is highlighted

1.2.1   Active lid tectonics

The active lid category (Table 1.1) is characterized by a fragmented mobile "lid" (lithosphere) that actively participates in the convection of the mantle (Lenardic, 2018). Modern style plate tectonics fall within this category and therefore it is the best known and studied style. In the theory of plate tectonics, the segments of the lithosphere (tectonic plates) are bounded by faults that form a globally interconnected network (Cawood et al., 2018, Lenardic, 2018). The plates move relative to each other along such faults creating three different types of boundaries: divergent, convergent and transform (Fig. 1.3a). At each boundary, but mainly at the convergent and divergent settings, particular rocks and mineral assemblages are formed that in principle could be used to characterize the operation of plate tectonics in any rocky body and through time (Condie and Kröner, 2008; Cawood et al., 2018; Palin and Santosh, 2020).
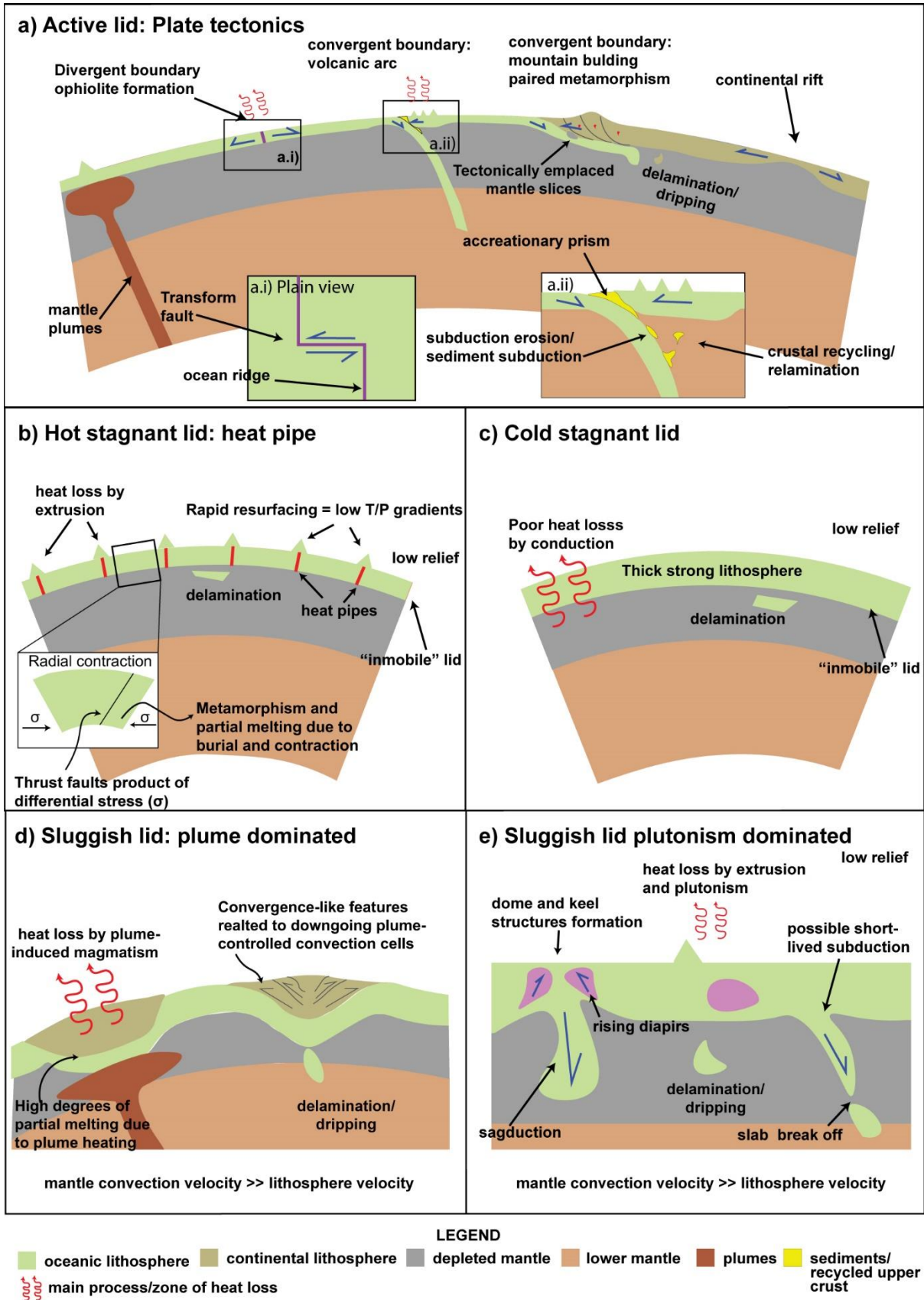
Figure. 1.3 Schematic representation of the different tectonic models proposed for the Archean and some of their characteristics. (a) Active lid: plate tectonics; (b) Hot stagnant lid: heat pipe model; (b) cold stagnant lid; (d) sluggish lid: plume dominated; (e) Sluggish lid (general characteristics).

A distinctive feature associated with the formation of oceanic crust at divergent boundaries is its architecture and petrological association known as ophiolites (Fig. 1.3a). Preservation of ophiolites typically requires tectonic emplacement due to plate convergence. This combination of extensional and collisional movements is used as strong evidence of the operation of plate tectonics (c.f. Condie and Kröner, 2008).

Subduction, which operates along convergent plate boundaries, is typically regarded as the defining feature of plate tectonics. Rocks, rock and mineral associations and resulting chemical signatures of subduction processes are well-studied as monitor of convergent plate movements. The long-standing operation of subduction allows for the metamorphism and possible preservation of blueschists, lawsonite-bearing rocks, jadeites and ultra-high pressure (UHP) rocks (Palin and Santosh, 2020). When subduction ends due to a continent-continent collision (Fig. 1.3a), the low T/P metamorphic rocks can preserved along with rocks metamorphosed in a high T/P gradient (e.g. ultra-high temperature rocks) forming what is classically known as paired metamorphic belts (Miyashiro, 1961, 1973). Thus, paired metamorphism is a proxy to subduction through the history of the Earth (Brown, 2010; Brown and Johnson, 2018).

Accretionary prisms are formed along subduction zones (Fig. 1.3a.ii). They are then commonly eroded and transported to the mantle, a process known as subduction erosion (von Huene and Scholl, 1991). It is also accompanied with subduction of sediments (von Huene and Scholl, 1991). When these rather felsic materials are subducted, the density contrast with the mantle allows for their rise as diapirs through the mantle wedge (Fig. 1.3a.ii) and interaction with the peridotites to contribute to magma generation (Gerya et al., 2004; Hacker et al., 2011; Kelemen and Behn, 2016). Consequently, the contribution of the old crustal material to magmas is reflected in the chemistry of the newly form rocks (e.g. Hf and O isotopes), such that recycling and crustal reworking can be recognized back in time and also

act as a proxy to the operation of subduction (Dhuime et al., 2012; Korenaga, 2018). Other

geochemical features that are commonly associated to subduction are the typical enrichment

in incompatible elements and depletion in Ta and Nb in rocks from arc settings.

Table 1.1 Summary of assumptions and general characteristics expected for the different geodynamic models

	Active lid (Plate tectonics)	Hot stagnant lid (heat-pipe)	Cold stagnant lid*	Sluggish lid (plume)	Sluggish lid (plutonism)
Assumptions	A thicker and more buoyant lithosphere[1-3] can be subducted A weaker lithosphere[1-3] can accommodate stress and strain within narrow zones Petrological igneous processes produce geochemical signatures were similar to the present[e.g.4]	Heat loss through small conduits (heat-pipes) [19-21] Dominated by volcanic activity [19-21] Lithosphere characteristics controlled by the extrusion and resurfacing rates[20-21] Thick, and relative cold and strong lithosphere[19-22] Plutonism mainly derived from intracrustal partial melting rather than mantle additions[20]	High viscosity contrasts across the mantle[39] Thick and rigid cold lithosphere[39] Heat loss by conduction[39]	Mantle convection controlled by plume dynamics[27-29] Lithosphere dynamics and deformation controlled by plume dynamics[27,29] Heat loss through plume-related magmatism[27,29-30]	Heat loss trough (mainly) plutonism and volcanism[33-35] Sluggish lithosphere movement Vertical movements driven by density contrasts[6,33,36]
Tectonic processes	Global subduction network[5-7] Global network of spreading centres[5-7] Transform faults[8] Accretion and continental collision[8] Efficient crustal recycling through subduction (tectonic erosion, sediment subduction, relamination) [3,9-13] Minor crustal recycling through delamination and dripping[14] Mantle slices tectonically emplaced in crustal sequences[38] Mantle plumes can occur	Lithospheric thickness controlled by volcanism and resurfacing[20-21] Localized and isolated mountains[20,22] Crustal recycling through delamination[21] Radial contraction in lower lithosphere levels[19-22] Possible local subduction episodes in last stages[21, 23-26]	Delamination[c.f. 40] Possible plumes [c.f. 41]	Efficient juvenile crustal production on top, or near to, mantle plume heads[27,29-30] Convergence on top of downgoing plume cells[30] Crustal recycling through delamination and dripping[27,29] Possible short-lived local subduction episodes[29]	Contraction-like processes driven by sagduction [32-33,37] Dome rising [32-33,35] Crustal recycling through delamination and dripping [e.g.32-34] Possible short-lived local subduction episodes[e.g.33]

Lithological, structural, and geochemical proxies				
Ophiolites[8] Paired metamorphism (low T/P and high T/P coexistence)[15-16] Cold high-pressure metamorphism (e.g. blueschist, lawsonite-bearing rocks, jadeites and UHP rocks)[8,17] Arc-like geochemistry (e.g. enrichment in incompatible elements and depletion in Ta and Nb)[e.g.4] Sedimentary basins with large diversity of constituents[18] Passive margins[8] Accretionary prisms[8] Juxtaposition of rocks with different geological histories along faults	Sedimentary basins with local detrital components and relative contemporaneous to sedimentation[18] Allows for cold T/P gradients depending on resurfacing rate[20-21,23] Dome and vertical structures at the latest stages[25]	Relative old surficial crust[c.f. 41]	Sedimentary basins with local detrital components and relative contemporaneous to sedimentation[18] Dome-and-keel structures[e.g.27] Possible metamorphic gradients controlled by the dome structures[31-32]	Sedimentary basins with local detrital components and relative contemporaneous to sedimentation Dome-and-keel structures Possible metamorphic gradients controlled by the dome structures

*Due to the temperature of the Earth the cold stagnant lid regime is very unlikely to have occurred.

Refereces: [1]van Hunen and van den Berg (2008); [2]Sizova et al. (2010); [3]Korenaga (2018); [4]Polat et al., (2004); [5]Cawood et al. (2018); [6]Lenardic (2018); [7]Stern (2018); [8]Condie and Kröner (2008); [9]Dhuime et al. (2012); [10]von Huene and Scholl (1991); [11]Gerya et al. (2004); [12]Hacker et al. (2011); [13]Kelemen and Behn (2016); [14]Göğüş and Pysklywec (2008); [15]Brown (2010); [16]Brown and Johnson (2018); [17]Palin and Santosh (2020); [18]Zuo et al. (2021a); [19]O'Reilly and Davies (1981); [20]McKinnon et al. (2001); [21]Moore and Webb, (2013); [22]Bland and Mckinnon, 2016; [23]Kankanamge and Moore (2016); [24]Moore et al. (2017); [25]Beall et al. (2018); [26]Tang et al. (2020); [27]Van Kranendonk (2010); [28]Gerya (2014); [29]Fischer and Gerya (2016); [30]Van Kranendonk (2011); [31]Sizova et al. (2018), [32]François et al. (2014); [33]Sizova et al. (2015); [34]Rozel et al. (2017); [35]Lourenço et al. (2020); [36]Foley (2018); [37]Collins et al. (1998); [38] Coleman, 1971, [39] Solomatov (1995); [40]Fowler and O'Brien (1996); [41]Fowler and O'Brien (2003).

Plate tectonics might have been operating since the earliest stages of the Earth. However, the dynamics of the plates are likely to have been slightly different to the present conditions. Some authors have argued that ridges might have spread faster or their length might have been larger, which would translate in smaller and/or faster moving plates (Hargraves, 1986). Subduction also might have been different in the early stages of the Earth. It could have been shallower due to lower slab densities (Abbott et al., 1994), episodic (O'Neill et al., 2007) or short-lived (Sizova et al., 2010). Since subduction is typically regarded as one of the defining features of plate tectonics, the interpretation of different geological characteristics as product of this process is typically used as the ultimate evidence of plate tectonics operating for most

of Earth's history (e.g. Komiya et al., 1999, Nutman et al., 2013). However, different numerical simulations indicate that short-lived subduction is viable in a system dominated by sluggish lid tectonics (e.g. Sizova et al., 2010) or by hot plumes (e.g.(Gerya et al., 2015). Therefore, the recognition of isolated subduction-related environments is not a definite proof of plate tectonics. For plate tectonics to be the dominant geodynamic style, a global network of interconnected plate boundaries must be stablished in the planetary body (Cawood et al., 2018, Lenardic, 2018, Stern, 2018).

1.2.2. Stagnant lid tectonics

The stagnant lid mode (Table 1.1) contrasts with the active mobile lid as it is distinguished by a non-segmented "immobile" lithosphere that does not participate in the convection of the mantle (Bédard, 2018; Lenardic, 2018). This style of tectonics is sometimes referred to as single-lid tectonics (e.g. Stern, 2018). It can be further sub-divided into hot and cold stagnant lid regimes (Fig. 1.3b-c; Lenardic, 2018, Stern, 2018). In both cases, deformation and material interchange between the lithosphere and the mantle are driven by vertical movements. For example, crustal material can be recycled to the mantle via delamination processes (Fig. 1.3b-c). In hot stagnant lid setting heat is mainly lost by heat pipes (e.g. Fig. 1.3b) or plumes, while in the cold case the lithosphere is too strong and thick and the heat loss is mainly controlled by conduction through the lid (Fig. 1.3c).

An example of hot stagnant lid tectonics currently operating in an observable rocky body is the heat-pipe mode (Fig. 1.3b). It is the dominant tectonic style in Jupiter's moon Io (O'Reilly and Davies, 1981). The satellite has a higher surface heat flow than Earth, which lead to the hypothesis that the early Earth could have operated in this tectonic mode in its early stages due to the higher heat flow at the time (McKinnon et al., 2001; Moore and Webb, 2013). The heat-pipe mode is characterized by conduits in the lithosphere (heat-pipes) that effectively transfer material and heat from the mantle to the surface (Fig. 1.3b). Volcanic

activity is vigorous in the heat-pipe mode and rapid resurfacing events are expected (O'Reilly and Davies, 1981). As the rocks are erupted to the surface, the rapid extraction of material thickens the growing crust and allows for cold gradients and high pressures at the base of the crust (O'Reilly and Davies, 1981; Moore and Webb, 2013; Moore et al., 2017). This results in a thick lithosphere that radially compresses as it subsides towards the mantle (Fig. 1.3b). Radial contraction creates differential stresses that can lead to the development of thrust faults that start at the bottom of the lithosphere (Fig. 1.3b) (Bland and Mckinnon, 2016). Such processes can form isolated mountains and associated extensional features as it has been described for Io (McKinnon et al., 2001; Bland and Mckinnon, 2016). These faults could also provide pathways for magma extrusion (Bland and Mckinnon, 2016).

As the crust thickens due to the rapid resurfacing, and pressure increases in the crust, metamorphism of the mainly basaltic crust allows for partial melting and the generation of TTG suites (Fig. 1.3b; McKinnon et al., 2001; Moore and Webb, 2013). Sedimentary basins in a heat-pipe scenario mainly recycle relatively young material, such that the maximum depositional age and the youngest zircon in their detrital population have similar values (Zuo et al., 2021a).

Different numerical simulations of the heat-pipe model indicate that as the heat flow of the terrestrial body is reduced with time, the lithosphere will either experience breaking event(s) that ultimately leads to the onset of plate tectonics (e.g. Earth; Moore and Webb, 2013; Kankanamge and Moore, 2016; Moore et al., 2017; Beall et al., 2018; Tang et al., 2020) or it will transit to a cold stagnant lid mode (e.g. Mars; c.f. Kankanamge and Moore, 2016; Moore et al., 2017). Some simulations suggest that transition events are responsible for the cratonization of the ancient crust. Deformation during these events can create thrust faults and the typical domes of the Paleoarchean (Beall et al., 2018). Finally, the heat-pipe mode is predicted to act globally and it cannot operate with other tectonic modes (Moore and Webb,

2013; Kankanamge and Moore, 2016), such that it is argued that its recognition in an ancient terrane would imply its global operation on the Earth at that time.

1.2.2 Sluggish lid tectonics

The sluggish lid mode (Table 1.1) can be regarded as an intermediate style between the stagnant lid and the active lid scenario. It is defined by an active mantle convection that drives horizontal movements in the non-segmented lithosphere. However, in that case, the lithosphere moves at lower rates compared to the convection velocity (Foley, 2018; Lenardic, 2018). Sluggish geodynamics has been proposed as a mechanism, where the Earth heat loss was dominated by mantle plumes (Fig. 1.3d) (Abbott et al., 1994; Van Kranendonk, 2010; Gerya, 2014; Fischer and Gerya, 2016) and/or extensive plutonism (Fig. 1.3e) (François et al., 2014; Sizova et al., 2015; Rozel et al., 2017; Lourenço et al., 2020). It typically involves a more ductile lithosphere due the higher mantle potential temperatures than present conditions (Herzberg et al., 2007).

In the plume sluggish lid scenarios, the plumes drive the mantle convection cells and their dynamic is responsible of some of the key features observed in the Archean. For example, a thick dominantly mafic crust will develop on top of the plume (Fig. 1.3d; Van Kranendonk, 2010, 2011; Fischer and Gerya, 2016). The weaking of the crust due to repeating melting events and plutonism (Sizova et al., 2015; Fischer and Gerya, 2016; Rozel et al., 2017) could promote crustal overturns that are typically invoked to explain the formation of the dome-and-keel structures (Fig. 1.3e; e.g., Collins et al., 1998). These processes are also invoked for sluggish lid scenarios where plutonism occurs due to higher melting degrees in a hotter Earth dominate (Fig. 1.3e; e.g. Rozel et al., 2017; Lourenço et al., 2020). Overturns or sagduction events (Fig. 1.3e) can also be facilitated by a denser metamorphosed lower crust. This mechanism triggers dripping events that recycle crust to the mantle and allow the rise of

plutonic diapirs (Sizova et al., 2015; Fischer and Gerya, 2016) again creating the typical dome-and-keel structures.

The 3D architecture of the plume might also account for some plate tectonics-like features. For instance, it has been suggested that the down going wells produced by the plumes could be responsible of stacking crustal materials (Fig. 1.3e), with apparent collision or accretion (Van Kranendonk, 2011). Observations of other planetary bodies (c.f van Kranendonk, 2010) and numerical modelling (Fischer and Gerya, 2016) suggested that subduction can occur in the outskirts of the plume. Some authors also argue that large mantle plumes could actively control and drive lithosphere deformation and movement contemporaneously with plate-tectonic processes as subduction (van Kranendonk, 2010). Episodic subduction is also possible in sluggish lid scenarios with dominant plutonism (Fig. 3e; e.g. Sizova et al., 2015).

In these models, TTG generation is a consequence of the melt-assisted metamorphism experience by the mafic rocks at different levels of the crust (François et al., 2014; Sizova et al., 2015; Fischer and Gerya, 2016) to produce the "low", "mid" and "high"-pressure signature of the TTGs (Moyen and Martin, 2012).

1.3 When did plate tectonics start?

If the Earth might have experience other geodynamic modes in its past, then the question of when plate tectonics started is of great importance to understand the evolution of our planet. Earth might have experienced more than one geodynamic regime during its past, thus the recognition of one tectonic style does not necessarily exclude another. For example, some authors argue that the Earth might have transitioned from heat-pipe tectonics (Fig. 1.3b) to a form of sluggish tectonics (Fig. 1.3d-e) and then plate tectonics (Moore et al., 2017; Lenardic, 2018; Palin and Santosh, 2020; Palin et al., 2020b; Zuo et al., 2021a). Other works argue that the Earth experienced several transitions of different tectonic styles until the fully

operation of plate tectonic was stablished during the Neoproterozoic (Stern, 2018). These different views are a response to the paucity of the geological record and the interpretations authors withdraw from it.

First order observations indicate that the Archean metamorphic record is different from that found in modern Earth. Among the main distinctions are: (i) the absence of blueschists before 800 Ma (Maruyama et al., 1996) and of ultra-high pressure (UHP) rocks before 620 Ma (Jahn et al., 2001); (ii) the lack of subduction-related eclogite facies rocks before 2.87 Ga (Mints et al., 2010); and (iii) the gradual appearance of paired metamorphism from the Neoarchean (Brown, 2007; Brown and Johnson, 2018; Holder et al., 2019). As discussed previously, in modern Earth, the thermal gradients where these rocks and features are formed solely occur (or mainly in the case of eclogites) in subduction-related convergent margins (Ernst, 1971; Miyashiro, 1973; Brown, 2010). Thus, they appearance marks a minimum age for the initiation of long-standing subduction.

In the case of other plate tectonics indicators like ophiolites and accretionary prisms their first widely accepted appearance in the known geological record is not older than 2.7 Ga (c.f. Condie and Kröner, 2008; Palin and Santosh, 2020) However, debate exist on the oldest ophiolite record, for example, some authors argue that > 3.5 Ga ophiolites occur in Barberton (de Wit et al. 1987) and Isua (Furnes et al., 2007). Additional analyses and observations of the geological record also point to a change in geodynamics on the early Earth. For instance, the global geochemical and zircon record indicate an increased contribution of reworked crust for magma generation while juvenile mantle additions decreased after 3.0 Ga (e.g. Dhuime et al., 2012; Moyen & Laurent, 2018). Moreover, Eoarchean basins present zircon ages that are relatively young compared to the maximum depositional ages of their rocks, while in younger basins older zircons appear more frequently (Zuo et al., 2021a). Furthermore, large-scale geological features like the dome and keel structures are common in the Archean record, but

they are scarce or absent in younger terranes (Collins et al., 1998). The enlisted evidence and interpretations, support the increasing agreement of a Meso-Neoarchean transition in tectonic regime (e.g. Brown, 2006; Van Kranendonk, 2011; Gerya, 2014; Sizova et al., 2015; Brown and Johnson, 2018; Cawood et al., 2018; Holder et al., 2019; Hawkesworth et al., 2020; Palin and Santosh, 2020; Palin et al., 2020b).

Other data and interpretations are used to argue for the operation of plate tectonics as early as the Hadean. Detailed characterization of Hadean zircons from Jacks Hills (Australia) suggests that they are derived from an andesitic source (Turner et al., 2020) in a cold P/T gradient (Hopkins et al., 2008). Both characteristics are invoked as evidence of subduction. On a similar note, subduction is typically inferred from the arc-like composition of some Archean meta-igneous rocks (Polat and Hofmann, 2003; Jenner et al., 2009) or is based on the apparent contamination of sediment-derived components in the tonalite–trondhjemite–granodiorite (TTG) suites (Antonelli et al., 2021). The combination of this geological record is commonly used to argue for an uniformitarian view of a transition from a magma ocean to plate tectonics since the earliest stages of the Earth evolution (Korenaga, 2013, 2018; Maruyama et al., 2018; Nutman et al., 2021; Windley et al., 2021).

Thus, two main competing schools of thought are typically presented in the Archean geodynamics literature: either plate tectonics has operated since the Earth solidified, or it transitioned from a non-plate tectonic mode to plate tectonic mode around the Meso-Neoarchean. Consequently, a proper understanding of the processes that shaped the >3.0 Ga geological record is key to discern between the two main hypothesis.

1.4. The Isua supracrustal belt
1.4.1. Importance of Isua supracrustal belt for understanding Archean tectonics

The Isua supracrustal belt (ISB) is at the centre of controversial discussions on the onset of plate tectonics, since it has classically been interpreted as evidence for the operation of plate

tectonics as early as 3.8 Ga (e.g. Komiya et al., 1999; Polat and Hofmann, 2003; Jenner et al., 2009; Nutman et al., 2013; 2015, 2020, 2021), but its geological features also allow for non-uniformitarian tectonics (Gardiner et al., 2019; Webb et al., 2020; Rollinson, 2021; Zuo et al., 2021). The belt offers a great variety of lithologies and structures of different ages providing a window to a wide range of geological processes that could help to resolve this controversy. Despite all rocks in the belt have been metamorphosed, and some of them extensively metasomatized, the protoliths of most of them can still be identified. Metaigneous rocks, both intrusive and extrusive, are documented with compositions that range from ultramafic (e.g., Dymek et al., 1988) to felsic (Nutman, 1986). Detrital and chemical metasedimentary rocks also occur throughout the belt (Moorbath et al., 1973). Prograde, retrograde (e.g. Boak and Dymek, 1982) and fluid-rock interaction (Rosing et al., 1996) features have been described in the rocks of Isua. Additionally, the bulk of the protoliths in the ISB and associated rocks formed between 3.8-3.6 Ga (c.f. Nutman and Friend, 2009) and some of the later dykes have crystallization ages as young as 2.4 Ga (Nutman et al., 2004). The metamorphic events also occurred from the Eoarchean to the Neoarchean, thus covering an important time range in our understanding of the Earth where the geological record is scarce. All this well-preserved geological archive allows for a comprehensive study of intracrustal processes as well surficial processes that could provide insights on the tectonic history of the belt and the larger geodynamics of the Earth.

1.4.2. Geological framework of Isua – points of controversy and open questions

The ~35-km-long, arcuate Isua Supracrustal Belt (Fig. 1.4) is part of the North Atlantic craton (Fig. 1.1; Bridgwater et al., 1973) and is located in southwest Greenland as part of the northern part of the Itsaq Gneiss Complex (Fig. 1.4; Nutman et al., 1996). The ISB comprises a series of felsic and mafic metavolcanic rocks intercalated with cherts, banded iron formations (BIFs), clastic metasedimentary rocks, and minor ultramafic meta-igneous rocks

(Nutman et al., 1984). Analysis of a large U-Pb zircon dataset revealed that the supracrustal rocks can be sub-grouped in two distinct meta-volcanosedimentary sequences of 3.8 Ga and 3.7 Ga age, separated by a < 1km-thick, c. 3.75 Ga discontinuous metasedimentary sequence of chert, BIFs, and carbonates known as the "dividing sedimentary unit" (Nutman and Friend, 2009). The ISB is flanked by two km-scale TTG bodies with distinct crystallization ages of 3.8 Ga and 3.7 Ga (Fig. 2). Field observations of the ISB suggest that each sub-unit is exclusively in contact with the similar-aged TTG (Nutman and Friend, 2009).
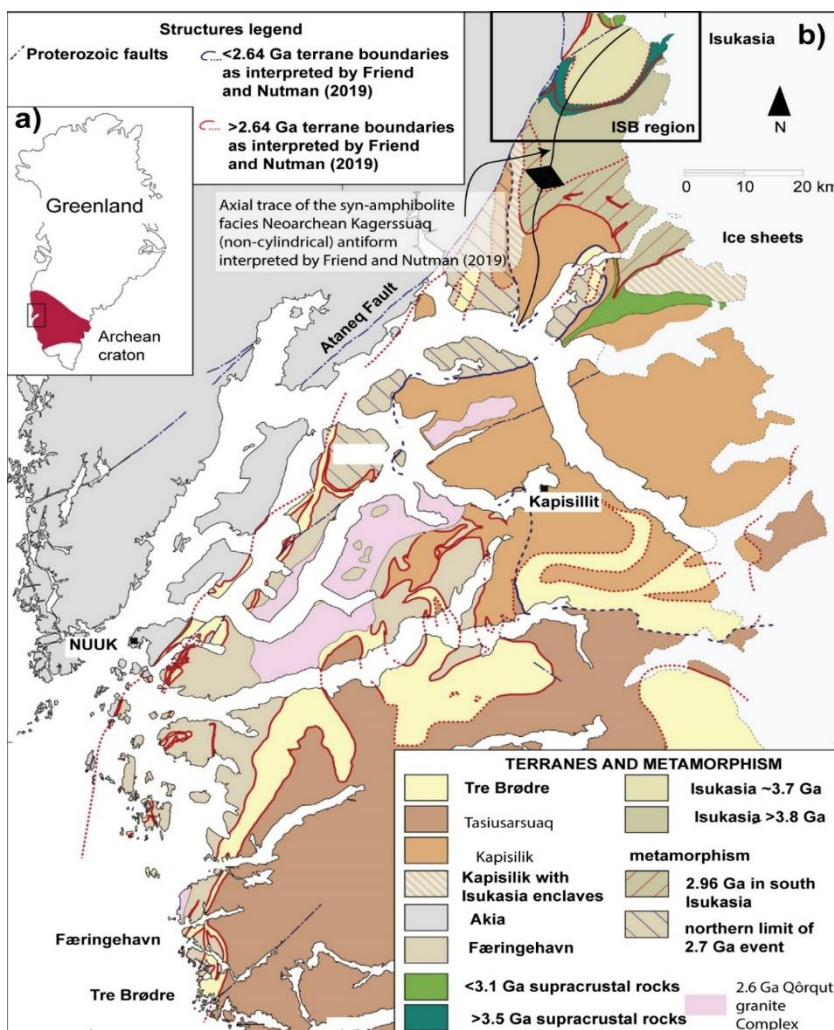
Figure 1.4 Geological map of the Nuuk Region (part of the North Atlantic craton). Some of the classic interpretations of the geology are highlighted. Modified after Friend and Nutman

Field work reports that supracrustal rocks within the belt and the associated TTG bodies were intruded by different dyke generations showing varying degrees of deformation. It has been

suggested that rocks across the entire belt were intruded by now strongly deformed tonalite-derived (Hiess et al., 2009, 2011) 3.66–3.60 Ga granitic dykes (Nutman & Friend, 2009). However, detailed inspection of the spatial distribution of these granitic intrusions recently revealed that they are mainly associated with the 3.7 Ga TTG or along its contact with the 3.7 Ga belt (Zuo et al., 2021b). The TTG bodies and the supracrustals are intruded by the E-W and N-S trending noritic to doleritic Ameralik dykes (Nutman, 1986; White et al., 2000). These dykes show weak deformation when crosscutting the TTG bodies, but their deformation is significantly higher towards and inside the supracrustals, such that there are reports of lineated plagioclase and hornblende in the dykes (Nutman, 1986; White et al., 2000). These dykes are typically used as markers to date the deformation and metamorphism, but their characteristics allow for contrasting interpretations of the tectonometamorphic history of the belt (c.f. Nutman et al., 2022; Ramírez-Salazar et al., 2022).

Mafic rocks of igneous origin comprise most of the bulk of the ISB. They generally display boninite-like (high Al_2O_3/TiO_2) and enriched tholeiitic-like (low Al_2O_3/TiO_2) compositions (Polat et al., 2002; Jenner et al., 2009; Hoffmann et al., 2010). The mafic rocks are typically enriched in incompatible elements, have negative Nb-Ta anomalies and fractionated REE patterns (Hoffmann et al., 2010; Jenner et al., 2009; Polat et al., 2002). The ultramafic lenses within the belt display harzburgitic and dunitic compositions with fractionated PGE trends and low Ir, Or, Pt and Pd contents and high abundance of Ni (Szilas et al., 2015; Waterton et al., 2022). Most of the ultramafic rocks show signs of carbonization and/or serpentinization (Dymek et al., 1988). The geochemical signatures of the igneous-derived rocks of Isua are commonly regarded as evidence for the operation of subduction and, by extension, plate tectonics. On the one hand, the basaltic rocks have chemical signatures broadly associated to arc-magmatism (Hoffmann et al., 2010; Jenner et al., 2009; Polat et al., 2002). On the other hand, the ultramafic rocks are thought to represent mantle slices (Friend and Nutman, 2011).

However, more recent interpretations of the geochemical and petrological record of these rocks propose that the petrogenesis of the basalts can be explained by the mixing of different mantle reservoirs (Rollinson, 2021) with the ultramafics as their cumulitic counterparts (Szilas et al., 2015; Waterton et al., 2022). The latter interpretations on the geochemistry of the metaigneous rocks point to the possibility that melts were generated in a non-uniformitarian setting (e.g., Gardiner et al., 2019; Rollinson, 2021).

Parts of the ISB show primary igneous and sedimentary structures including pillow basalts (Nutman et al., 1996), graded bedding (Nutman, 1984), cross lamination (Nutman et al., 2017), and potentially relic stromatolites (Nutman et al., 2016). These structures reveal deposition under water and they have been interpreted to mark areas of low deformation (e.g., Nutman et al., 2016). On the contrary, some authors argue that in some areas important shear localized structures (interpreted as ∼10-m-scale > 3.5 Ga shear zones) can be recognized in the belt (Komiya et al., 1999; Nutman and Friend, 2009). This classic interpretation of the geology of Isua points to the existence a differential intensity of deformation along the belt. However, recent field observations suggest that areas with apparently unaltered structures have also experienced penetrative widespread deformation and metasomatism (Allwood et al., 2018; Webb et al., 2020) and quantitative analysis of quartz fabrics in samples from different parts of the eastern arm of the belt, including areas interpreted as shear zones, show that the strain intensity across the belt is quasiuniform (Zuo et al., 2021b).

The data on the geology of Isua is vast, but as briefly summarized here the interpretations of these data have led to contrasting conclusions on the geodynamic settings in which the belt formed. Two main points of contention sitting at the centre of the contrasting tectonic models proposed for the ISB are its structural and metamorphic record. In the case of the structural record, two main interpretations invoke the distribution of the apparent shear zones in the belt. One of the interpretations argue for the occurrence of SE-vergence duplex structures that

exhibit the ISB as an old accretionary prism (Komiya et al., 1999) and then would reflect the operation of an ancient subduction zone (Model A, Fig. 1.5a). The alternative model suggests that the interpreted shear zones indicate tectonic juxtapositions of different tectonostratigraphic packages, with the main tectonic break being the c.3.75 Ga dividing sedimentary unit that separates two different terranes of c. 3.7 Ga and c. 3.8 Ga ages (e.g., Nutman and Friend, 2009). The existence is two terranes, in turn, would argue for a continent-continent collision (Model B, Fig. 1.5b). In both of these interpretations of the structure of the belt, the arcuate shape of Isua is consequence of a later folding event that affected other terranes in the Itsaq Gneiss Complex (Friend and Nutman, 2019).

A recent re-evaluation of the geochronological and structural data of the belt, however, proposed that the belt represents a continuous volcano-sedimentary sequence that was folded into a sheath fold during a major tectonometamorphic event (Webb et al., 2020). Parallelism between the metamorphic lineations and fold axis at different scales support this claim (Webb et al., 2020; Zuo et al., 2021b). Such interpretation argues for the operation of non-uniformitarian tectonics during the formation of the ISB (Model C; Fig. 1.5c).

These three main structural interpretations of the belt are also accompanied by distinct interpretation and predictions of the metamorphic record of the belt. They particularly differ in the major deformation event that created most of the lineations and foliations in the rocks. Model A indicates the presence of a metamorphic gradient with increasing metamorphic grade towards the SW of the eastern arm of the belt (Fig. 1.5a.i; Komiya et al., 1999, 2002; Hayashi et al., 2000; Arai et al., 2015). Model B argues for an increase in metamorphic grade from the 3.8 Ga belt towards the centre of the 3.7 Ga tonalite (Fig. 1.5b.i; Nutman et al., 2013; 2020) with the presence of paired metamorphism inferred in the chemistry of the tonalites and the mineralogy of supracrustal enclaves in the tonalites (Nutman et al., 2013; 2020). Finally, Model C predicts that the metamorphism of the belt, as well as the

deformation, were quasi-homogenous (Fig. 1.5c.i). Model B and C also differ in the number of the main metamorphic events recorded in the rocks of the belt. Model B invokes different metamorphic events with contrasting metamorphic grades. They are interpreted in mineralogy of the ultramafic rocks (e.g. Nutman et al., 2020) and the microstructures and chemical zoning of the garnets of the supracrustals (e.g. Gauthiez-Putallaz et al., 2020). On the other hand, Model C suggests that most of the metamorphic characteristics of the Isua rocks can be explain with a single tectonometamorphic event at amphibolite facies grade (Webb, et all., 2020; Zuo et al., 2021b, Ramírez-Salazar et al., 2022). It is also important to mention that the absolute age of the syn-metamorphic prograde events is not yet resolved as the timing of the post-tectonic metamorphism is also a matter of debate, but most authors agree this event is later to the one (or those) that created most the foliations and lineations of the rocks (Boak and Dymek, 1982; Rollinson, 2002, 2003; Nutman et al., 2013, 2020; Gauthiez-Putallaz et al., 2020; Webb et al., 2020; Zuo et al., 2021).

As briefly summarize here, deciphering the metamorphic evolution of Isua and discussing the different metamorphic interpretations for the belt is crucial to have a better understanding of its tectonic evolution. This is not only important for the history of the belt, but it has larger implications for the geodynamic interpretations of the early Earth. This works aims to provide new metamorphic data (P-T-X-D-t) for the ISB using an integrative approach. Summaries and details of the main points of contention of the metamorphic data presented so far are given in the different chapters. The new data is then used to discuss and analyse the different interpretations and their implications for the tectonic models proposed for the belt. Limitations and final discussion are provided at the end of these thesis, as well as a summary of future points to study to broaden our knowledge of the ISB.
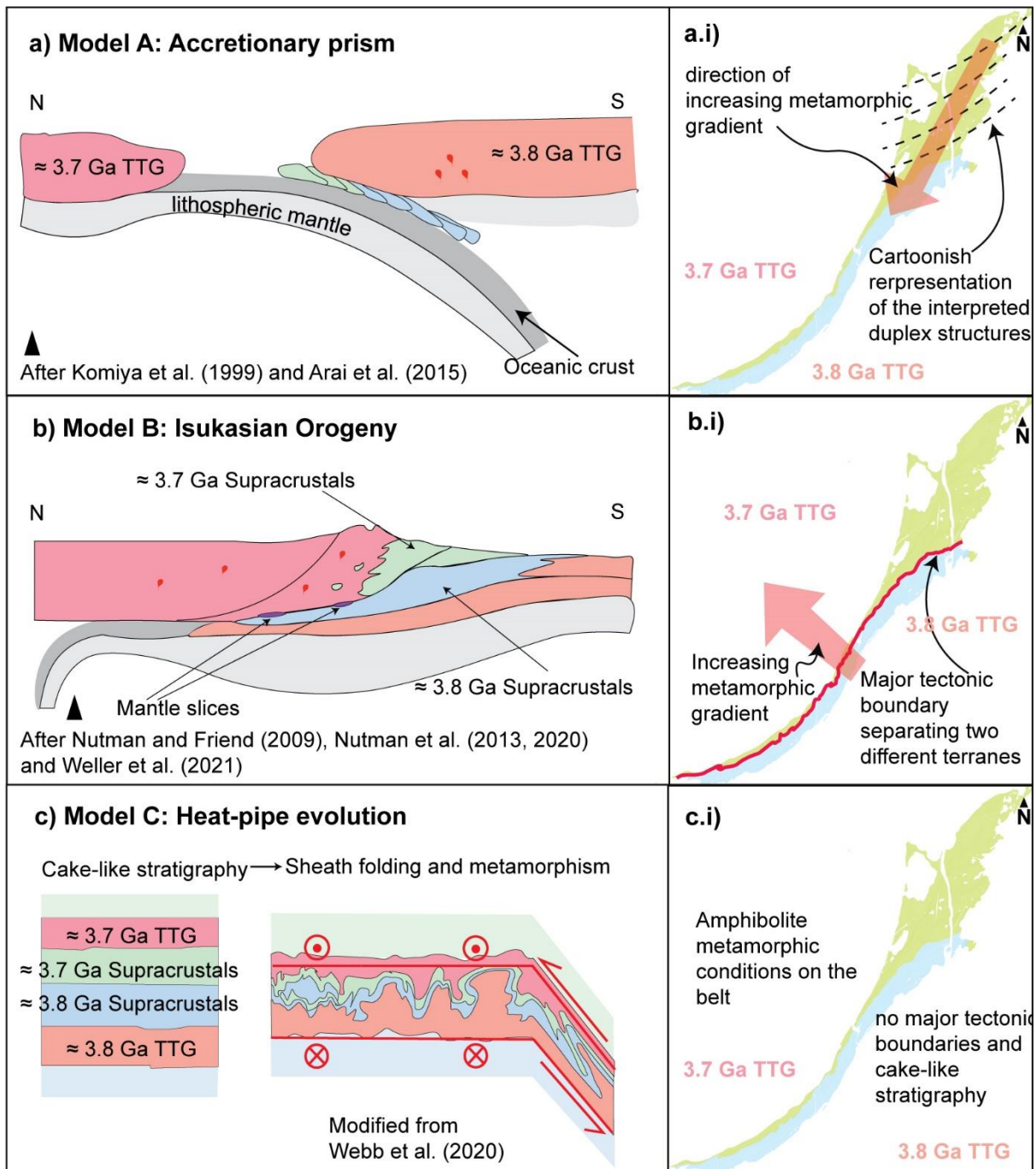
Figure. 1.5(a-c) Proposed models for the evolution of the Isua supracrustal belt and (a.i-c.i) their predicted major structures and metamorphic gradient. Most of these predictions have been made mainly in the eastern arm of the belt, therefore this is the part that is shown. Location of the tonalites is highlighted with their ages in colours.

1.5 Thesis aims and objectives

To date, studies focusing on the metamorphic evolution of the ISB result in contrasting

interpretations. There is no consensus on the timing and estimates of peak conditions related

to the main tectono-metamorphic events and apparent contradictions are rarely discussed. Therefore, this work aims to provide a comprehensive description of the metamorphic history of the Isua supracrustal belt to test the validity of the proposed tectonic models for the belt. As a result the main objective of this thesis is to reconstruct the P-T-X-D-t history of the ISB. The reach this objective, the detail metamorphic evolution of the ISB will be retrieve by using a combination of techniques in different rocks across the entire eastern arm of the belt to then test the proposed tectonic models. Hence, the following aims are defined:

•   Aim 1: To obtain the peak (P-T) conditions and identify the different metamorphic events recorded in the belt by using a combination of thermodynamic techniques and microstructural observations. They will be applied to a set of samples systematically collected from north to south of the belt to account for possible variations on the metamorphic condition.

•   Aim 2: To characterize in detail the garnets across the belt to understand the factors controlling their microstructural and chemical diversity. Garnets are known to be good metamorphic indicators (e.g. Tracy and Robinson, 1976; Spear et al., 1984; St-Onge, 1987) hence the garnet record in the ISB might reflect different metamorphic histories or they might be controlled by growth processes. Characterization of garnet chemistry, microstructural domains, crystallographic features and their associated context will be used to discern between hypotheses.

•   Aim 3: To obtain a robust P-T-X-D path for the ISB. Using garnets showing large equilibrium features, quantitative modelling testing different P-T-X paths will be carried to produce the observed garnet profiles. Information retrieved from the microstructures will complete the full characterization of the P-T-X-D path. Qualitative data will complete the dataset to account for possible variations across the belt.

• Aim 4: To date the different metamorphic events recorded in the belt by using a combination of geochronometers in different lithologies. Apart from supracrustal samples within the belt, enclaves and a meta-granite will be studied for comparison. The data aims to complete the P-T-X-D-t evolution of the ISB.

1.6 Thesis outline

The thesis consists of six chapters. Chapter 1 is this introduction and provides a general overview of the state of the art of the ISB and discussions on Archean geodynamics. Here, an overview of the relevant lithologies and cross-cutting relationships is provided as well as a summary of the main points of controversy on the belt. Specific aspects associated to the metamorphic record of the belt are described in the subsequent chapters. Chapter 2-4 include original research and contributions on the metamorphic evolution of the ISB and provide insights on garnet growth processes within the tectono-metamorphic context of the belt. Chapter 5 provides work in progress on the geochronology of the ISB using different metamorphic minerals from different microstructural domains. Chapter 6 consists of an overall discussion of the main findings presented in the thesis and its implications for the tectonic interpretations of the belt and it finally offers general conclusions of this work and suggestions for future avenues of research.

Chapters 1 and 6 are authored and solely written by the PhD candidate, while chapters 2, 3, 4, 5 represent work in collaboration with other scientists. For the latter cases, each Chapter is introduced in a Preamble outlining the authors contribution. Besides the contributions provided in this thesis, the candidate was involved in 3 additional pieces of work (Webb et al., 2020, *Lithosphere*; Zuo et al., 2021b, *Tectonics*; Ramírez-Salazar et al., 2022, *Tectonics*) contributing overall the gain in knowledge regarding the Isua Supracrustal Belt evolution. These were submitted with the thesis.

Chapter 2 (aim 1) is mainly based on the original paper by Ramírez-Salazar et al. (2021), which was published along with Zuo et al. (2021b). Therefore, parts of the chapter directly address findings of the sister study. In the study, a systematic selection of samples covering north-south and east-west transects are used to distinguish the main metamorphic events that affected the ISB. Microstructural and mineralogical descriptions in combination with quantitative phase equilibria thermobarometry and classic thermometry allowed to distinguish three main metamorphic events and their P-T conditions. The findings also provide a possible explanation for the apparent contradictions in the previous interpretations of the metamorphic record of the belt.

Chapter 3 (aim 2) is largely based on the content of Ramírez-Salazar et al. (in prep), which will be submitted for publication to Contributions to Mineralogy and Petrology. Using garnet-bearing samples presented by Ramírez-Salazar et al. (2021) and Zuo et al. (2021b) and an integral combination of techniques, the chapter centres around the growth mechanisms affecting the diversity of garnet microstructures. We present evidence to show that the different microstructures and chemical zoning of the Isua garnets are product of variations in bulk composition and local microstructures ultimately affecting the availability of garnet-forming material.

Chapter 4 (aim 3) builds on the findings presented in chapter 3. Here, garnets showing large-scale equilibrium characteristics are used to model the P-T-X-D-t evolution of the ISB. A quantitative P-T-X-D-t paths is reconstructed using thermodynamic modelling for a specific bulk compostion (X). Qualitative approximations to the metamorphic evolution of other samples are also presented to complete the dataset. Trace element data, quartz-in-garnet geobarometry, alongside thermodynamic data from chapter 1 are used for qualitative approximations. This chapter is written as a scientific publication draft. It is anticipated that this part of the PhD will be submitted soon after thesis submission.

Chapter 5 (aim 4) presents preliminary geochronological data. Here, Sm-Nd and Lu-Hf in garnet and U-Pb in-situ titanite and rutile data are presented in attempt to date two main medium temperature metamorphic events. This chapter is written as a scientific publication draft. It is anticipated that this part of the PhD will be submitted soon after thesis submission.

Notably, there is some inevitable overlap, especially in terms of the geological background and methods section as chapters 2-5 are written in form of individual self-standing scientific contributions.

Chapter 2: P-T-*X*-d constraints of the Isua supracrustal belt, a poly-metamorphic terrane

This chapter has been published in the journal *Tectonics* on February 6th 2021. The original of publication is entitled *Tectonics the Isua Supracrustal Belt 1: P-T-X-d Constraints of a Poly-Metamorphic Terrane* (Ramírez-Salazar et al., 2021). Minor modifications have been made for the format of the thesis (e.g. title of the Chapter), but most of it remains as the original published paper. I was the first author of the paper with Thomas Müller, Sandra Piazolo, A. Alexander G. Webb, Christoph Hauzenberger, Jiawei Zuo, Peter Haproff, Jason Harvey, Tsz Kin Wong, and Callum Charlton as co-authors. I was in charge of the conceptualization, manuscript writing, most of data collection, figures, thermodynamic modelling and analysis. Thomas Müller and Sandra Piazolo supervised and were involved in the conceptualization of the work. Sample collection was made by Thomas Müller, A. Alexander G. Webb, Jiawei Zuo and Peter Haproff. Tsz Kin Wong and Callum Charlton obtained microprobe data as part of his MSc thesis project. All authors were involved in the editing and reviewing of the work. Furthermore, review comments by Matthijs A. Smit and Hugh Rollinson improved the manuscript. This paper was submitted along with Zuo et al. (2021b) *Tectonics of the Isua Supracrustal Belt 2: Microstructures Reveal Distributed Strain in the Absence of Major Fault Structures*, thus parts of the chapter make direct reference to this work.

Abstract

The Eoarchean Isua Supracrustal Belt (ISB) has been interpreted as one of the earliest records of subduction processes, leading to the conclusion that a plate tectonic geodynamic system was likely operating since the early Archean. However, proposed tectonic models remain difficult to evaluate as our understanding of the metamorphic and structural evolution remains fragmentary. Here, we present a metamorphic study of the supracrustal rocks of the

ISB. We used petrographic and microstructural observations, phase equilibria, isopleth geothermobarometry and conventional thermometry to explore the prograde, peak, and retrograde metamorphic evolution of the northeastern ISB. Our results show that the ISB records a syn-tectonic, amphibolite facies metamorphic event (M_1) with peak conditions of 550-600 °C and 0.5 – 0.7 GPa. M_1 was followed by a static, lower amphibolite facies metamorphic event (M_2; < 540 °C and <0.5 GPa). Published constraints suggest that M_1 and M_2 occurred in the late Eoarchean (>3.5 Ga) and the Neoarchean (<2.9 Ga), respectively. These events are partially overprinted by late low temperature (< 500 °C) retrogression (M_3) that is most intensely developed in the northeastern part of the belt; it typically overprints some peak mineral phases while preserving the peak fabric. Our findings are consistent with spatially-homogeneous syn-tectonic amphibolite facies metamorphism and macroscale folding. Such features are predicted by a heat-pipe tectonic model. Therefore, our findings permit the interpretation of the Isua supracrustal belt as a record of early non-uniformitarian tectonic processes.

2.1 Introduction

Models to describe the nature of the Earth's crustal evolution during the Archean vary substantially, from horizontal lithospheric motions with subduction-like movement (Abbott et al., 1994), to vertical tectonics defined by sub-/intra-lithospheric diapirism (Collins, 1989; Sizova et al., 2015), extensive volcanism (Turcotte, 1989; Moore & Webb, 2013), and the formation of a single-plate lithosphere. First-order questions include when and how horizontal lithospheric motion (e.g., subduction) became the dominant process by which Earth's interior cools, deforms, and evolves (Lenardic, 2018). A change in geodynamics between ~3.2 – 2.5 Ga is proposed based on the global geochemical and zircon record indicating an increased contribution of reworked crust, typically associated with recycling along subduction zones, for magma generation while juvenile mantle additions decreased

during that time (e.g. Dhuime et al., 2012; Moyen & Laurent, 2018). A recent review of the existing metamorphic record suggests that Earth has experienced spatial and temporal changes of global crustal thermal gradients probably linked to transitions in the tectonic regime, from stagnant-lid tectonics to mobile-lid plate tectonics (Brown & Johnson, 2018). The main changes occurred at ~2.5 Ga, ~1.0 Ga, and 0.72 Ga, Ga which are associated with the widespread appearance of paired metamorphic belts, dominance of high T/P gradients (>775 °C/GPa ≈ 22°C/km[1]), and increasing abundance of low T/P gradients (< 375 °C/GPa ≈ 11°C/km), respectively. The presence of a distinct bimodality of low and high T/P gradients is indeed a feature commonly associated with plate tectonics (Miyashiro, 1961; 1973; Brown, 2010) and its gradual emergence argues for progressive onset and evolution to active lid geodynamics since the Neoarchean (Holder et al., 2019). In stark contrast with these interpretations, multiple subduction-driven events are invoked to explain the origin and evolution of the Eoarchean Isua Supracrustal Belt of southwest Greenland (Fig. 1), one of the oldest metamorphic terranes known, which some workers have interpreted to reflect the onset of plate tectonics as early as 3.6-3.8 Ga (Komiya et al., 1999; Nutman & Friend, 2009; Nutman et al., 2015). Structural studies of the belt (Webb et al., 2020) together with new geochemical data of the adjacent Eoarchean tonalite-trondhjemite-granodiorite (TTG) bodies (Gardiner et al., 2019) challenge the unequivocal interpretation that the Isua Supracrustal Belt was generated in an active lid tectonics regime (Fig. 1.3a) and alternatively suggest that a sluggish lid scenario (Fig. 1.3b) is equally plausible. Despite the importance of the metamorphic evolution in deciphering the geodynamic setting of an area (e.g. Miyashiro, 1961; Brown, 1993; Brown & Johnson 2018), studies of the metamorphic evolution of the Isua Supracrustal Belt are relatively scarce (e.g., Boak & Dymek, 1982; Dymek et al., 1988; Hayashi et al., 2000; Appel et al., 2001; Blichert-Toft & Frei, 2001; Frei et al., 2002; Komiya

---

[1] Assuming 1GPa=35 Km

et al., 2002; Rollinson, 2002, 2003; Heijlen et al., 2006; Arai et al., 2015; Gauthiez-Putallaz et al., 2020; Nutman et al., 2020), and existing studies present results with contrasting distributions of the P-T peak conditions across the belt and conflicting P-T evolutions.

In this contribution, we present a systematic analysis of the P-T-*X*-d-(t) evolution of the Isua Supracrustal Belt, linking metamorphic data to structural data at the micro to macro scale. In-depth petrographic observations combined with classic and phase equilibria geothermobarometry provide an extended dataset that allows us to identify the number of metamorphic events, their respective peak conditions recorded in the belt, and their spatial distribution. We present our results alongside a companion study on the microstructures and strain distribution recorded in the syn-tectonic fabrics of quartz-rich lithologies, centered on strain and shear sense analyses (Zuo et al., 2021b). The dataset presented here enables us to discuss in depth the metamorphic spatial and temporal evolution of the belt in terms of endmember tectonic models and hence implications for Archean geodynamics.

1.2 Geological setting, previous work and interpretations

The ~35-km-long, arcuate Isua Supracrustal Belt (ISB) (Fig. 2.1) is part of the North Atlantic craton (Bridgwater et al., 1973) and is located in southwest Greenland as part of the northern part of the Itsaq Gneiss Complex (Fig. 1.4; Nutman et al., 1996). The ISB comprises a series of felsic and mafic metavolcanic rocks exhibiting arc-like geochemistry (e.g. Polat et al., 2002) intercalated with cherts, banded iron formations (BIFs), clastic metasedimentary rocks, and minor ultramafic meta-igneous rocks (Nutman et al., 1984). The ISB is flanked by two km-scale TTG bodies with distinct crystallization ages of 3.8 Ga and 3.7 Ga (Fig. 2.2). Analysis of a large U-Pb zircon dataset revealed that the supracrustal rocks can be sub-grouped in two distinct meta-volcanosedimentary units of 3.8 Ga and 3.7 Ga age, separated by a < 1km-thick, c. 3.75 Ga discontinuous metasedimentary sequence of chert, BIFs, and carbonates known as the "dividing sedimentary unit" (Nutman & Friend, 2009). Field

observations of the ISB suggest that each sub-unit is exclusively in contact with the similar-aged TTG. In addition, some deformed 3.66-3.6 Ga granitic intrusions (Nutman & Friend, 2009) and the weakly-deformed, c. 3.5 Ga Ameralik dykes cross-cut both the 3.8 Ga and 3.7 Ga supracrustal rocks and the TTGs (Nutman et al., 2004) suggesting a shared history since at least 3.66 Ga.
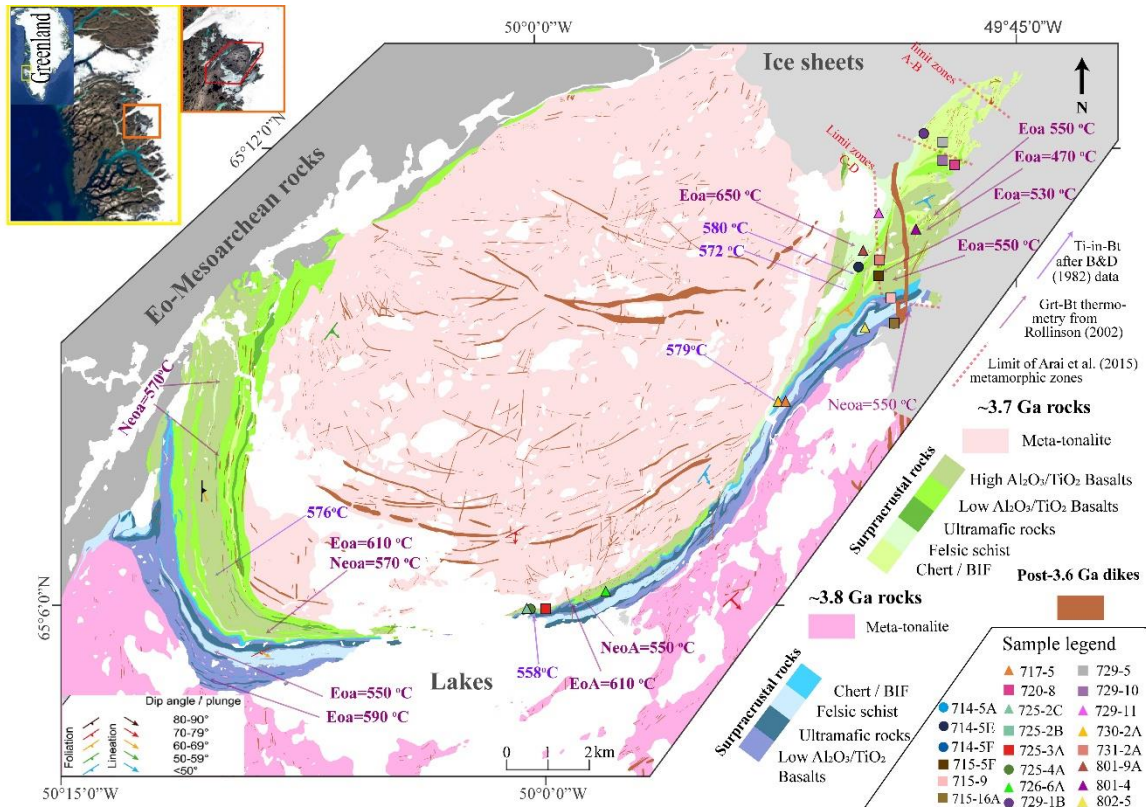
Figure. 2.1 Geological map of the Isua Supracrustal Belt showing the location of samples used in Chapter 2, modified from Zuo et al. (submitted) and Nutman & Friend (2009). Garnet-biotite temperatures from Rollinson (2002) are divided into Eoa=Earchean and Neoa=Nearchean metamorphic events, according to the interpretations of the author. Colour and symbol coding of the samples follows the rest of the figures, symbol coding represent the interpreted protolith: triangles: felsic meta-volcanic rocks; squares: meta-mafic rocks (amphibolites and mafic schists); and circles: meta-sedimentary rocks (metapelites and BIFs). Samples that share locality/outcrop: 714-5A, 714-5E and 714-5F; 725-2c and 725-2b; 729-1B and 729-1A.

Parts of the ISB show primary igneous and sedimentary structures including pillow basalts (Nutman et al., 1996), graded bedding (Nutman, 1984), cross lamination (Nutman et al., 2017), and relic stromatolites (Nutman et al., 2016); these have been interpreted to mark areas of low deformation (e.g., Nutman et al., 2016). However, the existence of some of these

structures and the differential intensity of their deformation have recently been questioned (Allwood et al., 2018; Webb et al., 2020), suggesting that most of the exposed rocks show signs of deformation and metamorphism that clearly modified the primary structures. In the literature, multiple metamorphic events have been documented in the ISB, some of which are only locally reported (e.g., low-grade sea-floor hydrothermal metamorphism; Appel et al., 2001), with broadly two major medium- to high-temperature episodes recognized and documented to have affected the entire belt. These events are typically placed in the Eoarchean and Neoarchean based on several isotopic ages that are interpreted to reflect the metamorphic age of the events (Fig. 2.2; Shimizu et al., 1990; Gruau et al., 1996; Frei et al., 1999; Rosing & Frei, 1999; Blichert-Toft & Frei, 2001; Crowley et al., 2002; Crowley, 2003; Nutman et al., 2013). The most pervasive metamorphic event is syntectonic to the penetrative foliations, that are parallel to the belt margins, and steep southeast-plunging lineation (Fig. 2.1; e.g. Webb et al., 2020) that are characteristic of the Isua rocks (e.g. Boak & Dymek, 1982). For this event, the weakly-deformed Ameralik dykes cross-cutting the belt provide a minimum age of c. 3.5 Ga (Nutman et al., 2004). The younger event is recognized in post-tectonic garnet rims (Blichert-Toft & Frei, 2001; Rollinson, 2002, 2003) and non-foliated lower amphibolite metamorphic paragenesis in the Ameralik dykes (Nutman et al., 2004). Additionally, detailed investigations of the textures and chemical composition of garnets across the belt revealed the common appearance of three to four distinct zones (core-annuli-rim) within individual grains (Rollinson, 2002, 2003; Gauthiez-Putallaz et al., 2020), leading to the interpretation that the core could represent an earlier medium-temperature metamorphic episode preceding the large syn-tectonic event (Fig. 2.2) responsible for most of the deformation (Rollinson, 2002; Gauthiez-Putallaz et al., 2020).
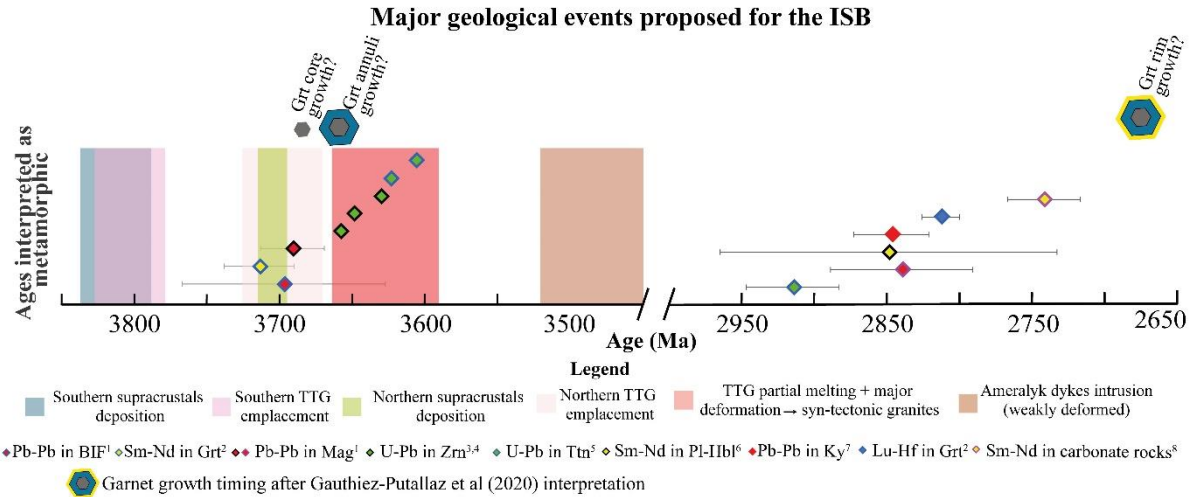
Figure 2.2 Timeline showing the major geological events interpreted for the ISB (bands) and ages interpreted as metamorphic (motifs with error bars). Interpretation of the garnet growth from Gauthiez-Putallaz et al. (2020). Geochronological data from Nutman & Friend (2009). Metamorphic ages references: 1. Frei et al., (1999); 2. Blichert-Toft & Frei (2001); 3. Nutman et al (2013) 4. Crowley, (2003); 5. Crowley et al., (2002); 6. Gruau et al. (1996); 7. Rosing & Frei (1999); 8. Shimizu et al., (1990)

2.1 Tectonic models for the Eoarchean evolution of the ISB and their relationship with the metamorphic record

The tectonic scenario responsible for the Eoarchean tectono-metamorphic event during which the most pervasive mineral, microstructural and deformational features of Isua developed is still debated. Three main models have been proposed (Fig. 3.3): two models proffer uniformitarian plate tectonic interpretations (e.g. Komiya et al., 1999; Nutman & Friend, 2009; Nutman et al., 2013, 2020; Arai et al., 2015), and a third model suggests that heat-pipe tectonics could explain the geological record of Isua (Webb et al., 2020).

Both plate tectonic models predict systematic metamorphic patterns across the area. The first plate tectonic model (Model A) suggests that the ISB represents an accretionary complex characterized by southeast-directed duplex structures in the supracrustal rocks (Komiya et al., 1999), which developed during the subduction of the oceanic plate attached to the 3.7 Ga TTG under the ≈3.80 TTG (Fig. 3a, Komiya et al., 1999; Arai et al., 2015). This model anticipates a metamorphic gradient with increasing P-T conditions from north to south across

the northeastern portion of the belt (Hayashi et al., 2000; Komiya et al., 2002; Arai et al., 2015). This is consistent with a suggested northeast-southwest increase in P-T conditions based on mineral composition and phase equilibria geothermobarometry from the end of the northeastern belt to the central part of it from 0.3 GPa and 380 ºC to 1.1 GPa and 800 ºC (Fig. 2.1; Arai et al., 2015).
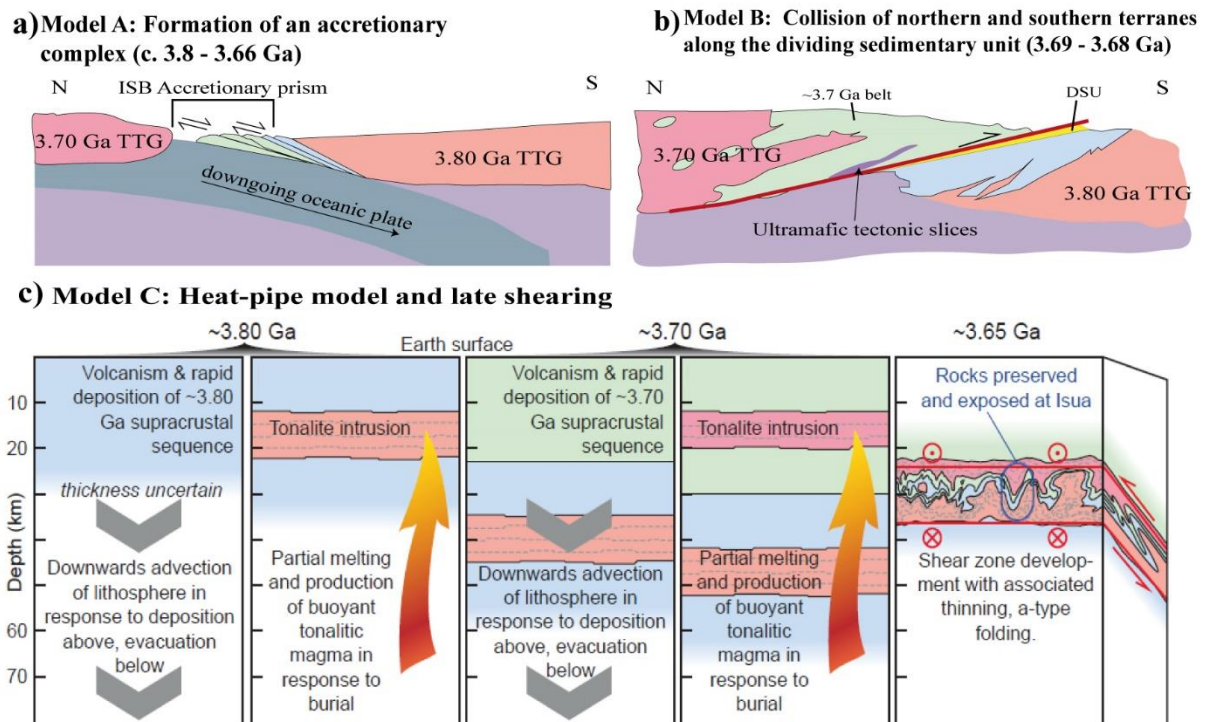
Figure. 2.3 Tectonic models proposed for the evolution of the ISB. (a) Model A: South-dipping accretionary complex model (modified from Arai et al., 2015) (b) Model B: North-dipping subduction-collision model (modified from Nutman and Friend, 2009); (b); and (c) Model C heat-pipe model (modified from Webb et al., 2020).

The second plate tectonics model (Model B) argues for orogenic crustal thickening in response to collision of two proto-arcs, with subsequent orogenic collapse via development of an extensional core complex (Nutman et al., 2013). In this model, north-dipping subduction of the 3.8 Ga belt under the 3.7 Ga belt drives the collision with the dividing sedimentary unit acting as the tectonic boundary (Nutman & Friend, 2009) (Fig. 3.3b). Syn-deformational Barrovian-type metamorphism is predicted for this model, with P-T conditions increasing continuously from the 3.8 Ga belt to the 3.7 Ga TTG (Nutman et al., 2013). The reported

early metamorphic event recorded in garnet cores of the 3.7 Ga sequence has been interpreted

in support of this model, attributed to the amalgamation phase of the proto-arc (Gauthiez-

Putallaz et al., 2020; Nutman et al., 2015). Based on the report of kyanite in metapelites of

the 3.7 Ga belt and garnet-clinopyroxene-hornblende-quartz-plagioclase assemblages in the

center of the 3.7 Ga TTG, Nutman et al. (2013) interprets an increase in P-T conditions, from

greenschist/lower amphibolite facies in the 3.8 Ga belt to amphibolites facies in the 3.7 Ga

belt and up to high-pressure granulite facies in the center of the 3.7 Ga TTG. The authors

then argue that this interpretation is consistent with subduction type tectonic model. In

addition, a metamorphic record typical for paired metamorphic belts characteristic of

convergence tectonics in young metamorphic belts (Miyashiro, 1961; 1973; Brown, 2010) is

expected for Model B, with low T/P gradients developing in the subducting plate and high

T/P gradients in the upper plate (Nutman et al., 2020). Nutman et al. (2020) argue using

phase equilibria diagrams from a mid-ocean-ridge basaltic protolith and zircon-TTG trace

element chemistry, that there is indeed a paired metamorphism preserved in Isua and the Itsaq

Gneiss Complex (Fig. 1.4). In their interpretation, cold T/P gradients (< 500 ºC/GPa) are

recorded in the high-pressure garnet-granulites and in the garnet/rutile chemical signature of

the TTGs, which may represent partial melting of garnet-rutile eclogites. In contrast, hot T/P

conditions (>1000 ºC/GPa) would be represented by TTGs with no signature of residual

garnet and in equilibrium with orthopyroxene-granulites (Nutman et al., 2020). Nutman et al.

(2020) suggest even colder gradients (<200 ºC/GPa) due to the interpretation of ultra-high

pressure (UHP) metamorphism on the basis of the presence of F bearing Ti-

chondrodite/clinohumites in some ilmenite-carbonate dunites. However, it is important to

bear in mind, that halogens, ilmenite and CO_2 have been shown to stabilize Ti-

chondrodite/humite to higher temperatures and lower pressures in other settings (c.f. Ehlers &

Hoinkes, 1987; Shen et al., 2015), thus questioning these rocks to unequivocally represent UHP conditions.

The heat-pipe model (Model C) suggests that the Isua supracrustal belt was emplaced via rapid volcanic resurfacing, depositing first the rocks from the 3.8 Ga belt and then the younger lithologies in straight stratigraphic sequence (Webb et al., 2020). Intervals of rapid deposition led to burial, static metamorphism, and melting of deeply buried hydrated mafic crust to form TTGs. Subsequently, a tectono-metamorphic episode produced amphibolite-facies syn-tectonic metamorphism and structural thinning across the whole belt in response to either (a) heat-pipe contraction (global lithospheric subsidence on a spherical body forces contraction) or (b) a plate-breaking event representing transition to plate tectonics. Within this shear zone an A-type fold developed (Webb et al., 2020) with randomly distributed opposite shear senses (Zuo et al., 2021b). Any early record of burial metamorphism should record increasing pressure conditions from the top to the bottom of the sequence, i.e., from 3.7 Ga rocks to 3.8 Ga rocks. For the subsequent thinning and syn-tectonic metamorphic period, the model anticipates nearly homogenous amphibolite facies metamorphism (Fig. 2.3c), in stark contrast to the metamorphic gradients predicted in plate tectonic models. To date, the heat pipe model is consistent with the apparent lack of metamorphic gradient interpreted from the amphibolite facies temperatures (550-650 ⁰C) returned from garnet-biotite thermometry (Boak & Dymek, 1982; Rollinson, 2002, 2003) that show no clear spatial variations (Fig. 2.1). The heat-pipe model is further supported by geochemical data identifying the TTGs as a likely product of the hydrated tholeiites from the ISB (Nagel et al., 2012; Hoffmann et al., 2014, 2019; Gardiner et al., 2019) and metasediments (Gauthiez-Putallaz et al., 2020) in a thickened / buried crust (Gardiner, 2019; Hoffmann, 2014, 2019; Nagel et al., 2012a; Smit et al., 2019).

2.3 Results

2.3.1 Petrography

For this study we selected samples based on (1) their spatial distribution, trying to cover transects along north-south and east-west directions in the eastern arm of the belt as well as samples from both the 3.7 Ga and the 3.8 Ga sequences (Fig. 2.1); and (2) their potential to provide geothermobarometric information (e.g. presence of important geothermometers such as garnet and biotite). The selection aimed to characterize the mineralogical changes along the belt and quantify the P-T peak distribution to test the presence or absence of metamorphic gradients. We conducted a detailed study on twenty-three samples, most of which are garnet bearing, from three main lithologies namely felsic meta-volcanics, amphibolites, and metapelites with minor mafic schists and BIFs. In the field, the rocks are characterized by a distinct foliation and lineation. Samples were cut parallel to lineation and perpendicular to foliation. Below we present a summary of the mineralogical and microstructural observations of the different samples (Table 1.1).

Table 1.1 Mineral relationships and data collected for each sample. Mineral abbreviations as in Whitney & Evans (2010). OB=Outer-belt; IB=inner-belt; M.C.=Mineral chemistry; Grt-Bt=Garnet-Biotite thermometry; TiB=Ti-in-Biotite thermometry; P.S.=Phase equilibria thermobarometry. Lithology: Mfv= Meta-felsic volcanics; Am= Amphibolite; Mp = Metapelite; Mmp= "mafic" metapelite. Most samples ID prefix is TM17-, (e.g. 714-5A = TM17714-5A), apart from those with JZ, which in case sample ID prefix is JZ17- (see Appendix 1 for details on the sample nomenclature)

Sample ID		Lithology	Age (Ga)	Inclusions in garnet	Syn-Tectonic parageneis (M₁)	Post-Tectonic Parageneis (M₂)	Low-T paragenesis (M₃)	P-T-X data				GPS Coordinates	
								M.C	Grt-Bt	TiB	P.S.	Longitude	Latitude
Meta-felsic rocks	717-5	Mfv	3.8	Qz, Bt, Ms, minor Ap, Cal, Tur, Aln, Zrn	Qz + Bt + Pl + Ms + Czo + Grt + Kfs minor Cal + Tur + Ilm		Ms, Sericitization	X	X		X	65.152608 65.152608 -49.84904	-49.84904
	725-2c	Mfv	3.7	Qz, Bt, Ilm	Qz + Bt + Pl + Grt + Ilm + minor Tur	Grt + Ilm		X	X	X	X	65.098302	-50.00803
	726-6A	Mfv	3.75	Qz, Bt, Pl, Ms, Ilm	Qz + Bt + Ilm + Grt + Pl + Ms Minor Ap + Hm +		Chl		X	X		65.101806	-49.967241
	JZ17729-1A	Mfv		Qz, Bt, Ms, Pl	Qz + Grt + Pl + Ms + Chl (?) + Ilm		Chl	X		X		65.111243	-50.017674
	729-11	Mfv /Mmp	3.7	Qz, Ap, Ilm, Aln	Qz + Bt + Ms + Pl + Grt + Tur + Ap + Ilm	Grt	Chl					65.183238	-49.82114
	730-2A		3.75		Bt + Qz + Pl + Grt + Czo + Ilm + Ms + minor Tur + Cal + Ap	Grt+Czo		X	X	X		65.142622	-49.87623
	801-9A	Mfv	3.7	Qz, Bt, Ilm	Qz + Bt + Plg + Grt + Cal + minor Ep/Czo + Ilm	Grt	Chl+Ms	X	X	X		65.18258	-49.80878
	JZ17801-4	Carbonated-Mfv	3.7	Qz, Bt, An	Qz + Grt + Bt + Ms + Ep + Pl minor Ttn + Ap +	Grt			X			65.179341	-49.803351
	802-5	Mfv	3.8	Qz, Cal, Ms, Tur, Ilm, Bt, Ep	Qz + Ms + Bt + Pl + Tur + Grt + Ep + Opaq	Grt+Cal	Sericitization					65.158051	-49.831399
Meta-mafic rocks	715-9	Am	3.8	Qz, Ap, Chl, Bt, Cal, An, Ilm, Wo	Qz + Bt + Grt + Pl + Amp + Ep minor Ilm	Grt + Cal	Chl, Cal veins	X	X			65.16436	-49.81711
	JZ17715-5F	Am		Qz, Cal, Bt, Ap, Amp, Hm	Qz + Bt + Grt + Cal minor Ap + Amp		Chl, Qz + Cal veins					65.169422	-49.823217
	JZ17715-16A	Am	3.8	Act, Ep, An, Cal, Bt, Qz, Ap	Qz + Bt + Grt + Amp + An + Ab + Cal minor Act + Ttn + Ap			X	X			65.158913	-49.815456
	720-8	Mafic schist	3.7	Cal, Qz, Ilm, Ap	Qz + Bt + Amp + Cal + Grt + Czo + Ilm	Qz+Grt+Czo+ Ilm	Cal	X		X		65.193078	-49.782867
	725-3a	Am	3.7	Qz, Ilm, Czo	Amp + Pl + Qz + Bt + Grt + Ilm	Grt+Czo+Ms+ minor Cal	Chl + Czo	X			X	65.098261	-49.998603

Table 1.1. *Continued*

	Sample	Rock	Age	Inclusions	Peak assemblage		Retrograde					Lat	Long
Meta-mafic rocks	725-2b	Amp	3.7		Act + Mg-Hbl + Chl		Chl + Tre + Cal	X				65.098302	-50.00803
	729-5	Mafic schist	3.7	Qz	Bt	Grt (?)+ Ilm	Chl					65.198128	-49.788794
	729-10	Mafic schist	3.7		Amp + Bt + Qz + Ilm (maybe Cal)		Cal+Chl	X		X		65.194247	-49.788856
	731-2A	Amp	3.7	Qz, Ilm, Ms, Ep/Czo, Ab, Pl	Grt + Amp + Bt + Qz + Czo + Zo +Ms + Ilm + minor Cal	Grt					X	65.173048	-49.822507
Meta-sedimentary rocks	714-5A	Mmp	3.7	Qz, Bt, Po, minor Cal and Amp	Qz+ Bt +Amp + Grt + Pl +Ilm	Grt	Chl+Act	X	X	X	X	65.171295	-49.833468
	714-5E	Mp	3.7	Qz, Ms, Ctd, Chl, Ilm, Tur, small Pl	Qz + Grt + Ms + Cld + Chl + Tur + Pyr	Grt	Chl+Ms	X			X	65.171295	-49.833468
	714-5F	Mp	3.7	Qz, Ms, Cld, Chl, Ilm, Tur	Qz + Grt + Chl + Ms + Tur + St + Pyr	Grt	Ms+Chl				X	65.171295	-49.833468
	725-4A	Chert	3.7	Bt, Qz, Ap, Zrn and minor Hbl	Hbl + Bt + Qz + Grt + Czo + Pl + minor Ilm	Grt			X	X		65.09825	-50.0062
	729-1B	Mmp	3.7	Qz, Ilm, Ms, Ep/Czo, Bt, minor Cal and Chl	Qz + Bt + Amp + Grt + Pl + Ilm + minor Cal+ early C(zo)	Grt_2	Chl+Czo(?)	X		X	X	65.20005	-49.798507

Nine samples of felsic meta-volcanics (Table 1.1, 717-5, 725-2c, 726-6A, 729-1A, 729-11, 730-2A, 801-4, 801-9A, 802-5) show peak mineral assemblages of quartz + biotite + plagioclase + garnet ± muscovite ± tourmaline ± epidote/clinozoisite ± ilmenite ± calcite ± K-feldspar ± apatite ± titanite. These samples typically exhibit a strong foliation with lepidoblastic layers intercalated with quartz-rich granoblastic layers that are deflected by large garnet poikiloblasts/clusters, typically developing pressure shadows (Fig. 2.4a,b; Fig. APP-A1a, in the supportive information) and occasional garnet boudin structures in some samples (725-2c and 726-6A). Different garnet microstructures can be identified in this lithology (Fig. 2.4; Fig. APP-A1). Garnet within sample 729-11, located in the north-central part of the 3.7 Ga belt (Fig. 2.1), shows up to three zones: (i) core with relatively small, mainly quartz, inclusions (<20 µm) without a clear internal foliation pattern, followed by (ii) annulus of larger inclusions (20-50 µm) with spiral-like internal foliation pattern, and (iii) an inclusion-poor rim with euhedral facets cutting the external foliation (Fig. 2.3b). Garnets of samples 725-2c (Fig. APP-A1b) and 801-9A (Fig. APP-A1c) from the 3.7 Ga belt show garnets with a clear inclusion-rich core and an inclusion-poor rim whereas garnets from
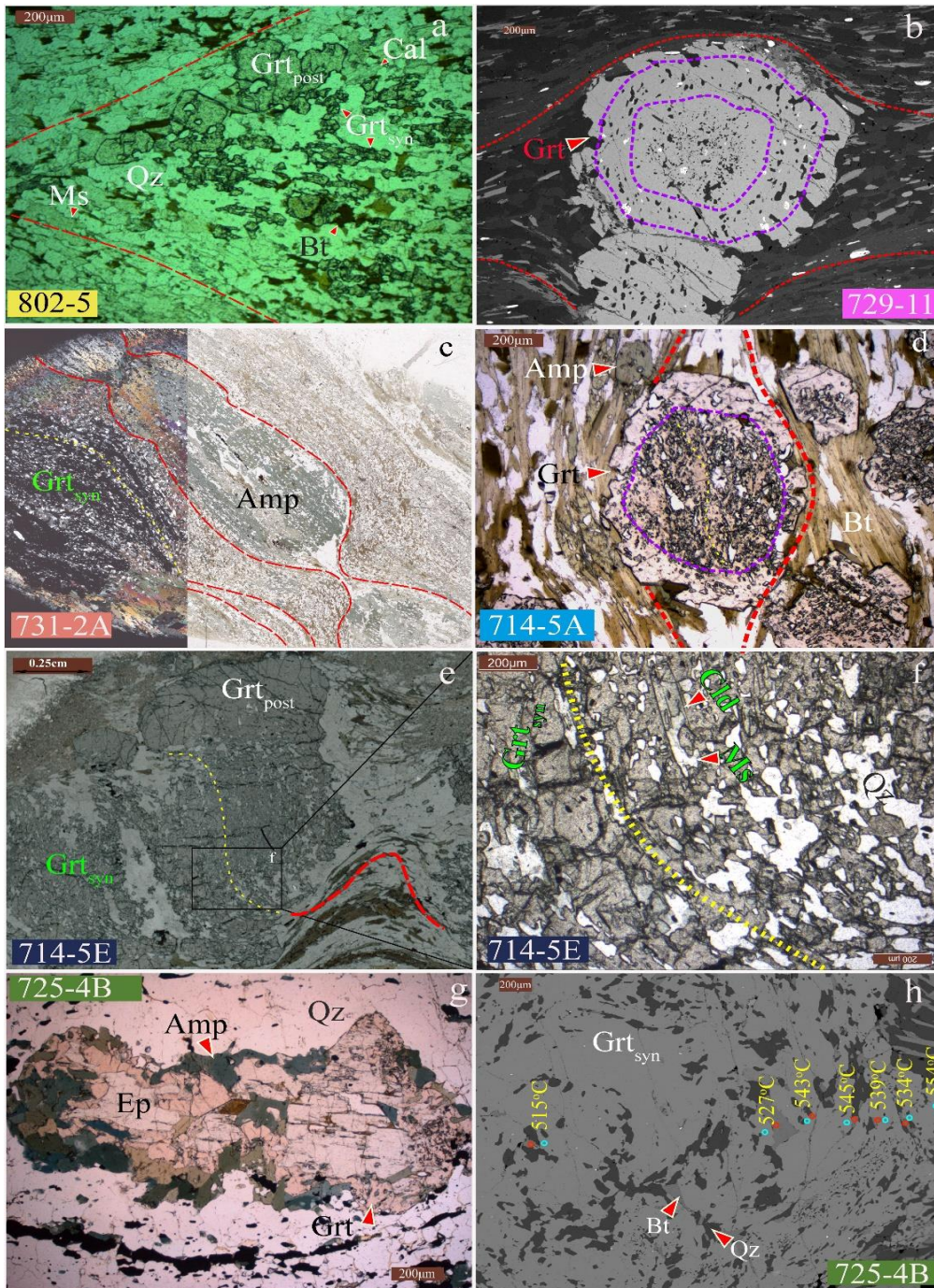
Figure2.4 Photomicrographs showing peak mineralogy and micro-structures. (a) skeletal-like syn-tectonic garnets and euhedral post-tectonic grains; (b) garnet showing three different micro-structural domains; (c) arc-like inclusions trails in garnet and boudinage structures; (d) garnet showing inclusion-rich core and inclusion-poor rims; (e) and (f) spiral-like garnet; (g) garnet-amphibole coronae on epidote; (h) Backscatter electron image of garnet showing garnet-biotite temperatures (Perchuk & Lavrent'eva, 1983) calculated along a grain transect. Scale in all images is the same (200 μm), except in (c) and (e). Red dotted lines indicate external foliation, yellow dotted lines internal garnet foliation and purple dotted lines limit between garnet microstructural zones

samples 717-5, 726-6A, 730-2A, and 802-5 from the 3.8 Ga belt and sample 801-4 from 3.7

Ga belt exhibit clusters of

skeletal-like microstructures (Fig. APP-A1), some of which contain small euhedral garnets that overgrow the foliation (Fig. 2.3a). The quartz trails in the cluster/porphyroblast from samples 802-5 and 717-5 (Fig. APP-A1a) show arc-like shapes converging in the pressure shadows, whereas in sample 726-6A (Fig. APP-A1e) the trials are parallel to the external foliation at the pressure shadows, but oblique at the body of the sigmoidal garnet/cluster. Sample 17725-2c contains well-developed S-C fabric structures in the external foliation. Late retrogression at upper greenschist/lower amphibolite facies conditions is commonly observed in the felsic rocks. For example, sample 717-5 displays micro-shear zones that overprint the peak assemblages, where muscovite grows along observed fractures (Fig. APP-A2a) that cross-cut the whole rock. Replacement of biotite by chlorite, mimicking the penetrative external foliation, is common in the rest of the samples as well as sericitization of plagioclase.

The peak assemblage of the eight amphibolites (Table 1, 715-5F, 715-9, 715-9, 720-8, 725-2b, 725-3a, 729-10, 731-2A) comprises amphibole + biotite + quartz ± garnetsyn ± plagioclase + epidote/clinozoisite ± ilmenite ± calcite ± muscovite. These rocks are foliated amphibolites typically containing garnet poikiloblasts, and minor amphibole porphyroblasts that deflect the external foliation. Sample 731-2A also shows boudinage structures (Fig. 2.4c). Garnets commonly contain inclusion-rich cores, with different inclusion patterns observed in various samples (Fig. APP-A1; see Table 1.1). The inclusions in the garnet core of sample 720-8 are randomly oriented (Fig. APP-A1f), whereas in samples 715-5F, 715-9 and 731-2A, the internal foliation in the ellipsoidal large garnets (typically >1cm) displays arc-like patterns that converge towards the pressure shadows and continue into the external foliation (Fig. 2.4c). In sample 725-3a, garnets occur as complex aggregates of large grains (>0.4 cm) with weakly curved inclusion patterns, discontinuous with the external foliation

(Fig. APP-A1f,g). The amphibolites show various post-tectonic upper greenschist-lower amphibolite facies features: (1) most of the garnets display inclusion-poor euhedral rims overgrowing the external foliation (Fig. APP-A1f); (2) in sample 715-9, a vein dominated by post-tectonic calcite cross-cuts one of the garnets perpendicularly to the internal foliation, and euhedral garnets crystals grow towards the centre of the vein (Fig. 2.5a); (3) in sample 720-8 calcite veins cross-cut the main external foliation at ~30° and are overprinted by garnet growth (Fig. 2.5b); (3) epidote grains, typically associated with muscovite and ilmenite, overprint amphibole (sample 725-3A ; Fig. APP-A2c) and grow in garnet fractures with no preferred shape or crystallographic orientation; and (4) randomly oriented biotite grains, and quartz-calcite crystals with a granoblastic texture replace garnets (sample 720-8) (Fig. 2.5c). Late (upper) greenschist facies replacement microstructures overprinting the syn-tectonic and post-tectonic medium temperature assemblages are commonly observed. They are characterized by epidotization of plagioclase, and mainly chlorite (sometimes associated with calcite), either randomly overgrowing peak minerals (Fig. 2.5d) or mimicking the foliation by replacing biotite (Fig. 2.5e).

Two metapelitic samples (714-5E and 714-5F) collected less than <10 m apart in the same outcrop reveal peak assemblages of quartz + garnet + muscovite + chlorite + tourmaline + sulfides ± staurolite. The rocks show lepidoblastic foliation and elongated quartz grains that are deflected by large garnet porphyroblasts (≈1 cm). Garnets display spiral-like inclusions patterns from the core to the annulus that are overgrown by an inclusion-poor rim (Fig. 2.4e, f), which typically shows euhedral facets and overgrows the foliation (Fig. 2.4e, 2.5f). The size of the inclusions in the trails is smaller in the core ($< 100 \, \mu m$) and larger towards the annulus ($> 200 \, \mu m$, Fig. 2.4 e,f). Staurolite crystals, typically overprinted by muscovite (Fig. S2d), appear in the matrix of sample 714-5F, in contrast to chloritoid, which only occurs as inclusions in the garnets, occasionally growing in contact with muscovite along irregular

borders (Fig. 2.4f). In these samples, retrograde chlorite replaces prograde biotite crystals by mimicking the foliation. Significant patches of late muscovite-sericite as well as chlorite overgrowing garnet are common textures in these rocks (Fig. 2.5f). Sample 714-5F contains chlorite- and muscovite-filled veins that are consistently oriented parallel to each other throughout the sample and cross-cut the peak minerals (Fig. APP-A2d).

Some rocks with a darker-colored outcrop appearance within the metapelitic packages, commonly referred to as "mafic metapelites" (e.g. Nutman et al, 1984) or Ca-rich metapelites, have a more Ca- and Mg-rich composition than the typical metapelites (Rollinson, 2002). Two of such rocks (samples 714-5A and 729-1B) show peak assemblages of quartz + garnet+ amphibole + plagioclase +ilmenite ± calcite ± sulfides ± apatite. These are foliated rocks with garnet and amphibole (in the case of sample 729-1B) porphyroblasts that deflect the foliation. Garnets in sample 714-5A show inclusion-rich cores with curved patterns and inclusion-poor rims that overgrow the external foliation (Fig. 2.4d), while garnets in sample 729-1B exhibit straight inclusions patterns or skeletal-like textures with smaller, more euhedral grains in the outer parts of the clusters (Fig. A1i). Chlorite can be seen overprinting garnet and amphibole, as well as filling fractures in minerals as well as some fractures cross-cutting the rocks.

Sample 725-4A (described in the field as BIF) is a banded rock with four distinct mineralogical domains. One domain is very rich in amphibole that occurs as porphyroblasts with inclusions of quartz, biotite, and opaques. A second domain is dominated by quartz and magnetite, with minor occurrence of amphiboles following the foliation. In this band, a medium-grained epidote crystal ($\approx$1500 μm) is surrounded by a corona of pink garnet and green amphibole, and the foliation is slightly deflected around the mineral (Fig. 2.4g). A third, plagioclase-poor band is rich in quartz and biotite. This band is followed by another band with biotite, amphibole, garnet, and quartz. Garnet in this band occurs as porphyroblasts

with curved inclusion patterns resembling in-places snow-ball fabrics (Fig. 2.4h, Fig. APP-A1j).
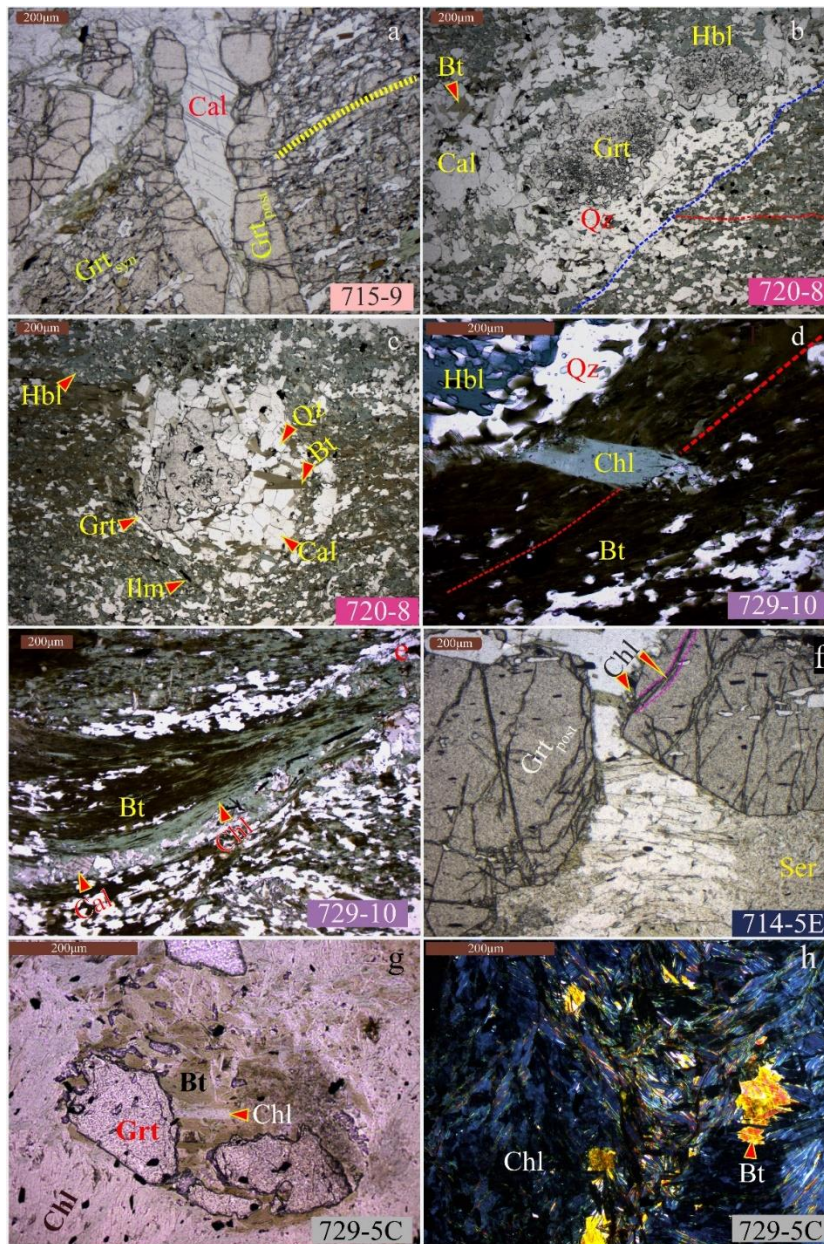
Figure. 2.5 Post-tectonic medium- and low-temperature paragenesis and micro-structures. (a) calcite vein cross-cutting garnet internal foliation and post-tectonic euhedral garnet growing towards the vein centre. (b) Late calcite veins cross-cutting the main foliation, which are overprinted by post-tectonic garnets. (c) Garnet replacement by calcite-quartz-biotite. Retrograde chlorite (d) overprints the foliation and (e) mimicks the foliation by replacing biotite and (f) growing along factures that cross-cut post-tectonic garnet. (g). Biotite pseudomorphing garnet and chlorite replacing biotite. (h) Extreme biotite chloritization. Scale in all images is the same (200 µm) Red dotted lines indicate external foliation, yellow dotted lines internal garnet foliation and blue dotted lines limit of veins.

The petrographic description of the different lithologies highlights the fact that retrogression is a common feature. Remarkably, mafic schist sample 729-5 collected the northern part of

the belt (Fig. 2.1; zone B of Arai et al., 2015) represents an extreme example of low temperature greenschist facies overprint. This particular sample exhibits crenulation cleavage (Fig. A1e) with inclusion-poor garnet porphyroblasts. The garnet crystals are replaced by randomly oriented biotite grains, which themselves are overprinted by chlorite (Fig. 2.5g) that comprises most of the matrix along with few relic biotite grains (Fig. 2.5h).

2.3.2. Mineral chemistry

The chemistry data of the garnet, amphibole, biotite, and plagioclase can be found in Ramírez-Salazar et al. (2020a) (database uploaded to EarthChem), some classification diagrams are shown in Figure APP-A3 and the methodology is described in the Appendix. For garnet, we present a detailed mineral chemistry map (processed using XMapTools version 3.3.1; Lanari et al., 2014) exhibiting the commonly observed three zones. The garnet stems from the metapelite sample 714-5E (Fig. 2.6). Notably, while the core (Grt$_1$) and annulus (Grt$_2$) zones exhibit a sharp change in chemistry, the inclusions trail is continuous from the core to the annulus (Fig. 2.6a). Specifically, the garnet core (Grt$_1$) shows low content in grossular ($X_{\approx 3}^{Gro}$), rises steeply in the garnet annulus (Grt$_1$; X_{3-8}^{Gro}) and then falls to values similar to Grt$_1$ in the rim (Grt$_3$; Fig. 2.6b; X_{8-2}^{Gro}). The almandine (Fig. 6c) content shows a concave increase in Grt$_1$ (X_{75-85}^{Alm}), follow by a nearly constant content in Grt$_2$ ($X_{\approx 85}^{Alm}$) and a slight increment in Grt$_3$ (X_{85-89}^{Alm}). The chemical map reveals no significant changes in pyrope content and a typical bell shape decrease in spessartine, with an almost constant content towards the rim (Fig. 2.6d).

2.3.2 Thermobarometry

To determine the peak metamorphic conditions, we combined classic geothermobarometry utilizing mineral pairs or assemblages and thermodynamic isochemical phase modelling. We applied the garnet-biotite Fe-Mg exchange geothermometer (Perchuk & Lavrent'eva, 1983) on eleven samples and the Ti-in-Biotite geothermometer (Henry et al., 2005) on thirteen

samples across the ISB (Table 1.1). The calibration from Perchuk & Lavrent'eva, (1983) was

applied to be consistent and comparable with results from Rollinson (2002).
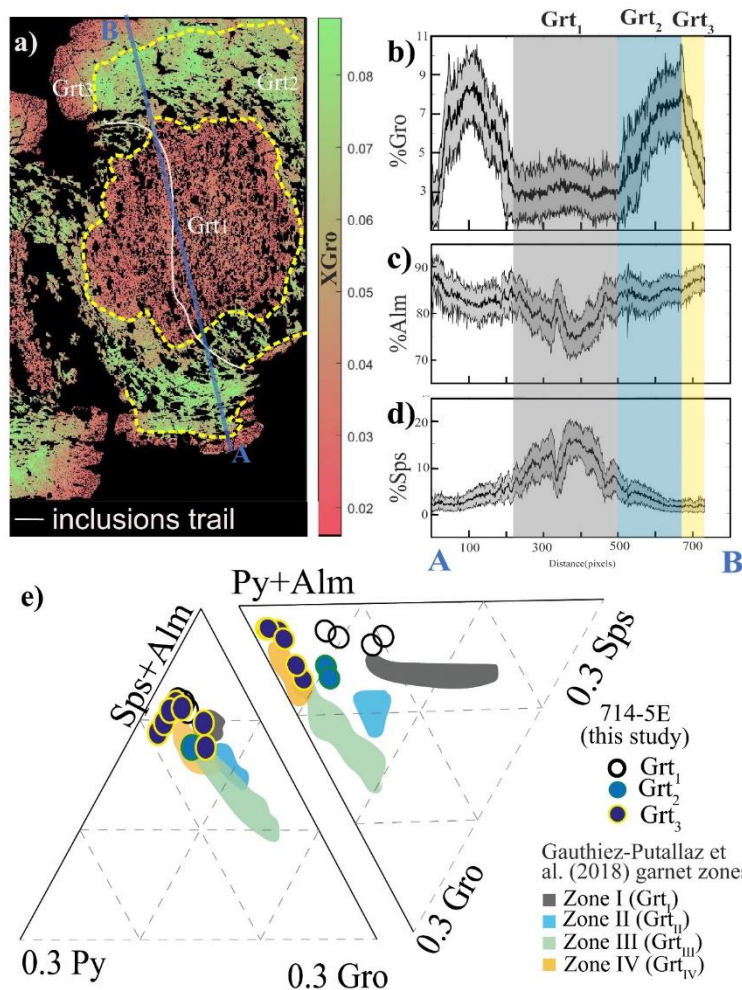
Figure 2.6 Geochemical characterization of spiral-like garnet in sample 714-5E. (a) Grossular content calibrated map and (b), (c), (d) compositional transects generated with XMapTools (Lanari et al., 2014). (c) Comparison of the different garnet zones composition presented in this work with Gauthiez-Putallaz et al. (2020) data.

The temperature range (470-570 °C) and mean values (490-530 °C) derived from the

exchange thermometer using garnet (cores) and biotite inclusions show no systematic

increase in temperature from the northeast to the southwest (Fig. 2.7a). The mean values of

samples are very similar throughout the belt. For six of these samples (714-5A, 715-9, 717-

5F, 715-16, 717-5, 725-4A and 801-4), we obtained the chemical composition for inclusion-

host mineral pairs along overall profile transects, which suggest an increase in temperature

from core to rim that is typically not greater than 50 °C (Figs. 2.4h & APP-A4) in all the

samples except 717-5F and 715-9, where the increment in temperature from core to rim is >60 °C, ranging from 505-589 °C and 468-535 °C, respectively. Modelled temperatures using inclusion-poor rim analyses of garnet and adjacent matrix biotite generally returned temperatures <550 °C, which are typically lower than those recorded in the cores (Fig. 2.7b), with the exception of sample 725-2c that returned mean temperatures of 487 °C in the core and 544 °C in the rims (Fig. 2.7b).
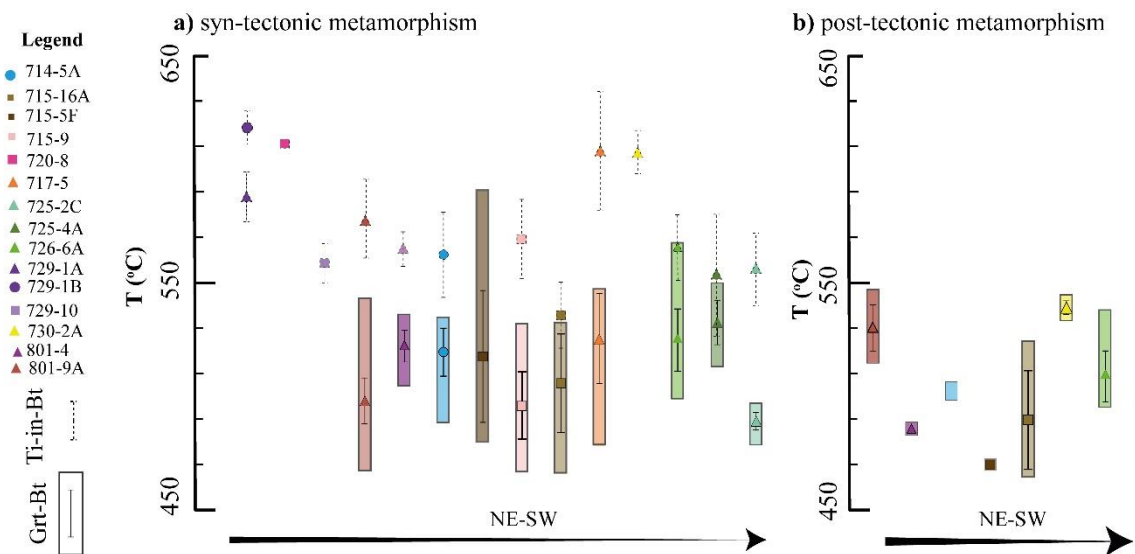
Figure 2.7 Classical geothermobarometry plots showing the mean (symbols with error bars) and range of (boxes) temperature values for garnet-biotite calculations (Perchuk & Lavrent'eva, 1983) and mean values returned from the Ti-in-Bt geothermometer (Henry et al., 2005)

Temperatures obtained with the Ti-in-Bt geothermometer (Henry et al., 2005) range from 510°C to 650°C (Fig. 2.7a & APP-A5) with the highest values returned from samples that are poor in ilmenite (e.g. 717-5) or with a low number of analysis (e.g. 729-1B, 720-8 and 730-2A; n<4). Apart from the samples showing temperatures in excess of 610 °C, the mean temperature modelled for the rest of the biotite analyses in different ilmenite-rich rocks ranges from 540-590 °C (Fig. 2.7a). Again, modelled temperatures yield no clear spatial pattern of systematic increase in temperatures in any direction such as North versus South, East versus West of ISB (Fig. 2.7a, Fig. APP-A5). The values were obtained mainly in biotite crystals that are part of the peak assemblage and that make up the main foliation of the rocks

(e.g. Fig. 2.4d, APP-A1a, d, f) and some as inclusions in garnets (e.g. Fig 2.4h), with no clear temperature difference among these groups.

A total of eight isochemical phase diagrams have been calculated using the Perple-X software (Connolly, 2005; ver. 6.8.6) and the database of Holland & Powell (2011, sd622). The calculations were performed in the MnNCKFMASHTO system for the meta-felsic volcanics and metapelitic rocks and in the NCKFMASHTO system for the amphibolites. More detailed specifications regarding the use of activity models and input parameters, as well as methodology for the bulk-rock composition are listed in Appendix A and the compositions are reported in Ramírez-Salazar et al. (2020b) and shown in tables A1 and A2. Results reveal that the overlap of stability fields covering the observed mineral assemblages do not show any systematic increase in pressure and/or temperature as a function of their spatial distribution (Figs. 2.8, 2.9 & A6). Most of the samples converge in a range of 0.5-0.7 GPa and 550-600 ⁰C (Fig. 2.9a). However, the stability fields of the two southernmost samples (725-2c and 725-3a) display higher temperatures from 585 to 625 ⁰C and up to 700 ⁰C for 725-3a, with similar pressure values as the other samples (Fig. 2.8e, f). To further constrain the stability conditions of the individual mineral assemblages, we plotted chemical isopleths for garnet compositions and other minerals from samples 714-5E (Fig. 2.9c) 17725-2c (Fig. 2.8d) 17725-3A (Fig. 2.8f), as well as the modal isopleths for sample 17714-5A (Fig. 2.8b). Here, we assume that the whole-rock composition of the samples and the selected a-x models are suitable for modelling the composition and abundances of the mineral in the rocks as isopleths; in that case, isopleths plot within or very close to the stability peak assemblage, possibly further limiting the stability of the rock within larger fields (e.g., Fig. 2.8 b, e, f & Fig. 2.9c). We also assume that the parameters used are suitable for modelling the evolution of the garnet cores, meaning that the intersection of the garnet end-member isopleths will

define small P-T fields under which garnet grew, which could be different from those for the

peak metamorphic assemblage (Fig. 2.9c).
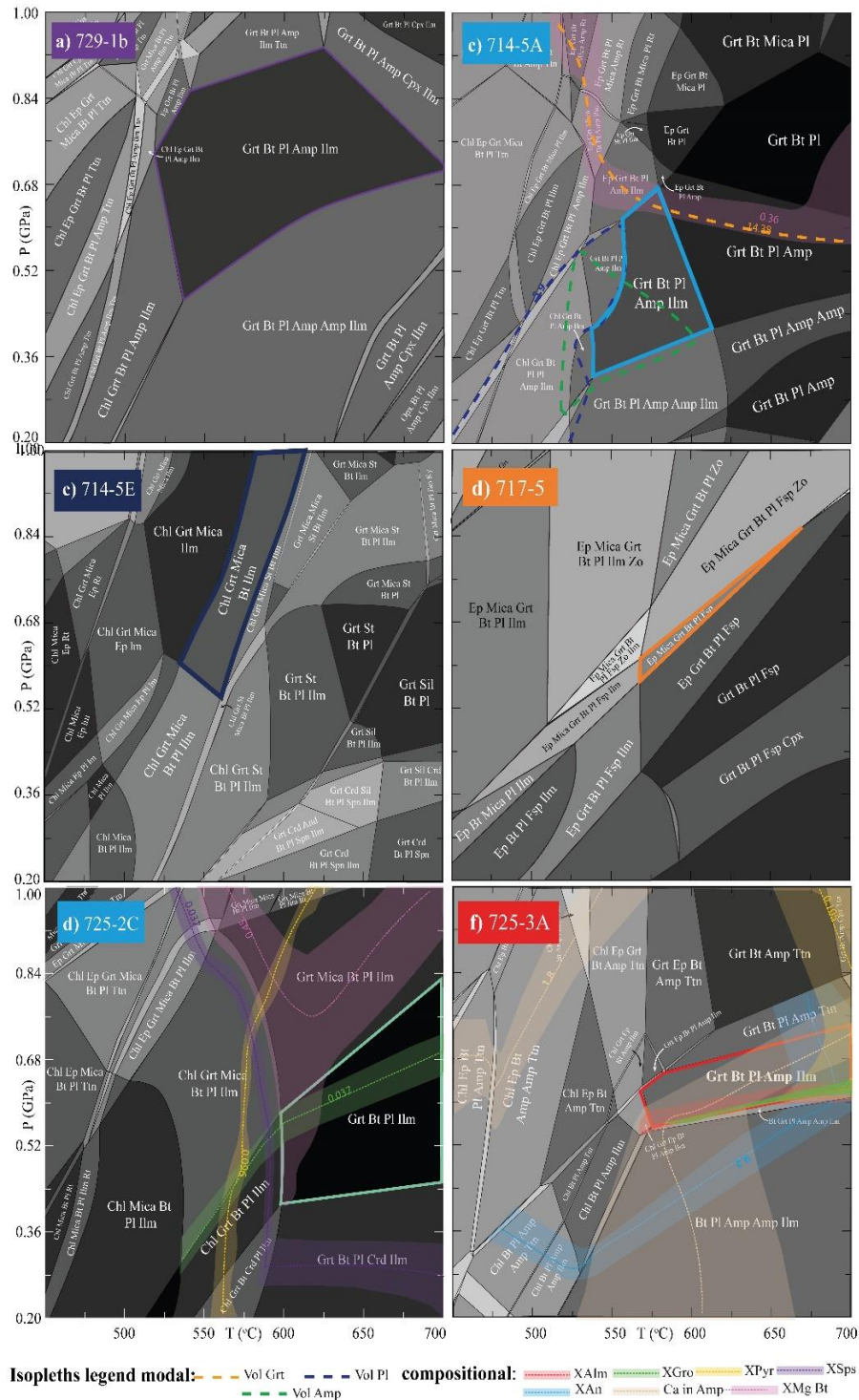
Figure. 2.8 Isochemical phase diagrams calculated using Perple_X (Connolly, 2005) in the MnNCKFMASHTO system with exception of samples 725-3a and 731-2A, calculated in the NCKFMASHTO system. All the phase diagrams were calculated assuming a water saturated system and Fe2O3 = 5% (See table A2). All fields contain quartz. Mineral abbreviations are after Whitney & Evans (2010). From (a) to (f) samples are arranged from northernmost to southernmost.

For sample 714-5A, the peak assemblage stability field indicates pressures of 0.36-0.68 GPa

and temperatures of 540-610 °C (Fig. 2.8b), essentially reflecting the same temperature range

obtained by garnet-biotite and Ti-in-Biotite geothermometry for the same sample (Fig. 2.8b,

Fig. 2.7a). The modal isopleths for garnet, plagioclase, and amphibole plot within the stability

field of the peak assemblage (dotted lines in Fig. 2.8b), showing that the a-x models used

reproduce well the abundance of the minerals in the rock. Apart from pyrope, the rest of the

end-members intersect in relatively small areas within the peak stability field (not shown).
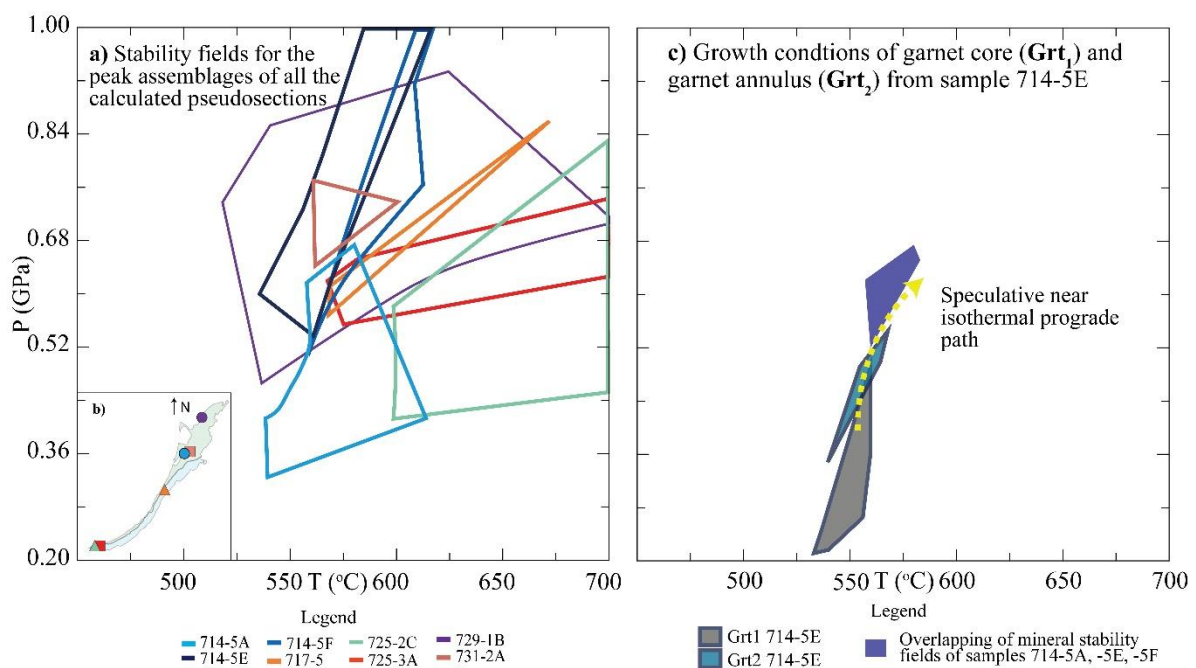
Figure 2.9 a) Overlap of all the stability fields of the calculated isochemical phase diagrams and (b) their schematic positions in the eastern arm of the ISB; samples 714-5A, 714-5E and 714-5F are from the same locality. (c) Stability fields created by the intersection of the garnet end-members for the core and annulus of garnet in samples 714-5-5E, suggesting a tentative isothermal path.

Metapelite sample 714-5E is part of the same outcrop as sample 714-5A with no visible

tectonic break between the two units. The equilibrium fields of these two samples and sample

714-5F, which also forms part of the same outcrop, overlap at 0.55-0.68 GPa and 550-590 °C

(Fig. 2.9c), suggesting this is the range of peak conditions. We used the mean composition of

the garnet core (Grt1) and garnet annulus (Grt$_2$) to plot the end-members isopleths of the

solid solution (Fig. 2.9c). Garnet compositional profile shows an increase in grossular content

from core to annulus and decrease in spessartine content (Fig. 2.6). In the plot illustrating the compositional intersection between Grt_1 and Grt_2, the four garnet end-members isopleths define two narrow fields at 550 °C, with the intersection for Grt_2 suggesting slightly higher pressures (Fig. 2.9c). Both compositions plot at lower pressures than the field equilibrium assemblage of the rock, within a stability field with mineral assemblage showing Chl + Grt + Bt + Pl + Ilm + Qz. We note that the garnet core does show abundant inclusions of quartz and minor inclusions of ilmenite, chlorite, and plagioclase. These findings suggest that the onset of garnet growth forming the core started at lower pressure conditions (≈0.4 GPa) followed by a nearly isothermal increase to form the mineral peak equilibrium assemblage (≈0.65 GPa; Fig. 2.9c).

An isochemical phase diagram calculated for sample 725-2c (Fig. 2.8e), collected near the contact to the 3.7 Ga TTG in the southernmost part of the belt, shows a stability peak assemblage ranging from 600 °C to >700 °C with similar pressures (0.4-0.7 GPa) as the samples collected further to the north (Fig. 9a). We calculated the isopleths for the garnet end-members of the garnet core which define a narrow region ~580 °C and 0.5-0.7 GPa, plotting next to the stability field of the peak assemblage (green, yellow and purple bands in Fig. 8e). In contrast, the X_{Mg} biotite isopleths (pink band in Fig. 8e) overlap within the peak stability field of 600-630 °C, suggesting that this range as the maximum temperature the sample achieved.

Garnet-amphibolite sample 725-3a, collected just north of meta-felsic volcanic sample 725-2c (Fig. 1), apparently shows the highest metamorphic conditions in all the samples. The stability field of the peak assemblage expands from 550 °C to 700 °C, showing similar pressures as the other samples from 0.45- 0.68 GPa. The isopleths for anorthite content in plagioclase, Ca content in amphibole (blue and cream bands respectively in Fig. 2.8f), and

garnet end-members intersect (green, red and yellow bands in Fig. 2.8f) within the stability field of the peak assemblage at temperatures >600 °C (Fig. 2.8f)

2.4 Discussion
2.4.1 General tectonometamorphic evolution of the ISB – a reappraisal

The detailed petrographic descriptions and metamorphic analyses presented in this work emphasize the complex textural-chemical relationships displayed in the rock record of the ISB, which essentially is the product of a poly-metamorphic history. Reading the rock record of such a geological setting is challenging and likely responsible for the existing contradictions in previous studies as outlined above. Based on our observations, we propose the occurrence of two medium temperature metamorphic events, followed by a pervasive low-temperature retrogression in the presence of variable amounts of fluid irrespective of terrane association and N-S location, whose characteristics we summarize below and illustrate in figure 2.10. Even though we only present data from the well exposed eastern arm of the belt and mainly from the northeastern part, we assume our interpretations to be valid for the entire Isua supracrustal belt.

The first event (M_1) is recorded in most of the ISB rocks and is characterized by a distinct foliation and SE-plunging lineation with amphibolite facies mineral assemblages (Table 1.1) and common appearance of garnet and amphibole porphyroblasts (Fig. 2.10a). Along the ISB from northeast to southwest, most samples display syn-tectonic inclusion-rich garnet cores, sometimes represented by curved (Fig. 2.4c) or spiral-like (Fig. 2.4e) inclusion trails that continue to the external foliation or sigmoidal garnets (see also Zuo et al. 2021b). The common appearance of post-tectonic, inclusion-poor euhedral overgrowth rims marks the late, apparently static, medium-temperature metamorphic event (M_2; Fig. 2.10b), which has been reported to be ubiquitous everywhere in the belt (Rollinson, 2002, 2003). Some microstructures, like the calcite vein where euhedral garnet grows away from the walls (Fig.

2.5a), suggest that this second generation of garnet growth might have been mediated by fluids in some parts of the belt.
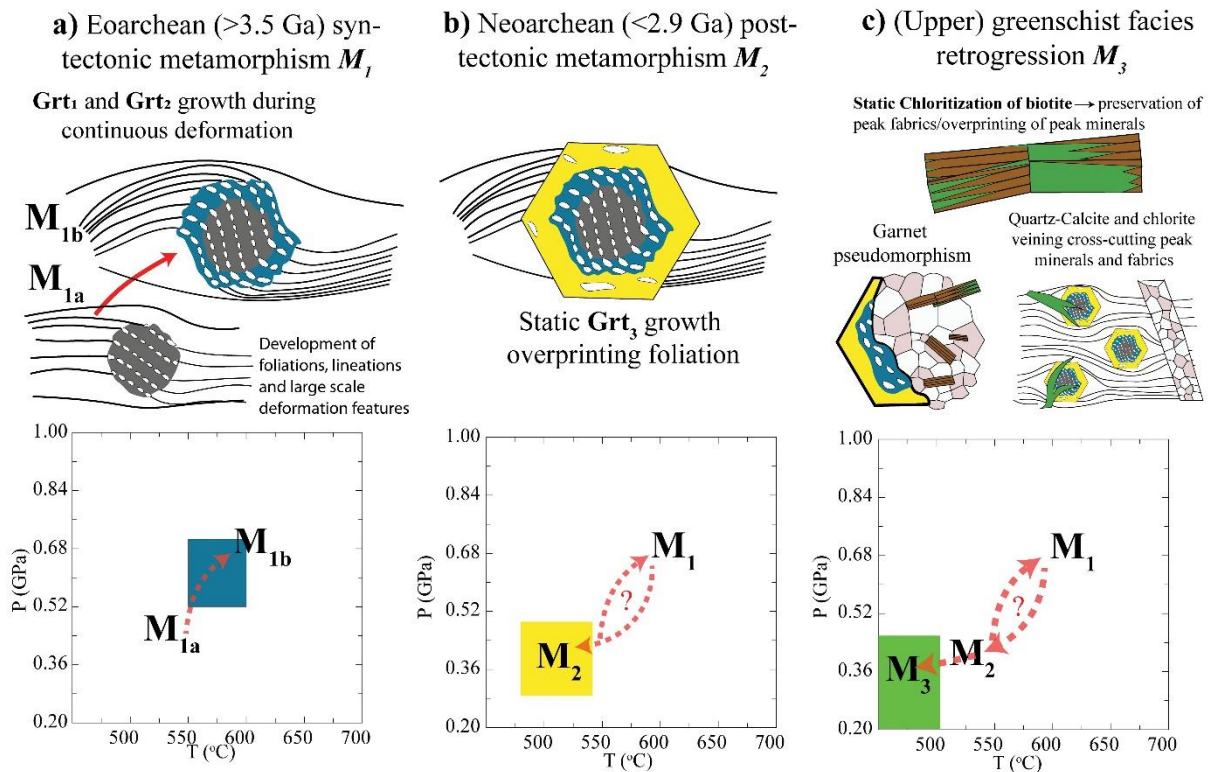
Figure 2.10. Metamorphic evolution of the ISB and schematic representation the characteristics of the three different metamorphic events reported in this Chapter. P-T diagrams show tentative P-T paths. Samples studied show signatures of these three different events irrespective of their location within the belt.

As documented here and in existing studies (Rollinson, 2002, 2003), garnets in the Isua samples show a remarkable range of micro-structures (Fig. 2.4 & APP-A1), as well as chemical zoning patterns (Fig. 2.6). Rollinson (2002) and other studies have linked them to up to three different medium-temperature metamorphic events: two in the early Archean and one in the late Archean (Rollinson, 2002, 2003; Gauthiez-Putallaz, 2020). Gauthiez-Putallaz et al. (2020) reported four chemical zones using major (Fig. 2.6e) and trace elements and $^{\delta 18}O$ that match micro-structural zones. The authors interpret that the core of their garnets (Grt$_I$) represent an early Archean event at 550 ºC and the garnet annuli (Grt$_{II\&III}$) represent later Eoarchean metamorphism at 610 ºC and 0.60 GPa (Fig. 2.2), whereas the inclusion-poor rim (Grt$_{IV}$) recorded final post-tectonic event in the late Archean (Fig. 2.2). Garnets in sample

714-5E shows very similar major element zoning pattern, with three zones predominantly marked by the change in Ca composition (Fig. 2.6). Our sample and sample G12/113 of Gauthiez-Putallaz et al. (2020) were collected within 50 m of each other and have similar bulk rock composition and mineralogy, and thus can be assumed to have experienced the same tectonic history. When the compositions of the different zones within the garnets are compared, it is clear that they follow a similar pattern: the garnet cores form a separate compositional group in the ternary diagram of Py+Alm-Gro-Sps (Fig. 2.6e), showing that they represent the same metamorphic event in both samples. The annuli and rim of both garnets also show similar trends (a relative Alm+Py enrichment towards the rim; Fig. 2.6e) suggesting that the different zones recorded similar processes in both samples. However, we argue that the inner zones core-annuli (Grt_{1-2} this chapter and Grt_{I-III}, Gauthiez-Putallaz et al., 2020) represent only one tectono-metamorphic event (M_1) instead of two based on our chemical-microstructural analysis (Fig. 2.10a). Note that the inclusion trail in the garnet shows a remarkable continuity from the core to the annuli (Fig. 2.4e,f and 2.6a), suggesting that they grew during a continuous deformation event so that the outline of the crystal shape would likely have followed the end of the inclusion trails. The observed chemical zonation pattern is not necessarily the product of different metamorphic episodes for garnet core, annuli, and the inclusion-poor rims, instead the observed chemical changes could be explained by the prograde path of the rock (see below) or by prolonged solid state diffusion. For example, an initial garnet with chemical growth zoning that is overgrown by an inclusion-free rim and experiencing diffusive re-equilibration is likely to produce a similar zoning pattern, where the original garnet grain boundary is obscured by diffusional re-equilibration. Examples of distorted zoning patterns following episodic overgrowth and diffusive relaxation are well documented for magmatic settings (e.g. Kahl et al., 2015) and are very likely to occur at prolonged amphibolite facies conditions (Müller et al., 2013). We

note, however, that more work regarding specific diffusion models would be necessary to confirm this interpretation. In summary, we interpret the observed microstructures and chemical zoning to only represent two distinct medium-high temperature events (M_1 and M_2 in Fig. 2.10) that might have experienced some diffusive re-equilibration rather than three distinct events.

Notably, Arai et al. (2015) suggests that retrogression in the ISB is negligible, whereas our results clearly demonstrate that, late low temperature retrogression forming mainly chlorite, muscovite, sericitization, and calcite (Fig. 2.4) are commonly observed features across the belt, thus defining a distinct retrograde metamorphism (M_3; Fig. 2.10c) for the ISB, which is tightly linked to local presence of external fluid infiltration, suggested by the presence of calcite (Fig. 2.5a, b) and chlorite veins (Fig. 2.5f). Chlorite is one of the most abundant retrograde minerals in the studied samples: it occurs as individual grains or in veins cross-cutting and/or overgrowing the M_1 and M_2 assemblages (Fig. 2.5c, f, g). Interestingly, chlorite also mimics the foliation replacing biotite in various samples (e.g. Fig. 2.5e). Retrogression and this type of chloritization are especially pronounced in the northeastern part of the ISB with an extreme example in sample 729-5, where biotite is pseudomorphing post-tectonic garnets revealing low-medium temperature retrogression (M_{3a}; Fig. 2.5g), followed by a nearly complete chloritization (M_{3b}) of the rock (Fig. 2.5h). These data are good examples of how retrogression can obliterate the peak assemblages while preserving the original fabrics (Fig. 2.10c). We note that the distinction between potentially prograde chlorite and retrograde chlorite mimicking the foliation in the belt might be difficult to differentiate without more detailed observations, thus leading to the erroneous conclusion of an existing metamorphic gradient from the north, where retrogression is more pronounced, towards the south, which dominantly records the peak conditions most likely due to limited or even absence of external fluid infiltration. Thus, we argue that the greenschist

assemblages, previously reported as prograde in the northern part of the belt, are essentially

the product of poor preservation through enhanced metasomatism/retrogression (Fig. 2.10c),

and that the proposed medium P/T gradient (Arai et al., 2015) is likely a record of greenschist

facies alteration rather than a record of southward-increasing peak metamorphic conditions.

This interpretation is also supported by field observations that document enhanced alteration

and metasomatism reflected in an increase in quartz-calcite vein density (Webb et al., 2020)

2.4.2 Quantitative P-T constraints

Both quantitative and qualitative P-T data have been published for the ISB and related rocks

by various groups (Boak & Dymek, 1982; Dymek et al., 1988; Nutman et al., 2013, 2020;

Arai et al., 2015). However, a discussion about the nature and extent of the observed

differences in these estimations is still elusive. In this section, we discuss our P-T results in

the light of previously published data.

Classic geothermometry (Fig. 2.7) and phase equilibria modelling (Figs. 2.8 and 2.9)

demonstrate a consistency of P-T values recorded by the rocks across most of the ISB. From

north to south, the samples reveal similar temperatures when applying the garnet-biotite

geothermometer (Fig. 2.7), and our results fall within the same range as previous garnet-

biotite calculations for the Eoarchean (Fig. 2.1, 510-650 ºC; Boak & Dymek, 1982;

Rollinson, 2002). Nevertheless, the results tend to return lower values than those reported by

Rollinson (2002), although both studies applied the same calibration of Perchuk &

Lavrent'eva (1983). This could potentially be the consequence of increased late stage

alteration being more pervasive in our samples. To complement our thermometry dataset, we

also applied the Ti-in-Bt geothermometer (Henry et al., 2005) to our samples. However, these

results (Fig. 2.7, Fig. APP-A6) should be considered with caution as the geothermometer was

empirically calibrated in ilmenite/rutile-bearing metapelites, and most of our samples cannot

be classified as this type of lithology, although most samples do show titanium saturation

(e.g. significant presence of ilmenite; Table 2.1). For comparison, we also applied the thermometer to five ilmenite-bearing metapelites reported by Boak and Dymek (1982), obtaining temperatures ranging from 558-580 ⁰C (Fig. 2.1). The mean temperature for most of our samples fall within this range, indicating that our Ti-in-Bt results (Fig. 2.7) are generally a good proxy for the peak conditions of the ISB confirming a homogeneous distribution of metamorphic conditions throughout the belt.

Thermodynamic modelling of our samples reveals that most of the modelled stable assemblages overlap at 0.5-0.7 GPa and 550-600 ⁰C (Fig. 2.9a), which we interpret as the best estimation for the peak syn-tectonic metamorphism of the entire ISB (M_1; Fig. 2.10a). These conditions are consistent with the Ti-in-Bt and the highest garnet-biotite values (Fig. 7), as well as previous estimations (Boak & Dymek, 1982; Rollinson, 2002). However, two samples collected from the southernmost part of the belt (725-2c and 3a) show higher temperature conditions (> 600 ⁰C; Fig. 2.8e, f). On the one hand, isopleth thermometry in the meta-felsic volcanic sample 725-2c suggests that the garnet core equilibrated at 570-600 ⁰C at pressure > 0.5 GPa and that the possible maximum temperature of equilibrium is 625 ⁰C, according to biotite isopleth and the peak equilibrium assemblage (Fig. 2.8e). On the other hand, the thermodynamic modelling of the garnet-amphibolite sample 725-3a, collected from adjacent to the 3.7 Ga tonalite and less than 0.5 km to the east of sample 725-2c, shows a peak assemblage equilibrium field that expands from 550-700 ⁰C at similar pressures to the rest of the samples (0.5-0.7 GPa; Fig. 2.8f). Moreover, most of the element isopleths for different minerals in the sample (e.g., amphibole, plagioclase, and garnet; colored bands in Fig. 8f) intersect this stability field at T> 625 ⁰C, suggesting significantly higher temperatures than those recorded in the rest of the samples. Notably, the outcrops of samples 725-2c and 725-3a are located relatively close to each other (Fig. 2.1), and we take a conservative approach to assume both of the samples experienced similar peak metamorphic conditions

ranging from 570-625 ⁰C at 0.5-0.7 GPa, falling in the same P-T range as the rest of the

rocks. This is consistent with the quartz fabric thermometer applied to sample 725-2c,

calculating deformation temperatures ranging from 500-650 ⁰C (Zuo et al., 2021b). The fact

that the pressure estimations are consistent throughout the belt from north to south suggests

that the rocks were subjected to similar burial conditions during the syn-tectonic

metamorphism and that the apparent slightly higher temperatures recorded only in the

southernmost samples are most likely to be a consequence of uncertainties in the

thermodynamic models or potentially local slightly anomalous higher heat influx rather than

reflecting a distinctly different tectonic environment. In general, the syn-tectonic

metamorphic record (M_1) of the Isua supracrustal rocks reveals a dominance in amphibolite

facies metamorphism with no clear spatial metamorphic gradient (Fig. 2.9a, b).

The combination of the compositional garnet profiles and the thermodynamic modelling

potentially provides insights into the prograde evolution of M_1. As discussed in previous

sections, the sharp compositional changes in the garnets clearly record the same deformation

event as shown by the microstructures preserved in sample 714-5E (Fig. 2.4e, f and 2.6a).

The chemical zoning then could be a consequence of the metamorphic path experienced by

the rock and/or late diffusion. Gauthiez-Putallaz et al. (2020) already suggested an increase in

pressure from core to annuli based on the lack of Eu negative anomaly in the annuli, which is

indicative of plagioclase being consumed, typically associated to the increase in pressure (e.g.

Spear et al., 1991). We plotted the mean composition (intersection of compositional

isopleths) of Grt_1 (core) and Grt_2 (annulus) for sample 714-5E. The narrow stability field for

the garnet core plots at lower pressures than, but similar temperatures to the annulus,

suggesting that the samples experienced a near isothermal prograde path from 0.40 to 0.65

GPa at ~580 ⁰C (Fig. 2.9c & 2.10b). Spear et al. (1991) stated that garnet growing in

equilibrium along an isothermal prograde path in a classic metapelite would show

compositional profiles with increasing grossular component and to a lesser extent, almandine content, accompanied by a decrease in the spessartine component and a near flat profile of pyrope. These predictions are remarkably similar to the observed compositional profile of the spiral-like garnet in the metapelite sample 714-5E (Fig. 2.6). However, given the uncertainties on the thermodynamic activity models, the apparent differences in pressure determinations within garnet core and annulus might be the artificial product of chosen parameters for the modelling and further work is needed to test the validity of this interpretation.

The garnet euhedral rims–matrix biotite pairs provide thermal constraints for the conditions of garnet overgrowth (M_2). The calculated temperatures here range from 470-580 ℃, with most of the values < 540 ℃ (Fig. 2.7b), which might be the best estimate and in agreement with previous studies that report similar results (Fig.12.; Boak & Dymek, 1982; Rollinson, 2002, 2003; Gauthiez-Putallaz et al., 2020). Gauthiez-Putallaz et al. (2020) report post-tectonic garnet rims in the metapelites to show negative Eu anomaly, suggesting plagioclase crystallization during M_2. According to our thermodynamic modelling, plagioclase in the metapelites at T < 540 ° C appears at pressures <0.5 GPa (Fig. 2.8c & APP-A6a) putting a maximum limit to the pressure conditions of M_2 (Fig. 2.10b). For M_3 we did not obtain any quantitative data for the P-T conditions, however, the prevalence presence of (upper) greenschist facies minerals such as chlorite, sericite and calcite suggest temperatures <500 ℃ (Fig. 2.10c) for the retrograde metamorphism.

2.4.2.1 Comparison with previous interpretations of the metamorphic record of the ISB

Our results for the peak metamorphic conditions of M_1 contrast the interpretation of Arai et al. (2015) who suggest that the northeastern part of the belt could be divided into four different zones (A-D, Fig. 2.1), with zone A and B showing upper greenschist facies assemblages (<500 ℃ and <0.6 GPa). While we did not quantitatively study samples from

zone A, our qualitative petrographic results and field data (Webb et al., 2020) clearly demonstrate that some samples experienced very pervasive retrogression in zone B (e.g. 729-5, Fig. 2.5g, h) and that retrograde greenschist facies minerals such as chlorite can mimic the foliation (Fig. 2.5e). Therefore, calculated greenschist conditions could actually represent the retrograde metamorphism (M_3; Fig. 2.10c) for zone B, which we assume is also true for zone A. Here, our modelled isochemical phase diagram from sample 729-1B suggests that the proxy temperatures from Ti-in-Bt in sample 729-1A and 729-1B, in addition to quartz fabric thermometry presented in the corresponding part of this study (Zuo et al., 2021b), all agree with T >550 ⁰C for samples located in zone B and thus showing similar conditions to those reported for zones C and D by Arai et al. (2015). However, Arai et al (2015) also reported P-T estimations for three samples in zone C and three in zone D (Fig. 2.1) using isochemical phase diagrams and concluded that there is an increase in both pressure and temperature from zone C (0.4-0.7 GPa, 500-600 ⁰C) to zone D (0.5-1.1 GPa, 540-800 ⁰C). Careful inspection of the diagrams, however, reveals that only a single calculated stability field of a reported mineral assemblages (sample K755, located in the 3.8 Ga belt) extends to pressures and temperatures higher than 0.8 GPa and 650 ⁰C. All mineral assemblages reported for zone C and D overlap around 550-600 ⁰C and 0.5-0.7 GPa (Fig. 12 in Arai et al, 2015), which is indistinguishable from the range of conditions presented in this work. As such, the results of Arai et al. (2015) show no clear systematic increase in metamorphic conditions, and hence there is no clear evidence of a metamorphic gradient from north to south, in consonance with our results.

The data presented here, and the spatial resolution given by our samples does not a priori rule out an increase in pressure and temperature towards the center of the 3.70 Ga TTG body (Nutman et al., 2013) nor the record of paired metamorphism interpreted from the TTGs/zircon chemistry and granulites (Nutman et al., 2020). However, our results

convincingly demonstrate that both the 3.7 Ga and 3.8 Ga belts record similar peak conditions for M_1, arguing that at least for the supracrustal rocks there is no clear metamorphic gradient. Moreover, we propose that the chemical record of the TTGs/zircon and the mineralogy of the granulites of the IGC can be explained in simpler terms with the available data reported in the literature and that they do not necessarily recorded paired metamorphism. Using Isua tholeiitic basalts as starting composition and phase equilibria modelling, Hoffman et al. (2019) showed that melts in equilibrium with garnet and rutile formed at 1.3 GPa and 885-1020 ºC, and melts in equilibrium with orthopyroxene-granulites that formed at 0.8 GPa and 870-980 ºC would have a similar major and trace element chemistry as observed in the natural TTG samples of the Itsaq Gneiss Complex. In their model, the stability field of the orthopyroxene-granulites expands up to 1.1 GPa (Fig. APP-A7, check also Fig. 3 in Ramírez-Salazar et al., 2022), suggesting that tonalites with no garnet signature can be produced in T/P gradients as low as 800 ºC/GPa, while those with residual garnet would have been generated at T/P ≈700 ºC/GPa (Fig. APP-A7). Therefore, (1) the presence or absence of a garnet signature in the tonalite/zircon chemistry does not necessarily represent two very different gradients (<500 vs >1000 ºC/GPa, respectively); and (2) the geochemical record of the plutonic bodies, as well as the appearance of a garnet granulite and an orthopyroxene granulite could be easily explained within a much narrower P-T field (Fig. APP-A7) with a gradient ranging from ≈700 to ≈900 ºC/GPa. This range is in agreement with independent estimations (e.g. Gardiner et al., 2019) and fall within the gradient obtained from our peak mineral conditions. While our analyses benefit from geologically-constrained data within Isua and the Itsaq Gneiss Complex, Nutman et al. (2020) uses a more generalized approach applying simplified mineral reactions in P-T space as well as a simplified estimate of the general parent material composition (MORB) that may or may not be appropriate to represent geochemical and mineralogical characteristics of the Archean

record protolith (e.g. Smithies et al., 2009; Johnson et al., 2017). We therefore conclude that more detailed P-T data is needed for the samples reported by Nutman et al. (2020) to be able to retrieve and compare changes in their metamorphic record and, most importantly, assess the possible presence or absence of paired metamorphism.

2.4.3 Implications for the tectonic evolution of the Isua supracrustal belt

The data and discussion presented in this work have profound implications evaluating the validity of the three different tectonic models that are currently put forward for the evolution of Isua (Fig. 2.3). Two variants of horizontal tectonic models interpret the pervasive deformation and metamorphism throughout the ISB as a product of subduction and/or collision of the 3.7 Ga and 3.8 Ga belts (Fig. 3a, b; Komiya et al., 1999; Nutman & Friend 2009; Arai et al., 2015). Both predict, accordingly, the development of a systematic metamorphic gradient across the area (Nutman et al., 2013, 2020; Arai et al., 2015). However, petrography and extracted P-T constraints presented here are inconsistent with any north-south metamorphic gradient predicted by the south-dipping subduction model (Model A, Fig. 3a; Komiya et al., 1999; Hayashi et al., 2000; Arai et al., 2015). The limited thickness of the belt and the distribution of our samples precludes the necessary spatial resolution of P-T data to adequately test the existence of an east-west gradient towards the interior of the 3.7 Ga TTG and with that the viability of the north-dipping subduction model (Model B, Fig. 3b; Nutman et al. 2013). Notwithstanding, our results confirm amphibolite conditions for the 3.8 Ga part of the belt which contrast the reported greenschist facies peak conditions for this belt based on field observations (Nutman et al. 2013). Model B argues further that the garnet cores in the 3.7 Ga belt record a different tectono-metamorphic event (Gauthiez-Putallaz et al., 2020), related to the formation of a 3.7 Ga proto-arc in a subduction zone (Nutman et al., 2015). However, this study's garnet analyses results offer an alternative, more prudent interpretation of the different core-annuli garnet domains, suggesting that they do not

necessarily reflect different tectonic events, but rather a continuous metamorphic-deformation episode. Furthermore, our evidence is consistent with homogenous metamorphism all along the belt rather than a systematic metamorphic gradient. In summary, our results and existing geochemical, isotopic, and structural data could be equally, if not better be explained by the predictions of non-uniformitarian models.

Vertical tectonic regimes such as the heat-pipe model (Moore & Webb, 2013) predict that the ISB was emplaced as a continuous volcano-sedimentary sequence formed by rapid resurfacing events and subsequent crustal melting to generate the TTGs (Webb et al., 2020). This model (Fig. 2.3c) provides a scenario consistent with the data presented here as well as reported field relationships. The model predicts an amphibolite facies metamorphism across the entire ISB, that was syn-tectonic to deformation related to shearing that folded the volcano-sedimentary sequence (Fig. 2.3c, 2.10a) which is inferred by the A-type fold geometry of the ISB (Webb et al., 2020). Additional support for the viability of a heat-pipe like model are the following observations: (1) the model allows for the formation of a stable crust necessary to generate the reported multiple melting events directly related to TTG emplacement (Hiess et al., 2011; Hoffmann et al., 2014); (2) nearly non-existent contamination of the igneous rocks consistent with the efficient extrusion of hot materials envisaged (Polat et al., 2002); (3) rapid resurfacing and burial inhibit the sedimentary recycling of the older units and allows for continuous basalt-surface water interactions that is required to produce the oxygen isotopic composition of the TTG zircons from melting of a deep seated hydrated basaltic source (Hiess et al., 2009). Furthermore, A-type folding explains the two opposing shear sense and the quasi-homogenous strain intensities recorded in the macro- and micro-structures across the belt (Zuo et al., 2021a). Thus, in summary, we argue that the syn-metamorphic record of the ISB is more easily explained with the predictions of heat-pipe model rather than a plate tectonic scenario which would predict

significant spatial differences in recorded peak metamorphic grade both in temperature and pressure. However, as expected by the constraints of the heat-pipe model, a previous burial metamorphism must have affected the ISB. The microstructures and minerals of this earliest recorded event (Pre-M_1, Fig. 2.10a) were probably completely recrystallized and replaced during the pervasive syn-tectonic deformation, but some relics might have been preserved in the cores of some of the garnets exhibiting randomly oriented inclusions (Fig. 2.4b, APP-A1f). Further studies on those cores could give inside on the changes in pressure from the 3.7 Ga to the 3.8 Ga belts, to test the model of a continuous thickened supracrustal sequence.

2.5 Conclusions

The ISB is one of the best preserved >3.5 Ga terranes and its study has been crucial to our understanding of Early Earth processes. However, the nature of its metamorphic record has long been overlooked, despite it being key to understanding the tectonic evolution of the belt. Our comprehensive study on the metamorphism of the ISB provides new micro-structural and thermobarometric data that allows us to reconcile previously published interpretations and contradictions of the metamorphic history of the ISB. Our study shows that:

- Petrographic observations shed light on the problem of preservation of the metamorphic record. Our observations reveal significant overprinting of peak assemblage by retrograde minerals while preserving the original fabrics (e.g. the penetrative external foliation, Fig. 2.5e & 2.10c). Such selected preservation may have led to previous misinterpretations of the metamorphic record.

- The combination of micro-structural analysis and chemical zoning applied to garnet offers a simpler explanation for the different compositional zones within garnet typical of the ISB, showing that the core and annuli grew during a continuous tectono-metamorphic event (Fig. 2.10a), followed by a post-

tectonic metamorphism recorded in garnet rims overgrowing the syn-tectonic fabrics (Fig. 2.10b).

- The ISB experienced at least three distinct metamorphic events recognisable throughout the belt (Fig. 2.10): a M_1 event defined by nearly homogeneous syn-tectonic amphibolite facies metamorphism with peak conditions at 550-600 °C and 0.5-0.7 GPa ; a M_2 lower amphibolite facies (<540 °C and <0.5 GPa) post-tectonic thermal event; and a M_3 event(s) defined by (upper) greenschist facies (<500 °C) pervasive retrograde metamorphism associated with local brittle failure and fluid infiltration.

- The metamorphic and geological records of the ISB are consistent with non-uniformitarian, pre-plate tectonic models.

Our findings on the poly-metamorphic history of the ISB do not necessarily exclude the possibility of horizontal movements during its evolution. However, the metamorphic evidence presented in this work and previously published data argue that the early Archean evolution of the ISB is consistent with a regime dominated by heat-pipe tectonics (Fig. 1.3b). Thus, the ISB provides direct evidence that the Early Archean geodynamics was distinct to that of modern Earth. We stress that, despite the evidence presented here, a more detailed and spatially constraint P-T-X-d-t evolution of the ISB, as well as petrochronological constraints on the different metamorphic events are necessary develop a time constraint tectonic model for Isua.

Chapter 3. Quantitative microstructural and chemical analyses reveal compositional and mineralogical effects on inclusion-rich garnet growth in medium-grade rocks: An example from the Isua supracrustal belt, Greenland

This chapter will be submitted to the journal *Contributions to Mineralogy and Petrology*. I will be the first author of this contribution with Sandra Piazolo, Thomas Müller, Dominik Sorger, Jiawei Zuo, Joyjit Dey, A. Alexander G. Webb, and Peter J. Haproff as co-authors. I was responsible for conceptualization, manuscript writing, most of the data collection (apart where it is indicated below), data processing, figures, and data analysis. Sandra Piazolo and Thomas Müller supervised and were involved in the conceptualization. Sandra Piazolo and Joyjit Dey collected the EBSD data. Dominik Sorger obtained the high-resolution images of the thin sections. Jiawei Zuo obtained the SEM compositional maps. Sample collection was made by Thomas Müller, A. Alexander G. Webb, Jiawei Zuo and Peter Haproff. All authors participated in editing.

Abstract

Factors controlling inclusion-rich garnet growth is a topic rarely discussed in the literature, despite their common occurrence in medium-grade metamorphic rocks. Garnets of the Eoarchean Isua supracrustal belt show a diversity of microstructures, internal morphologies, chemical and crystallographic orientation patterns, even though P-T and finite strain within the belt were largely homogenous. Two garnet types can be distinguished: Type-I garnets are inclusion rich, hence "skeletal", show irregular internal morphologies with thin interconnected garnet branches often closely mimicking pre- syn-metamorphic foliations. Patchy chemical zoning is coupled with changes in crystallographic orientation. Type-II garnets have lower proportions of inclusions than type I garnet (<40% vs > 60%), therefore classified as "non-skeletal". They exhibit concentric chemical zoning and sharp boundaries

between zones suggesting a continuous euhedral growth. Crystallographic orientation changes within individual garnet grains are less pronounced than in Type I garnets.

Our analyses shows that rocks' mineralogy, (local) composition and microstructures play an important role in determining which garnet type is present. The chemical signature is highly dependent on the local equilibrium volume for Type I garnets; therefore, such garnets should be used cautiously for metamorphic interpretations such as geothermobarometry. This type of garnets appears to be more common in felsic rocks. On the other hand, Type-II garnets present larger scale equilibrium features such as concentric chemical zonation, consequently application of different geothermobarometric tools and garnet growth modelling can provide more meaningful information.

According to our results the documented diversity of inclusion-rich garnet microstructures is not the result of different tectonostratigraphic sequences or multiple metamorphic events expected if the tectonometamorphic evolution ISB signatures was related to plate tectonics as we know it today.

3.1. Introduction

Inclusion-rich garnet porphyroblasts are common in medium-grade metamorphic rocks (e.g., Spear and Daniel, 2001; Yang and Rivers, 2001; Rollinson 2002; Wilbur and Ague, 2006; Whitney et al., 2008; Faleiros et al., 2010; Staples et al., 2013; Dempster et al. 2020; George and Gaidies, 2020). Such inclusion-rich garnets are commonly used to decipher the deformation history of rocks as the geometric relationships between internal, inclusion-defined foliations and external foliations are directly related to pre-, syn-, post-tectonic garnet growth (e.g., Bell and Johnson, 1989; Johnson, 1999; Passchier and Trouw, 2005; Robyr et al., 2007). The included phases may provide information of the early stages of the rocks' tectonometamorphic evolution (e.g., St-Onge, 1987). These characteristics in combination with garnet chemical zoning (Tracy and Robinson, 1976; Spear et al., 1984) offer a wealth of

information that is typically used to understand the tectonometamorphic evolution of the studied rocks. However, some inclusion-rich garnets show complex irregular zoning and morphologies that rather reflect local equilibrium which could potentially mislead metamorphic interpretations, for example in estimating peak conditions (Daniel and Spear, 1999; Yang and Rivers, 2001; Hirsch et al., 2003; Ague and Carlson, 2013; Carlson et al., 2015; Dempster et al., 2017). Thus, understanding why and how garnet porphyroblasts enclose minerals and what inclusions can tell us about porphyroblasts growth mechanisms is important for a correct interpretation.

It has been suggested that inclusion-rich garnets are the consequence of growth in relatively low temperature conditions (Yang and Rivers, 2001; Hirsch et al. 2003), low solubility of the garnet-forming elements in CO_2-rich intergranular fluids (Carlson et al., 2015), low grain boundary diffusivity in quartz-rich, mica-poor domains (Dempster et al., 2017; George and Gaidies, 2020) or diffusion-controlled growth (Miyazaki, 2015). So far, such studies have mainly focussed on metapelitic rocks based on their common abundance of garnet. However, inclusion-rich garnets occur in a variety of compositions as exemplified in the rocks from the Isua supracrustal belt (ISB). Here, different lithologies contain garnet porphyroblasts with cores rich in inclusions (Rollinson 2002, 2003; Gauthiez-Putallaz et al., 2020; Zuo et al., 2021b; Chapter 2), where inclusion proportion, garnet internal morphologies and microstructures, as well as chemical zoning vary in samples across the belt at the mm to 100 m scale. Nonetheless, recent studies interpreted the P-T conditions under which garnet grew as being homogeneous throughout the area (Zuo et al., 2021b; Chapter 2). This provides the opportunity to explore the effects of rock composition and mineral assemblages on porphyroblast growth.

In this chapter, using quantitative microstructural observations along with chemical, modal abundance, and quantitative orientation data, we assess the availability of garnet forming

elements, presence of reactant and non-reactant phases and its implications for characteristics of garnet growth and resultant microstructural patterns. We base our study on the analysis of 19 samples from the ISB. Based on our analyses, we develop a scheme using quantitative microstructural and chemical data to understand growth mechanisms and element availability in medium-grade rocks which in turn will help to improve metamorphic interpretations utilizing garnet porphyroblasts. We conclude with an assessment of the implications of our findings for the tectonometamorphic interpretations proposed for the ISB.

3.2. Case study area: The Isua supracrustal belt
3.2.1. Geological background

The Isua supracrustal belt (ISB) is one of the best preserved supracrustal sequences of the Eoarchean located in southwestern Greenland (Nutman et al., 1996). It is comprised of meta-volcano-sedimentary rocks with a protolith age ranging from S to N from 3.8 and 3.7 Ga, separated by a thin (<1 km-thick) metasedimentary sequence with an estimated age of 3.75 Ga (Nutman and Friend, 2009). ISB rock compositions range from ultra-mafic (Dymek et al., 1988) to felsic rocks (Nutman, 1986) including chemical sedimentary rocks such as banded iron formations (Moorbath et al., 1973). The belt is bounded by two big tonalite-trondhjemite-granodiorite (TTG) bodies (Fig. 3.1), one to the north with an age of 3.7 Ga which is in contact with the meta-volcano-sedimentary rocks of similar age, and another one to the south with an age that overlaps the 3.8 Ga sequence in direct contact with it (Nutman and Friend, 2009). The belt is intruded by tonalite-derived (Hiess et al., 2009, 2011) 3.66–3.60 Ga granitic dykes that are interpreted to be syn-tectonic (Nutman & Friend, 2009). The belt is also cross-cut by variably deformed E-W and N-S trending noritic to doleritic Ameralik dykes (Nutman, 1986; White et al., 2000) with zircon ages ranging from ca. 2.4 Ga to 3.5 Ga (Nutman et al., 2004).
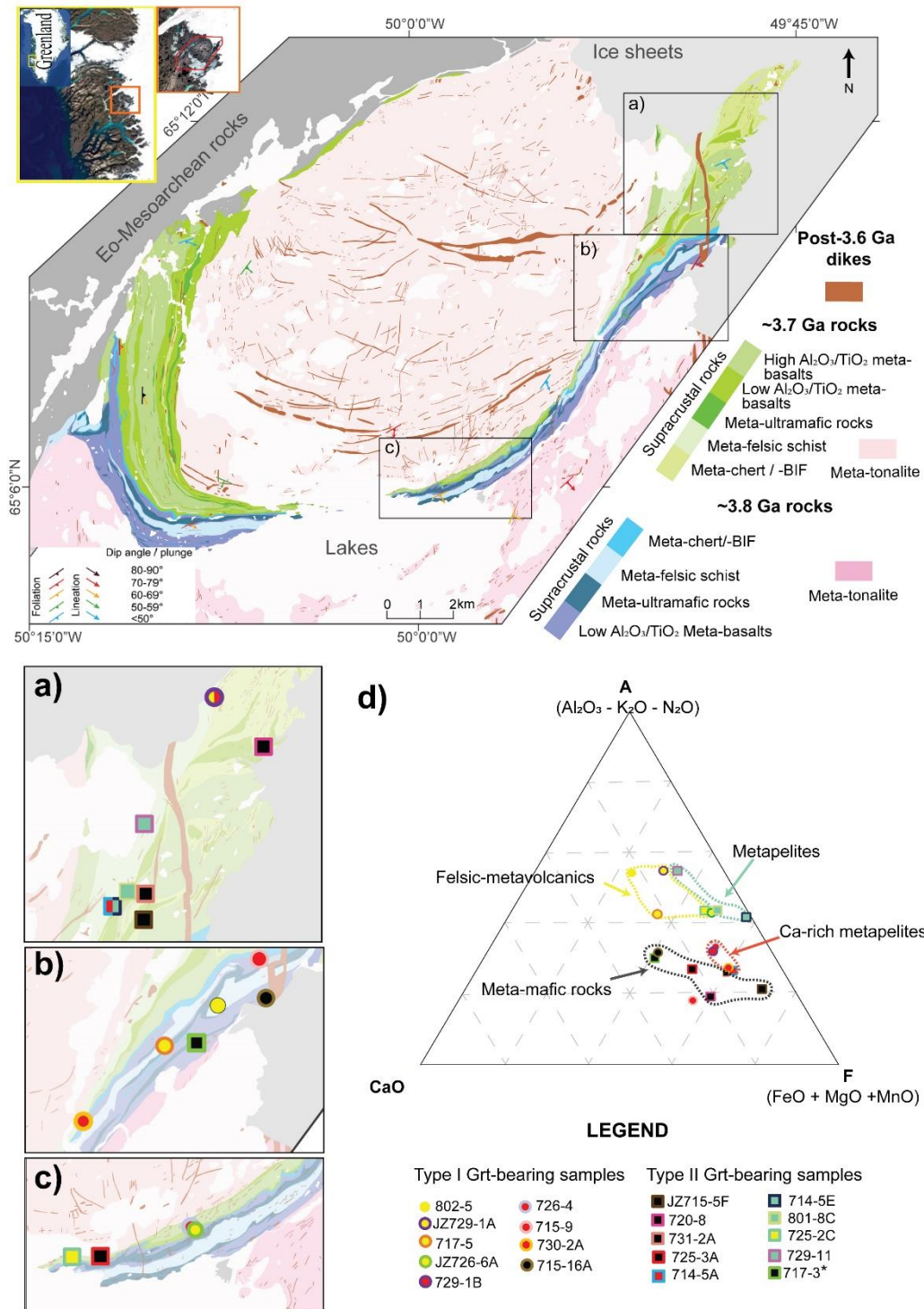
Figure 3.1. Geological map of the Isua supracrustal belt, showing the location of the samples (a-c) studied in chapter 3. d) AFC ternary diagram showing the compositional groups identified. Note adoption of 3.7 Ga and 3.8 Ga supracrustal sequences after Nutman and Friend (2009). Map after Zuo et al. (2021) with information of Nutman and Friend (2009). Motif shape code: circles=Type I-"skeletal" garnet bearing samples and square= Type II-"non-skeletal" garnet bearing samples. Colour codes for motifs fill: black = meta-mafic rocks; yellow=meta-felsic volcanics; cyan= metapelites; red= Ca-rich metapelites.

Garnet-biotite and Ti-in-biotite geothermometry combined with phase equilibria geothermobarometry have been used to show that the ISB experienced syn-tectonic amphibolite facies metamorphism with peak conditions at 0.5-0.7 GPa and 550-600 °C (Chapter 2). In Chapter 2 it is also demonstrated that the observed metamorphism does not exhibit any significant gradient across or along the Isua supracrustal belt. The lack of gradient is also observed with the quartz fabric thermometer, applied to a similar set of samples, that equally suggest temperatures within the same 550-600°C range across the belt (Zuo et al., 2021b). This major metamorphic event was syn-tectonic to the main and pervasive deformation event recorded by the formation of sheath and curtain folds (Webb et al., 2020), which is suggested by field measurements showing that fold axis and metamorphic lineations are parallel. Strain intensity during this event appears to be quasi-uniform across the belt as suggested by quantitative analysis of quartz fabrics in samples from different parts of the eastern arm of the belt, including areas interpreted as shear zones (Zuo et al., 2021b). The syn-tectonic metamorphism (M_1) was followed by a post-tectonic lower amphibolite facies metamorphism (M_2) at < 0.5 GPa and < 550 °C (Fig. 2.10; Boak and Dymek, 1982; Rollinson, 2002; Chapter 2), which is typically recognized by the growth of post-tectonic inclusion-poor garnet rims or overgrowths (Boak and Dymek, 1982; Blichert-Toft and Frei, 2001; Rollinson, 2002, 2003; Gauthiez-Putallaz et al., 2020). Garnet porphyroblasts are generally not affected by retrograde reactions (see Chapter 2).

3.2.2 Previously reported garnets characteristics and interpretations

Garnets within the ISB have been reported in rocks with different compositions including metapelites (Boak and Dymek, 1982; Rollinson, 2002; Hayashi et al., 2000; Gauthiez-Putallaz et al., 2020; Chapter 2), Ca-rich metapelites (Rollinson, 2003, 2002), amphibolites (Rollinson, 2002, 2003; Chapter 2), felsic meta-volcanics (Zuo et al., 2021; Chapter 2) and even banded iron formations (Dymek and Klein, 1988; Zuo et al., 2021; Chapter 2).

Garnets have been reported to typically show two distinct microstructural domains: an inclusion-rich syn/pre-tectonic core and a post-tectonic inclusion-poor rim with well-developed facets (e.g. Fig. 2.4; Boak and Dymek, 1982; Rollinson, 2002, 2003; Gauthiez-Putallaz et al., 2020; Zuo et al., 2021; Chapter 2). Early works also showed that garnets exhibit varying chemical zoning patterns (Boak and Dymek, 1982; Rollinson, 2002, 2003). This diversity has led to different interpretations that are summarized here.

Rollinson (2002, 2003) suggested that garnets are often characterized by three (core-annulus-rim) distinct, generally concentric, chemical zones. In his studies, Rollinson (2002, 2003) argued that the overall chemical patterns refer to five different tectonostratigraphic domains, whereas four of them shared a common syn-tectonic and post-tectonic metamorphic history represented by the annuli and rims, while the cores recorded earlier, probably different, tectonic histories.

Gauthiez-Putallaz et al., (2020) described in detail two garnet grains in metapelitic rocks from the central-northern portion of the 3.7 Ga sequence. They reported quantitative compositional maps alongside with trace elements and $\delta^{18}O$ profiles and distinguished four distinct chemical zones. Their interpretation of the chemical patterns is similar to Rollison's (2002, 2003), arguing for three different tectono-metamorphic events in the 3.7 Ga sequence, represented by the core, annuli, and rim. They contend that the core composition is not found anywhere else in the belt, and therefore interpret that these cores represent a metamorphic event that occurred before the assemblage of a composite arc that is now represented by the 3.7 sequence (Nutman et al., 2015)

Chapter 2 presented new data of a spiral-like garnet from a metapelitic rock originating from the 3.7 Ga supracrustal sequences with similar bulk chemistry, mineralogy, and locality as those reported by Gauthiez-Putallaz et al. (2020). The comparison of the data showed that both garnets have a similar geochemical pattern and therefore can be assumed to have

experienced identical tectono-metamorphic evolution. However, in Chapter 2 it is argued that the inclusion trails in the spiral-like garnet continue across the apparent chemical zones (Fig. 2.6) and thus concluded that the core and annuli most likely evolved in a continuous tectono-metamorphic event. Consequently, in their interpretation the Isua garnets only recorded two different tectonometamorphic events, represented by the inclusion-rich cores and the inclusion-poor rims. The different chemical zones described in the syn-tectonic garnets are therefore interpreted to be a product of changes in the garnet-forming reactions and/or later diffusion.

An improved understanding of the growth mechanism and its controlling factors is crucial for a solid interpretation of the tectonometamorphic evolution of the ISB, especially since the conclusions derived from the study of garnets bear implications for the tectonic models proposed to explain the evolution of the belt, where both uniformitarian (e.g., Nutman et al., 2013) and non-uniformitarian (Webb et al., 2020) models have been proposed. Discerning between these contrasting models is key for resolving the discussion of Archean geodynamics and potential associated onset of plate tectonics.

3.3. Methods
3.3.1. Sample selection

We investigated 19 samples representing a wide range in chemical compositions and garnet microstructures. Rocks were collected along the eastern arm of the Isua supracrustal belt (Fig. 2.1), covering transects from north to south and west to east. The selection of samples is specifically aimed to test for systematic relationships in microstructures regarding their spatial distribution within the belt (e.g., differences of garnets from the 3.7 and 3.8 Ga sequences), mineral assemblage, modal abundance, and chemical bulk composition.

3.3.2 Thin Section µXRF mapping and phase mapping using XMapTools processing

Thin sections were cut parallel to the mineral lineation and perpendicular to the foliation.

Mineral modal abundances in most of the thin sections were calculated using phase maps

processed with the software XMapTools version 3.3.1 (Lanari et al., 2014, 2019) based on

elemental maps obtained with a Bruker M4 Tornado micro-X-ray fluorescence (µXRF)

scanner at the Geoscience Centre, University of Göttingen. Conditions used for the elemental

map acquisition were 50 kV accelerating voltage, 500 µA current, a spot diameter of 20 µm

and step size from 20-25 µm. This translated a total pixel count of >1 million for most of the

rocks, i.e., a significantly higher count than the 500 to few thousand points typically used in

classical point counting analysis in thin section (Kretz, 1969; Palin et al., 2016). For a few

samples (715-5F, 729-1A, 726-6A, 715-16A and second thin section of 717-3) high-

resolution phase SEM maps (5-10 µm step size and 1 µm spot size) reported by Zuo et al.

(2021) were used. Matrix grain size in the studied rocks typically range from 20 - 200 µm,

with most of the grains having sizes > 50 µm in diameter. The general microstructures and

distribution of the phases in the rock that are observed in thin sections are successfully

represented in the phase maps after data processing, validating the modal percentages derived

by the image processing. It should be noted though that due to the relatively large spot and

step size (20-25 µm), small phases such as <30 µm inclusions in the porphyroblasts could not

be resolved.

3.3.3 Garnet elemental mapping, point analysis and phase mapping

For comparison of bulk mineral chemistry and chemical zoning patterns of garnet grains in

different samples, calibrated element maps and quantitative point analyses were obtained and

processed for at least one garnet porphyroblast in each sample.

Chemical point analyses and major element mapping of garnet grains and adjacent areas and

additional mineral phases were performed in the Goettingen Laboratory for correlative light

and electron microscopy (GoeLEM) at the Geoscience Centre, University of Göttingen with

an Electron Probe Micro Analyzer (EPMA) JEOL JXA 8900 RL equipped with an energy-dispersive (ED) and five wavelength-dispersive (WD) spectrometers. For the element maps, Al, Mg, Mn, Ca and Fe were obtained with the WD detectors and Si and Ti with the ED detector using a step size between 2 to 7 µm depending on garnet size. The instrument operated with an accelerating voltage of 20 kV, an 80 nA beam current, a beam size of 1 µm and 50 ms dwell time. To assess the chemical zoning of garnet porphyroblasts transects consisting of 30 to 60 point analyses from core to rim or rim to rim were acquired. An acceleration voltage of 15 kV, spot diameter of 5 µm and a beam current of 20 nA was used. Scanning Electron Microscope (SEM) maps were acquired at the University of Leeds with the Tescan VEGA 3 XM SEM equipped with an Oxford Instruments X-max 150 EDS detector. Used conditions where an accelerating voltage of 20 kV and 20 nA current and step size typically > 5 µm.

Phase maps and chemical calibrated maps were obtained using the software XMapTools version 3.3.1 (Lanari et al., 2014, 2019), using the X-ray elemental maps and the point analysis collected in this work and some reported in Chapter 2.

3.3.4 Quantitative image analysis of garnet porphyroblasts

The software ImageJ (Schneider et al., 2012) was used to quantify the relative area proportions of the syn-tectonic garnet, inclusions, and post-tectonic garnet overgrowth. High resolution images of thin sections containing garnet porphyroblasts, were mainly obtained with the automated Olympus polarization microscope BX53M being part of GoeLEM at the Geoscience Centre, University of Göttingen. In addition, some of the high-resolution SEM phase maps presented in Zuo et al. (2021b) have been analysed.

Garnet porphyroblasts show two very distinct and well-defined microstructural domains in most of the samples: the relatively inclusion-rich core and an inclusion-poor overgrowth with well-developed facets (cf. Fig. 3.2). For each grain, first the overgrowth areas were defined

and their percentage calculated by dividing the area of the inclusion-poor overgrowth by the

total area of garnet in the porphyroblast (Fig. APP-B1).
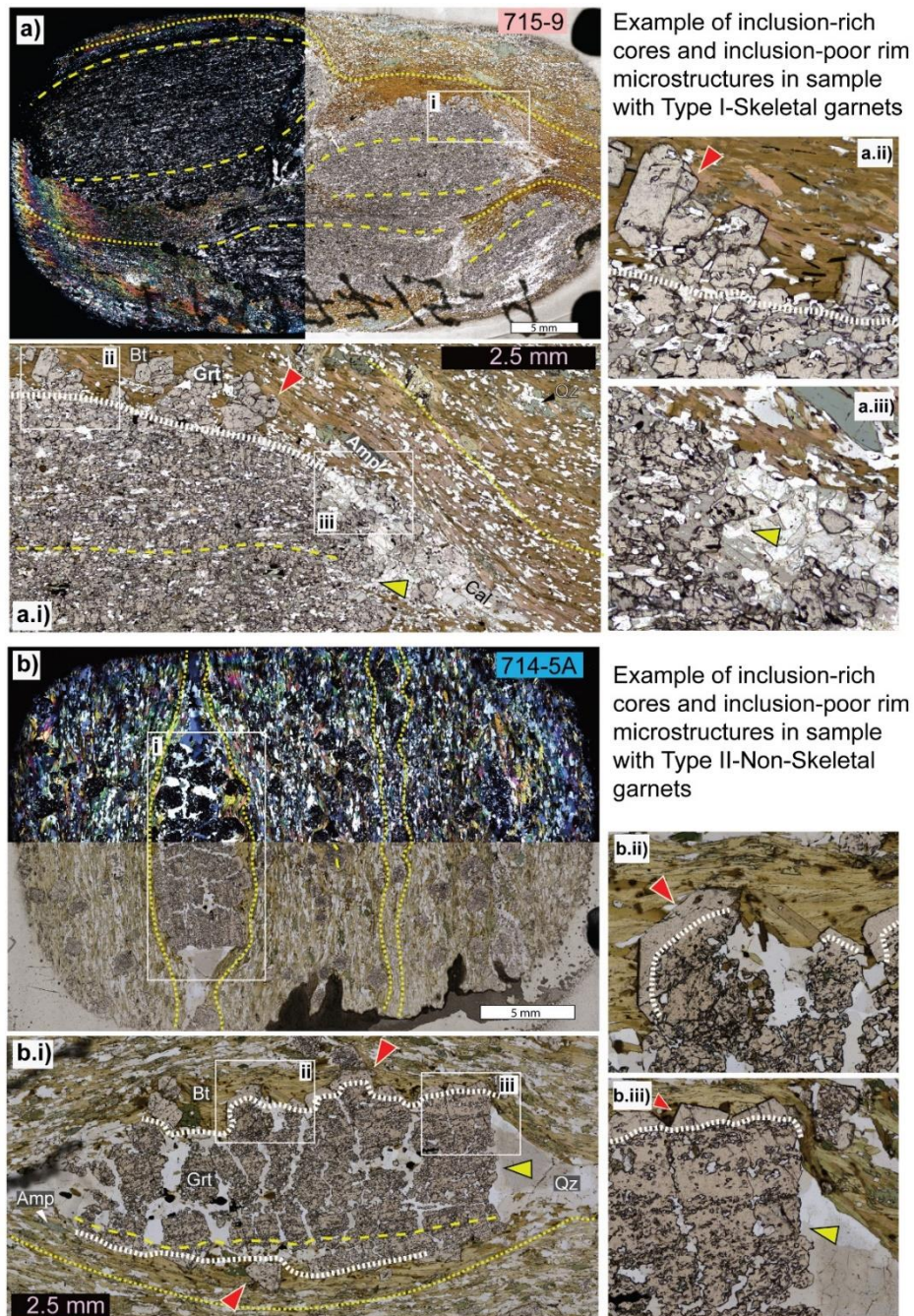
Figure 3.2. Characteristics of garnets in Ca-rich metapelitic rocks. a) Thin section of mafic rock bearing type-I garnets; sample 715-9. a.i) Section of a large (>1 cm) garnet porphyroblasts with internal (yellow dashed lines) and external foliation (yellow dotted lines) texture; foliation pattern A (c.f. Fig. 3d.i); a.ii) post-tectonic euhedral garnet (highlighted with white dotted line) overgrowing on top of biotite; a.iii) limited post-tectonic growth where core is next to quartz-calcite-rich zones. b) Thin section of Ca-rich metapelitic rock bearing Type-II garnets, sample 714-5A. b.i) Large garnet with fractures affecting it perpendicular to the external foliation; foliation pattern B and C (c.f. Fig. 3d.ii-iii); b.ii) continuous inclusion-poor rim overgrowing biotite; b.iii) no post-tectonic garnet growth where core is next to quartz-rich zones. Red arrows point to well-developed post-tectonic rim and yellow arrows point to zones where post-tectonic rim was limited or inhibited.

Subsequently, the proportion of garnet and inclusions was determined for the core. We define

the coefficient φ as a normalized parameter describing the relative proportion of inclusions in

the garnet (Fig. APP-B1):

$$\varphi = \frac{area\ of\ inclusions\ within\ the\ core}{area\ of\ inclusions\ within\ the\ core\ +\ area\ of\ garnet\ core}$$

The coefficient φ provides a measure of the degree of garnet "skeletalness", such that a

garnet core with φ=0 would be a grain completely devoid of inclusions, and φ=1 would refer

to a "porphyroblast" consisting of "inclusions" only.

Aspect ratio or ellipticity E of the cores was also calculated:

$$E = \frac{Long\ axis\ of\ the\ inclusion - rich\ core}{Short\ axis\ of\ the\ inclusion - rich\ core}$$

3.3.5 X-ray fluorescence bulk rock chemistry
Powders for bulk rock chemistry were obtained from twin chips of those used for the thin

sections. Weight difference of powders before and after overnight heating at 1025 °C were

used to determine the loss on ignition (LOI). Fused glass beads used for X-ray fluorescence

(XRF) were prepared with a mix of 0.4 g dried sample, 4.0 g of 66% Li tetraborate: 34%

metaborate flux and 1-2 drops of lithium Iodide solution in a $Pt_{95}Au_5$ crucible. Mixtures were

fused in the furnace at 1150 °C for a total of 40 minutes, gently swirling the samples at the

20, 30, 35 min intervals to ensure a proper mixing before cooling. Major elements bulk rock

chemistry was acquired from the fused beads by XRF spectrometry using a Rigaku ZSX

Primus II spectrometer at the University of Leeds. Accuracy in major elements for the certify

standard STSD4 was ±≤1 % relative for SiO_2, CaO and K_2O, ≤ 2.5 % relative for Al_2O_3,

≈3.5% relative for FeO_{tot}, 1 to 5% relative for MgO, 4 to 6 % relative for MnO, ≈6% relative

for TiO_2 and 2 to 12% relative for P_2O_5 and Na_2O.

3.3.6 Quantitative orientation analysis – Electron Backscatter Diffraction analysis (EBSD)

A total of 9 garnet porphyroblasts were analysed using EBSD to document the crystallographic characteristics of the porphyroblasts, with special emphasis on the changes within individual porphyroblasts. All thin sections were polished using a syton fluid and coated with 3 nm of carbon. EBSD analyses were performed using FEI Quanta 650 FEG–Environmental SEM equipped with an Oxford Instruments INCA 350 EDX System and Symmetry EBSD detector at the University of Leeds. Conditions were set at an acceleration voltage of 20 kV, 80 nA beam current, working distance of ~23 mm, sample tilt of 70° and a step size of typically 2.5 µm. Data was processed with the AztecCrystal© software. Data is presented as maps showing the spatial variation of the grain reference orientation distribution (GROD) within individual garnet grains. These GROD Angle maps are generated by determining the average orientation for each porphyroblast and plotting the angular deviation from this mean orientation for each pixel, i.e. analysis spot. In addition, pole figures of the measured main crystallographic axes of the garnet are shown illustrating crystallographic character of the orientation spread within a porphyroblast. This pattern of orientation spread seen in the pole figures can be used to evaluate whether the orientation spread is resultant from dislocation creep, i.e. organized crystal slip along a specific slip plane and along a specific slip direction (e.g., Reddy et al. 2007; Piazolo et al. 2008) or growth related orientation spread (Smith et al. 2015; Spruzeniece et al. 2016). As the spread of orientation is to some extent influenced by the size of the porphyroblast considered, we introduce an area normalize orientation spread parameter ψ:

$$\psi = \frac{\text{maximum orientation spread angle}}{\text{total analysed area}}$$

3.4. Results

All samples in this study are porphyroblastic foliated rocks with garnet as the main, and in most of them, only porphyroblast. A brief petrographic description, quantification of the

mineral assemblages in addition to the bulk chemical composition of the rocks and an extensive microstructural and chemical analysis of the garnet porphyroblasts are provided here. A more detailed petrographic description of the samples and field context has previously been reported in Webb et al. (2020), Zuo et al. (2021b) and Chapter 2 (section 2.3.1)

3.4.1 Garnet types

While most garnets exhibit an inclusion-poor/free rim and a variably inclusion-rich core, the proportion of inclusions in the core (Fig. 3.3b) and the habit of the inclusion-poor overgrowth substantially vary between individual samples (Fig. 3.3c). To simplify descriptions, we define two main garnet types based on their φ-values (e.g., Fig. 3.2) with Type I and Type II defined by a φ-value above and below 0.4, respectively. This dividing φ-value was chosen considering in addition to other changes in characteristics such as dominantly irregular versus concentric chemical zoning. However, it should be noted that there is, in fact, as continuum. *Type I* garnet exhibit a core with a mean φ-value > 0.4 (i.e., the garnet comprises up to 60% of the area of the inclusion-rich core); they are "skeletal". *Type II* is referred to as "non-skeletal", with syn-tectonic cores that yield a φ-value < 0.4. Patterns of inclusion defined foliations, i.e., internal foliation (Passchier and Trouw, 2005) relative to foliations in the matrix surrounding the porphyroblasts (external foliations) can be divided into four main groups: Pattern A (Fig. 3.3e.i) has arc-shaped internal foliations that converge to the pressure shadows of the porphyroblast and external foliations bending symmetrically around the garnet. Pattern B (Fig. 3.3e.ii) shows spiral-like internal foliations that typically continue to the external foliation which in turn is wrapping around the garnet. Pattern C (Fig. 3.3e.iii) is characterized by straight, or slightly curved, inclusion trails parallel or subparallel to the external foliation. In pattern D (Fig. 3.3e.iv), inclusions are randomly oriented and external foliation bends around the garnet porphyroblast. These different garnet patterns do not show a

clear spatial correlation as the other characteristics (Fig. 3.3d), different patterns appear in samples from the same outcrop.
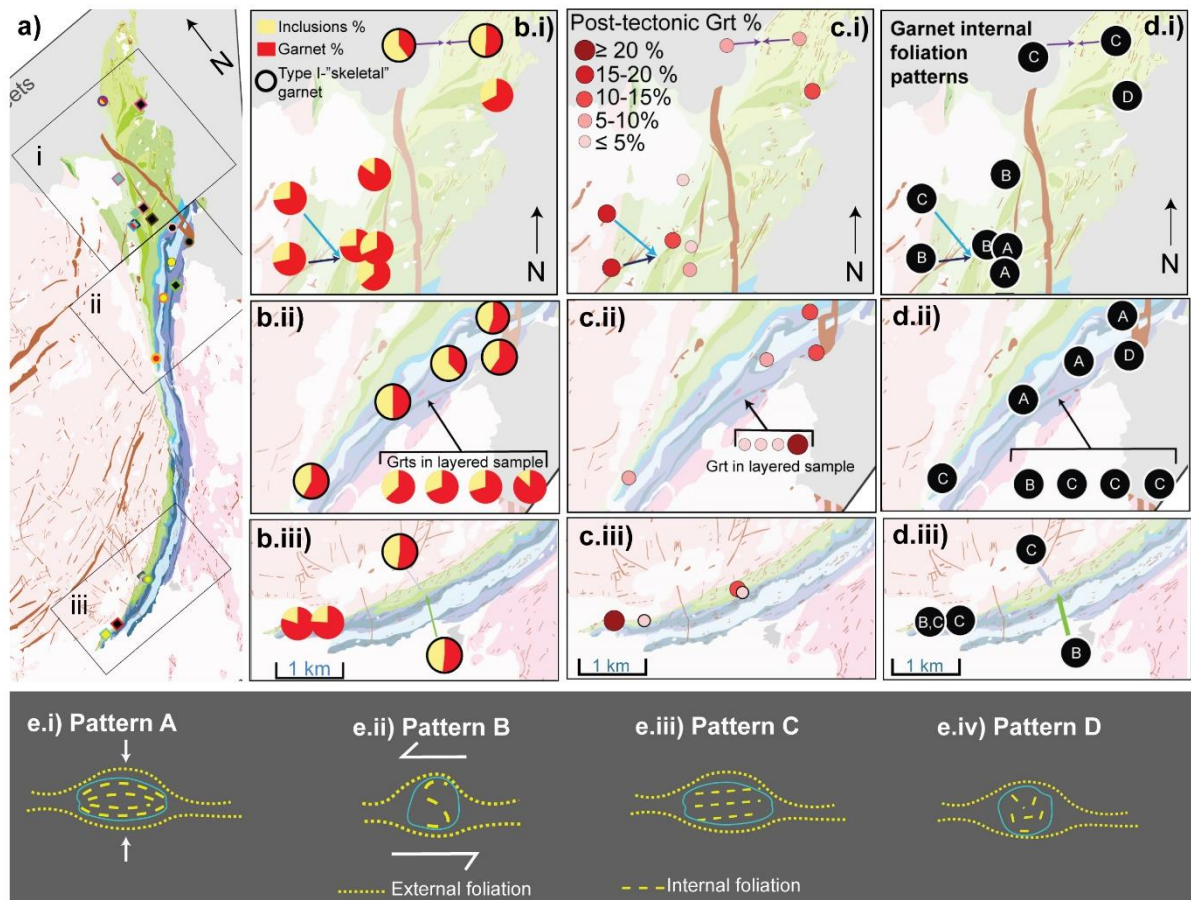
Figure 3.3 Maps showing the distribution of different features of the garnets in the ISB. a) eastern arm of the ISB with samples and with the location of the inlets. b) Pie charts of the proportion of garnet and inclusions in the inclusion-rich cores; charts enclosed with black rings represent Type-I skeletal garnets. c) Visual representation of the proportion of post-tectonic garnet in the grains. d) Distribution of the 4 groups of garnet internal patterns. e) Schematic representation of 4 groups of external and internal foliation patterns described for the garnets with inclusion-rich cores. Motifs for external and internal foliations are the same as for the rest of the figures. e.i) Pattern A: syntectonic – pure shear, e.ii) Pattern B: syntectonic simple shear, e.iii) Pattern C: intertectonic/two stage growth, e.iv) pattern D: pre-tectonic

We first briefly describe the bulk composition of the rocks and their mineralogy and mention the type of garnets they bear. We then summarize the characteristics of the two types of garnets. We compare the inclusion assemblages to the minerals in the rocks and describe microstructures, size, aspect ratio and the chemical zoning of the two garnet types. Unless otherwise stated, the descriptions and analysis refer to the inclusion-rich cores only.

3.4.2. Bulk rock chemistry

To investigate the relationship of the garnet microstructures and spatially resolved chemistry with bulk chemistry, the measured bulk composition, and mineral modes, along with fieldwork observations, were used to classify the different rocks. The identified rock groups are defined as meta-mafic rocks, Ca-rich metapelites, metapelites and meta-felsic volcanics. They exhibit clear distinctive bulk rock compositions (see AFC diagram, Fig. 3.1d) Samples 715-5F, 715-16A, 717-3, 725-3A, 731-2A are garnet-amphibolites and 720-8 is garnet-bearing schists. Their SiO_2-content is <55 wt. %, and they are typically enriched in FeO, MgO and CaO compared to rocks from other lithologies (Fig. APP-B2). Samples 717-3, 725-3A and 715-5F have Al2O3/TiO2 values >58, while the others show ratios <17 (Table B1). The samples are characterized by the presence of amphibole and/or other Fe-Mg bearing minerals (Table 3.1). Garnets from these rocks are of Type-II, apart from two samples (715-9 and 715-16A).

The Ca-rich metapelite group include samples 714-5A, 726-4, 729-1B, 730-2A, and 715-9. These rocks have similar contents of Al_2O_3 and K_2O compared to the meta-mafic rocks but higher proportions of SiO_2 (Fig. APP-B2a,e). In addition, they are enriched in CaO compared to typical metapelites described below (Fig. APP-B2d). The relatively high content in CaO translates in the appearance of $\leq 10\%$ of amphibole in most of these rocks, which does not occur in typical metapelites. All samples, apart from 714-5A ($\varphi=0.26$), contain Type-I porphyroblasts with similar φ-values of 0.47 – 0.59. Bulk composition of 715-9 is different from most of the Ca-rich metapelites (Fig. 3.1, APP-B2), but the chip used mostly was dominated by garnet which probably shift the composition.

Table 3.1. Mineral assemblages of the different rocks reported in this work and mean garnet proportion in the analysed porphyroblasts. All mineral abundances in area percentage. Mineral abbreviations after Whitney & Evans (2010). Cmp=Ca-rich metapelite; Mp=Metapelite; Grt-Amp= Garnet Amphibolite; Mafic Schist= MscMfv=Meta-felsic volcanics.

"TM17" samples	Protolith Age (Ga)	Lithology	Garnet inclusions	Garnet pattern	Syn-Tectonic mineral assemblage	Qz	Bt	Ms	Chl	Amp	Pl	Grt	Fsp	Ep/Czo	Cal	Ilm	Sill/Ky	St	Fe-Ox	Titanite	Other
802-5	3.8	Mfv	Qz, Cal, Ms, Tur, Ilm, Bt, Ep	A	Qz + Ms + Bt + Pl + Tur + Grt + Ep + Opaq	54.43	12.47	9.7	-	-	20.63	2.77	<1	-	-	-	-	-	-	-	-
JZ729-1A	3.7	Mfv	Qz, Ms, Bt, Chl	C	Qz + Bt + Ilm + Grt + Ms + Rt +	50	1	5	5	-	30	5	-	-	-	3	-	-	-	-	2
717-5	3.8	Mfv	Qz, Bt, Ms, minor Ap, Cal, Tur, Aln, Zm	A	Qz + Bt + Pl + Ms + Czo + Grt + Kfis minor Cal + Tur + Ilm	58.13	8.59	8.48	-	-	21.26	3.54	-	-	-	-	-	-	-	-	-
729-1B	3.7	Cmp	Qz, Ilm, Ms, Ep/Czo, Bt, minor Cal and Chl	C	Qz + Bt + Amp + Grt + Pl + Ilm + minor Cal+ early C(zo)	24.17	17.33	-	-	26.7	26.17	5.62	-	<1	-	<1	-	-	-	-	-
JZ726-6A	3.75	Mfv	Qz, Pl, Bt, Ilm, Ap	B	Qz + Bt + Ilm + Grt + Pl + Ms	30.16	20.23	4.48	-	-	31.02	5	-	-	1	0.15	-	-	-	-	-
726-4	3.7	Cmp	Qz, Bt, Fe-Ox, Ap	C	Qz+Bt+Amp+Grt+Ep+Ms+Pl+Fe-Ox+Tur (?)																
715-9	3.8	Msc	Qz, Ap, Chl, Bt, Cal, An, Ilm, Wo	A	Qz + Bt + Grt + Pl + Amp + Ep minor Ilm	20.86	22.45			1.62	<1	39.04	-	-	16.03		-	-	-	-	-
730-2A	3.75	Cmp	Qz, Cal, Bt, Ilm, Ep	C	Bt + Qz + Pl + Grt + Czo + Ilm + Cal + Ms(?) + minor Tur + Cal + Ap	33.69	35.25	<1	-	-	12.87	10.14	-	-	4.78	3.27	-	-	-	-	-
715-16A	3.8	Grt-Amp	Amp, Act, Ep, An, Cal, Bt, Qz, Ap	A	Qz + Bt + Grt + Amp + An + Ab + Cal minor Act + Ttn + Ap	17.61	14.91	-	-	20.74	5.39	6.66	-	21.71	1.58	-	-	-	-	1.17	-
JZ715-5F	3.7	Grt-Amp	Qz, Cal, Bt	D	Qz + Bt+Grt+Chl + Amp	25	60	-	5	1	-	15	-	-	-	-	-	-	-	-	<5
720-8	3.7	Grt-Amp	Cal, Qz, Ilm, Ap	D	Qz + Bt + Amp + Cal + Grt + Czo + Ilm	27.13	20.25	-	-	30.84	-	5.41	-	<1	16.37	0.05	-	-	-	-	

Table 3.1 *Continued*

Sample		Type	Minerals	Grp	Assemblage															
731-2A	3.7	Grt-Amp	Qz, Ilm, Ms, Ep/Czo, Aln, Bt, minor Cal and Chl	A	Grt + Amp + Bt + Qz + Ep/Czo + Ilm + minor Cal	34.78	-	-	21.02	-	-	-	-	-	-	-	-	-	-	-
714-5E	3.7	Mp	Qz, Ms, Ctd, Chl, Ilm, Tur, small Plg	B	Qz + Grt + Ms + Bt + Chl + Ilm + minor Tur + Pyr	-	-	29.32	-	-	-	14.87	-	-	<1	-	-	-	<1
714-5A	3.7	Cmp	Qz, Bt, Po, minor Cal and Amp	C	Qz+ Bt +Amp + Grt + Pl +Ilm	37.7	30.22	-	1.72	10.18	5.45	14.73	-	0.5	<1	-	-	-	-
801-8C	3.7	Mp	Qz, Ilm, Rt, Ms, Chl	B	Qz+Chl+Pl+Grt+Ms+Ilm+Bt	17.2	-	4.65	32.25		37.35	7.61	-	-	0.84	-	-	-	-
725-3A	3.7	Grt-Amp	Qz, Ilm, Czo	C	Amp + Pl + Qz + Bt + Grt + Ilm	15.99	7.82	-	2.52	46.76	11.1	13.42	2.31	0.06	-	-	-	-	-
725-2c	3.7	Mfv	Qz, Bt, Ilm	B, C	Qz + Bt + Pl + Grt + Ilm + minor Tur	8.58	17.98	-	-		69.87	3.57	-	-	<1	-	-	-	<1
729-11	3.	Mp	Qz, Ap, Ilm, Aln	D, B	Qz + Bt + Ms + Pl + Grt + Tur + Ap + Ilm														
717-3 Cal-Rich	3.8	Grt-Amp	Qz, Cal, Bt, Pl, Tur, Ep/Czo, Amp	B	Qz + Cal + Pl + Amp + Grt + Bt + Opaque + minor Ep/Czo + Tur	20.31	27.7	-	-	10.14	12.03	13.3	<1	16.49	<1	-	-	-	<1
717-3 Qz-rich	3.8	Grt-Amp		C	Qz + Cal + Pl + Amp + Grt + Bt + Opaque + minor Ep/Czo	38.03	28.19	-	-	10.67	7.79	12.17	<1	3.14	<1	-	-	-	<1
JZ717-3 –Qz-rich	3.8	Grt-Amp	Qz, Bt, Cal, Pl	C	Bt + Pl + Grt + Qz + Amp + minor Cal + Ilm and Ms	37.95	19.28	0.13	-	22.87	11.75	7.71	-	0.17	-	-	-	-	-
JZ717-3 –Pl-rich	3.8	Cmf	Pl, Cal, Bt, Qz	C	Bt + Pl + Grt + Qz + Amp + minor Cal + Ilm	16.46	30.94	0.29	-	1.15	41.74	9.01	-	0.27	-	-	-	-	2.46

Rocks 714-5E, 729-11, and 801-8C are classified as metapelites. They have SiO_2 contents

ranging from ≈54 to 62 wt.%. The silica-poor samples correlate with relatively high values of

Al_2O_3 and Na_2O (Fig. APP-B2a,f), stabilizing the abundant plagioclase (Table 3.1). These

rocks contain Type-II porphyroblasts.

The group of meta-felsic volcanics is comprised of samples 802-5, 717-5, 725-2, 726-

6A,729-1A, and 802-5. They are characterized by high contents of SiO_2 (>63 wt.%, Fig.

APP-B2), relative low abundance of FeO and MgO when compared to the other groups (Fig.

APP-B2b,c) and variable concentrations of K_2O and Na_2O (Fig. APP-B2e,f). They are

typically rich in quartz and mica and most of them contain skeletal garnets, apart from one

sample (725-2C) which has higher content of Na_2O, stabilizing high proportions of

plagioclase (Table 3.1).

3.4.3. Chemical and microstructural characteristics of garnets
3.4.3.1 Type I: "skeletal" porphyroblasts

Type I "skeletal" porphyroblasts (φ-value: c. 0.40 to 0.63) are poikiloblastic and are found in

samples across the whole eastern belt, both from north to south and in the 3.7 and 3.8 Ga

sequences (Fig. 3.3b; samples 802-5, 729-1A, 717-5, 726-6A, 729-1B, 726-4,715-9, 730-2A,

715-16A; Fig. 3.3b). The inclusion assemblages are dominated by quartz, which typically

accounts for 30 to 50% of total area in the core (Fig. APP-B3) and make up >50% of the total

inclusion assemblage. Biotite, muscovite, and calcite are also common, with minor

abundance of other minerals like tourmaline, ilmenite, chlorite, and amphibole (Table 3.1). In

some inclusion-rich cores calcite is almost as abundant as quartz (e.g., 715-9; Fig. 3.2a). The

proportion of quartz and calcite in the cores is similar to the proportion of those phases in the

whole rock (Fig. APP-B3). All other minerals, e.g. amphibole, plagioclase and biotite occur

in lower proportions in the porphyroblasts cores compared to the matrix. (Fig. APP-B3).

Foliation patterns (Table 3.1, Fig. 3.3d-e) are dominated by patterns A (Fig. 3.2a, 3.3e.i, 3.4a,

B4a) and C (Fig. 3.2d.iii). Porphyroblasts typically form elongated grains with their long axis

parallel to the internal foliation (Fig. 3.2a). Ellipticity values (E) are generally above 1.7.
There is a general positive correlation between the skeletalness and ellipticity (E vs φ; Fig.
3.5a). Individual sections of the inclusion-rich cores are typically interconnected by thin
irregular garnet branches (Fig 3.2a, 3.4, APP-B4). This microstructure is most pronounced in
porphyroblast with high φ-values. For the most skeletal grains (e.g., Fig. 3.4) not all garnet
branches are interconnected in thin section view. Nevertheless, they do behave as a single
grain deflecting the surrounding external foliation (Fig. 3.4, APP-B4). Some of the thin
elongated branches in these grains are growing on top of sheet silicates showing a similar
geometrical orientation and width (Fig. 3.4b, B4b). The shape of the inclusions is irregular,
but they tend to be more elongated in less skeletal porphyroblasts (e.g., 730-2A, Fig. 3.6f).
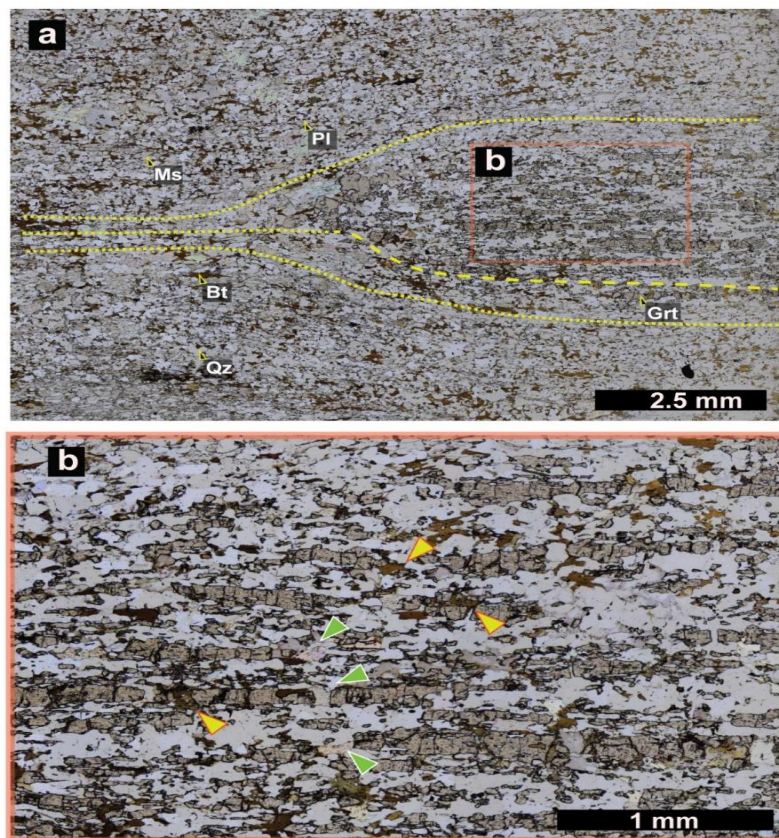
Figure 3.4. Characteristics of Type-I garnet in felsic rocks; sample 802-5. a) Overview of garnet showing internal foliation converging towards the pressure shadow; foliation Pattern A. b) Microstructure showing some garnet branches growing on top of micas. Green arrows point to muscovites and yellow to biotites.
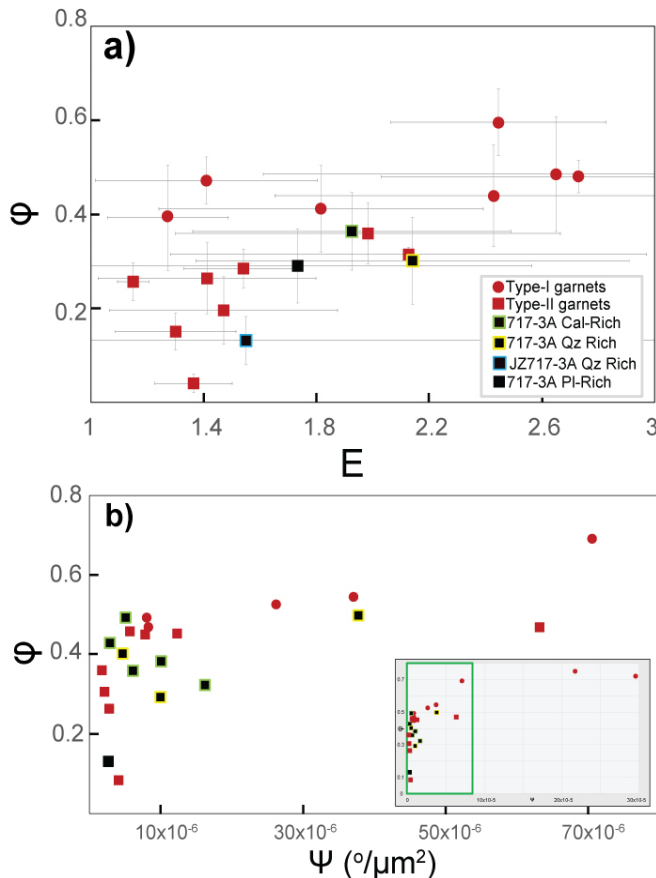
Figure 3.5 Textural parameter correlations. a) E (elongation) against φ (skeletalness) values (all samples) and b) ψ (normalized maximum orientation spread) against φ-values for subregions of garnets in samples 802-5, 717-5, 729-1A, 730-3A, 717-3 and 714-4E. Motifs for garnets in the layer sample 717-3 are highlighted for clarity. Inlet in figure b) shows the whole spread of the data, green rectangle shows area of figure b). In b) the data presented is from subregions in the garnets, therefore some Type II garnets (squares) plot above de dividing φ-values 0.4.some garnet branches growing on top of micas. Green arrows point to muscovites and yellow to biotites.

Post-tectonic garnet appears as faceted overgrows almost devoid of inclusions (Fig. 3.2a.iii; 3.6a,e). Overgrowth occurs at the contact with zones showing a high abundance of Fe-Mg bearing foliated silicates such as biotite (Fig. 3.2a.ii). In contrast, areas where the inclusion-rich core is in contact with matrix that is dominated by quartz and/or calcite, garnet overgrowth is very limited or absent (Fig. 3.2a.iii). In most of the Type I garnets, the volume percentage of post-tectonic growth represents <10% of the total garnet grain volume, and thus slightly smaller than the proportion of overgrowth observed in Type II garnets (Fig. 3.3c). There is no clear systematic dependence linking the proportion of post tectonic garnet

growth to the spatial location of the samples in the belt (Fig. 3.3c).

Chemical zoning patterns in the skeletal garnets share some systematic features. Patchy patterns are common in all of the mapped grains (Fig. 3.6, APP-B5). Although overall concentric zoning appears in some of the grains (e.g., 802-5-Fig. 3.6a, 729-1A-Fig. 3.6b, 730-2A-Fig. 3.6f or 726-4-Fig. APP-B5c; 726-6A-Fig. APP-B4b), irregular compositional

changes appear to be dominant within zones with irregular branching and/or in inclusion-rich zones as illustrated by the erratic local changes in composition in garnet from sample 802-5 (Fig. 3.6a) Short-wave ($<30\mu m$) change in concentration along inclusion-host boundaries (e.g. inlet in Fig. 6d) is observed in most of the skeletal grains (Fig. 3.6, APP-B4). Porphyroblasts in sample 730-2A show a smooth concentric zoning for X_{Sps} with no apparent changes in concentration for this end-member along the boundaries with the inclusions, but an obvious patchy zoning appears for X_{Gro} and X_{Alm} (Fig. 3.6f) related to grain boundaries but also to crystallographic orientations (see section 3.4.2). Note that garnets in this last sample show some of the lowest φ-values ($\varphi \approx 0.4$) of the skeletal type. Remarkably, chemical patterns vary in garnets originating from the same rock (e.g., sample 717-5; Fig. 3.6c, APP-B5a).

The overall chemical composition in Type-I garnets seems to be correlated with bulk rock chemistry. Compositions of the inclusion-rich cores in Ca-rich metapelites and meta-mafic rocks overlap (Fig. 3.7a-b). Notably, such lithologies contain amphiboles, unlike the meta-felsic and metapelitic rocks. Garnets in meta-felsic rocks generally show similar compositions within the group, and they tend to be richer in spessartine and poorer in grossular when compared to the meta-mafic rocks and Ca-rich metapelites (Fig. 3.7a-c). Garnets in meta-felsic sample 726-6A, however, have higher contents of almandine than those in the other meta-felsic rocks (Fig. 3.7c). Notably, this sample also has slightly higher plagioclase content and lower quartz abundance (Table 3.1).

A total of four Type I grains (802-5, 717-5, 729-1B and 730-2A) were analysed using EBSD. They show similar features in the Grain Reference Orientation Deviation (GROD) maps revealing subtle but important changes in orientation (ca. 5-10°) over distances of a few microns (GROD maps in Fig. 3.8a-d). For grains in samples 802-5 (Fig. 3.8a) 717-5 (Fig. 3.8b), and 730-2A (Fig. 3.10d) and from which also chemical maps were obtained, the
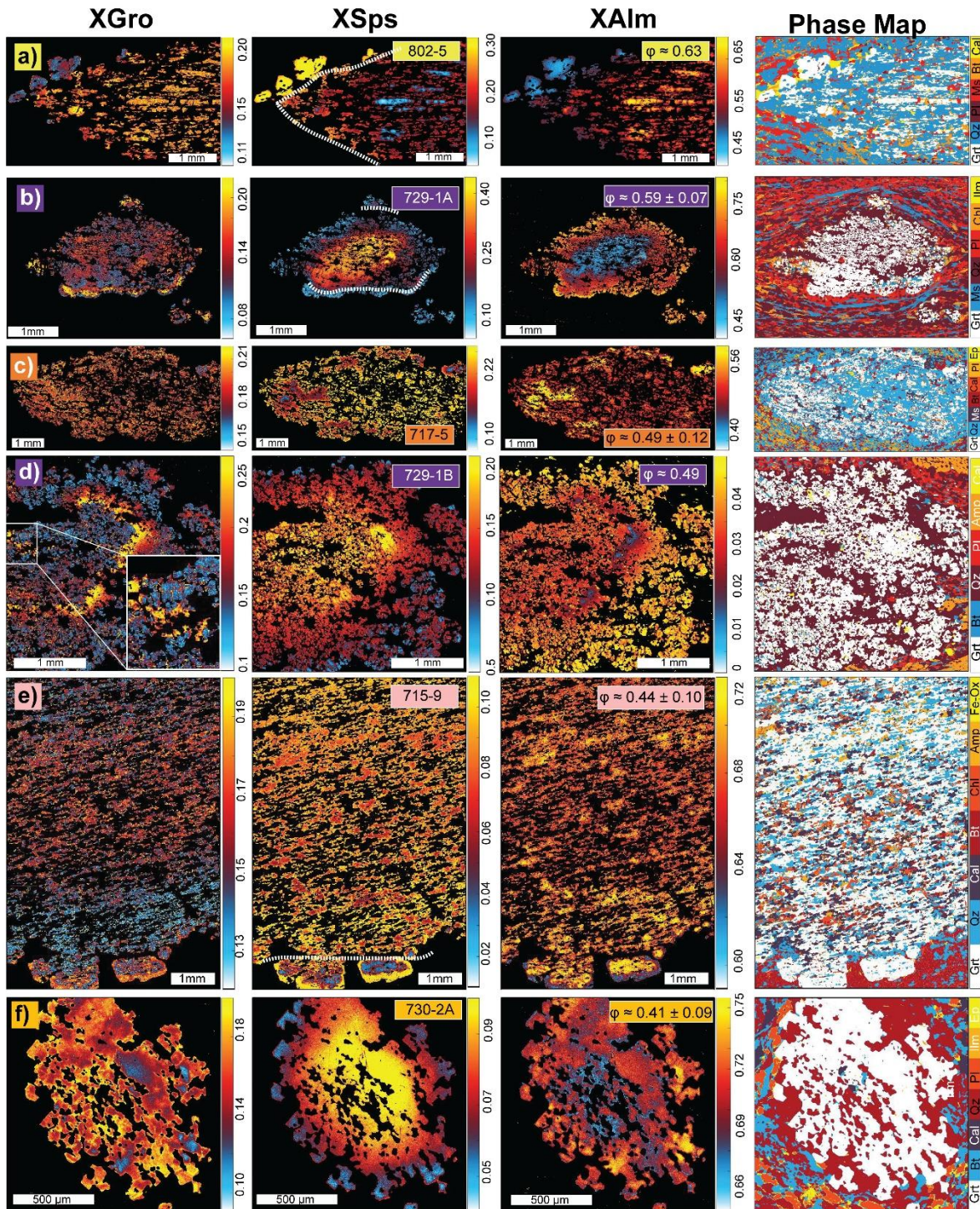
Figure 3.6. Quantitative chemical maps and phase maps of Type-I garnets. Meta-felsic volcanics (a) 802-5; pattern A, (b) 729-1A; pattern C, and (c) 717-5; pattern A; (d) Ca-rich metapelite 729-1B; pattern C; (e) Ca-rich metapelite 715-9; pattern A; and (f) Ca-rich metapelite 730-2A; pattern C. All maps are WDS maps except for 729-1A. φ value represents mean value in the sample. Post-tectonic overgrowths are highlighted with white dotted line.

pattern of orientation changes matches the patchy pattern of chemical variations of the grains.

For the garnet in sample 802-5 the length (c. 80-410 µm) of the patches in orientation

changes (Fig. 3.8a.i-iii) overlaps with the size (50-380 µm) of the micas and plagioclase

included and located in the matrix surrounding the grain. For the garnet in sample 717-5, the

length (95-420 µm) of the patches in orientation changes (Fig. 3.8b.i-ii) is slightly larger than

the grain size of the sounding matrix and inclusions (70-320 µm), but the values generally

overlap. Pole figures of the analysed grains show overall similar orientation spread patterns

with a random arrangement with varying maximum orientation spread angles (Fig. 3.8a.i-iii,

b.i-ii, c.i, d.i). ψ-values vary in the subregions (Fig. 3.8a.i-iii, b.i-ii, c.i, d.i) of the grains from

2.62×10^{-05} to 2.17×10^{-4}, with the largest values calculated in the most skeletal subregions

(Fig. 3.5b and inlet in there).
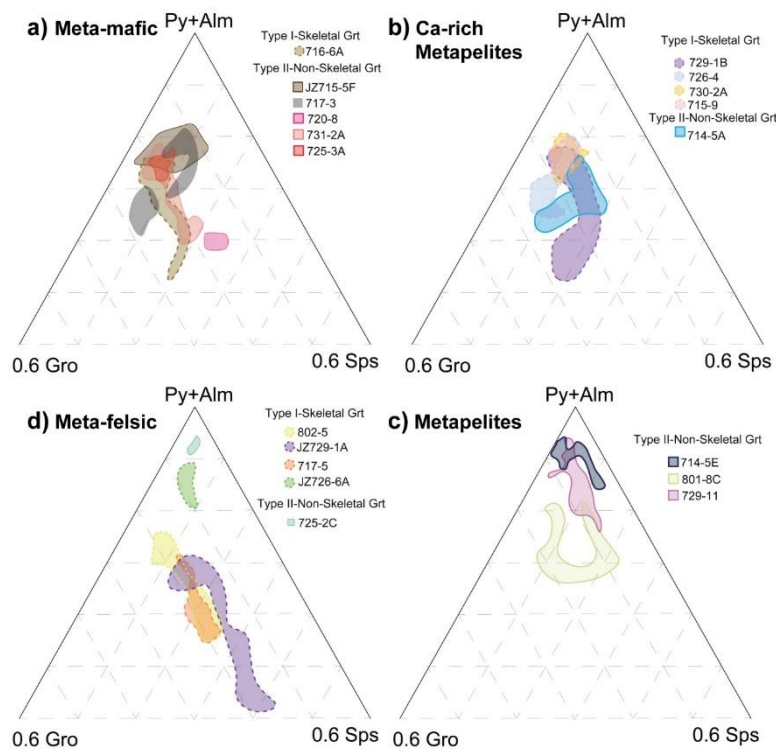
Figure. 3.7 Pyrope+Almandine (Py+Alm)-Spessartine (Sps)-Grosssular (Gro) ternary diagrams
for garnet composition. a) Meta-mafic rocks; b) Cal-rich metapelites; c) Meta-felsic rocks; and d)
metapelites. Fields show the spread of composition of the inclusion-rich garnets.
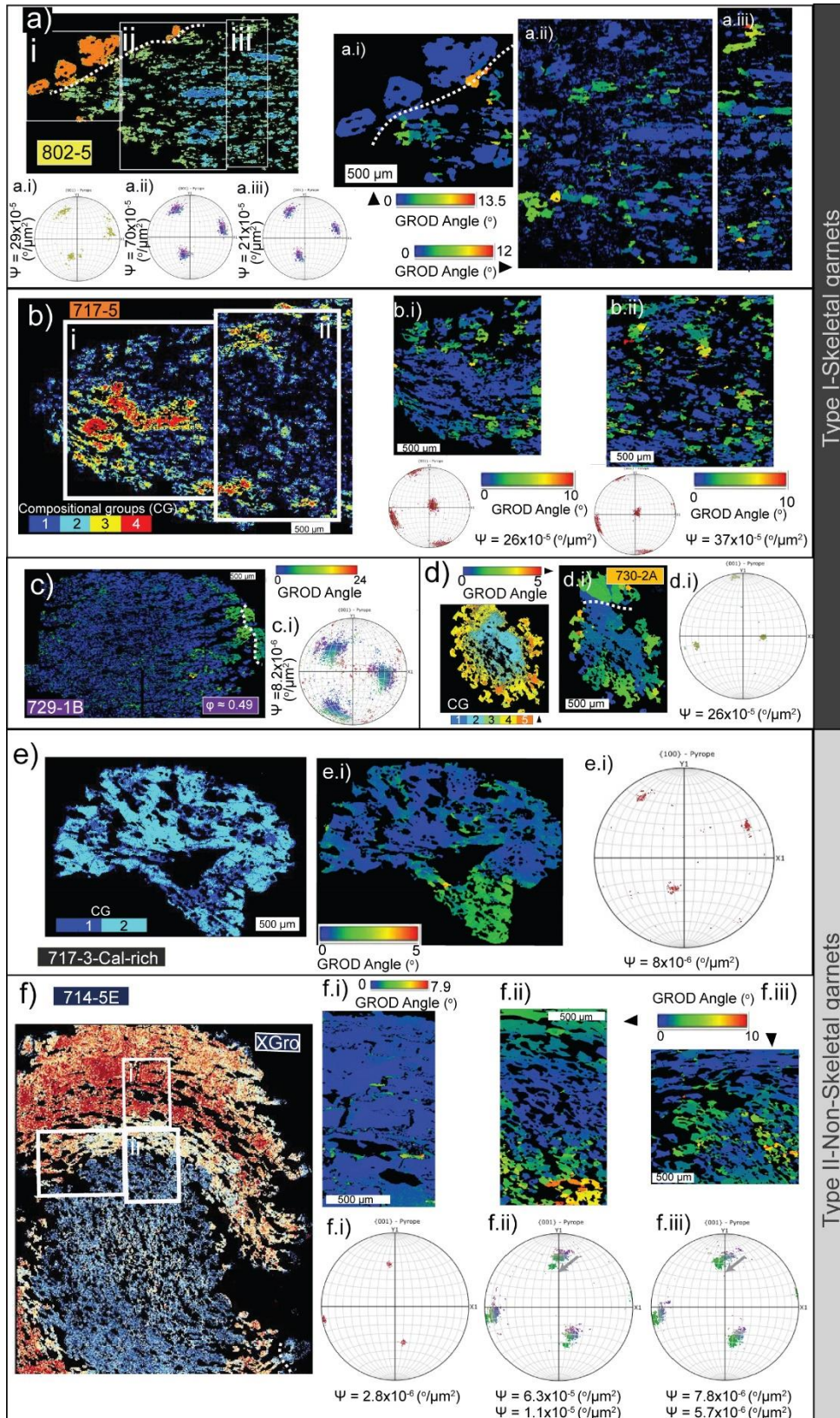
Figure. 3.8 Comparison of Grain Reference Orientation Deviation (GROD) maps (blue and green colours) compared with some chemical maps (warm colors), stereographic projections of the {001} garnet planes for different grains and ψ-values. (a) to (d) Type-I garnets and (e) to (f) Type-II garnets. Compositional maps for a), c) and d) are compositional groups in a Py+Alm-Gro-Sps space created with XMapTools (Lanari et al., 2014). Arrows in f) show the change in crystal orientation from core to rim. Post-tectonic overgrowths are highlighted with white dotted lines.

3.4.3.2 Type II: "non-skeletal" porphyroblasts

Type II garnets (φ-values < 0.4) also tend to be poikilitic and occur throughout the area (samples 715-5F, 720-8, 731-2A, 725-3A, 714-5E, 714-5A, 801-8C, 725-2C, 729-11, Fig. 3.3b). The inclusion assemblage is dominated by quartz, with relative abundance of >75% over other inclusion phases. If calcite is abundant in the whole rock, it is the dominant inclusion phase (Fig. 3.9b). Biotite and muscovite and in minor abundance tourmaline, ilmenite, chlorite, and amphibole appear as inclusions. As for Type-I, quartz and calcite proportions in the cores are similar to those measured in the overall rock, while the rest of the phases are underrepresented in the cores (Fig. APP-B3)

Foliation patterns (Fig. 3.3d, Table 3.1) include group A (e.g., 731-2A, Fig. 3.9c); group B (e.g., 801-8C; Fig. 3.10b), group C (e.g., 714-5A; Fig. 3.2b); and group D (e.g., 720-8; Fig. 3.9b and Fig. DR2C in Webb et al., 2020). Type II garnets are less elliptical than Type I but E also generally increases with φ (Fig. 3.5a). The internal garnet morphology resembles a cohesive grain contrasting the thin garnet branches interconnected through the inclusions of Type I garnets. However, in zones of the porphyroblasts where the density of inclusions is higher, they also tend to be more irregular in shape (Fig. 3.9c), resembling more like those described for the skeletal group.

The post-tectonic overgrowths typically form continuous rims enveloping parts of the core with well-developed euhedral facets (Fig. 3.2b, 3.9b-c, Fig. 3.10). However, some of the slightly more skeletal cores, being part of the same sample but in quarts-rich zones, present the faceted overgrowths (Fig. APP-B7a) resembling the post-tectonic microstructures in the skeletal group. Rims are asymmetrical and their growth is also controlled by the microstructures surrounding the inclusion-rich cores, such that they are larger when facing a matrix with high biotite proportions (Fig. 3.2b.ii, APP-B7b), while the overgrowth is limited or inhibited next to quartz-rich matrix (Fig. 3.2b.iii, APP-B7b). No correlation can be found

linking the area of post-tectonic garnet growth and its spatial location within the belt (Fig.
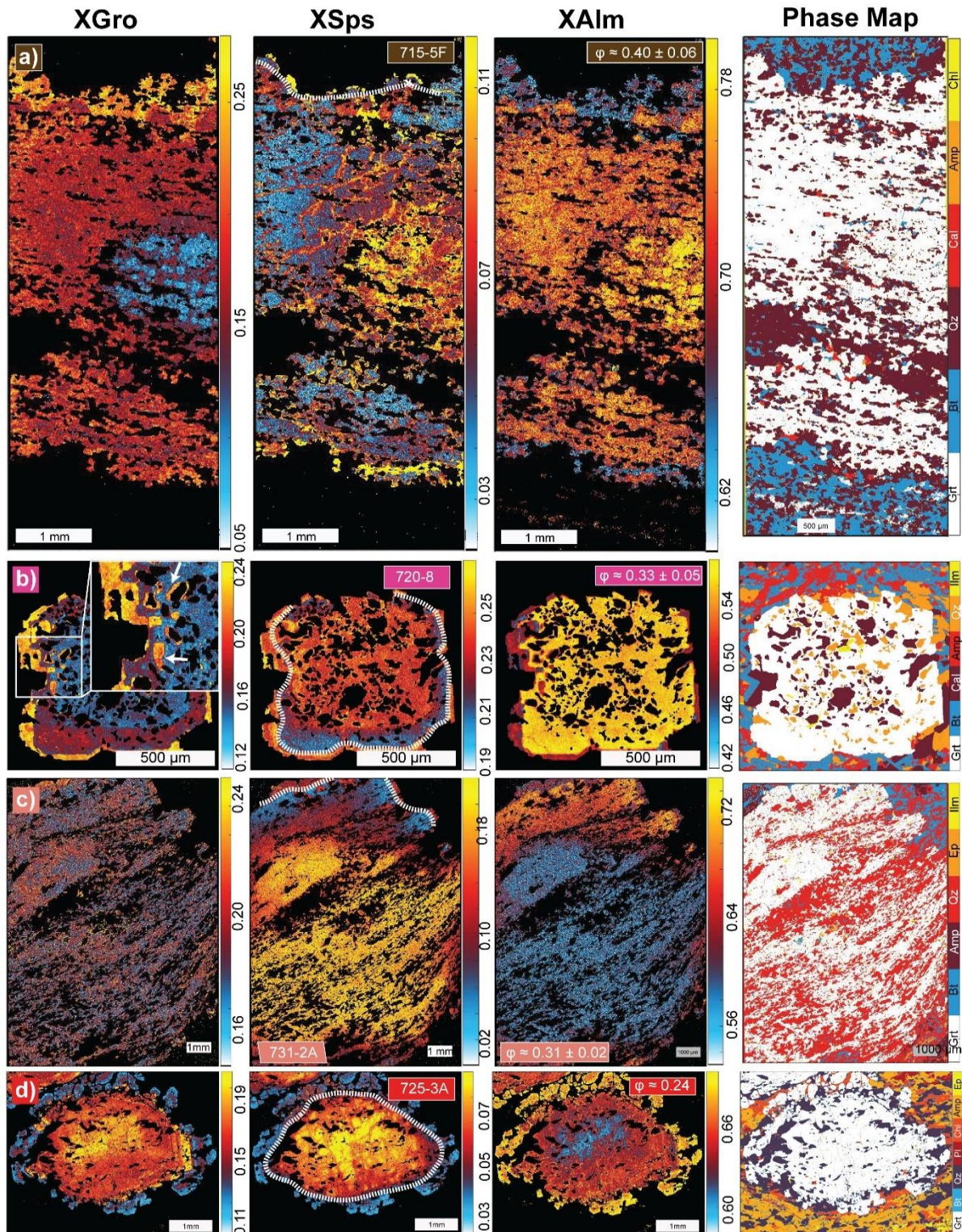
Figure 3.9 Quantitative chemical maps and phase maps for Type-II garnets for meta-mafic rocks (a) 715-5F; pattern A. (b) 720-8, showing halos of composition associated to inclusions; pattern D (c) 731-2A; pattern A. (d) 725-3A; pattern C. (a) and (c) EDS maps and (b) and (d) WDS maps. Post-tectonic overgrowths are highlighted with white dotted lines.

3.3c).

Type II porphyroblasts dominantly display concentric chemical zoning patterns observed for all compositional end-members (Fig. 3.9-10, APP-B8c). Chemical transitions are sharp, resembling well-developed crystals facets (Fig. 3.9b,d; 3.10c-d). Some oscillatory zoning is visible in the outer core of the garnet in sample 725-3a (Fig. 3.9d). Importantly, inclusion trails continue through multiple compositional zones (e.g., Fig. 3.8f; 3.9c; 3.10b, d). Contrasting with Type I garnets, sudden short-wave (<20µm) changes in concentrations along the boundaries with the inclusions are uncommon, although minor occurrences are preserved in sample 714-5A (Fig. 3.9a, APP-B9b). Halos of local higher X_{Gro} and X_{Sps} and lower X_{Alm} and X_{Py} associated with lobate inclusions may occur (e.g., sample 720-8 Fig. 3.9b). Erratic chemical patterns occur and are associated with late fractures (Fig. 3.9a,d; 3.10b,c). Notably, individual garnet porphyroblasts within a single sample show similar chemical patterns on different scales (Fig. 3.8e, APP-B9c). In some cases, some short-wave (≈20-40 µm) oscillatory zoning may be present in the post-tectonic overgrowths (Fig. 3.9d, 3.10a, c).

As for Type I garnets, the overall mineral composition of the non-skeletal garnets has a correlation with the bulk composition of their bearing rocks. Garnets in meta-mafic rocks and Ca-rich metapelites have compositions that overlap, and they are also similar to the chemistry of the Type-I garnets in the same lithologies (Fig. 3.7a-b). All metapelites bear Type II garnets and the inclusion-rich cores have composition that are enriched in almandine relative to the garnets in the rest of the lithologies (Fig. 3.7d). The only meta-felsic sample with non-skeletal garnets (725-2c) has a similar composition to the metapelites (Fig. 3.7c-d). This sample is rich in plagioclase and poor in quartz when compared to all the other meta-felsic rocks (Table 3.1)
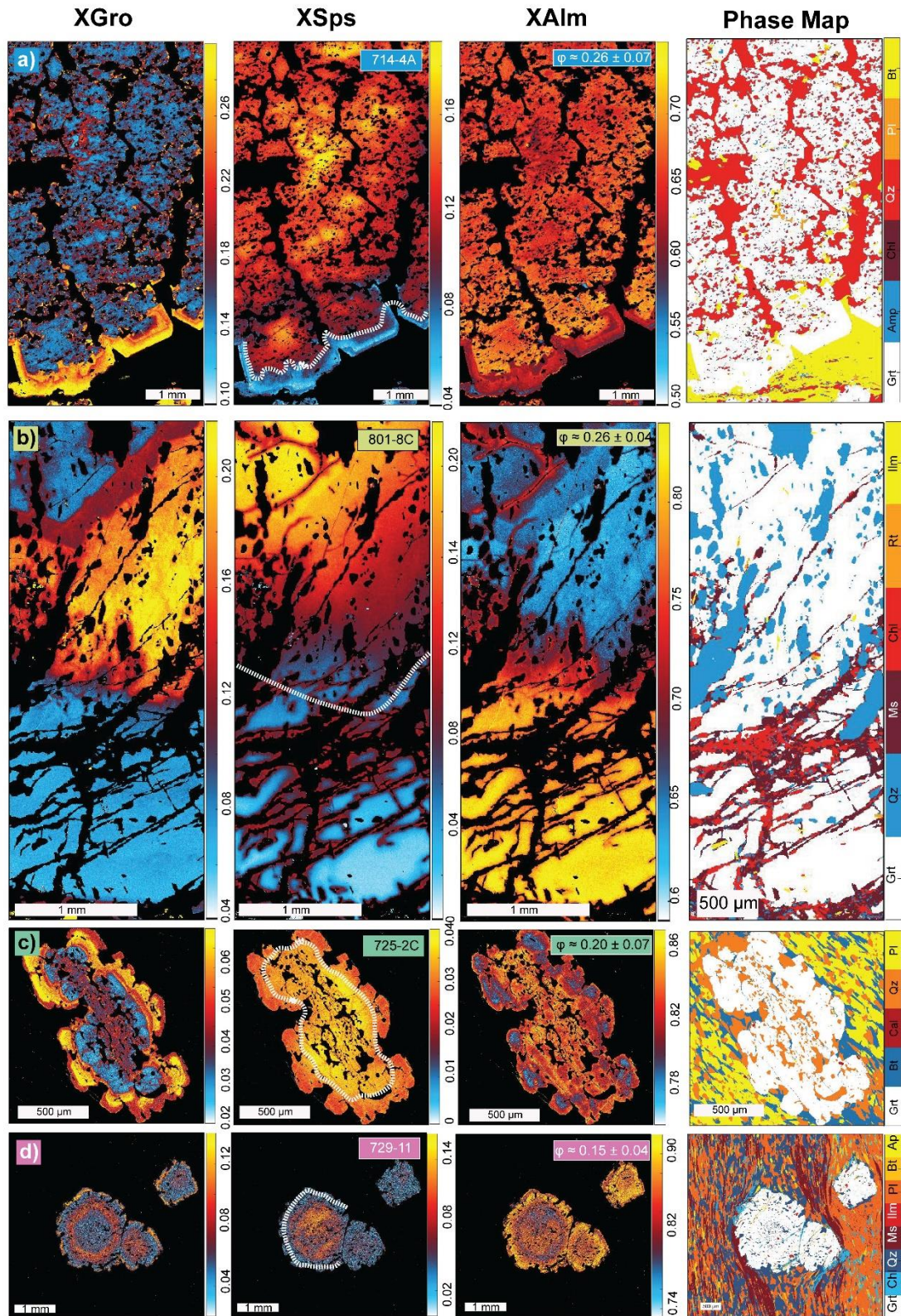
Figure 3.10 Quantitative chemical maps and phase maps for Type-II garnets for (a) Ca-rich metapelite 714-5A; pattern C. (b) metapelite 801-8C; pattern B. (c) Felsic metavolcanic 725-2C; pattern B and C. (d) Metapelite 729-11; patterns B and D in the inner core. All WDS maps except (d). Post-tectonic overgrowths are highlighted with white dotted lines.

A total of six Type II garnets were analyzed using EBSD. Two of them are spiral-like garnets from metapelite 714-5E (the rest are described in the next section). GROD maps of the metapelitic garnets also display subtle crystallographic orientation changes from core to rim that are associated to variations in inclusions orientation (Fig. 3.8f.i-iii). These shifts in the inclusion trails are also coupled with elongated patterns in the pole projection figures (i.e. pole projections plot along a great circle, Fig. 3.8f.i-iii). Notably, the other spiral-like garnet mapped in the same sample (Fig. APP-B6i-v) does not show this elongated pattern, but the changes in inclusion trails from core to rim are not as abrupt as in the one in Fig. 3.8f (see also Fig. APP-B8). They both show an identical concentric compositional pattern (Fig. 3.10e, APP-B7c).

3.4.3.3 In sample variability: Chemical and microstructural variability in a meta-mafic layered sample

In general, the observed garnet microstructures and chemical composition of garnet porphyroblasts do not vary significant within the same rock. A remarkable exception is the layered meta-mafic sample 717-3 located within the 3.8 Ga sequence (Fig. 3.1b). Here, garnet grains show substantial variations in shape, inclusion proportion and internal morphologies, overgrowth characteristics, and composition within the centimetre scale while being consistent within one individual compositional layer. Two thin sections were made of the sample covering three layers with distinctive mineral assemblages: a calcite-rich (Cal-rich) layer, a quartz-rich layer (Qz-rich; present in both thin sections) and a plagioclase-rich (Pl-rich) layer. The general mineral assemblage is similar in the three domains, but the modal abundance changes considerably (Table 3.1, Fig. 3.11d.i, f.i, g.i).

All garnets in this samples are classified as Type II. Porphyroblasts in the Cal-rich layer are the most skeletal, displaying φ-values close to the division between the two groups ($\varphi \approx 0.36$; Fig. 3.11d.ii). They are poikiloblastic with quartz and calcite as the main inclusions. Inclusion-rich cores of the Qz-rich layers have mean $\varphi \approx 0.3$ (Fig. 3.11e.ii), and quartz is the

dominant constituent of the inclusion assemblage. In contrast, porphyroblasts located in the Pl-rich layer are relatively poor in inclusions, with mean $\varphi \approx 0.13$ (Fig. 3.11f.ii) and they are the only grains reported in this work that have plagioclase being the dominant inclusion phase. Overgrowth is limited in the Cal- and Qz-rich zones, even to the extent that it is not found in most of the grains. Overgrowth in the Pl-rich region, in turn, reveal large rims that are typically asymmetric, growing mainly next to zones rich in biotite and plagioclase (Fig. APP-B7b). Rotated garnets appear in the three layers. There is a general positive trend between E and φ values in the layers (Fig. 3.5a), again showing that more skeletal grains tend to be more elliptical.

Compositional mapping of a garnet grain in the Cal-rich layer revealed a weak patchy zoning pattern (Fig. 3.8e, APP-B9a) and increments in X_{Sps} along the boundaries with the inclusions (Fig. APP-B9a). Generally, garnets are richer in grossular and poorer in almandine in the Cal-rich layer ($Alm_{55-61}Py_{5-9}Gro_{22-28}Sp_{6-10}$) compared to the Pl-rich zones layer ($Alm_{63-73}Py_{6-8}Gro_{12-19}Sp_{6-13}$) (Fig. 3.11c). In addition, although not quantitative, μXRF mapping also shows that content of grossular in Qz-rich layer garnets is lower than in the Cal-rich region and the composition probably falls between the two fields shown in Fig. 3.11c.

A small Type II garnet grain (<3 mm) in sample the Cal-rich layer of 717-3 also show changes in composition that match changes in crystallographic orientation (Fig. 3.8e) as Type I grains do, but show relatively low ψ-values (5.1×10^{-6}) similar to other Type II garnets (Fig. 3.5b). Rotated garnets in the Cal-rich and Qz-rich layers present almost identical elongated pole figure patterns with orientation changes that are systematically related to the morphology of the grains (Fig. 3.9d.iv, e.iv). The change in orientation in the pole generally changes across one side of the grain to the other (Fig. 3.9d.iii-iv and 3.9e.iii-iv). Contrary to general trend described in the rest of the garnets and subregions of them, ψ-values in

subregions of the Cal-rich medium grain garnet have a negative correlation with skeletalness

(Fig. 3.5b).
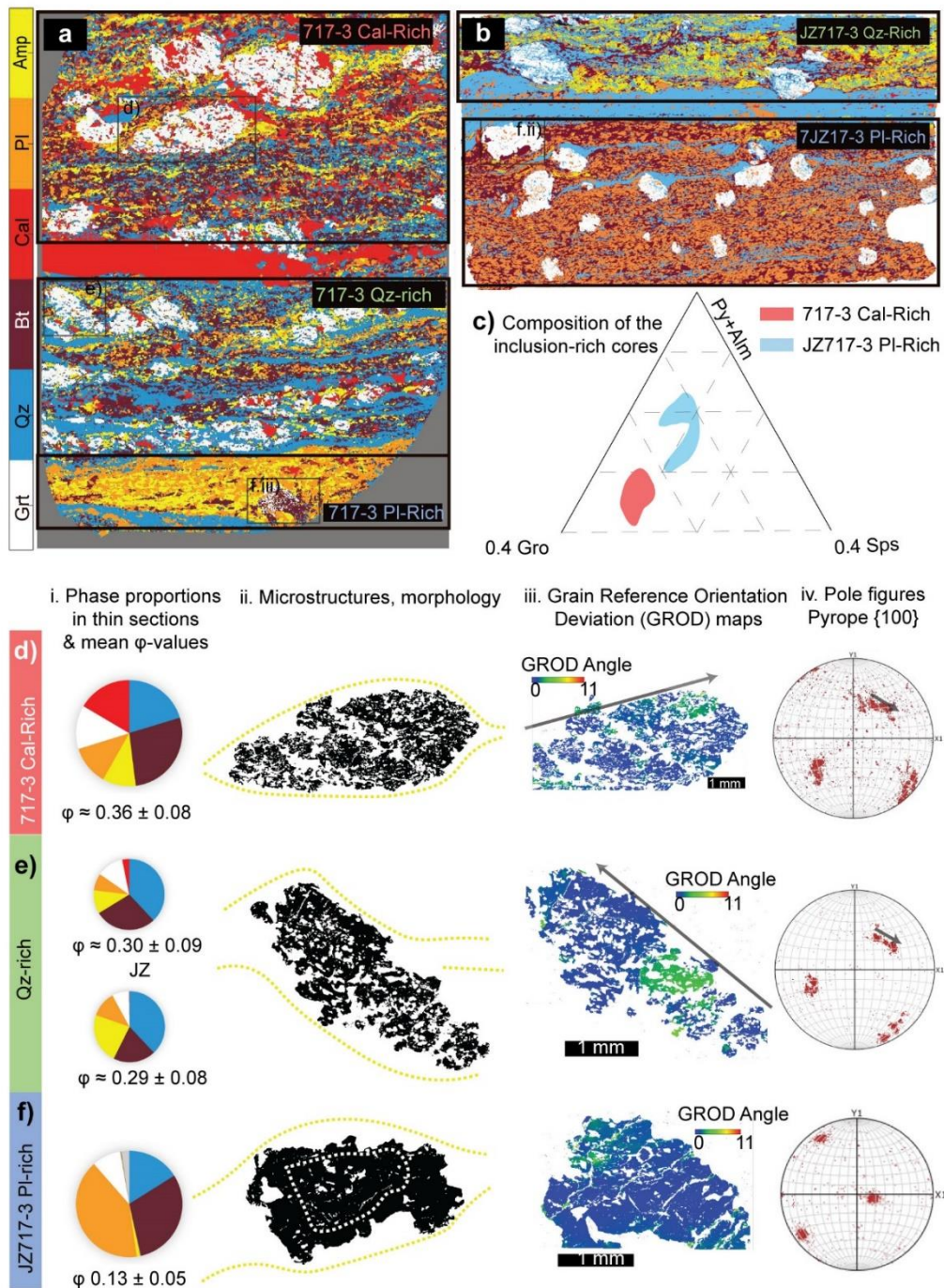
Figure. 3.11 Description of changes in the layered sample 717-3. a) and b) Phase maps of the thin sections showing the division of the different layers. c) Ternary diagram showing the composition of the inclusion-rich garnets in Cal-rich and Pl-rich layers. d.i) φ-values in garnets in Cal-rich layer and pie chart with main phases abundances in thin section; d.ii.) Schematic morphology of a representative garnet in Cal-rich layer (black portion garnet, white inclusions) and dotted lines representing the foliation; d.iii) GROD map for a garnet; d.iv) pole figure. e.i-iv.) and f.i-iv) same as di-.iv) but for Qz-rich and Pl-rich layers. Arrows in d.iii-iv) and e.iii-iv) show changes in crystal orientation from one side of the grain to the other in the pole figures.

3.5. Discussion

3.5.1. Microchemical and microstructural variability in garnet porphyroblasts: A signature of large scale tectonometamorphic evolution?

The detailed characterization of the garnet porphyroblasts in the ISB shows that inclusion-rich garnets are common across the belt. Changes in microstructures and chemical patterns have previously been interpreted as products of different geodynamic histories in different parts of the belt (Gauthiez-Putallaz et al., 2020; Rollinson, 2002; 2003). This contrasts with conclusions of Chapter 2 and Zuo et al. (2021b) who interpreted that ISB rocks experienced nearly homogenous syn-tectonic metamorphism at amphibolite facies conditions of 550-600 °C, 0.5-0.7 GPa and quasiuniform strain intensities. Most of the samples investigated in this study are part of the set of samples presented in Chapter 2 and Zuo et al. (2021b). Therefore, we conclude that strain intensity and metamorphic grade are not likely factors controlling the diversity of garnet microstructures.

Different to the smaller datasets presented by previous workers (Rollinson, 2002; 2003; Gauthiez-Putallaz et al., 2020), our data demonstrates that Type I and Type II garnets are not spatially confined to specific areas. There is no systematic spatial pattern; neither along the strike of the belt, nor across it. Both types occur in the 3.8 and 3.7 Ga sequences (Fig. 3.1). There are no clear systematic changes in the proportion of the inclusions related to geographic distribution of the different porphyroblasts (Fig. 3.3b). Moreover, layered sample 717-3 (Fig. 3.11) shows that different populations of porphyroblasts with distinct aspect, such as φ-values, composition, and morphologies, can appear within the same hand specimen. These observations strongly suggest that the geographic distribution of the rocks is not a controlling factor in the diversity of the Isua garnets. In other words, differences in the observed garnet microstructures do not discriminate the 3.7 vs. 3.8 Ga domains of the belt or appear to define multiple 10 km-scale tectonostratigraphic domains (cf. Rollinson, 2002, 2003).

With this in mind, we explore an alternative model for the observed microchemical and – structural variability, namely the effect of local element availability on garnet growth patterns.

3.5.2. Factors controlling microchemical and microstructural variability in garnets

3.5.2.1. Garnet forming reactions

The garnet forming reactions will not only affect the chemistry of the growing garnet but changes along the P-T path inevitably result in chemical zoning of the garnets (e.g., Spear et al., 1991; Konrad-Schmolke et al., 2008). Our data confirms this intuitive sensitivity of garnet chemistry to the reactant mineral phases of the rock. For example, the metapelites characterized by a high modal abundance in plagioclase produce garnets with a higher grossular component (Fig. 3.7d). In the following, we use both, our petrographic observations as well as the phase equilibria modelling reported in Chapter 2 to identify the possible general mineral reactions, and therefore determine the reactants involved in the growth of the Isua garnets.

In Chapter 2, using a qualitative approach, it is suggested that the ISB experienced an evolution along a near isothermal path; an interpretation based on isopleth thermobarometry and almost constant garnet-biotite temperatures obtained along garnet transects across the belt. To the best of the authors knowledge, no other P-T path has been proposed for the belt. Hence, changes in mineral modal abundances along a near isothermal path (550-580°C and 0.3-0.7 GPa) have been calculated using the Werami software, which is part of the Perple_X software package (Connolly, 2005). We interpret the possible garnet forming reactions from P vs percentage diagrams (Fig. 3.12) for the samples from which phase diagrams are reported and assume similar reactions might have occurred in samples with akin bulk composition, since garnet chemistry is similar and mineral relationships too.

Although meta-mafic and Ca-rich metapelites are rich in amphibole and/or plagioclase, inclusions of these minerals in the garnet are nearly absent (Fig. APP-B3). Even in layers

with large modal abundance of amphibole/plagioclase, the garnets normally only present

inclusions of quartz (Fig. 3.12a.i, APP-B3) or other minerals in lower abundance like biotite

(Fig. APP-B3). The systematic absence of these minerals suggest they might have

participated as reactants in the garnet growth. Other microstructures that indicate

participation in the garnet forming reactions are some symplectitic-like features typically

associated to the interface of epidote inclusions with garnet in sample 731-2A (Fig. 3.12b.i).
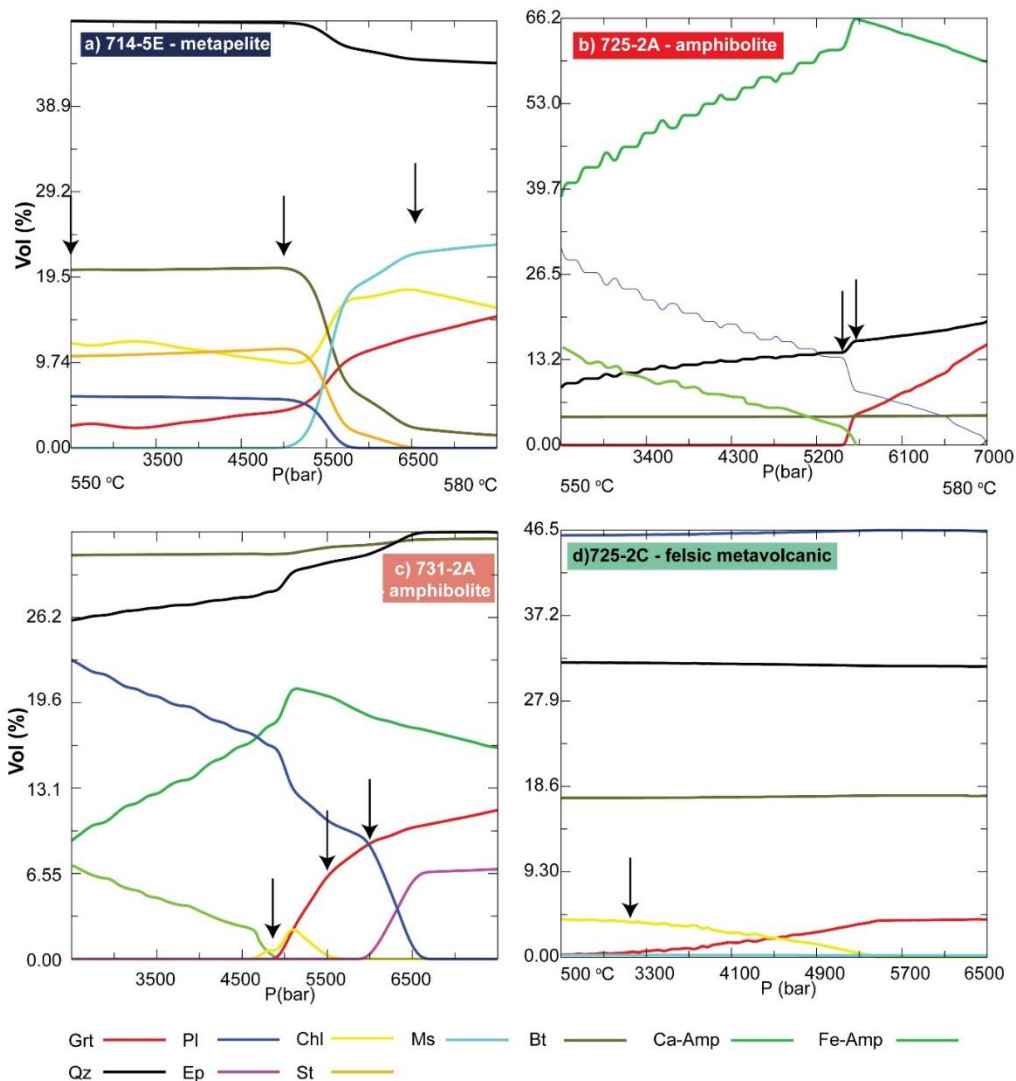
Figure. 3.12 Pressure vs volume diagrams obtained from Chapter 2 phase equilibria modelling. Plots show changes in modal abundance along a nearly isothermal P-T path. a) 725-3A garnet amphibolite and a.i) image showing the lack of amphibole and plagioclase inclusions in an amphibole-rich zone. b) 731-2A garnet-epidote amphibolite and b.i) image showing symplectitic-like structures associated to epidote inclusions in garnet. c) 714-5E metapelite and c.i) image showing garnet inclusions of chloritoid-muscovite intergrowths interpreted as staurolite pseudomorphs (e.g. Gauthiez-Putallaz et al., 2020). Black arrows point where the trends of minerals being consumed and garnet production change.

These assumptions interpreted from the petrographic observations agree with the modelling. Amphibole, plagioclase, and early chlorite, decrease in abundance while garnet proportion increases (Fig 3.12a-b). Late garnet modal increments are also associated to higher abundance of epidote in sample 731-2A (Fig. 3.12b). Although exact compositions of the reactants and products vary from rock to rock, reactions of the following general form can be deduced:

$$Chl + Pl + Qz = Grt + H_2O \quad (1)$$

$$Pl + Amp = Grt + Ep/Amp + Qz \quad (2)$$
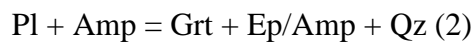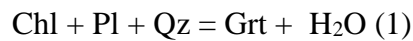
These reactions are interpreted for both meta-mafic rocks and Ca-rich metapelites, since the modelled changes in minerals proportions are similar in both groups. Moreover, this is also consistent with the overlapping in garnet compositions that both groups show (Fig. 3.7a-b). Reactions involving epidote have also been reported by other studies using thermodynamic modelling (Inui and Toriumi, 2004; Konrad-Schmolke et al., 2008).

For the metapelites, phase equilibria diagrams are only reported for 714-5E (Chapter 2). For metapelites with almost identical mineralogy and composition, Gauthiez-Putallaz et al. (2020) suggested the consumption of plagioclase to form garnet due to the presence of Eu positive anomalies in the garnet annulus. Rare relics of plagioclase are found in the garnets of our sample, but no plagioclase is described in the matrix. Such features might point to a complete consumption of plagioclase accompanying garnet growth. Inside the garnets of sample 714-5E a few inclusions of chloritoid-muscovite pairs growing with irregular boundaries are found (Fig. 3.12c.i). Gauthiez-Putallaz et al. (2020) also documented muscovite-chloritoid intergrowths and identified them as pseudomorphs after staurolite. These intergrowths are not present in the matrix of our rock.

The modelling also predicts the participation of plagioclase and staurolite in the garnet growth. Plagioclase, staurolite, chlorite, biotite, and quartz, decrease along the selected P-T

path while garnet modal abundance increases (Fig. 3.12c). From this, we interpret the following general reactions:

$$Chl + Qz = Grt + H_2O \quad (3)$$

$$Bt + St + Pl + Qz = Grt + Chl + Ms \quad (4)$$
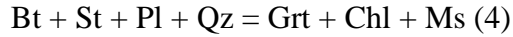
Garnet forming reactions are more difficult to interpret from the phase equilibria diagrams for the meta-felsic volcanics. Garnet, especially in quartz-rich samples like 717-5, is predicted in small proportions (<1%), which is expected for meta-felsic rocks (Waters, 2021) and it is consistent with the observed assemblages (Table 3.1). Thus, changes in modal abundances are not that obvious. However, from the modelling of sample 725-2c we interpret reactions similar to (3) (Chl+Qz) and quartz + muscovite +chlorite = garnet + biotite. Although no clear reactions involving plagioclase and garnet were identified, the constant lack of plagioclase as inclusions and the contents of grossular in the garnets (up to X_{Gro}=0.2) in samples were plagioclase in the main source of Ca suggest this mineral also participated in the formation of garnet.

3.5.2 Compositional and mineralogical control

The fact that within the same sample (717-3), the characteristics of garnets is closely correlated with the compositional banding (Cal-rich, Qz-rich and Pl-rich; Fig. 3.11c, d-f.ii) suggests that there is a compositional control on garnet textures which is also directly linked to the abundance and microstructure of pre-existing minerals. While the main mineral phases in the matrix of the three different layers are similar (garnet, plagioclase, amphibole, quartz, and calcite), their relative proportions vary significantly (Fig. 3.11d.i-f.i). Main variability is seen for the phases that are related to the formation of garnet (reactions 1 and 2. Fig. 3.12a). Garnets in layers with high abundance of Fe-Mg bearing phases that participate in the garnet forming reactions such as amphibole, plagioclase, and biotite, are associated with lower φ-values, i.e., these garnets are less skeletal (Fig. 3.13a). Consequently, a higher abundance of

reactant minerals will facilitate the development of garnets with less inclusions as required

distances for element transport are shorter.
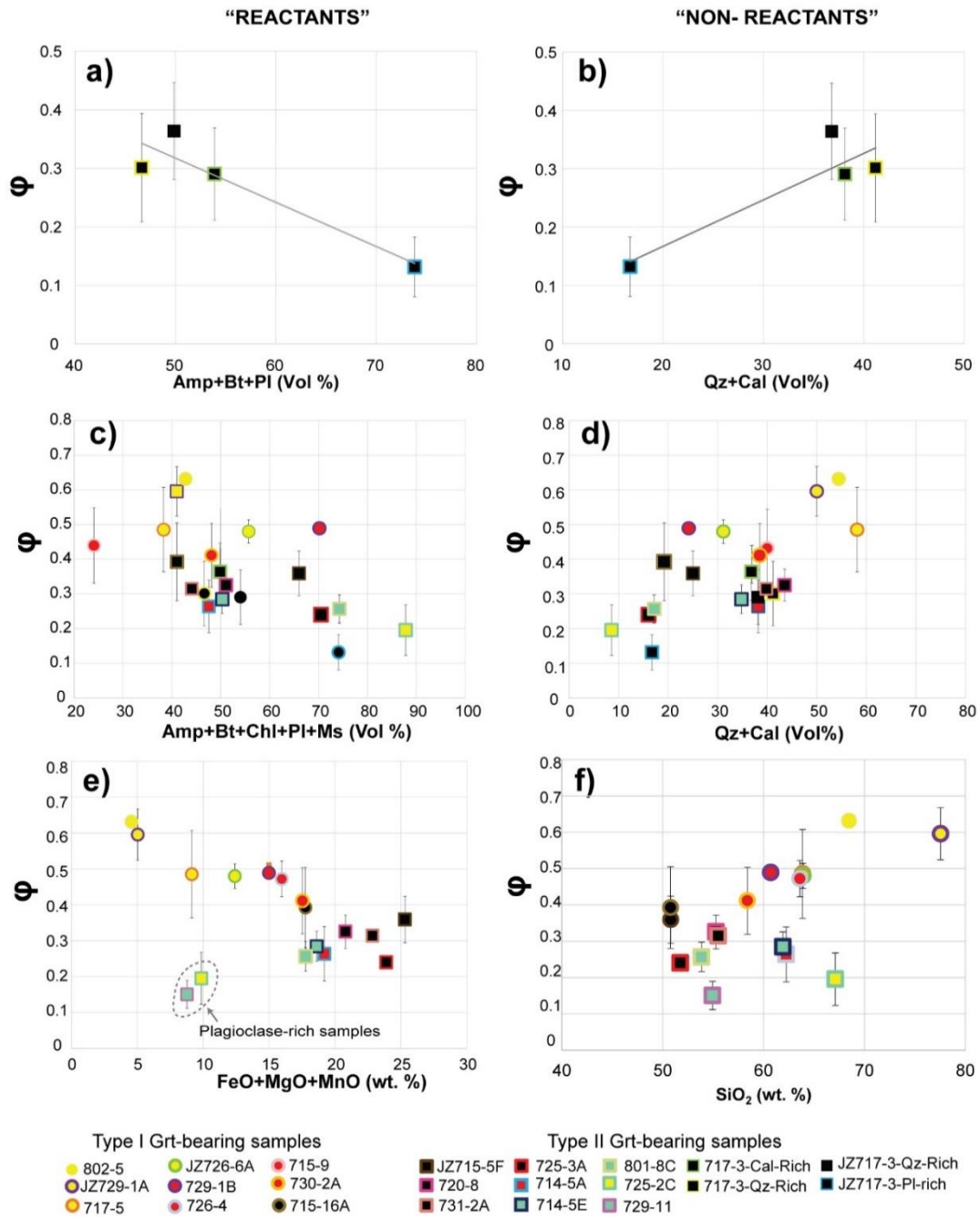
Figure. 3.13 Diagrams showing changes in φ with respect to mineralogy and bulk rock chemistry. (a) and (b) diagrams are for the layered sample 717-3, while c-f) are show all the rocks. (c) Reactant phases in the rock vs φ (skeletalness), (d) quartz + calcite in the rock vs φ; (e) sum of FeO, MgO, and MnO bulk rock chemistry and (f) SiO2 vs φ.

Quartz participates in the garnet forming reactions both as reactant and product (reactions 1 and 2). However, it is most likely that quartz is the phase in excess as it forms the main inclusion phase in most of the garnets (see phase maps in Fig. 3.6, 3.9, 3.10). Apart from quartz, calcite, when present, also appears as one of the main inclusions in the garnets as can be seen in porphyroblasts in Cal-rich layers (Fig.B9a). Both observations suggest that developing microstructures are not only controlled by element availability to the growing garnet interface, but also by the effectiveness of removing quartz, or other non-reactant phases like calcite, from the region where garnet is nucleating and growing. This interpretation is in agreement with data from sample 717-3 illustrating that the sum of calcite + quartz abundance in the different chemical domains of the sample shows a positive correlation with the φ-values (Fig. 3.13b). Thus, porphyroblasts growing in a matrix rich in calcite and quartz will tend to develop a more skeletal morphology.

The observations from the layered sample 717-3 suggest that similar patterns for rocks with different chemistry should be present. Generally, a trend towards less skeletal garnets with increasing abundance of reactant minerals can be observed (Fig.3.13c). However, this trend is more pronounced in the meta-mafic or meta-felsic rocks. For the abundance of quartz and calcite, i.e., the excess or non-reactant phases, the general trend is analogous the correlation found in the layered sample for all lithological groups, with higher φ-values for garnets growing in calcite-quartz rich matrix (Fig. 3.13d).

To test for the effect of bulk chemistry we explore the relation of bulk oxides to φ-values. The bulk content of the major garnet forming elements (Ca, Fe, Mn, Mg, Al, and Si) is plotted against extracted φ-values (Fig. 3.13e-f; APP-B10). Here, a negative correlation with FeO+MnO+MgO is generally present for all samples, and it is more pronounced for the Type I garnets, excluding one metapelite and one meta-felsic volcanic that are rich in plagioclase and micas (Fig. 3.13e). With respect to SiO_2, the samples with skeletal garnets, especially

meta-felsic rocks and Ca-rich metapelites, show higher φ-values at higher contents of silica. However, the non-skeletal samples do not show a clear general pattern for all the samples (Fig. 3.13f). Again, the higher abundance of the garnet-forming elements results in effectively shorter transport distances along the grain boundaries and increases element availability controlling the developing microstructure of growing garnet.

3.5.4. Reactant availability and distribution pattern govern microchemical and microstructural patterns in inclusion-rich garnet porphyroblasts at low to medium temperature conditions

Once a porphyroblast has nucleated, its growth is a serial process including the two main steps: transport of material in and out of the site of growth and addition to and/or dissolution of material at the interface of the growing product phase and diminishing reactant phase, respectively (e.g., Müller et al. 2010 and references therein). Owing to the serial nature of this process, the slowest processes will determine the overall growth rate. If elemental transport by diffusion is rate limiting growth is referred to as "diffusion-controlled", while "interface-controlled growth" occurs if the material addition is rate limiting (Loomis, 1983; Carlson, 1989, 2011; Müller et al., 2010). Rate limiting mechanism can affect the distribution of the porphyroblasts (Kretz, 1966l; Carlson, 1989), influence their growth rate (Kretz, 1974), morphology (Kretz, 1993; Spear and Daniel, 2001; Zeh and Holness, 2003; Miyazaki, 2015; George and Gaidies, 2020) and chemical zoning (Loomis, 1983; Daniel and Spear, 1999; ; Yang and Rivers, 2001; Hirsch et al., 2003; Carlson et al., 2015; Dempster et al., 2017). Therefore, the final configuration and characteristics of the garnets from Isua could shed light on the surface and elemental transport processes operating during the growth of the inclusion-rich garnets within the belt.

Garnets with contrasting characteristics similar to those of Type I and Type II garnets have been reported for other metamorphic sequences (Hirsch et al., 2003; Carlson et al., 2015). The growth of irregular inclusion-rich garnets has previously been attributed to change in element transport rates either at low temperature (Hirsch et al., 2003) or in the presence of

fluids with low solubility of garnet forming elements (Carlson et al., 2015). Therefore, grains with lower contents of inclusions, as Type-II garnets, are supposed to grow at elevated temperatures or in the presence of fluids mediating the transport of elements. Differences in temperature are unlikely to play a role in the diversity of the Isua garnets as previously discussed, and there is no concise evidence to argue for important changes in the fluid composition from one group to the other. However, our data clearly demonstrates that the garnet chemistry and microstructures (e.g., φ-values) are tightly related to the bulk rock composition (Fig. 3.7, 3.13f-g), the local distribution of reactants (Fig. 3.13a, c) and the abundance of non-reactant phases (Fig. 3.13 b, d). Thus, element availability and transport distances are likely the factors controlling the garnet growth.

Internal microstructures of Type I garnets are characterized by high proportions of inclusions (φ-values >0.4) and branching irregular thin strips of garnets growing between the enclosed minerals (e.g. Fig. 3.2, 3.4, APP-B4). The interpretation of this morphology holds even for the most skeletal grains that in thin section do not show a clear continuous interconnection (Fig. 3.4), but that share a common crystallographic orientation suggesting a single interconnected garnet grain in 3D space (Fig. 3.9a-d). Moreover, highly skeletal grains always deflect the foliation acting as a single porphyroblast (Fig. 3.4a, APP-B4a). The development of such microstructures is inevitably affected by the mobility of the garnet-forming elements and reactants. In samples where garnets nutrients are limited, and thus more scarcely distributed, garnet will either need to go around an immobile non-reactant phase (as quartz or calcite) or grow towards an element supplying reactant phase.

As the branching garnet grows, the ability to remove or overgrow phases in excess or non-reactant phases likely controls the number of inclusions in the porphyroblasts as suggested by the positive correlation between quartz+calcite and φ-values (Fig. 3.13b, d). If garnet is growing around quartz and calcite, then in a hypothetically homogenous rock each growing

porphyroblast will enclose a representative modal abundance of these phases. A 1:1 relation could be expected then for the total area of quartz and calcite in the garnet cores and the percentage of such phases in the overall sample. Data retrieved from our samples and representative porphyroblasts show that quartz and calcite have a positive correlation close to the 1:1 line (Fig. 3.14a-b). In contrasts, all the other main phases are underrepresented in the garnet cores and plot above the 1:1 line, suggesting their consumption, in agreement with the thermodynamic modelling (Fig. 3.12) and the interpreted reactions. Therefore, in medium-grade rocks, in samples with higher abundance of quartz and/or calcite (like felsic rocks) Type I garnet are predicted to be formed.
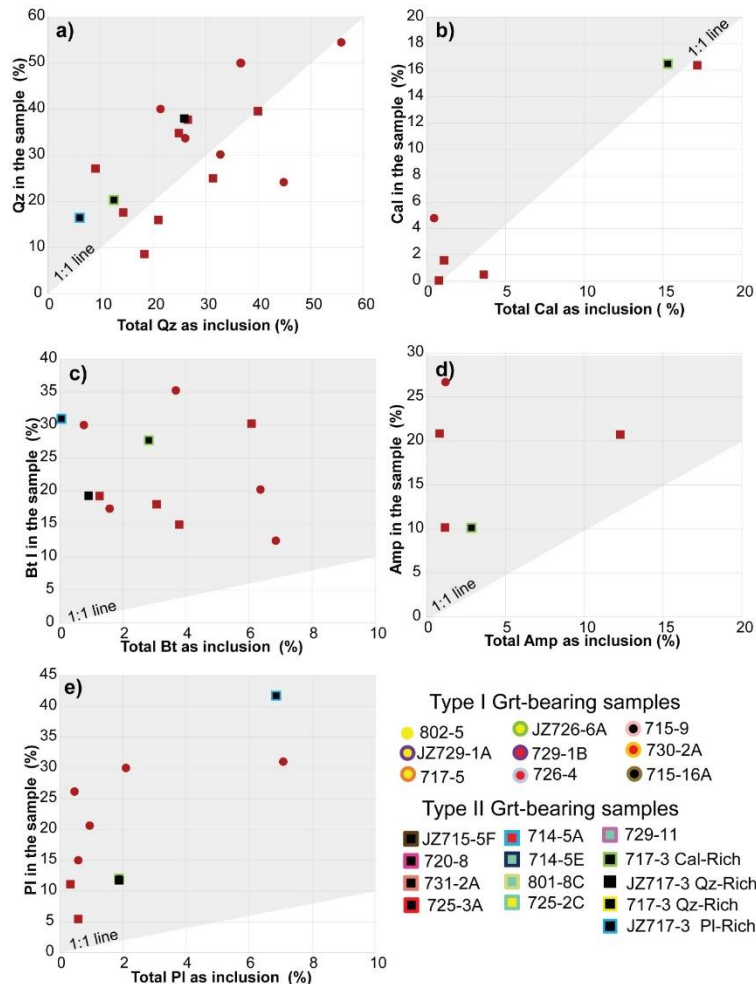
Figure. 3.14 Plots comparing total volume of a phase as inclusion in representative garnets vs total percentage of the same phase in the whole thin section. a) quartz, b) calcite, c) biotite, d) amphibole, e) plagioclase. Grey field represents values above the 1:1 line.

The control of garnet growth by the element supplying reactant phase is also supported by the data presented here. Thin branches of garnets in the most skeletal grains grow on top of sheet silicates showing a similar orientation and width (Fig. 3.4, APP-B4). Growth will be facilitated along the micas because they provide garnet forming elements, high affinity surfaces for nucleation and growth (e.g., Nagurney et al., 2021) and pathways for faster intergranular diffusion (Dempster et al., 2017; George and Gaidies, 2020). This is also reflected in the overall aspect ratios of the Type I garnets that tend to be more elliptical at higher φ-values (Fig. 3.5a). Since micas are typically defining the foliation, a preferential growth along them due to limited availability of nutrients will tend to create elongated garnets with high content of inclusions. The pattern of skeletalness mimics directly the pattern of biotite distribution in the matrix (e.g. Fig. 3.4, APP-B4).

All these garnet microstructural features indicate that localized sources and previous microstructures are controlling the characteristics of Type I garnets. This is also revealed by the chemical and crystallographic orientation maps. Short length scales of equilibrium can produce patchy chemical zoning (Spear and Daniel, 2001; Hirsch et al., 2003) that can potentially mimic previous microstructures overgrowth by the garnet (Spear and Daniel, 2001). For garnets in sample 802-5 (Fig. 3.7a), 717-5 (Fig. 3.7b), and 730-2A (Fig. 3.7d), from which we obtained both EBSD data and chemical element maps, the patchy zoning is coupled to subtle changes in the crystallographic orientation, reflecting the influence of the distribution of the available elements and pre-existing microstructures during garnet growth. In garnets from samples 802-5 and 717-5, these patches have similar lengths to the size of the micas included and surrounding the grains (Fig. 3.4, 3.8a-b, APP-B4), suggesting that garnet orientation is influenced by the orientation of the phases replaced (Bestmann et al., 2005). Growth of garnet and replacement in specific microstructures and phases will create crystal distortions (Spuzience et al. 2016). Defects built into the crystal lattice during growth are

interpreted from the randomly dispersed orientation patterns in Type I grains (Fig. 3.7a-d) (Smith et al., 2015; Spuzience et al. 2016). Since growth of the most skeletal garnets is more controlled by the previous microstructures, they should present a higher density of defects as shown by the generally larger ψ-values compared to Type-II garnets (Fig. 3.5b). Additionally, as the microstructures and garnet-forming elements or phases are not homogenously distributed around the rock, the overall chemical zoning from grain to grain is expected to be different. This is observed in sample 717-5 where two grains in the same rock show rather different chemical patterns (Fig. 3.6c, APP-B4a). Finally, the preservation of small length scale (<30 µm) changes in composition in the interface of garnet-inclusions of the skeletal garnets point to inefficient diffusion homogenization or late post-growth diffusion (Fig. 3.5) (Dempster et al., 2017).

In summary, larger distances to the garnet growth site and inefficient transport are common in rocks with low concentrations and scarce distribution of garnet-forming materials, particular in medium grade metamorphic rocks. This translates in preferential growth in specific sites of local favourable growth sites resulting in the characteristic of Type I garnets. In contrast, Type II, non-skeletal garnets grow in rocks with overall higher concentrations of garnet forming elements (Fig. 3.13a, c, e), thus shortening the transport distances for garnet growth making intergranular diffusion less restrictive. This is reflected in the characteristics of the Type II garnets. Their inclusion-rich cores exhibit smoother and more defined boundaries between garnet and inclusions, and irregular branching morphologies are restricted to zones with a high density of inclusions (e.g., Fig. 3.8c). Grains are more spherical (Fig. 3.5a) and generally present less density of lattice defects, i.e. crystal lattice distortions (Fig. 3.5b) since they depend less on specific loci to grow and elements are readily available enabling equant growth. Chemical zoning is typically concentric and similar between grains of the same sample (e.g., 714-5E, Fig. 3.8f, APP-B9c), which is a feature

expected in porphyroblasts growing in a medium with larger-scale chemical equilibration (e.g., Gaidies et al., 2008). Sharp boundaries between chemical zones are typical for continuous garnet growth resulting in euhedral garnets grains (Figs. 3.8b, d; 3.9b, d); such equant and euhedral grains have been linked to garnet growth that is not limited by element transport (George and Gaidies, 2020; Kretz, 1993; Loomis, 1983; Zeh and Holness, 2003). Finally, orientations spread patterns described for spiral-like grains (Fig. 3.10e) and rotated garnets (Fig. 3.9d, e), are systematic with dispersions along great or small circles within the pole figure that suggesting crystal growth pattern is directly related to growth direction and not local overgrows of particular phases similar to fibrous growth in veins (e.g. Bons et al. 2012)

Our results emphasize that growth of inclusion-rich garnets will be largely influenced by bulk rock composition, mineralogy, and microstructures. Although we separated our analysis in two main garnet groups, all the presented correlations (Fig. 3.5, 3.13, 3.14) show that the skeletalness and changes in garnet characteristics are continuous. This is also evidenced by garnets that have φ-values close to the lower limit Type-I group (≈ 0.4) and upper limit of the Type-II group which show mixed characteristics. For example, grains in sample 730-2A exhibiting a clear concentric zoning for the spessartine (Fig. 3.6f) and pyrope components, but patchy chemical zoning, coupled with changes in crystallographic orientations (Fig. 3.8d), for grossular and almandine (Fig. 3.6f) components.

The control of matrix in the growth and characteristics of inclusion-rich garnets has already been demonstrated in previous works. For example, garnets growing in mica-rich domains in metapelites tend to have less skeletal garnets, which is interpreted to be the result enhanced intergranular diffusion in these zones (Spear & Daniel, 2001; Hirsch et al., 2003; Carlson et al., 2015). On the other hand, inclusion-rich garnets with irregular compositional zoning are common in quartz-rich domains (Yang and Rivers, 2001; Carlson et al., 2015; George and

Gaidies, 2020) and it has been suggested that a slowed intergranular diffusion along quartz-garnet boundaries could account for slowed transport (Dempster et al. 2017). Although our data clearly show that composition and mineralogy play the major role in the growth of the analysed inclusion-rich garnets, the aforementioned factors or others might be contributing to the individual characteristics of the studied grains. For example, the compositional halos surrounding inclusions in garnets from sample 720-8 (inset in Fig. 3.9b) could be consequence of microtopographic features during garnet growth and the nature of the porphyroblast-inclusion boundary as suggested by Dempster et al. (2020).

The microstructures and mineralogy of the rock do not only affect the growth of the inclusion-rich cores. The observations presented here suggest that they also play a role in the growth of post-tectonic garnets. Overgrowths is mainly seen to occur where Fe-Mg minerals like biotite dominate (Fig. 3.2a.ii, b.ii. 3.7), while they are almost absent when an inclusion-rich core is in contact with a quartz-rich domain (Fig. 3.2a.iii,b.iii, APP-B7). Here, overgrowths' appearance is controlled by the character of the inclusion rich cores. Overgrowths on highly skeletal grains are commonly faceted (Fig. 3.2a.ii, APP-B4) while for grains with lower φ-values (Type II) overgrowths forms continuous rims (Fig. 3.2b.ii). However, a detailed discussion of the specific growth mechanism of the overgrowths is beyond the scope of this paper.

3.5.6 Garnet porphyroblast characteristics and tectonometamorphic interpretations

Our results show that within an area where garnets grew at the same P-T conditions, the different chemical zoning patterns along with microstructural variations can be explained by changes in the intrinsic property of (local) bulk composition (Fig. 3.13-14). We interpret that transport distances in rocks with high modal abundance of quartz in the matrix and low concentration of garnet forming elements will be relatively large during growth of garnet, hence, it will be common in felsic rocks. Consequently, the availability of garnet-forming

elements and element transport must be considered when interpreting chemical zoning patterns and other microstructural characteristics in inclusion-rich garnet porphyroblasts. Garnets growing in such systems will tend to show local chemical equilibrium features like those described for the Type I garnets. Consequently, the use of garnet chemistry for isopleth thermobarometry or chemical patterns to infer tectono-metamorphic histories is challenging for such garnets. Compositional information retrieved from such grains will reflect rather local conditions than large scale equilibration. In a broader perspective, the quantitative analysis and detailed description of the garnet internal microstructures indicates that garnets with high density of inclusions (high φ-values) and irregular internal morphologies grew under local equilibrium. Therefore, highly skeletal garnets should be avoided when interpreting regional metamorphic histories.

The importance of taking bulk chemistry into account when interpreting the tectonometamorphic evolution of an area is nicely illustrated by our case study. The Isua garnets do not only vary in their chemical characteristics, but also in other characteristics such as the number of inclusions or internal crystallographic orientations. This diversity has previously been interpreted as reflecting different tectono-stratigraphic domains and thus implying the operation of horizontal tectonic movements that brought them together (e.g. Rollinson, 2002, 2003; Gauthiez-Putallaz et al., 2020). However, there is no spatial systematic occurrence in any of the characteristics described here (Fig. 3.3). Therefore, interpretations of different tectono-stratigraphic sequences in Isua cannot be made using the garnet record only. Additionally, the combination of the chemical zoning and inclusion patterns of the Isua garnets has been used to argue for and against the different tectonic models proposed for the belt. For example, uniformitarian models argue that the inclusion-rich garnets recorded at least two different tectonometamorphic events that are consequence of multiple amalgamation episodes driven by subduction at convergent margins (e.g.,

Gauthiez-Putallaz et al., 2020). However, other authors have suggested that the inclusion-rich garnets only reflect one tectonometamorphic event (e.g. Ramírez-Salazar, et al., 2022). A single major tectonometamorphic event is predicted in the non-uniformitarian heat-pipe model proposed for the belt (Webb et al., 2020). Our microstructural descriptions agree with the latter interpretation. The data show that the inclusion-rich cores in the ISB have inclusion trails continuing through different chemical zones (e.g., Fig. 3.8f, 3.9b-d, 3.10c, 3.9b, and APP-B6) suggesting they grew in the same tectono-metamorphic event (Chapter 2) and did not record different events. This interpretation is also supported by the EBSD data in the metapelite 714-5E showing compositional, inclusion orientation and crystallographic orientation changes are coupled, suggesting growth during shear deformation (Fig. 3.8f). Nontheless, to have a better and more robust interpretation of the garnet record in Isua, it is necessary to obtain absolute ages of the different garnets to properly address their complete P-T-t-X-D evolution.

3.6. Conclusions

This study provides a comprehensive quantitative microstructural and chemical description of inclusion-rich garnet porphyroblasts within a range of bulk rock compositions. The analysis of the data allowed us to identify that inclusion-rich garnet growth in medium-grade rocks is largely controlled by bulk rock compositions, mineralogy, and microstructures. On the one hand, the concentration of garnet-forming materials in the rock influences the availability of elements for growing and thus the required transport distances. At lower concentrations, garnet grows in high affinity surfaces and previous microstructures and will show local equilibrium features. (Type I garnets) At larger concentrations, transport distances are shorter and transport less restricted thus garnets will develop large-scale equilibrium characteristics (Type II garnets). On the other hand, excess or non-reactant phases (e.g., quartz and calcite) present in the rock will be included in the growing porphyroblast, such that large proportions of such minerals will facilitate the grow of heavily included garnets. Our analysis shows that

Type I garnets with high proportion of inclusions and erratic chemical and crystallographic patterns should be cautiously used when interpreting the metamorphic evolution of a rock. Type I garnets are more common in felsic rocks with high modal abundance of quartz, while rocks with high abundance of rock forming elements and minerals, like mafic rocks, or minerals with high affinity surfaces and boundary diffusivities, like metapelites, will tend to bear Type-II garnets. Our analysis provided evidence that the diversity of microstructures and chemical zoning in the ISB is most likely the product of the growth mechanisms operating during garnet formation and that they all most likely experienced the same metamorphic history.

Chapter 4: Constraining the prograde metamorphic and tectonic evolution of garnet porphyroblasts in the Isua supracrustal belt, SW Greenland

The following chapter is presented as a manuscript draft to be submitted after the thesis defence. It should be noted that this chapter is written in a manner where reference is made to features shown in other chapters. For a manuscript to be published, these parts will need to be changed. The authors and their contributions to this chapter are as followed: Anthony Ramírez Salazar (Original manuscript, figures, data analysis, thermodynamic modelling, data collection, conceptualization, review and editing), Thomas Müller (conceptualization, supervision, review and editing, sample collection), Sandra Piazolo (conceptualization, supervision, review and editing), Dominik Sorger (conceptualization).

Abstract

Reconstruction of the complete P-T-X-D-t path of a metamorphic rock is important to decipher their origin and evolution in a tectonic setting. While peak metamorphic conditions are often readily recorded, detailed and quantitative information on the prograde P-T-X-D-t path remains commonly elusive. In the case of the Eoarchean Isua supracrustal belt (ISB) of West Greenland, this knowledge gap bears consequences for interpretations of Archean tectonics as different proposed tectonic models require distinct P-T evolutions. In this contribution, we present the first quantitative prograde P-T-X-D-t path the ISB using a combination of different techniques based on spatially resolved chemical and microstructural analysis of garnets in the belt. Modelling of garnet growth in a metapelitic rock suggests a clockwise P-T path, where an initial near isothermal burial from 0.46 GPa to 0.7 GPa at c. 550 °C is followed by a pressure decrease to 0.61 GPa while temperatures increased to up to 580 °C, with c. 765 °C/GPa and 950 °C/GPa gradients constraint with maximum P and T, respectively. Garnet elastic barometry put an absolute upper bound of maximum pressure to 1 GPa. Diffusion modelling shows that it is impossible to establish the time that passed

between peak pressures and peak temperatures. The initial near isothermal P-T path is supported by qualitative data retrieved from isopleth thermobarometry and garnet trace element measurements from samples across the belt. The consistency of various datasets provides confidence that the obtained P-T path represents a robust proxy for the syn-metamorphic evolution of the belt. The derived P-T path is consistent with a tectonometamorphic evolution within both a subduction zone or a heat-pipe Earth, however, the latter is more consistent with mapped field relationships. Thus, our results open the possibility that the long-standing interpretation of the ISB as a record of plate tectonics-like processes may need to be re-evaluated.

4.1. Introduction

The quantification of peak metamorphic conditions is useful to explore the thermal evolution of individual rock samples to infer the corresponding tectonic regime of a study area. However, knowledge of peak conditions only offers a distinct snapshot within the full evolution of metamorphic rocks. In contrast, P-T-X-D-t reconstructions provide information on the tectonic environment, e.g., fast or slow subduction versus mountain building (e.g., Bucher and Frey, 2002), details on burial (e.g., Bohlen and Mezger, 1989; Nicoli et al., 2016) and exhumation processes (e.g., Thompson and Ridley, 1987) or they can help to recognize different tectonometamorphic events (e.g., Krogh et al., 1994; Maldonado et al., 2018). Information on the complete metamorphic path of a terrane including prograde and retrograde evolution provide additional information that can, in combination with field data, enhance our understanding of its geological and tectonic evolution through space and time.

The analysis through Earths' history of well-studied metamorphic terranes has revealed a secular change in peak P/T gradients from the earliest geological record to modern rocks. Such changes are documented to vary from intermediate to high P/T in the early Archean (c. 750-1000 °/GPa) to the dominance of contrasting low and high T/P gradients in the Phanerozoic (c. 250 °C/GPa vs c. 1000 °C/GPa) (Brown and Johnson, 2018). This change in

the metamorphic record might reflect a change in geodynamics, i.e., onset of plate tectonics (Holder et al., 2019). However, to quantitatively evaluate the advent of plate tectonics on Earth, a detailed characterization of the P-T-X-D-t paths is needed.

In recent years, advances in geodynamic modelling resulted in a set of numerical models investigating possible Archean crustal evolutions. These models do not only provide information about peak metamorphic conditions but in some cases provide the predicted P-T-t path (François et al., 2014; Sizova et al., 2018). Comparison of these models with the metamorphic evolution recorded in natural rocks of Archean age, along with other geological features, have pointed to the possibility of non-uniformitarian tectonics in the Paleoarchean (François et al., 2014; Brown, 2015; Sizova et al., 2018). This interpretation contrasts with research advocating for the operation of plate tectonics during the Eoarchean that is mainly based on geochemical signatures (Polat and Hoffman, 2003; Jenner et al., 2009) and interpreted field relationships (e.g., Nutman and Friend, 2009; Friend and Nutman, 2019). Contrasting interpretations on the nature of Archean geodynamics have been presented for the Isua supracrustal belt (ISB; Fig. 4.1). Three main competing models have been proposed: a subducted accretionary prism (Model A, Fig. 4.2a; Komiya et al. 1999), an orogeny (Model B, Fig. 4.2b; Nutman and Friend, 2009, Nutman et al., 2013, 2020) and, more recently, an evolution within a heat-pipe (Model C, Fig. 4.2c; Webb et al., 2020). All models predict a clockwise P-T path but the metamorphic record of the rocks of the ISB is predicted to differ in each scenario and the contrasting structural and tectonic nature of each model most likely produced different P-T paths topologies in the rocks across the belt. Therefore, the reconstruction of the metamorphic evolution of rocks from the ISB provide additional constraints allowing improved interpretations on the tectonic settings controlling the formation of the ISB.

Figure 4.1 Map showing the location of the samples used in Chapter 4 after Zuo et al. (2021b) with information of Nutman and Friend (2009).
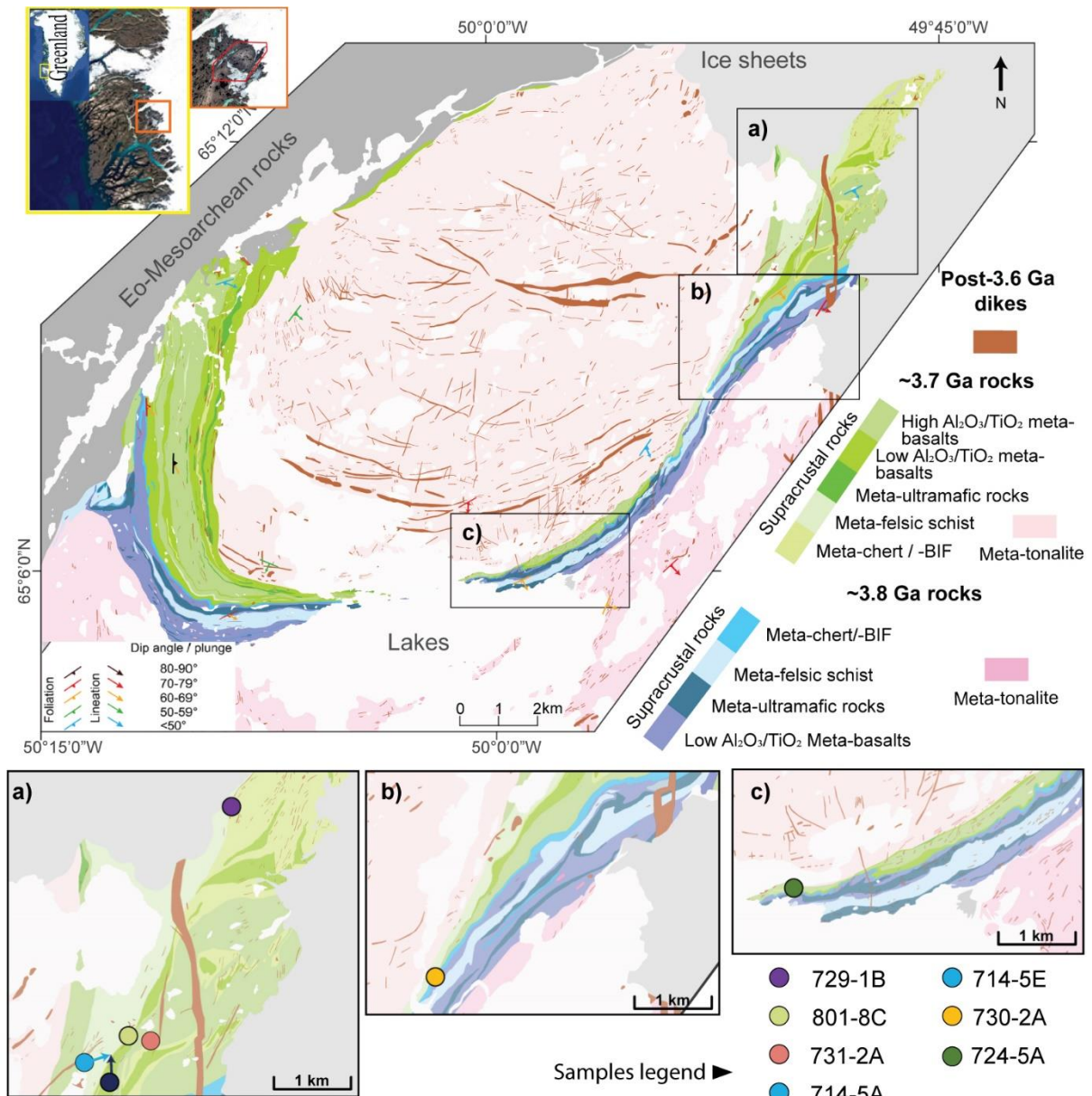
To date, quantitative studies on the dynamic P-T-*X*-D-t evolution of the ISB are largely

missing from the literature. This contribution aims to fill this gap in our knowledge by

providing the first attempt to recreate a quantitative P-T-*X*-D-t path for the Isua supracrustal

belt. To attain this, we combine thermodynamic phase equilibria modelling results with

prograde garnet growth modelling using the Theria_G software package (Gaidies et al.,

2008). Resultant P-T-*X*-D-t paths are compared to new quartz-in-garnet elastic barometry

data derived from ISB rocks. In-situ garnet trace element data is also used to qualitatively

understand the metamorphic evolution of the rocks along the belt and thus provide further

constraints on the possible metamorphic evolution of the ISB.

4.1.1 Reconstructing P-T-*X*-D-t paths using garnet as a proxy: Approaches and Models

The reconstruction of a complete P-T-*X*-D-t evolution is complicated by a number of factors.

For example, minerals in the matrix equilibrate, react, and transform as pressure and

temperature change, leaving no or only few traces of earlier stages of the rocks' evolution.

Metamorphic porphyroblasts, however, may enclose phases as they grow, acting as a shield

for these inclusions, thus preserving a part of its prograde paths (St-Onge, 1987). Similarly,

chemical zoning of minerals growing during progressive metamorphism can be used to

retrieve earlier prograde P-T conditions (Tracy and Robinson, 1976).

In medium-grade rocks, garnet is a common mineral typically showing systematic chemical

zoning (e.g., Hickmott et al., 1987; Chernoff and Carlson, 1997; Daniel and Spear, 1999;

Gaidies et al., 2015; George and Gaidies, 2017; Dempster et al., 2017). As the garnet grows

along a distinct P-T path, the composition, mineral reactions and mineral modes governing

porphyroblast growth will change continuously as a result of the effective bulk rock

chemistry (*X*) surrounding the growing garnet (Spear et al., 1984, 1991; Evans, 2004; Inui

and Toriumi, 2004; Gaidies et al., 2008; Konrad-Schmolke et al., 2008). As a result, the P-T-

X paths producing the garnet zoning patterns in a rock can be modelled for a given initial

bulk rock composition (Spear et al., 1984, 1991; Gaidies et al., 2008; Faryad and Ježek,

2019).

P-T-*X* modelling using chemical garnet zoning is performed either by isopleth

thermobarometry of different zones within an individual porphyroblast (Cutts et al., 2014;

Maldonado et al., 2018) or by forward modelling (Spear et al., 1991; Gaidies et al., 2008;

Caddick et al., 2010; Faryad et al., 2019). To apply these methods, garnet porphyroblasts are

assumed to have grown in equilibrium with the modelled bulk composition (Gaidies et al.,

2008). If garnets show evidence of local equilibrium growth (Chapter 3) or high degrees of overstepping (Spear et al., 2014; Wolfe and Spear, 2018) results might be less accurate or it might not be able to reproduce the observed composition of the garnet at all. Signatures of such locally controlled or far-from-equilibrium growth include irregular chemical zoning (Spear and Daniel, 2001; Chapter 3), dendritic internal morphologies (Spear and Daniel, 2003; Miyazaki, 2015), depleted compositional halos around the grain (Carlson, 1989), highly variable crystallographic orientations (Chapter 3), and high proportions of inclusions (e.g. Chapter 3).

A number of software packages such as Theria_G (Gaidies et al., 2008) and CZGM (Faryad and Ježek, 2019) have been developed to reproduce the chemical profiles of garnet populations growing along a specific P-T path. Apart from the P-T conditions, these models are sensitive to the bulk rock composition (X), the crystal size distribution of the garnets in the sample, and time of growing (Gaidies et al., 2008), which then provides information on the relevant timescales (t) of the metamorphism. Thus, the usage of such software packages potentially allows to obtain quantitative P-T-X-t information, but they do present some limitations. For instance, the rocks that are shown to be successfully modelled are pelitic in composition as these show the most extreme changes in chemical zoning owing to the wealth of reactions occurring during their prograde metamorphic path (Bucher and Frey, 2001; Gaidies et al., 2008, 2015; George and Gaidies, 2017, 2020) and because most of the available compositional models were calibrated in their compositional system (e.g., Holland and Powell, 1998; White et al., 2014).

Rocks with the "ideal" composition and/or bearing garnets that show large-equilibrium features might be rare in a metamorphic terrane. Such is the case for the ISB, where metapelites are not abundant (c.f. Nutman and Friend, 2009; Fig. 4.1) and garnets showing local equilibrium characteristics are common (e.g., Chapter 3). However, alternative

approaches offer possibilities to enhance the reconstruction of P-T paths for a larger set of samples and compositions. For example, a spatially resolved (core to rim) use of a combination of geothermobarometers within garnets porphyroblasts can return a well-defined P-T path (e.g., St-Onge, 1987). In addition, recent advances in geothermobarometry provide an increasing number of tools for this task. For instance, quartz in garnet (QuiG) barometry yield pressure estimations independent of thermodynamic data and can potentially be used to track pressure variations in different parts of the garnet (e.g. Wolfe et al., 2021; Mulligan et al., 2022). Combined with other independent thermometers (e.g., Ti-in-Quartz; Gonzalez et al., 2019) a fair approximation of the metamorphic path can be obtained.

Trace element zoning in garnet is common (e.g., Hickmott et al., 1987) and can also be used to further constrain the P-T history of a rock. Changes in trace element concentrations shed light on nature of minerals that are reacting to form the garnet or those that are growing contemporaneously. For example, the bulk content of HREE in garnet is strongly controlled by zircon, such that garnet growth in the presence of zircon will tend to show flat HREE profiles (Hermann and Rubatto, 2003). Another monitor for such phases is Eu, which is highly compatible with plagioclase and takes most of the bulk of this element (e.g. Fujimaki et al., 1984). In the case of garnet, negative Eu anomalies would thus suggest the presence of plagioclase during garnet growth, while positive anomalies indicate consumption of plagioclase (e.g. Buick et al., 2006; Clarke et al., 2013). Therefore, placing the trace element zoning of garnets within the context of garnet forming reactions and data from thermodynamic modelling, is essential to define P-T-*X*-t paths for different types of rocks (e.g. Konrad-Schmolke et al., 2008).

Additionally, garnets also provide information on the deformation (D) history occurring during metamorphism. As garnet grows distinct inclusion patterns such as internal foliations, these can be directly related to pre-, syn-, post-tectonic garnet growth by comparison with the

external, i.e. matrix foliation (e.g. Passchier and Trouw, 2005, fig. 4.3e). Therefore, it is possible to link different microstructural domains to the quantitative metamorphic data retrieved from garnets to reconstruct a P-T-*X*-D-t path for different rocks.

4.2 Existing tectonic models for the ISB and their inferred corresponding P-T paths

Interpretations of the geological record, and ultimately of the tectonic history of the ISB differ (e.g. Komiya et al., 1999, Nutman and Friend, 2009, Webb et al., 2020). In simple terms, the belt consists of a meta-volcano-sedimentary rocks with a protolith age ranging from S to N from 3.8 and 3.7 Ga (Fig. 4.1; Nutman and Friend, 2009). The belt is sandwiched between a c. 3.7 Ga north and a c. 3.8 Ga south big tonalite-trondhjemite-granodiorite (TTG) body (Fig. 4.1; Nutman and Friend, 2009). Tectonic breaks and sedimentary hiatus have been interpreted within the supracrustal rocks, which support the tectonic models described below. These geodynamic scenarios should produce distinct metamorphic patterns, both in the record of peak conditions as well as their spatial and temporal evolution. In this section, a brief description of the main competing tectonic models for the ISB is provided, focusing on the metamorphic and structural record. Along with this, a simplified P-T path representing each proposed tectonic setting is hypothesized based on general model predictions, numerical models, if available, and their analyses and examples of natural rocks. The expected P-T paths for each model will be used for comparison with the P-T(-*X*-D-t) paths retrieve from the rocks of the ISB.
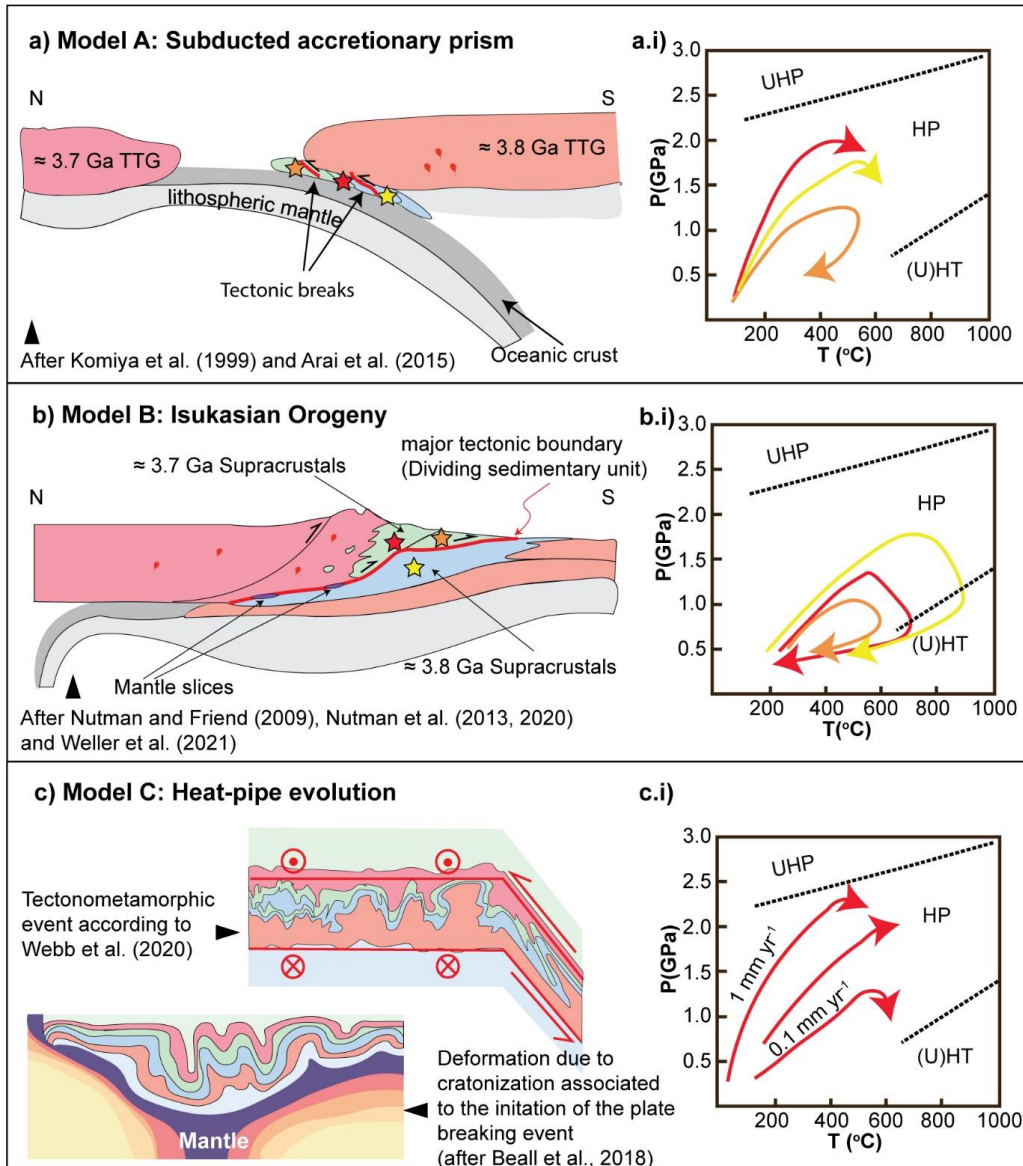
Figure 4.2 (a)-(c) Tectonic models proposed for Isua and (a.i)-(c.i) their predicted P-T paths. In (a) and (b) stars in the models show different positions of rocks, the expected path for each location is shown in the P-T diagrams with arrows with the same colours as the star (a.i-b..i). The paths in (c.i) represent different geothermal gradients due to different burial rates, the colder the higher the rate. Colours in the tectonic model schematically represent the sequences and tonalites of the belt

4.2.1 Model A: Subducted accretionary prism

Model A proposes that the ISB is a subducted accretionary prism (Fig. 4.2a; Komiya et al., 1999). Komiya et al. (1999) argues that southeast-directed duplex structures could be identified in the northeastern part of the belt, suggesting south-dipping subduction (Fig. 4.2a). Exhumation of the subducted accretionary prism along northwest-striking thrust faults resulted in the juxtaposition of four zones with different peak metamorphic grade that increases from NE-SW (Arai et al., 2015).

Rocks experiencing metamorphism within a subduction zone will show distinct P-T trajectories. The subducting slab is comparatively colder that the surrounding mantle causing the depression of the isotherms, and consequently a thermal anomaly upon its descent (Peacock, 1996). Therefore, a rock being part of a subducting plate system (e.g., a subducting accretionary prism) will first experience minor changes in temperature and large changes in pressures before sluggish heat transport leads to increasing temperatures. Such an evolution will create a clockwise prograde P-T paths (Fig. 4.2a.i), as those described in some exhumed subduction-related rocks (Brouwer et al., 2005; Cheng and Cao, 2015; Goscombe et al., 2017; Maldonado et al., 2018; Negulescu et al., 2018; Jin et al., 2021). Depending on the exhumation path, the retrograde evolution will differ, but numerical simulations (Burov and Yamato, 2008; Li et al., 2010; Sizova et al., 2014) suggest that for a relatively high-angle slab, most of the rocks will evolve along a steep tight P-T path, attaining higher pressures and temperatures as they are carried deeper into the mantle (Fig. 4.2a.i). In the case of flatter or slower subduction zones, prograde P-T paths flatten, but are yet often steep in their first prograde section (Manea et al., 2004; Sizova et al., 2014). Numerical simulations predict a similar behaviour for modelled Precambrian subduction zones (Sizova et al., 2014). Notably, modelled paths show flatter initial paths (Fig. 4.2a.i) for the rocks of the upper parts of the subduction zone (Fig. 4.2a; Li et al., 2010; Sizova et al., 2014). Therefore, in model A (Fig. 4.2a), it should be expected that the different metamorphic zones limited by faults should show not only different peak conditions but also slightly different P-T prograde trajectories.

4.2.2 Model B: Isukasian Orogeny

Model B contends that the ISB is the product of a collision of two separate terranes each one comprised of a supracrustal sequence and a TTG body of similar age (Fig. 4.2b; Nutman and Friend, 2009; Nutman et al., 2013; 2020). Extension following collision juxtaposed rocks with different metamorphic grades and an increase in pressure and temperature towards the centre of the 3.7 Ga TTG body is suggested (Nutman et al., 2013; 2020). In this model an

earlier accretion process to form the 3.7 Ga belt is also inferred from the inner cores in garnets (Nutman et al., 2015; Gauthiez-Putallaz et al., 2020).

The predicted P-T trajectories for rocks evolving in an orogeny is different to that expected for rocks undergoing subduction. As the rocks are buried the temperature and pressure rises, creating P-T paths with relatively shallow slopes (Fig. 4.2b.i; Brown, 1993, 2001; Goscombe et al., 2017; Weller et al., 2021). As the rocks get closer to the core of the orogen (Fig. 4.2b), they will experience higher peak conditions and wider P-T paths (Fig. 4.2b.i; Goscombe et al., 2017; Weller et al., 2021). Tectonic horizontal movement and tectonic breaks will tend to juxtapose rocks with different metamorphic grade and distinct P-T prograde evolution in terms of absolute peak conditions while the topology of P-T gradients are expected to be similar. In the case of Model B, rock packages with different tectonometamorphic evolutions are supposed to be in contact along localized shear zones, with a major tectonic break, marked by the sequence known as the dividing sedimentary unit (Fig. 4.2b), separating the two proposed terranes (Nutman and Friend, 2009; Nutman et al., 2013; 2020).

4.2.3 Model C: Heat-pipe evolution

Model C argues that the ISB has been evolving in a heat-pipe Earth (Webb et al., 2020). In this model, the ISB is a continuous volcanosedimentary sequence with a c.100 m.y. unconformity that divides the 3.8 and 3.7 Ga packages (Webb et al., 2020). Field observations and quantitative strain analysis (Zuo et al., 2021) suggest that there are no important tectonic boundaries within the belt and that strain is almost homogenous throughout the belt (Zuo et al., 2021). Later deformation in a km-scale sheath fold caused the metamorphism and created the present fabrics of the belt (Webb et al., 2020). The heat pipe evolution proposed for Isua (Webb et al., 2020) culminates in a sheath-folding event (Fig. 4.2a) that, according to Zuo et al. (2021b), might be related to the initiation of the plate breaking event expected for the end of the transition from heat-pipe to an active lid tectonics

(Beall et al., 2018). No juxtaposition of samples with different metamorphic grades is expected due to the absence of major tectonic breaks and large intra-tectonic movements. For the rocks evolving in a heat pipe scenario, no explicit P-T paths have been suggested and so far no terrane on Earth has been widely accepted to be the product of this type of tectonics. Thus, comparison with natural rocks is not possible at this stage. However, numerical simulations revealed that the geothermal gradients in rocky bodies with heat-pipe geodynamics operating will depend on the depositional and burial rates (Moore and Webb, 2013). On the one hand, rapid burial rates (e.g. 1mm/yr) will translate into steep, clockwise P-T paths (Fig. 4.2c.i), similar to those described for subduction zones, i.e. model A (Fig. 4.2a.i). A similar evolution is expected in the case of the plate breaking event, as it initiates with small pulses of mantle-induced contraction that deforms the crust producing large vertical structures (Fig. 4.2a) and preserves domes that also allow for steep P-T prograde paths (Fig. 4.2c.i). On the other hand, low burial rates (e.g. 0.1mm/yr) will produce P-T paths with shallower P-T evolutions (Fig. 4.2a), resembling those expected for model B (Fig. 4.2b.i). Thus, operation of a heat-pipe model will be hard to distinguish from the other models solely based on the shape of the P-T paths. However, in combination with field data such as the lack of tectonic breaks between sedimentary packages of different ages (e.g. Zuo et al. 2021b) arguments on the plausibility of model C over the other models may be drawn.

4.2.4 Previous P-T constraints derived from Isua garnets

Estimates of the P-T conditions of the ISB in general (Boak and Dymek, 1982; Arai et al., 2015) and some of the garnet porphyroblasts in particular (Rollinson, 2002) have been previously published. In Chapter 2 of this work, it is argued that the garnet microstructures and chemical zoning represent two main metamorphic events: a syn-tectonic, amphibolite facies metamorphism (M_1) with peak conditions at 0.5-0.7 GPa and 550-600 °C forming the core and annuli, and a later post-tectonic metamorphic event (M_2) at >0.5 GPa and >540 °C represented by the inclusion-poor rims. This interpretation is consistent with other

temperature estimates from samples in the western and eastern part of the belt (Boak and Dymek, 1982). It is also consistent with the detailed analysis of the garnets presented in Chapter 3. In Chapter 2, isopleth thermobarometry is used to indicate that the garnet core and annuli evolved along a near isothermal compression path. On the contrary, other authors argued that the garnets recorded three metamorphic events: (1) metamorphism at 550 °C represented by the core of the grains, (2) peak syn-tectonic metamorphism at 610 °C and 0.7 GPa, and (3) a post-tectonic episode at 500 °C (Rollinson, 2002, 2003; Gauthiez-Putallaz et al., 2020; Nutman et al., 2020). The main contrast in the interpretations of the garnet growth is centred around the timing of the core and annuli growth. While in Chapter 2 of this work, continuous inclusion trails are used to argue for a continuous growth in a single tectonometamorphic event, Gauthiez-Putallaz et al. (2020) suggested that the changes in chemical composition and microstructures from core to annuli marked a 10-50 m.y. hiatus of garnet growth, thus representing two different events. The hiatus is inferred by sedimentation of younger units after the metamorphism that formed the garnet core (Gauthiez-Putallaz et al., 2020).

4.2. Methodology: Sample selection and general approach

Garnet porphyroblasts with large-scale equilibrium features are required to successfully reconstruct the P-T-X-D-t paths recorded by the garnets of the ISB metapelitic rocks. In this study, two metapelites (801-8C and 714-5E) from the northeastern part of the belt, located within >500 m from each other (Fig. 4.2a) are investigated in detail for this task. Garnets in these samples are relatively poor in inclusions contrasting other garnets common in the ISB (see Chapter 3). We also analysed samples 729-1B, 714-5A, 730-2A and a band in sample 725-4A which are classified as Ca-rich metapelites. They are spatially distributed from the north to the south of the younger sequence of the belt (Fig. 4.1a-c), with one of them (730-2A) being part of the 3.75 Ga part of the older sequence (Fig. 4.1b). Additionally, one garnet-

epidote amphibolite (731-2A) was included in this study originating from the northeastern

part of the belt (Fig. 4.1a).

For this study, P-T data was first retrieved using isochemical phase equilibria diagram and

garnet isopleths for the metapelites along with additional pressure constraints by applying

quartz-in-garnet (QuiG) elastic barometer to the chosen metapelites for two additional

samples from the northeastern part of the 3.7 Ga sequence (714-5A and 731-2A, Fig. 4.1a)

and one sample from the central part of the 3.8 sequence (730-2A, Fig. 4.1b). Then P-T

constraints guided the modelling of the P-T-X-t paths, which was fitted by direct comparison

of measured chemical profiles in garnet presented in Chapter 3; such data was complimented

with microstructural observations to obtain information on the deformation (D). Finally,

qualitative information of the P-T-X trajectories across the belt was obtained by using in-situ

LA-ICP-MS trace elements data and interpretations on the phases involved in garnet growth.

4.2. P-T conditions from phase equilibria and isopleths

Peak assemblages were determined from thin section analysis and P-T quantification was

carried out with phase equilibria diagrams and garnet compositional isopleths that were

calculated with the Theriak-Domino package (de Capitani and Brown, 1987; de Capitani and

Petrakakis, 2010). The calculations used the Holland and Powell (1998) ds55 thermodynamic

dataset in the MnNCKFMASHT system with saturated water conditions. The solid solution

a-x models employed were garnet, epidote, cordierite, spinel (Holland and Powell, 1998),

chlorite (Holland et al., 1998), white mica (Coggon et al., 2002), plagioclase (Newton et al.,

1980) biotite and ilmenite (White et al., 2007). Bulk rock compositions for the calculations

were obtained from the data presented in Chapter 2 and 3.

4.2.2 Micro-Raman spectroscopy for Quartz in Garnet barometry

Doubly polished thick sections (150 µm) were used for micro-Raman analysis to apply the

quartz in garnet (QuiG) elastic barometer. Sections were cut from the same chip as the thin

sections used for petrographic analysis. Large garnets (>0.5 cm) were preserved in both

glasses. Measurements were run at room temperature 22-25 °C. Raman spectra were acquired at the University of Göttingen using a confocal Horiba Yvon LabRam HR800 UV Raman system attached to an Olympus BX 41 microscope. The samples were analysed using an unfiltered 488 nm laser excitation, a 2400 gr/mm grating 45mW.DO, and with ICS correction. The spectra were collected in a single spectral window centred at 313 cm^{-1} to allow simultaneous measurement of the 464, 206 and 126 cm^{-1} quartz peaks. All Raman quartz spectra were acquired in four cycles of 60 seconds.

To correct for the drift of the instrument a silica standard was used. For peak-shift calculation, a free euhedral quartz crystal was used, always measuring parallel to the c-axis of the crystal. A serial set of unknown quartz inclusion, free quartz crystal and silica standard spectrum were systematically acquired a for each quartz inclusion. Unknown and reference quartz peaks were corrected with the value of the silica in each set and unknown peak shifts were calculated with the respective values of the free quartz in each set.

Selected quartz inclusions range in size from 5-30 µm. They were completely included in the garnet grain and were mostly separated from any fracture or free surface for a distance of three times their radius in all directions. Most of the inclusions were elongated but none of them exhibit short to long axis ratios larger than 3:1. Selected inclusions generally presented a smooth surface, however, some of them display angular edges or irregular shapes. Since all studied garnet grains consists of inclusion-rich cores, finding inclusions with the ideal characteristics for elastic barometry has proven to be difficult and for most of the samples only a few grains are reported. Notably, some of these measured inclusions were still <3x radius closer to other inclusions.

Raman shifts were processed using the methodology described in Mazzucchelli et al. (2021). To account for deviatoric stresses due to the non-isotropic nature of quartz, the residual strains for the peaks 464, 206 and 126 cm^{-1} were first calculated using the Grüneisen tensor

with the software stRAinMAN (Angel et al., 2019). Subsequently. the residual strains were imported to the online software EntraPT (Mazzucchelli et al., 2021) to calculate the isomekes and entrapment pressures.

Quartz inclusions from a sample with known P-T peak conditions were measured as an independent check for the calibration of the QuiG methodology. The selected sample is from the Breaksea Orthogneiss, New Zealand, and presents a mineral assemblage comprised of omphacite + garnet + rutile + feldspar + plagioclase + quartz and minor zircon. Rutiles needles systematically arranged at 60-120° intersections are observed in garnet grains. The peak P-T conditions calculated with conventional thermobarometry are ≈1.8 GPa and ≈850 °C (de Paoli et al., 2009; Chapman et al., 2017). Garnets exhibit a few quartz inclusions but only five of them were big enough and thus suitable for Rama analysis. Calculated quartz-in-garnet pressures at 850 °C returned values ranging from 1.76 ± 0.03 to 1.97 ± 0.04 (Fig. APP-C4.1). The highest QuiG values are slightly larger than the ≈1.8 GPa data obtained with conventional thermobarometry (de Paoli et al., 2009; Chapman et al. 2019). The elastic barometry and thermodynamic pressure values, however, largely overlap, suggesting the calibration of the QuiG barometer was successful.

4.2.3 Forward modelling of garnet growth

Modelling of garnet growth and resulting chemical profiles was performed using the software Theria_G (Gaidies et al., 2008) which is part of the software package Theriak-Domino (de Capitani and Brown, 1987; De Capitani and Petrakakis, 2010) using the same thermodynamic dataset and compositional models as for the phase equilibria calculations (see section 4.2.1). Theria_G models the composition and size of a garnet population that is growing along a previously specified P-T-X-t path. Garnets are modelled as perfect spheres growing bigger with new garnet shells overgrowing the existing grains. After every garnet growth "event" the software assumes the garnet does not further interact with the matrix and thus extracts the weighted composition of the garnet population to adjust the matrix composition for the next

timestep (t). Consequently, a new reactive bulk composition (X) is used for each iteration. As the software uses bulk rock compositions, it is assumed that the garnets grew in large-scale equilibrium. Additionally, the internal garnet composition is adjusted by diffusion potentially providing a timescale (t) as the grain grows (Gaidies et al., 2008).

Apart from the initial bulk rock composition and the thermodynamic input, Theria_G uses three main parameters for the calculations: (1) a P-T-t trajectory, (2) the crystal size distribution (CSD) of the garnets in the modelled sample and (4) diffusion coefficients for the structure forming elements in the garnet. The first one is typically varied to obtain a best fit (e.g., George et al., 2017), while the second one is obtained by direct measurements in the rock. The diffusion coefficients can be selected between the parameters of Chakraborty and Ganguly (1992) and Loomis et al., (1985). For the calculations presented here, the diffusion coefficients by Chakraborty and Ganguly (1992) were selected. Unfortunately, direct measurements of garnet CSD's from micro-tomography were not accessible due to the lack of statistics associated with the large garnet size (>0.5 cm), contrasting available small sample size. Therefore, a hypothetical CSD was assumed for the samples that recreated the size of the garnet to model and used for all different models run. As a result, the P-T-X-t path was the only parameter space tested by the simulations.

Garnets of the ISB rocks show two main microstructural domains: a syn-tectonic inclusion-rich core and a post-tectonic inclusion-poor rim (Rollinson, 2002, 2003; Gauthiez-Putallaz et al., 2020; Zuo et al., 2021). However, as shown in Chapter 3, the post-tectonic rims are largely controlled by the microstructures of the rock. They only grow in the vicinity of foliated Fe-Mg minerals suggesting a strong influence of local composition (e.g. Fig. 4.2). This growth mechanism is also in disagreement with the assumption of radially growing spheres used in the Theria_G model (Gaidies et al., 2008). Consequently, only the syn-tectonic core is attempted to be modelled for most of the paths presented here (referred as

Case 1, 2 and 3). Nevertheless, individual attempts tyring to calculate the compositional profiles including the rims are presented. For details see Case 2 below. The ultimate aim of all cases is to find the best possible match of predicted and measured chemical pattern.

In cases 1-3, P-T stability fields, garnet isopleths intersections and QuiG data were used to define the different modelled P-T-*X*-t trajectories for the syn-tectonic inclusion-rich garnets. Notably, all modelled pathways start at the same P-T condition, which is defined by the intersection of the isopleths of all garnet end-members retrieved from the garnet innermost composition. For Case 1, the intersection of the compositional isopleths of the garnet's annuli were used as guidance to infer the P-T evolution. Duration time started in 3.6 m.y. (Case 1a) and adjustments to the P-T path were made until the measured garnet profiles were reproduced (referred as "best fit" path). Then, to explore kinetic effects such as diffusive relaxation of the compositional growth zoning accompanying porphyroblast growth, the duration of the metamorphism time was changed. In other words, the same P-T trajectory obtained from Case 1a ("best fit") was run with 18, 30, 48, 60 and 90 m.y. durations (Cases 1b, 1c, 1d, 1f, 1g). Additionally, to account for a possible hiatus in garnet growth as suggested by Gauthiez-Putallaz et al. (2020), a time period of constant P and T inhibiting further growth but allowing for diffusive relaxation between 20 and 50 m.y. was introduced (Case 1f and 1g).

For Case 2, the construction of the P-T trajectory of the syn-tectonic core was guided by the results of the QuiG combined with the isopleth intersections of the core, which aimed to account for higher pressures. For case 3, an additional path for the syn-tectonic core with shallower P-T slope was also modelled to simulate tectonic scenarios with such similar evolution. For both cases (3 and 4), the duration (3.6 m.y) and the assumed CSD were the same as case 1.

Finally, a final modification to the "best fit" tried to account for the post-tectonic overgrowth. Here, four prolonged different trajectories of the "best fit" path, continuing from its last P-T point, were modelled (Cases 4a-d). For these models the compositional isopleths (calculated with the matrix composition after extraction of the syn-tectonic garnet) of the garnet rim were used as guidance.

4.2.3 LA-ICP-MS analysis of garnet trace elements

Garnet trace element measurements were performed at the NAWI Graz Central Lab for Water, Minerals and Rocks of the University of Graz and Graz University of Technology. Analyses were done on polished thin sections using an ESI New Wave 193 Excimer Laser coupled to a quadrupole Agilent 7500 CX mass spectrometer. Garnets were ablated over 60s with a laser beam of 50 μm. The glass BCR-2G (Strnad et al., 2005) was used as standard and Si as the internal calibration element.

4.3. Results

4.3.1 General petrography, prograde reactions and mineral chemistry

Metapelite 801-8C exhibit a peak assemblage of plagioclase + garnet + chlorite + ilmenite + biotite and minor muscovite, and metapelite 714-4E shows a peak assemblage of quartz + garnet + muscovite + biotite + chlorite + ilmenite + minor tourmaline and sulphides. Sample 801-8C is richer in Al_2O_3, Na_2O and CaO compared to 714-5E, in agreement with the larger modal abundance of plagioclase (see Chapter 3, Table C4.1). Garnets in both metapelites have inclusion proportion <30% (classified as type II as defined in chapter 3) and contain spiral-like inclusion trails and concentric chemical zoning (Fig. 4.3a-b). In each grain, four distinct zones can be classified and are best illustrated using the grossular content (Fig. 4.3a-b, Table S4.2). Grains have bell-shaped spessartine profiles (Fig. 4.3a.i, bi), sharp increase and decrease in grossular making step-like shape (Fig. 4.3a.i, bi), while there is a slight increase in pyrope (Fig. 4.3a.i, bi) and almandine components towards the rim (Fig. 4.3a.ii, b.ii). The outermost zone 4 is interpreted to be part of the post-tectonic overgrowth based on
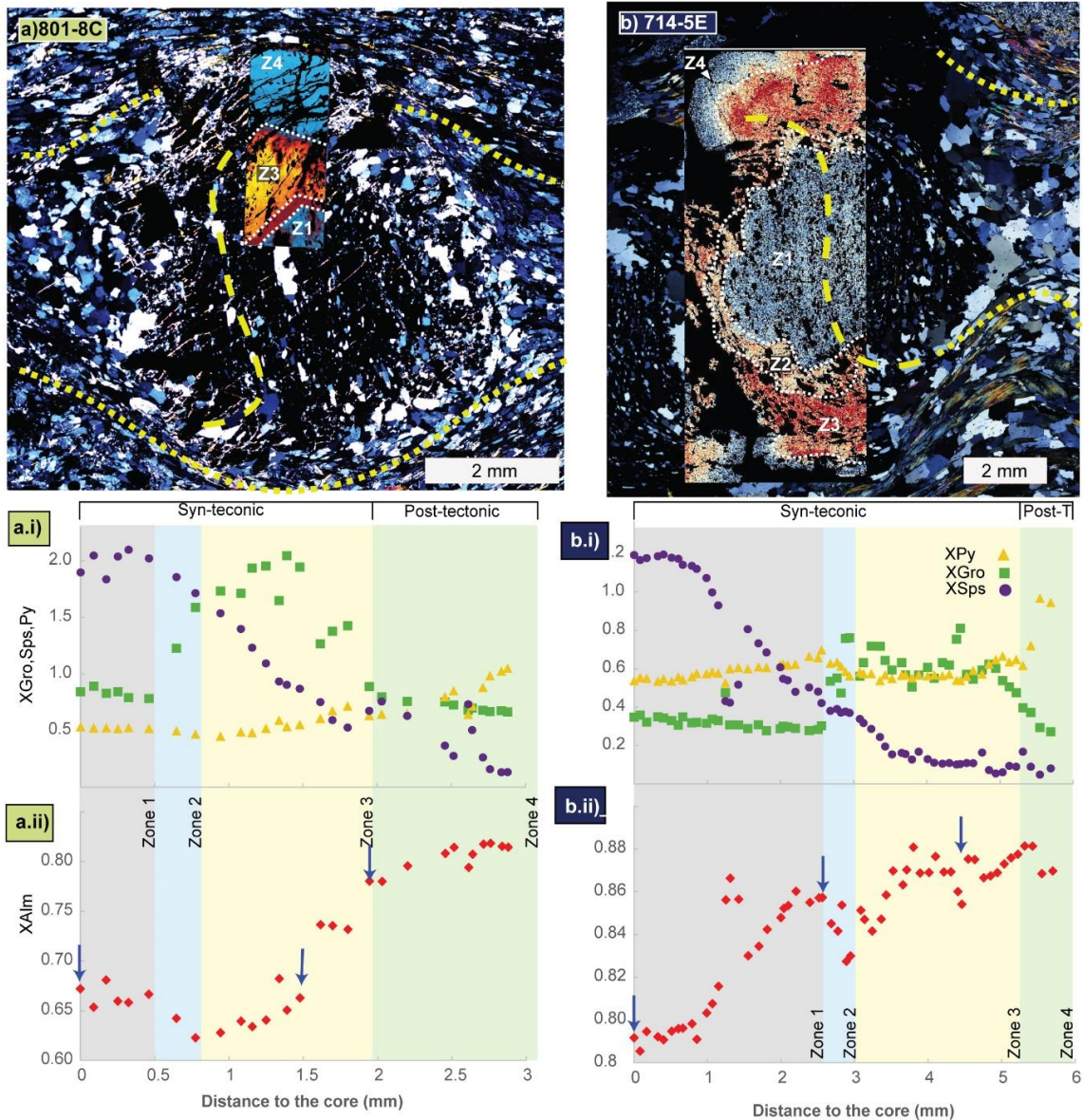
Figure 4.3 Garnet petrographic images of metapelites (a) 801-8C and (b) 714-5E with overlap compositional maps (X_{Gro}) showing four different zones. Garnet profiles for (a.i-b.i) grossular, pyrope, spessartine and (a.ii-b.ii) almandine highlighting the different zones. Arrows indicate compositions used for the isopleth intersections in Fig. 4.7.

the lack of inclusions and overgrowth of the foliation (Fig. 4.3a-b). Consequently, zones 1-3 are interpreted as part of M_1 while zone 4 represents the post-tectonic M_2. Quartz is the dominant inclusion in the garnet porphyroblasts. In addition, muscovite, ilmenite, chlorite, and a few small (<100 µm) rutile grains are present as inclusions in garnet of sample 801-8C (Fig. 4.4a). Notably, rutile is not present in the matrix of the rock. Garnets of metapelite 714-5E contain inclusions of muscovite and chloritoid with irregular borders (Fig. 4.4b). These

are interpreted as possible pseudomorphs after staurolite that might have participated in the garnet forming reaction (see Chapter 3). Plagioclase relics in garnets from sample 714-5E and the lack of this mineral in its matrix has also been interpreted as microstructural evidence of plagioclase as a reactant for garnet (see Chapter 3). Elongated prismatic pseudomorphs of fine-grained muscovite, and relics of plagioclase, quartz and epidote, in sample 801-8C are observed in the matrix, with larger sizes than other matrix minerals (Fig. 4.3c-d). Both kinematic indicators and crystallographic preferred orientations (CPO) of quartz in the matrix indicate a top-to-southeast shear sense for sample 801-8C (Zuo et al., 2021).

Samples 729-1B, 714-5A, 730-2A and the bands of sample 725-4A reveal a peak assemblage consisting of quartz + garnet + amphibole + plagioclase + ilmenite ± epidote/clinozoisite ± calcite and rare tourmaline and apatite. Garnets of type I (729-1B and 730-2A) and type II (730-2A and 725-4A) appear in these rocks. The foliation is deflected around the garnets and the porphyroblasts display straight or slightly curved internal foliations (Fig, 4.4e-g; Type C in Chapter 3) and spiral-like internal foliations (Fig. 4.5a; type B in Chapter 3). Although plagioclase and amphibole are major constituents of the matrix, they are rarely present as inclusions (e.g. Fig. 4.4e-g).
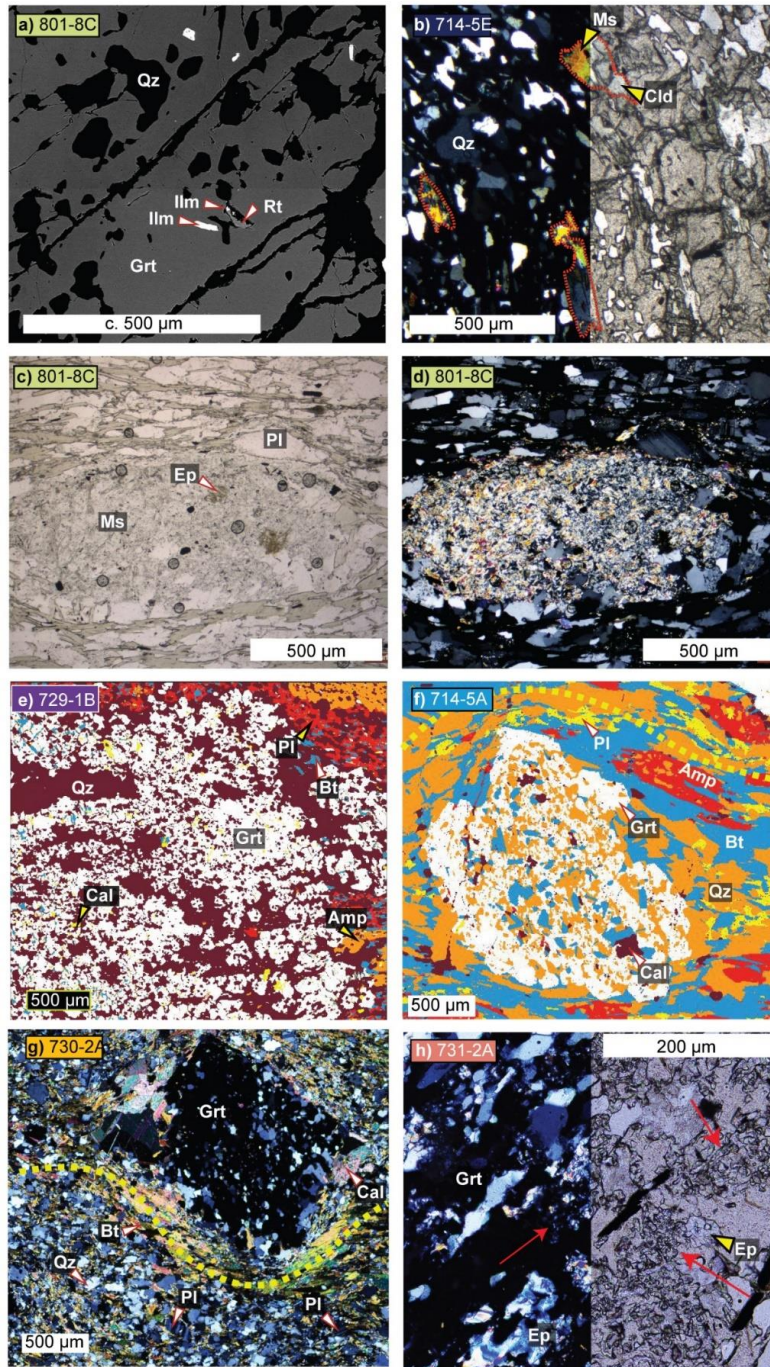
Figure 4.4 Images of garnets and microstructures described in the samples. (a) SEM image of inclusions of garnet showing small rutile grains. (b) Pseudomorphs of chloritoid and muscovite after staurolite as inclusions in garnet. (c-d) images of fine-grained muscovite pseudomorphs. (e-f) phase images and petrographic photograph (g) of garnets and surrounding microstructures; phase images processed with XMapTools (Lanari et al., 2014). (h) petrographic image of symplectitic-like microstructures between garnet and epidote.
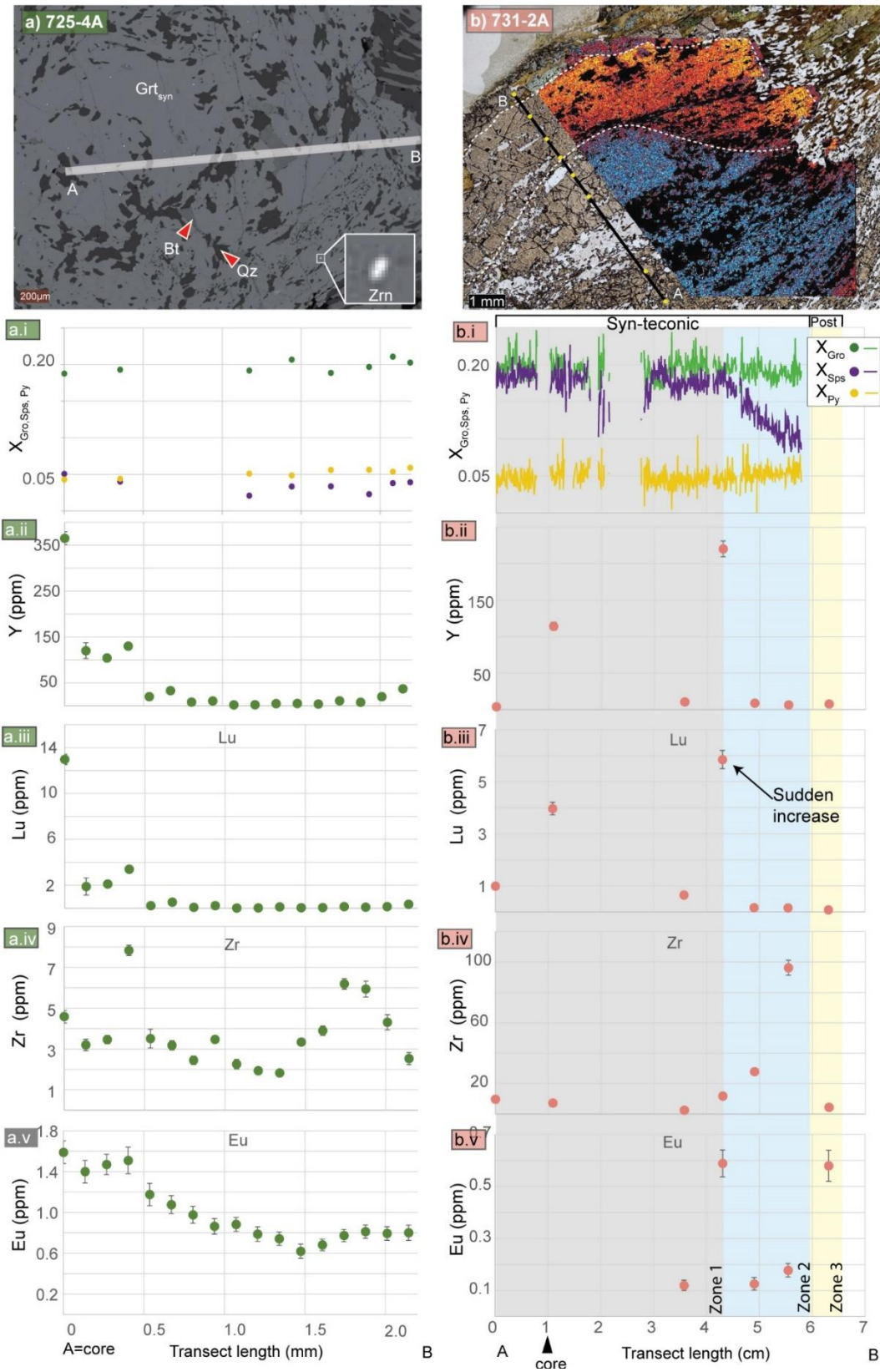
Figure 4.5 (a) SEM and (b) petrographic images of garnets; (b) shows overlap of compositional map. (a.i-b.i) profiles for major elements, (a.ii-b.ii) Y, (a.iii-b.iii) Lu, (a.iv-b.iv) Zr, (a.v-b.v) Eu. Points with concentrations below detention levels are not plotted.

In the garnet-epidote amphibolite (sample 731-2A), garnet + amphibole + biotite + quartz + epidote + ilmenite and minor calcite comprise the peak assemblage. Studied garnets are classified as Type II (cf. chapter 3). These grains show inclusion trails that are parallel to the foliation curving towards the centre of the grain and converging within the pressure shadows (Fig. 4.5b, type A of Chapter 3). A slight increase in pyrope component towards the annuli can be seen (Fig. 4.5b.i) coinciding with a sharp decrease in spessartine component (Fig. 4.5b.i) and increase in the annuli. The distribution of the grossular component is relatively homogeneous (Fig. 4.5b.i), albeit subtle increments in the rim can be noted.

4.3.2 Phase diagrams and garnet isopleths

Phase equilibria calculations using garnet isopleths and measured bulk rock compositions (Table C4.1, 4.2) reveal that the interpreted peak mineral assemblage of sample 801-8C is stable at 540-620 °C and 0.6 up to 1.0 GPa (Fig. 4.6). Almandine (X_{Alm}), pyrope (X_{Py}), and spessartine (X_{Sps}), isopleths for the core in garnet 801-8C intersect at c. 538 °C and c. 0.46 Gpa (Fig. 4.6), while grossular (X_{Gro}), isopleth plots at $\approx$ 5 °C lower (Fig. 4.6, 4.7a). The core intersection plots in the stability field of the assemblage plagioclase + ilmenite + garnet + chlorite + 2 micas. Rutile, also included in garnet, does not appear in the any of the stable assemblages in the isochemical phase diagram, which might be consequence of the assumption of a Fe_2O_3-free system for the calculations. Representative isopleths of the annuli also show tight intersections at c. 0.69 Gpa and 540 °C and c. 0.67 Gpa and 560 °C (Fig. 4.6). The annuli isopleths intersection, using the measured bulk rock composition, plot in the same mineral assemblage field as the core (Fig. 4.6). One of them, however, plots within error with the interpret stability field (Fig. 4.6).

Phase diagrams for samples 714-5E, 731-2A and 714-5A have already been presented in chapter 2 and the interpreted stability fields are shown in Fig. 4.7b-d (coloured outlines inside the diagrams). Compositional isopleths of the garnet core (Zone 1) in sample 714-5E intersect at c. 0.22 GPa and 535 °C (Fig. 4.7b). Grossular, pyrope and spessartine isopleths of the zone

2 annulus (c.f. Fig. 4.7b) create a larger field at 0.37-0.52 GPa and 550-570 °C (Fig. 4.7b).

Representative isopleths of all end-members of the zone 3 garnet annulus of sample 714-5E

intersect at 0.7 GPa and 560 °C (Fig. 4.7b). Compositional isopleths for a large (>1 cm)

garnet in sample 714-5A typically do not overlap. The garnet from which compositions were

obtained show some local equilibrium features, typical of garnet Type I (see Chapter 2) that

might account for this.
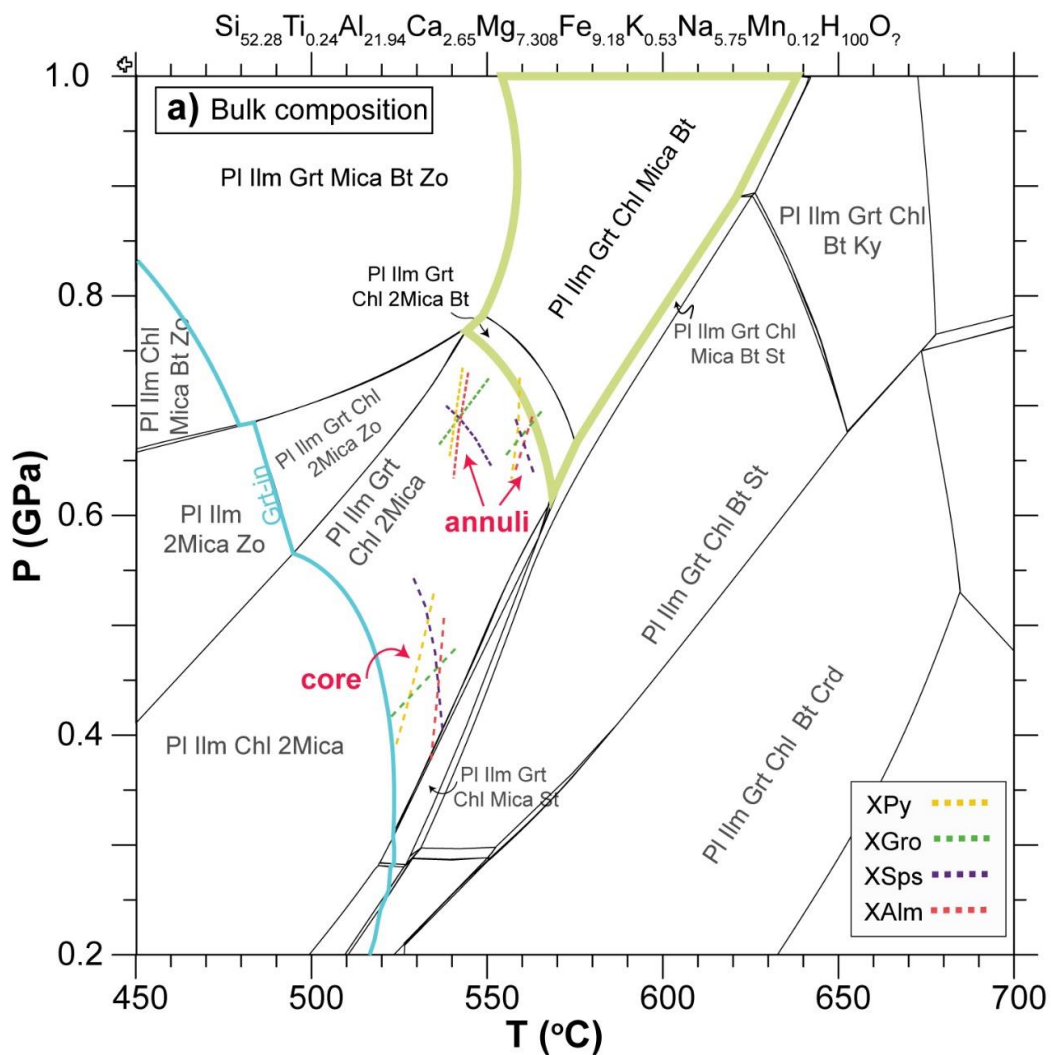
Figure 4.6 Phase diagram obtained with theriak-domino for sample 801-8C highlighting the interpreted peak assemblage and showing the compositional isopleths of garnet zones.

4.3.3 Further constraints in pressure using QuiG barometry

QuiG isomekes calculated for the samples (801-8C, 714-5E, 714-5A, and 731-2A) and for

which phase equilibria diagrams were obtained tend to either overlap with the stability fields

derived in this chapter and chapter 2 (Fig. 4.7a-c) and/or plot at somewhat higher pressures (Fig. 4.7a-d). Most of the measured quartz inclusions in the garnets were located in the annuli of the grains. The exact composition of the area nearby the measured inclusions was not determined, thus not allowing for a direct comparison between QuiG and isopleth thermobarometry. However, approximations can be made with the known compositions of the annuli of garnets in the twin thin sections. For sample 801-8C, isopleths intersection yield lower P values of up to ≈ 0.30 GPa compared to the QuiG isomekes (Fig. 4.7a). For garnets in metapelite 714-5E, differences of up to ≈ 0.25 GPa are described between isopleth geothermobarometry of the annuli and the highest isomeke. Although isopleths intersections were not obtained for 714-5A, garnet-biotite thermometry (see Chapter 2) in this sample points to garnet growth at ≈ 525 °C. QuiG barometry of the two analysed inclusions in this sample give pressures of 0.66 and 0.80 GPa, which are higher than the stability field of the peak equilibrium assemblage (Fig. 4.7d).

It is worth noting that some of the quartz inclusions that returned the highest-pressure values are small inclusions (<10 µm) with pointy edges, e.g., the highest isomeke in sample 731-2A (Fig. 4.7d.i) and the second highest isomeke in sample 801-8C (Fig. 4.7a.i)

4.3.4 Forward P-T-*X*-t path modelling utilizing chemical zonation of selected garnets

Only the modelling of one garnet profile of sample 801-8C using Theria_G (Gaidies et al., 2008) produced reliable results. Attempts to recreate the compositional profiles of the garnet in sample 714-5E was not successful. Some paths similar to that obtained for garnet in 801-8C show some features of the profiles (e.g. the "step" in grossular or similar contents for all the endmembers) but they are not satisfactory for other features such as size and the location

in changes of composition. Thus, the following description of the best-fit P-T-*X*-t trajectory is

focussed on the garnet from metapelite 801-8C.
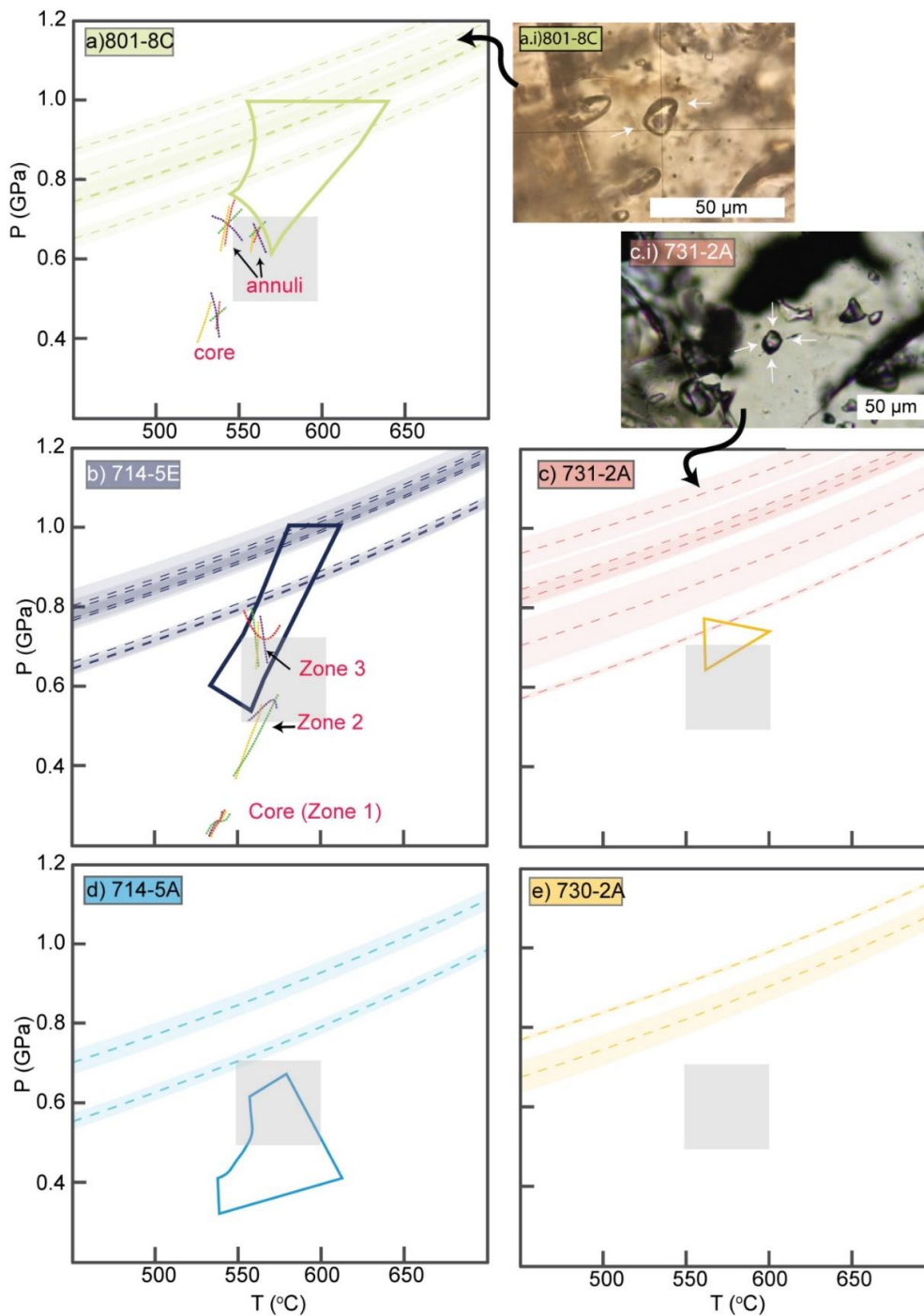
Figure 4.7 (a)-(e) Calculated isomekes for the quartz-in-garnet barometry. (a.i) and (c.i) show quartz inclusions which returned exceptionally high-pressure values; arrows point to the irregular and sharp edges. Colour polygons highlight the P-T stability fields of the interpreted metamorphic peak assemblage as derived from phase equilibria modelling and grey box highlights the interpreted peak metamorphic conditions. (c.f. Fig. 4.6 and 2.8, Chapter 2)

Case 1 – best fit syn-tectonic PT path: The P-T-X-t path with the "best fit" that reproduced the syn-tectonic (M_1) compositional profiles (Fig. 4.8a.i) shows a near isothermal increase in pressure, followed by a decrease in pressure and increase in temperature (Fig. 4.8a). The trajectory starts at 533 °C and 0.46 GPa with increasing pressure up to 0.7 GPa and 550 °C with a constant temperature rise and pressure drop culminating at 580 °C and 0.61 GPa. Peak equilibration of the garnet plots at 25 °C higher and 0.05 GPa lower conditions than the interpreted equilibrium assemblage (Fig. 4.8a), which is within accepted errors for phase equilibria modelling (Palin et al., 2016). Variations of the duration of metamorphic garnet growth ranging from 3.6 m.y. up to 90 m.y. did not significantly affect the resulting chemical profiles (Cases1b-f; Fig. APP-C4.2b-f). Only small changes in the initial spessartine content (as shown in the inset of Fig. 4.8a.i) are visible results from increasing durations. Modelling of a 20-50 m.y. hiatus as suggested by Gauthiez-Pautallaz et al., (2020) between the core and the annuli resulted in similar results with no visible changes to the modelled chemical profiles (Cases 1g-h; Fig. APP-C4.2g-h).

Case 2 – maximum possible pressure: QuiG barometry was used to guide the modelling of the P-T-X-t path of the syn-tectonic core. The data suggest a maximum of pressure of up to c.1.0 GPa was reached at temperatures around 550-600 °C for sample 801-8C. An analogous trajectory to case 1a is obtained for a path reaching pressures up to 1.0 GPa (Fig. 4.8b) keeping the duration constant at 3.6 m.y. In this case, both spessartine and pyrope show a relatively good match with the measured profile (Fig. 4.9b.i). However, the predicted grossular profile reaches significantly higher contents while almandine displays an almost flat profile (Fig. 4.9b.i) in clear disagreement with the measured profiles (Fig. 4.9b.i).

Case 3– shallower P-T path: The final test for the syn-teconic core aimed to examine the possible effects of a path with slightly shallower P-T slope, where pressure increases with temperature (Fig. 4.8c). This was to contrasts to the near isothermal path of the "best fit"

where temperature is almost constant as pressure rises and trying to account for tectonic scenarios with such type of paths (c.f. 4.2). Spessartine profiles and, within error, pyrope profile reproduced with this path resemble the changes in composition in the garnet (Fig. 4.8c.i). Modelled grossular exhibit a smoother increase and lower absolute values, while almandine shows a constant increment that does not match the observed variations in the garnet grain (Fig. 4.8c.i). Notably, for both, case 2 and 3 the modelled garnet growth also produced larger grains (Fig. 4.8b.i, c.i) even though the initial CSD was the same as for the original model.

Case 4– post-tectonic growth: Inspection of different extended paths to the obtained "best fit" (Case 1a; Fig. 4.8a) were carried out, aiming to reproduce the chemical profiles of the post-tectonic garnet growth (zone 4, Fig. 4.3a). For this it is assumed post-tectonic growth continue when syn-tectonic growth stopped. First order observations were retrieved from isopleths calculated with the reactive bulk composition after the extraction of the composition of the syn-tectonic garnet (phase equilibria diagram shown in Fig. 4.8a, d). Here, almandine and grossular isopleths for compositions in the rim typically intersect, but pyrope isopleths plot at lower temperatures (with differences of up to 40 °C; Fig. 4.8d). Four different extended paths were modelled following the same trajectory as the "best fit" and continued from its last point (i.e., 580 °C and 0.61 GPa; dotted lines in Fig. 4.8d). One extended path carried on until the intersection of the almandine and grossular isopleths (c. 600 °C and 0.65 GPa, C4.3a) while the rest tested for the effect of higher peak temperatures and lower peak pressures (Fig. 4.8d; APP-C4.3). None of the extended paths could reproduce the chemical profiles of zone 4 (Fig. 4.8d.i; APP-C4.4). The models typically show a sharp increase in the pyrope component to contents > 0.11 at the start of the post-tectonic growth (Fig. 4.8d.i; APP-C4.4). However, the highest measured X_{Py} values in the garnet are <0.1 (Fig. 4.3a.i).
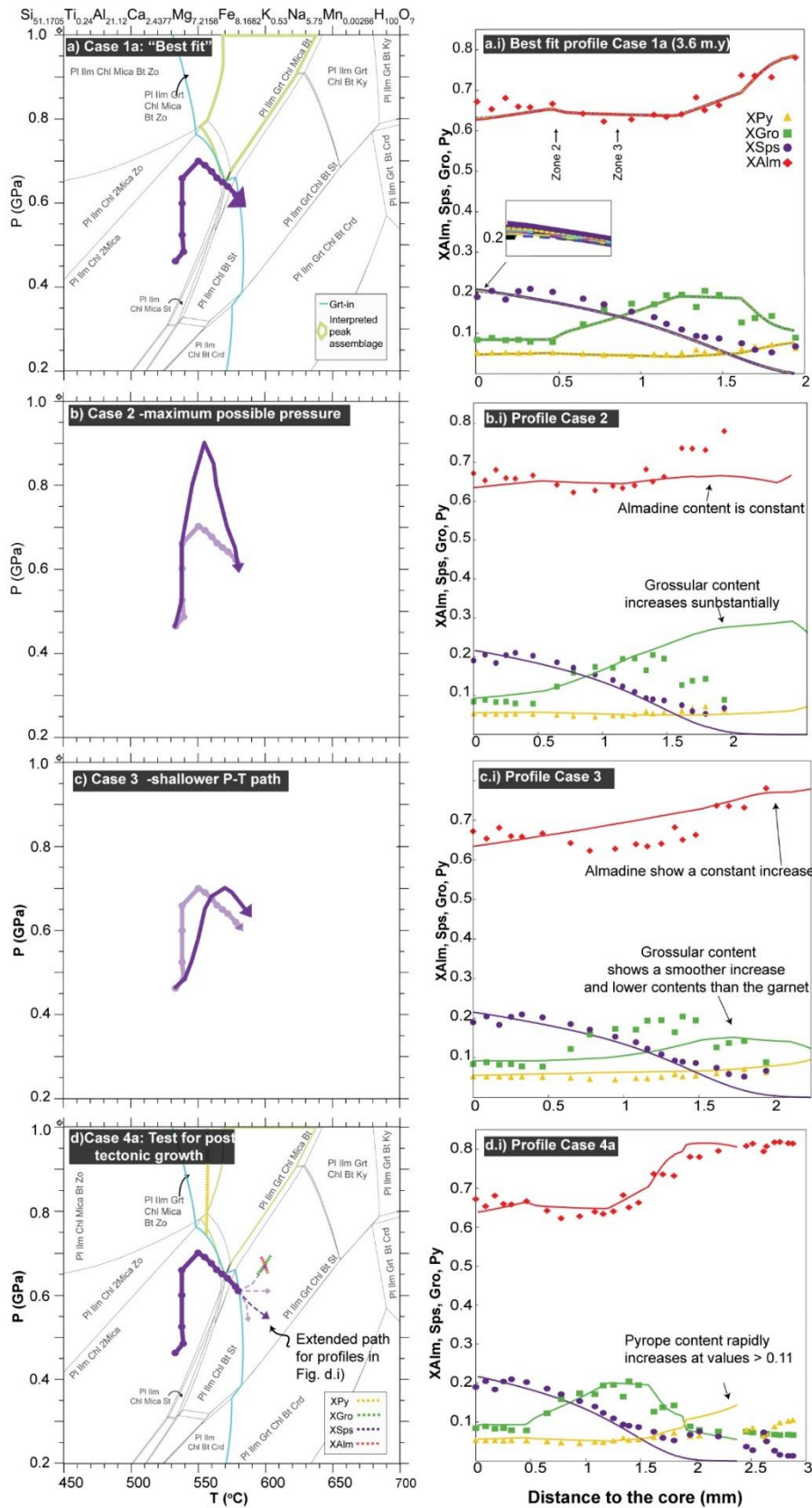
Figure. 4.8 (a-d) Modelled P-T paths for garnet in sample 801-8C and (a.i-d.i) comparison of the modelled and measured garnet profiles. Stability fields in phase equilibria diagrams shown in (a) and (d) were calculated after extraction of the syn-tectonic garnet.

4.3.3 Spatially resolved trace element concentrations in garnet.

Transects of trace element concentrations were obtained for garnets in samples 731-2A and 725-4A (Fig. 4.5). Grains typically exhibit an enrichment in Lu and Y in their cores (Fig. 4.5a.ii, b.ii). Garnet in 731-2A shows an anomalous enrichment in Y (Fig. 4.4b.ii), Lu (Fig. 4.5b.iii), and Eu (Fig. 4.4a.i) that coincides with the interface of its zone 1 and 2, as well as coinciding with a significant decrease in spessartine component (Zone 2, Fig. 4.5b.i). Both grains in samples 731-2A and 725-4A display some spots showing an enrichment in Zr (Fig. 4.5a.iv, b.iv), which are interpreted to be the result of contamination with small zircon grains inferred from SEM imaging (e.g. Fig. 4.5a). For samples 729-1b and 714-5a, only core-rim and core-annulus-rim analyses were made. All grains of samples 731-2A, 725-4A, 729-1b and 714-5A exhibit some similar characteristics in their trace element patterns. All the points show a positive anomaly of Eu (Fig. 4.9), with Eu/Eu* ($Eu_{(N)}/ (Sm_{(N)*}Gd_{(N)})^{1/2}$) ratios ranging from 1.22-6.92. They present negative anomalies of Ti and are relatively flat REE element patterns (Fig. 4.9).

4.4. Discussion
4.4.1 Comparison between equilibrium geothermobarometry and elastic barometry

Different methods and data have been presented in this Chapter to provide further constraints on the metamorphic conditions of the samples in Isua and their P-T-*X*-D-t evolution. As a first order observation, this new approach leading to an independent dataset highlights a remarkable consistency in derived P-T estimates and compositional characteristics (e.g. garnet trace elements), for rocks across the ISB. This, in turn, confirms the absence of a significant metamorphic gradient within the belt as previously proposed in Chapter 2 and suggested by the analysis of garnets in Chapter 3. For example, peak conditions retrieved from phase equilibria and isopleth thermobarometry of sample 801-8C (Fig. 4.6) overlap with those calculated for the rest of the samples across the ISB (550-600 °C and 0.5-0.7 GPa, Fig.

4.7a). Similarly, although the QuiG dataset is relatively small, the results between samples are largely within a similar range (c. 0.7 GPa and c. 1.0 GPa; Fig. 4.7).
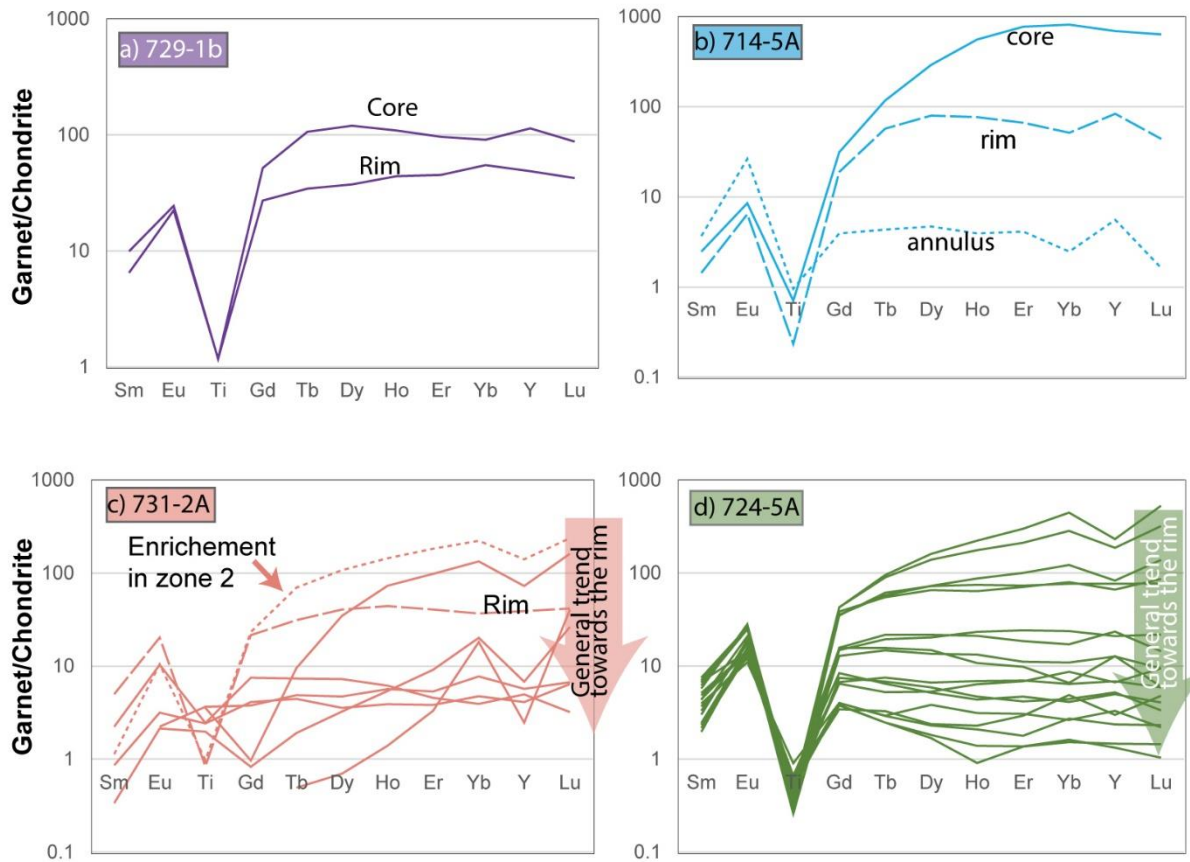
Figure 4.9 (a)-(d) Chondrite-normalized diagrams of garnet trace elements.

In general, we note that pressure estimates obtained using phase equilibria and isopleth barometry are lower than those calculated with the QuiG elastic barometer (0.7 vs up to 1.0 GPa; Fig. 4.7). Such discrepancy appears to be common in medium-grade rocks where both elastic and equilibrium-based barometry have been applied (Spear et al., 2014; Spear and Wolfe, 2019; Mulligan et al., 2022). It has been suggested that higher pressures retrieved from the QuiG methodology might be evidence of garnet growth with higher overstepping. In this regard, higher values have been used to argue that extracted P-T data and P-T-*X*-t paths obtained using equilibrium approaches might be less accurate or even erroneous (e.g. Spear et al., 2014; Spear and Wolfe, 2019). If true, it is possible, that the QuiG data indicate that the results calculated with equilibrium-based thermobarometry are underestimating the actual P-

T conditions accompanying garnet growth. However, a more detailed look at the nature of the inclusions that provided higher pressures may explain the largest QuiG values to be artifacts of the approach. Consequently, derived pressure estimated would not substantially vary from the equilibrium calculations.

In the present case, inclusions providing high pressures tend to be the smaller inclusions with pointy ends. Most studies on QuiG barometry focus on mechanisms that modified the inclusions and lower their entrapment pressures after quartz is enclosed in the garnet (e.g. Mazzucchelli et al., 2018). Notably, a few studies highlight some sensitivity of measurements and demonstrate that selection of inclusions with less than ideal conditions can produce higher apparent P-estimates (Whitney et al., 2000; Murri et al., 2018). Here, edge and corner effects are important for anisotropic inclusions like quartz, such that peak shifts will be larger when the measurement is taken closer to the edge of the inclusion (Murri et al., 2018). Moreover, detailed characterization and modelling of quartz inclusions in garnets have shown that the stress tends to concentrate in sharp corners of inclusions as well as in irregular ones (Whitney et al., 2000). In summary, geometrical constraints, which are present in the case of some of the inclusions measured in this study might account for higher apparent pressures of entrapment that will shift Raman peaks to larger artificial numbers. Despite efforts to select ideal inclusions to apply the methodology (e.g. isolated smooth spherical or elongated inclusion with a ratio <3:1, c.f. Mazzucchelli et al., 2018), some of the well-isolated inclusions were small, showing sharp edges and/or irregular shapes (e.g. Fig. 4.7a.i-b.i). Resolution of the laser beam was approx. 5 µm at depth. All the measurements were made on the centre of the grains but for small grains (<10 µm, e.g. Fig. 4.7a.i-b.i) such resolution could already shift Raman peaks to larger values due to the edge effect (c.f. Murri et al., 2018). Moreover, the pointy edges and irregular shapes most likely influence the Raman shifts due to the differential concentration of stresses (Whitney et al., 2000). When excluding

the larger values, QuiG differences between elastic and equilibrium barometry are slightly lower and show lower differences within 0.10-0.20 GPa (Fig. 4.7).

The pressure differences returned by the elastic and equilibrium geobarometers could nevertheless still point to small degrees of overstepping in the Isua samples. However, the consistency of the quantitative paths, the microstructural and petrographic observations, along with the qualitative constraints provided by the trace element data argue that the P-T trajectory obtained for 801-8C is a good proxy to the evolution of the ISB. In concluding this section, we note that a systematic study of QuiG barometry, careful chemical zoning, trace element thermometry using quartz and rutile can provide a powerful dataset to draw P-T-X-t trajectories.

4.4.2 Quantitative and qualitative P-T-X-D-t path determination using a multi-technique approach

Different possible P-T-X-t trajectories were modelled aiming at reproducing the compositional profiles of the syn-tectonic garnet in metapelite 801-8C (Fig. 4.8). Among them, a path reaching pressures up to 1.0 GPa was computed (case 2; Fig. 4.8b) to test the potential of higher pressures describe in the larger QuiG dataset. Modelling of garnet growth along this high-pressure path does not reflect the observed composition in the garnet (Fig. 4.8b.i). Hence, such high pressures are inconsistent with the measured chemical data and negate previously suggested higher-pressure conditions for the metamorphism of the ISB. The modelled profiles for case 3 (Fig. 4.8c) are also incompatible with the measured garnet profiles (Fig. 4.8c.i). In contrast, a trajectory with an initial isothermal burial followed by decrease in pressure and increase in temperatures (case 1a; Fig. 4.8a), referred here as the "best fit", reproduces reliably the topology of the chemical profiles, i.e., the compositions of the different syn-tectonic zones and the size of the porphyroblast (Fig. 4.8a.i). This trajectory describes a P-T-X-t evolution that sample 801-8C experienced during the syn-tectonic event M_1. However, attempts to acquire limits or restriction on the timescale from this trajectory

were inconclusive. Here, varying the duration of the metamorphism up to 90 m.y. did not significantly affect the compositional profiles (inset in Fig. 4.8a.i; Fig. APP-C4.2b-f). In particular, attempts to model the 20-50 m.y. hiatus proposed by Gauthiez-Putallaz et al. (2020) did not modify the compositional profiles either (Fig. APP-C4.2g-h). Therefore, neither the metamorphic timescales (t) nor the possible hiatus in garnet growth can be resolved with the modelling approach presented here. Previous studies have readily demonstrated that diffusive relaxation modelled in Theria_G does not substantially affect large garnet grains and is thus more relevant for the interpretation of smaller ones (George and Gaidies, 2017). In addition, the modelled temperature range in this study is well below 600 °C, i.e., a temperature range in which diffusion in garnet becomes sluggish (Borinski et al., 2012, Müller et al. 2013). Our data is consistent with this conclusion. Additionally, information on the deformation (D) for metapelite 801-8C can also be added to the P-T-X evolution already described. The spiral-like nature, the asymmetrical pressure shadows and the CPO of the quartz grains in the matrix (c.f. Zuo et al., 2021b) show that the rock underwent shearing during the garnet growth.

The data acquired for the other garnets qualitatively point to a similar evolution to that described for metapelite 801-8C. For instance, isopleth intersections of representative compositions of zone 1, 2, and 3 of the spiral-like garnet in metapelite 714-5E (Fig. 4.3b) suggest an increase in pressure from c. 0.22 to 0.7 GPa with a small change in temperature from c. 535 to 560 °C (Fig. 4.7b). The systematic intersections of the isopleths from the different garnet zones that represent M_1 confirms the interpretations of a near isothermal burial provided in Chapter 2, and suggest the initial near isothermal burial might have started from lower pressures. This grain also shows spiral-like inclusion trails that change in direction with the composition of the grain (Fig. 4.3b), showing shearing affected the sample during the main phase of metamorphism.

A consistent P-T path throughout the belt is not only supported by the thermodynamic data but also by the trace element data presented here. Trace element content in garnet has been commonly used to track the garnet forming minerals (e.g. Hickmott et al. 1987; Buick et al., 2006; Konrad-Schmolke et al., 2008; Clarke et al., 2013). This, along with P-T estimates and determination of garnet forming reactions recovered from phase equilibria diagrams provide a powerful tool to understand qualitatively and quantitatively the P-T evolution of a rock (e.g. Konrad-Schmolke et al., 2008).

All garnets in the Ca-rich metapelites and the amphibolite (731-2A, 729-1b, 714-5A and 725-4A) show the consistent presence of a positive Eu anomaly (Fig. 4.9). This enrichment in Eu is typically interpreted as a monitor of plagioclase consumption to produce garnet (e.g., Buick et al., 2006; Clarke et al., 2013; Gauthiez-Putallaz et al., 2020). The lack of plagioclase in most of the garnet cores suggests this phase to be one of the reactants producing the porphyroblasts. Interpreted reactions also point to the consumption of plagioclase to produce the garnets in both Ca-rich and meta-mafic rocks (c.f. Chapter 3). Thus, the Eu anomaly is in perfect agreement with previous interpretations. Detailed inspection of changes in the plagioclase mode in a P-T space provide more information about the shape of the P-T path. Plagioclase volume isopleths were obtained using the thermodynamic modelling presented in Chapter 2 (Fig. 4.10). For samples 731-2A (Fig. 4.10a), 714-5A (Fig. 4.10b), and 729-1B (Fig. 4.10c), plagioclase volume isopleths show topologies that are typically inclined $\geq 30°$ (Fig. 4.10a-c). Consequently, the rocks needed to evolve along a rather steep path for the plagioclase to react-out (e.g. arrows in Fig. 4.10a). Therefore, the combined microstructural, thermodynamic and chemical data of the garnets in Ca-rich metapelites and mafic rocks equally suggest a near isothermal prograde path for rocks from the north to the south of the belt.
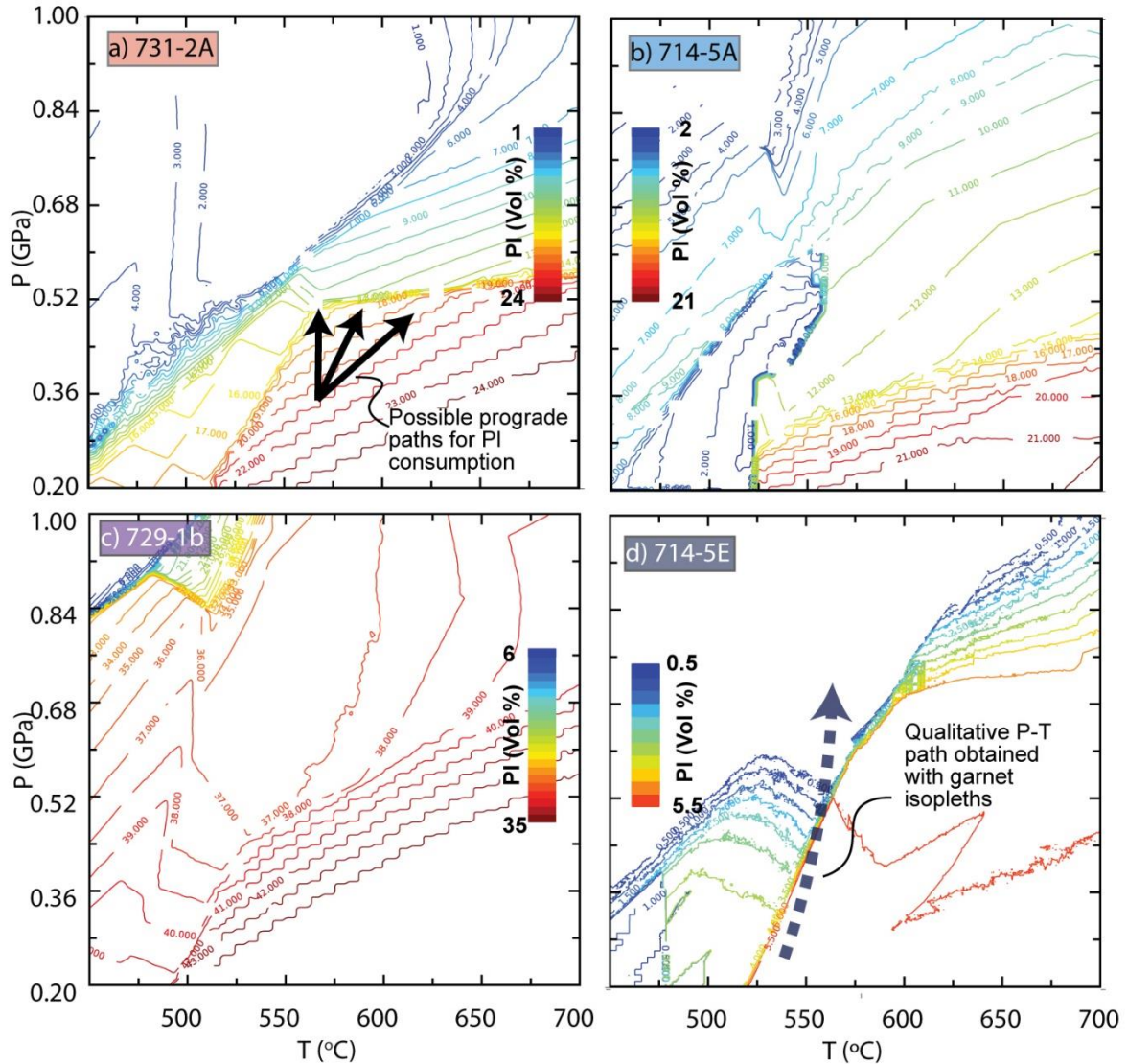
Figure 4.10 (a)-(d) Plagioclase volume isopleths for different samples were trace element contents were measured. (d) Also shows the qualitative P-T path obtained with garnet compositional isopleths from the different syn-tectonic zones (c.f. Fig. 4.7b).

A similar analysis can be made for metapelite 714-5E. Plagioclase is absent from the matrix of the rock, but a few relics are found in the garnet cores, suggesting a breakdown reaction of plagioclase as the prograde metamorphism evolved. Plagioclase reacting to produce garnet has also been argued for based on positive Eu anomalies in garnets' annuli (Gauthiez-Putallaz et al., 2020) from rocks with almost the same mineralogy and composition as sample 714-5E. The near isothermal path inferred for this sample (Fig. 4.7b, 4.9d) agrees with plagioclase consumption, since plagioclase volume isopleths also show inclined topologies (Fig. 4.9d).

The qualitative, albeit multi-technique, analysis of samples 731-2A, 729-1b, 714-5A, 725-4A

and 714-5E suggests a near isothermal path for part of the evolution of these rocks. Notably,

they are spatially distributed in different parts of the belt (Fig. 4.1), covering the whole area

from the north to the south. Therefore, it is argued that the quantitative near isothermal path

followed by heating and decompression obtained with garnet in metapelite 801-8C (Fig. 4.8a;

4.11) provides a reliable approximation of the prograde path the ISB experienced during the

syn-metamorphic event M_1.
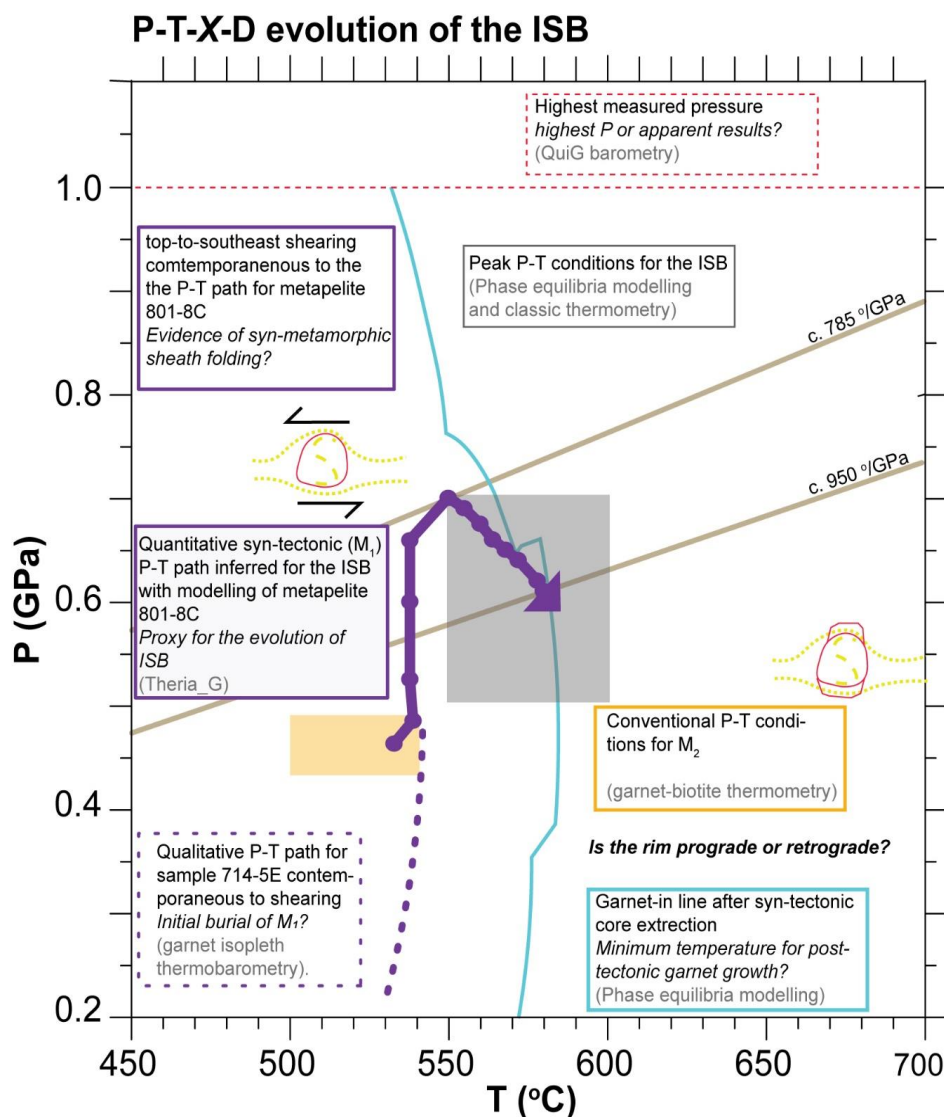
Figure 4.11 Summary of the P-T-*X*-D evolution obtained for the ISB. Outlined squares describe the quantitative constraints and observations (normal typography), interpretations (italics) and method used (grey). Colour of the outlined square corresponds to the constraint/observation, e.g. solid purple outlined square describes the solid P-T path.

The data and analysis presented here successfully reproduced the syn-tectonic evolution (M_1) of the ISB. However, at present, quantitative constraints on the evolution covering M_2, represented by the garnets overgrowths remain to be investigated in a future study (e.g. Fig. 4.11). The phase equilibria and isopleth thermometry presented for metapelite 801-8C are at odds with most of the calculations for the temperature of M_2. Garnet-biotite of garnet rim and matrix biotite typically returns <540 °C values (Boak and Dymek, 1982; Rollinson, 2002; Gauthiez-Putallaz et al., 2020; Chapter 2). However, the reactive composition of metapelite 801-8C after syn-tectonic garnet extraction (Fig. 4.11) suggest minimum temperatures of 550 °C. This might imply that the post-tectonic growth has similar or higher temperature conditions than M_1 and that it probably forms part of the same prograde event or that the reactive bulk composition of the large matrix does not reflect the reactive composition of the rims (Fig. 4.11). The lack of large-scale equilibrium during post-tectonic garnet growth is suggested both by the microstructures and isopleth thermobarometry. On the one hand, garnet microstructures suggest that the growth of the garnet rim was locally controlled by the phases in the matrix (Fig. 4.2, Chapter 3). On the other hand, only the almandine and grossular isopleths calculated for the inclusion-poor overgrowth composition after extraction of the syn-tectonic garnet intersect (Fig. 4.9b). The lack of equilibrium at a larger scale potentially explains why modelling with Theria_G was not successful for the late garnet overgrowth (Case 2; Fig. 4.d) and that previous calculations of <540 °C reflect the growth of the post-tectonic garnets (Fig. 4.11). More information for the garnet rims might clarify the apparent disagreement.

4.4.3 Comparison of the metamorphic evolution of the ISB with proposed tectonic models

The different tectonic scenarios proposed for the ISB predict distinct metamorphic signatures and evolutions. The quantitative and systematic study of the Isua rocks show that belt experienced nearly homogenous peak metamorphic conditions, with inferred peak pressures

of 0.7 GPa and peak temperatures of 550-600 °C (this Chapter and Chapter 2). Moreover, although no quantitative conclusions for the relative timing (t) were obtained, the P-T-*X*-D evolution (Fig. 4.11) of the rocks located in various parts from north to south support the interpretation of a common metamorphic history with analogous P-T-*X*-D trajectories across the belt. This interpretation is supported by the quantitative (Fig. 4.9) and qualitative (Fig. 4.7b, 4.10) data presented here. Consequently, while quantitative geodynamic modelling is beyond the scope of this thesis, such information can be at least qualitatively compared to the proposed tectonic models (Fig. 4.2).

The quantitative metamorphic evolution obtained here for the ISB (Fig. 4.11) agrees with the predicted clockwise prograde steep P-T path (Fig. 4.2a.i) for model A (Fig. 4.2a). However, the subducted accretionary prism scenario (Fig. 4.2a) argues that faults juxtaposed rock blocks with different metamorphic grade (Komiya et al., 1999; Arai et al., 2015). Such blocks should then have been subducted at different depths and thus most likely experienced at least slightly different P-T evolutions (Fig. 4.2ai) along with different peak conditions. Changes in metamorphic grade across the belt are not recorded (c.f. Chapter 2) and the P-T trajectories in different parts of the belt seem to be similar (e.g. Fig. 4.8a; 4.10d). Therefore, the metamorphic record of the ISB does not support Model A as presented by their authors (Komiya et al., 1999; Arai et al., 2015).

The hairpin-like evolution described for the ISB (Fig. 4.11) is not consistent with the paths with a shallower P-T evolution (Fig. 4.2a.i) expected for model B (Fig. 4.2b). Moreover, this model also invokes the presence of localized shear zones that accommodate rocks with different metamorphic grade (Nutman et al., 2013), and thus distinct P-T evolution (c.f. Fig. 4.2b). On the one hand, contrasting metamorphic grade and histories are not confidently reported within the belt (c.f. Chapter 2, this chapter). On the other hand, localized strain zones cannot be quantitively distinguished, because no strain concentration can be

distinguished in the proposed shear zones, and the strain is rather homogenous throughout the belt (c.f. Zuo et al., 2021b). Thus, the orogenic model for the ISB is also in dissonance with the structural and metamorphic record of the belt.

As previously discussed, it is not possible to distinguish the heat pipe scenario with the P-T evolution alone. The predicted P-T paths for model C are similar to model A and B depending on the depositional and burial rates (Fig. 4.2c.i). However, complementary lines of evidence can be used to test the viability of model C. This model assumes that no major tectonic breaks occur within the ISB and thus the rocks should have experienced similar P-T trajectories and peak conditions since they evolved together (Webb et al., 2020), which is supported by the metamorphic and structural data retrieved from the belt (Chapter 2, this chapter, Webb et al. 2020, Zuo et al. 2021). Furthermore, the full P-T-*X*-D (Fig. 4.11) information obtained in this work could also shed some light on the tectonic process. The syn-metamorphic top-to-southeast shear sense reported for sample 801-8C (Fig. 4.11) forms part of a larger dataset showing two shear sense directions (the other top-to-northwest) spread across the belt (Webb et al., 2020; Zuo et al. 2021). Such distribution has been interpreted as product of a sheath folding event that created the arc-like shape of the belt (Fig. 4.1) invoked in the heat-pipe model (Webb et al., 2020). Our data indicates that this deformation was contemporaneous to the hairpin-like path described here (Fig. 4.11), which is also expected for model C (Fig. 4.2c.i). Therefore, the data presented shows that a non-uniformitarian evolution for the supracrustal rocks of the ISB is plausible. However, there is no P-T data on the evolution of the TTGs (apart from what is presented in Chapter 5), which would be necessary to retrieve to understand the complete evolution of the Isua area. Additional information for the Archean geodynamic might be drawn from the T/P gradients the metamorphic evolution of the belt suggests. Peak pressure and peak temperature obtained in for the P-T-*X*-d path returned T/P gradients of c. 740°C/GPa and c. 950°C/GPa respectively

(Fig. 4.11). These gradients are within the values calculated for the Early Archean where non-uniformitarian geodynamics have been proposed. (Brown and Johnson, 2018).

P-T trajectories with similar "hairpin"-like topology have been described for other Archean terranes, such as the supracrustals rocks of the Barberton granitoid-greenstone belt (Cutts et al., 2014). Comparison with numerical models suggest rocks evolving in a vertical tectonics setting would show similar P-T paths, in the case of Barberton during the formation of dome-and-keel structures (François et al., 2014; Brown, 2015; Sizova et al., 2015). Notwithstanding, other authors argue that the same path describes a subduction-accretion process (Cutts et al., 2014, 2015). Then, although the comprehensive evaluation of the metamorphic record of the ISB favours model C, a subduction setting cannot be ruled out. Comparison with numerical models run for the specific characteristics of the ISB and a larger quantitative P-T-X-D-t dataset should improve our interpretations on the metamorphic evolution of the belt.

4.5. Conclusions

This study provides the first quantitative P-T-X-D-(t) path for the metamorphic evolution of the ISB. We followed a methodology using a multi-technique approach to quantitative and qualitative retrieve the prograde metamorphic evolution of different rocks across the ISB. Our results provide maximum pressures for the belt of 1.0 GPa that need to be evaluated un more detail. Moreover, the data presented shows that the ISB most likely experienced an initial near isothermal burial followed by heating and exhumation. This metamorphism was contemporaneous to deformation, showing shearing that might point out to the development of a large sheath fold in the ISB. The obtained P-T-X-D path, the field relationships and the metamorphic record of the ISB were compared to expected evolutions of the different tectonic scenarios proposed for the belt. The data favours the predictions of the heat-pipe model, but do not completely rule out a form of subduction process. A better characterization

of the P-T-*X*-D-t in the ISB could be made by making more systematic approach to the

methodologies used here (e.g. QuiG) combined with more tools.

Chapter 5. Geochronological constraints on the metamorphic evolution of the Isua supracrustal belt, West Greenland: Preliminary results

This chapter represents a manuscript draft centred on preliminary geochronology data of the Isua supracrustal belt. The draft contains sample descriptions, textural context of grains analysed and results, as well as preliminary interpretations. A final and robust data analysis and conclusive interpretations of the data will be accomplished after thesis submission. The plan for this chapter is for myself to be the first author of this publication with Thomas Müller, Sandra Piazolo, Dominik Sorger, and Ian Millar being co-authors. I was responsible for writing the original manuscript draft, figures, data analysis, sample preparation and conceptualization. Thomas Müller and Sandra Piazolo supervised and were involved in the conceptualization and review of the draft manuscript. Dominik Sorger contributed to the geochronological data for Sm-Nd garnet analysis, as well as titanite and rutile ages processed at UGoe after the end of my second research visit (Sept-Nov 2021). Additional geochronology data have been prepared and measured at the British Geological Survey by Ian Millar for which I wrote a small research proposal (NEIF 2247.0420, granted to Jason Harvey) and prepared mineral separates.

Abstract

Extensive geochronological data shows that the protoliths of the main components of the Isua supracrustal belt were emplaced and deposited from 3.8 to 3.6 Ga. However, the lack of accurate dating of the metamorphic history that affected the ISB and associated tonalites limits our understanding of the tectonometamorphic evolution of the belt. In this work, we present a new geochronological dataset using different geochronometers (Sm-Nd and Lu-Hf in garnet, and U-Pb in rutile and titanite) together with detailed microstructural and P-T analyses to provide new constraints on the timing of the different tectonometamorphic events the belt experienced.

Mafic enclaves within the c. 3.7 Ga tonalite adjacent to the ISB record 3.6-3.8 Ga local contact metamorphism at 650-675 °C and 0.40-0.60 GPa conditions confirming the previously suggested intrusion age of this tonalite at ~3.7 Ga. Additional information on the magmatic history is provided by a meta-granite that shows magmatic garnet crystallized at c. 3.55 Ga. Sm-Nd and Lu-Hf dating of metamorphic garnet within ISB supracrustals rocks show no evidence of a major syn-tectonic metamorphism (M_1) before 3.3 Ga, which disagrees with most of the previous interpretations mainly based on indirect structural relationships and depositional ages. Instead, M_1 might be c. 3.3 Ga or 2.7 Ga in age. New U-Pb data of post-tectonic titanite suggests that static, post-tectonic metamorphism (M_2) occurred during the Neoarchean (2584.9 ± 98.3 Ma), while late retrogression event(s) are most likely Paleoproterozoic (<2200 Ma) in age. Final considerations and suggestions for further work to help constrain the timing of the geological evolution of ISB and surroundings are provided.

5.1 Introduction

Obtaining the age of the metamorphism that a terrane experienced along with information of the pressure, temperature and deformational conditions during an event can shed light the general tectonic evolution (Brown, 1993) Since the discovery of the Eoarchean age associated with the tonalites of the Isua region (Black et al., 1971; Moorbath et al., 1972), a large number of studies have provided zircon-based U-Pb geochronological data to constrain the timing of the main geological events recorded in the evolution of the Isua supracrustal belt (ISB, Fig. 5.1a; see Nutman & Friend, 2009; Webb et al., 2020; see Zuo et al., 2021, for a more detail discussion). Only a handful of studies, however, have reported ages aimed to directly date metamorphic events. In general, two main episodes of metamorphism are suggested where M_1 and M_2 are early and late Archean, respectively (Fig. 5.1e). Indirect timing constraints for these events have algo been interpreted from cross-cutting relationships equally suggesting early and late Archean minimum and maximum ages (Fig. 5.1e; Nutman

et al., 2004, 2015; Nutman and Friend, 2009). Nevertheless, the exact timing of the metamorphism in the ISB and the number of events remain debated (c.f. Nutman et al. 2022; Ramírez-Salazar et al., 2022).

To establish a complete and robust metamorphic evolution of a terrane, P-T determination, making use of the geothermobarometry, is combined with dating of mineral(s) interpreted to be in equilibrium with the paragenesis of interest. Microstructural context of such minerals is used to establish mineral growth and its age relative to deformation events. Moreover, multiple P-T-X-D-t data can be retrieved from the so called petrochronometers, i.e., minerals which microstructural and chemical characteristics can be used to interpreted petrological processes and conditions of formation, and that additionally can be dated (Engi et al., 2017). Some commonly used petrochronometers are garnet (Baxter et al., 2017), titanite (Kohn, 2017), and rutile (Zack and Kooijman, 2017). In this chapter, we thus explore the potential of a multi-technique approach to unveil different aspects of their tectonometamorphic history in terranes with a complicated history using the example of the ISB.

Garnets, rutile and titanite are commonly used for geochronological studies (Baxter et al., 2017; Kohn, 2017; Zack and Kooijman, 2017) and occur in various rocks of the ISB (e.g. Blichert-Toft and Frei, 2001; Crowley et al. 2002, Crowley, 2003). Garnets are found across the supracrustal belt in various lithologies (e.g., Rollinson 2002; Chapters 2-4); rutile has been described in mafic samples (e.g., Arai et al., 2015) and even metapelites (Zuo et al., 2021b; Chapter 4); and titanite occurs in rocks within the tonalites (Crowley et al. 2002, Crowley, 2003). This diversity in mineralogy and location allows for a systematic study combining different geochronometers currently available in the rocks of the Isua area.
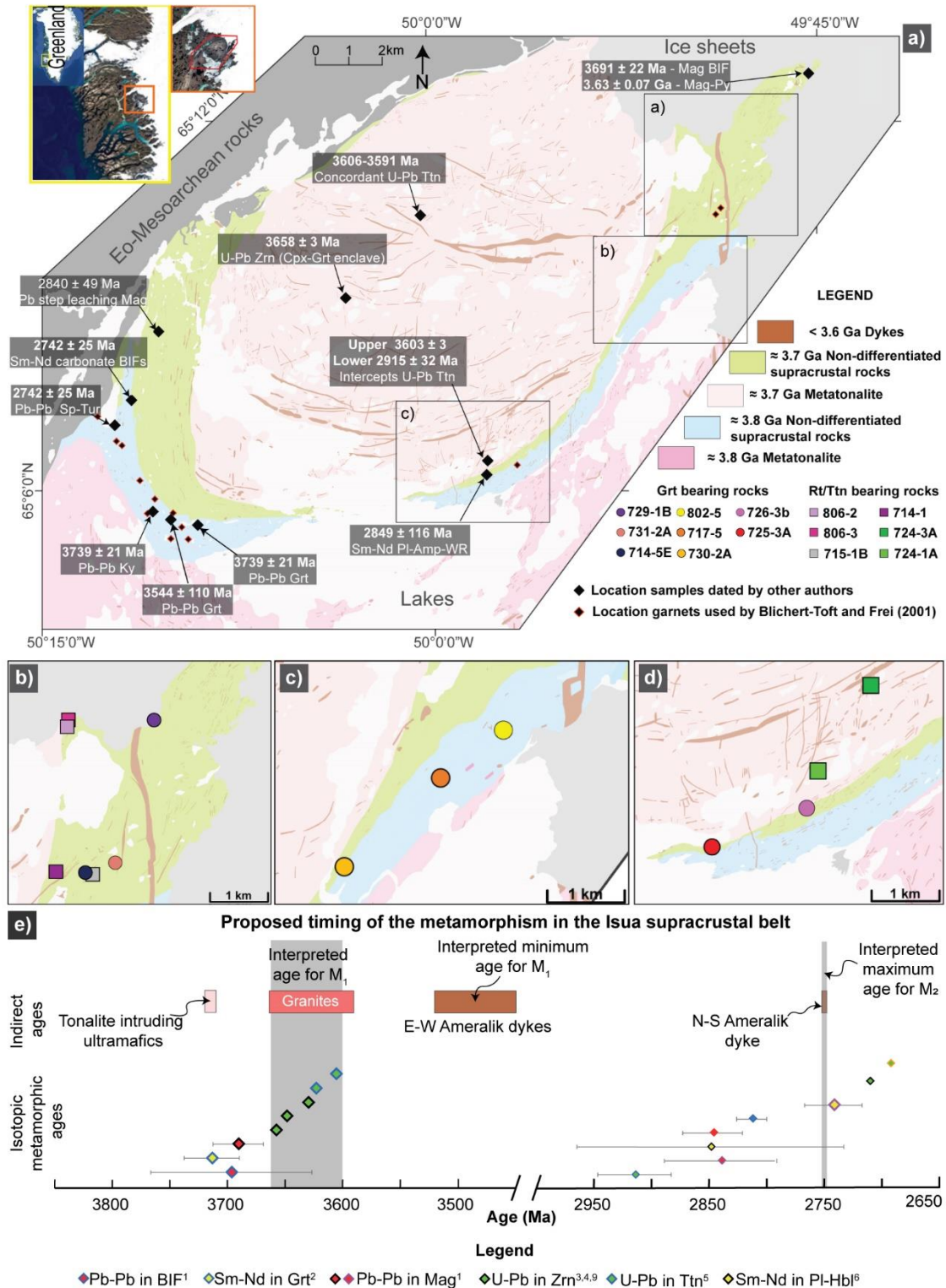
Figure 5.1 Geology and geochronological information previously reported for the ISB. (a) Map showing the geochronological data obtained within the ISB and the 3.7 Ga Tonalite (Modified from Zuo et al. 2021b with information of Nutman and Friend, 2009). (b)-(d) location of the samples reported in this study. (e) Graphical summary of the indirect and direct ages used to constraint the metamorphism of the ISB. Geochronological data from Nutman and Friend (2009). Metamorphic ages references: 1. Frei et al. (1999); 2. Blichert- Toft and Frei (2001); 3. Nutman et al. (2013); 4. Crowley (2003); 5. Crowley et al. (2002); 6. Gruau et al. (1996); 7. Rosing and Frei (1999); 8. Shimizu et al. (1990); 9 Nutman & Collerson (1991); 10 Friend and Nutman (2005).

The aim of this chapter is to present new, but preliminary geochronological data retrieved from garnet, rutile and titanite for which the microstructural and metamorphic context is established. Apart from rocks collected in the belt itself, this study also provides geochronological and, for the first time, geothermobarometric data for enclaves within the 3.7 Ga tonalite to allow for a more detailed comparison with rocks from within the belt. A discussion of the new data and its relationship to previously reported geochronology data is presented to provide further constraints on the timing of the events in the ISB.

5.2. Previous attempts to date metamorphism of the ISB

Existing constraints on the timing of metamorphism can be divided into two main groups, direct and indirect dating. Indirect constraints utilize crosscutting relationships such that the metamorphic event cannot be younger than the depositional age of the crosscutting rock unaffected by such an event. Direct dating involves dating of isotopic ages using whole rock chemistry, chemistry of minerals that grew and/or that have undergone chemical modification during metamorphism. Here, depending of the diffusive closure temperature of a system, growth versus cooling ages can be distinguished. Both methods have been used in the ISB (e.g., Fig. 5.1e; Shimizu et al., 1990; Nutman and Collerson, 1991; Gruau et al., 1996; Frei et al., 1999; Blichert-Toft and Frei, 2001; Crowley et al., 2002; Crowley, 2003; Friend and Nutman, 2005; Nutman et al., 2013) in order to constrain the timing of the proposed two major metamorphic events. In chapters 2 and 4, it is established that the first significant metamorphic event (M_1) is syn-tectonic and prograde at conditions of 550-600 °C and 0.6-0.7 GPa. Microstructural analysis (e.g., Fig. 2.6a 3.2a, 3.4, 4.3) shows that M_1 is synchronous with pervasive deformational features (e.g., foliation, lineation and folds) in the belt. There is a post tectonic event (referred here as M_2; <540 °C and <0.5 GPa; Chapter 2) mainly observed in the form of inclusion-poor garnet overgrowths (e.g. Boak and Dymek, 1982). The M_1 and M_2 terminology is adopted from Chapter 2 for simplicity and because most of the geochronological ages reported for Isua have been associated to these two well-documented,

regional events which effected the ISB rocks pervasively. However, it is worth noting that some authors have interpreted the presence of localized, additional metamorphic events which might be older than M_1. For example, early metamorphism has been interpreted in the inner cores of the garnet grains (c. 3675 Ma, Gauthiez-Putallaz et al., 2020) and an ultra-high pressure (UHP) metamorphic event has been interpreted in ultramafic rocks (>3700 Ma, Nutman et al., 2020).

5.2.1 Indirect dating: crosscutting relationships

Indirect constraints for Isua metamorphism stem from analysis of crosscutting (meta)igneous rocks and their interpreted crystallization ages. The meta-tonalites and supracrustal rocks are intruded by "meta"-granitic dykes that show different degrees of deformation and are reported as contemporaneous to the main foliation of the belt (Crowley et al., 2002; Crowley, 2003). The granites typically yield U-Pb zircon ages ranging from 3.66 to 3.60 Ga, suggesting this as being the maximum age range for the deformation and the accompanying metamorphism of the most pervasive, syntectonic M_1 event (Nutman and Friend, 2009; Fig. 5.1e). A minimum age for the syn-kinematic, M_1 event has been defined based on the intrusion of the Ameralik dykes which do not exhibit any signatures of the M_1 event (Fig. 5.1e). This group of E-W and N-S striking dykes show little to no deformation inside the 3.7 Ga tonalites, but their deformation increases towards the contact with the supracrustals. Nevertheless, dykes intrude the metamorphic rocks within the belt at high angles to the foliation. However, they show mineral alignment (White et al., 2000; Nutman et al., 2004). The resulting interpreted M_1 minimum age (Fig. 5.1e) is typically restricted by the interpreted 3.26-3.51 Ga crystallization age of the oldest E-W striking Ameralik dykes (White et al., 2000; Nutman et al., 2004). It is important to note that some of the dated zircons in the E-W striking dykes reveal concordant ages as young as c. 2.6 Ga, that are currently interpreted as recrystallization ages being the product of a late Neoarchean event (Nutman et al., 2004).

The Ameralik dykes have been suggested to also provide timing constraints for the second M_2 event (Fig. 5.1e). In its southern sector, the N-S trending dykes intrude the ISB at high angles and exhibit hornblende grains aligned with the general SE-plunging lineation of the adjacent ISB rocks as well scarcely aligned epidote and garnet, indicating an epidote amphibolite facies metamorphism overprinting the M_1 and/or the igneous fabrics of these dykes (Nutman, 1986, White et al., 2000). U-Pb discordant zircon ages of one of these dykes show values from 2800-2750 Ma interpreted as dyke crystallization age (Nutman et al, 2015). Consequently, these authors interpret this late M_2 lower amphibolite facies metamorphism, as the event that is recorded in the supracrustal rocks as static garnet overgrowths, to be younger than 2750 Ma (Fig. 5.1e). However, the age of the N-S dyke has also been recently associated by the same authors to M_1 (Nutman et al., 2022). Here, the authors pointed out that the lineations measured in the field and in thin section with the crystallographic axes of the quartz from different samples (Zuo et al. 2021b) are parallel with the directions of alignment of the minerals in the N-S Ameralik dykes. Such observation led Ramírez-Salazar al. (2022) to propose that all the SE-dipping lineations in the belt might have been produced in the same tectonometamorphic event. If true, this major event cannot be older than the interpreted Neoarchean age of the N-S dyke. Hence, these new observations and arguments open up the possibility that the main deformation event in Isua (M_1) might be much younger than what most authors generally agree on up to date.

5.2.2 Direct dating: isotopic ages in different systems
A handful of studies report direct metamorphic ages resulting in a considerably range of values. In general, they can be categorized into two groups (Fig. 5.1e): one showing Eoarchean ages and another Meso- to Neoarchean ages. So far, these two groups are typically interpreted to represent the two main (lower) amphibolite facies episodes M_1 and M_2, respectively (Fig. 5.1.e).

Concordant titanite U-Pb ages from a tonalitic gneiss and a doleritic dyke in the centre of the 3.7 Ga TTG yield values between 3606-3591 Ma. This age range has been associated with the syn-tectonic metamorphism M_1, observed within the ISB, although they might represent igneous ages (Crowley et al., 2002). Slightly discordant titanite grains from samples in the centre and southwestern margin of the 3.7 Ga TTG form a discordia fixed at 3603 ± 3 Ma with lower intercept at 2915 ± 32 Ma. Here, the lower interception is interpreted as late re-equilibration (Crowley et al. 2002), probably during M_2. Titanites extracted from foliated meta-tonalites south of the belt typically form discordias with lower intercepts at 2670-2600 Ma interpreted as metamorphic ages, and one fraction also shows upper intercepts at 3623.7 ± 8.5 Ma interpreted as an igneous intrusive age (Crowley, 2003). In the case of zircons collected from a metasedimentary gneiss within the 3.8 Ga meta-tonalite, the discordia intersects at c. 3550 and c 2660 Ma, both interpreted as metamorphic zircons, with the latter related to M_2 (Crowley, 2003). Additionally, some authors argue that concordant zircons represent early Archean M_1 metamorphic growth. Examples are: (i) zircon ages (3630.5 ± 1.3 Ma) from a garnet amphibolite and from a clinopyroxene-amphibole-quartz gneiss (3548.9 ± 1.5 Ma) which are both enclaves in the 3.8 Ga tonalite (Crowley, 2003); and (ii) zircons ages (3658 ± 3 Ma) from a garnet-clinopyroxene enclave in the 3.7 Ga tonalite (Nutman et al., 2013).

The Pb-Pb methodology has been applied to different geological materials of the ISB, albeit returning contrasting ages. For example, Pb-leaching of a kyanite from a quartzo-feldespathic mica-schist was dated as 2847 ± 26 Ma and was linked to the M_2 event (Frei et al., 2002). A similar result (2840 ± 48 Ma) was obtained from Pb-leaching of magnetite recovered from a BIF in the western section of the 3.7 Ga sequence (Frei et al., 1999). Magnetite separates were also recovered from a banded ironstone sequence in the northeastern part of the belt (Fig. 5.1a). The Pb-Pb isochrons calculated from these grains returned an age of 3691 ± 22

Ma. Magnetite-pyrite fractions from a mineralized vein cross-cutting this sequence yielded Pb-Pb values of 3.63 ± 0.07 Ga (Fig. 1). These two ages are identical within error, but they were interpreted as the age of the syn-metamorphism (M_1) and the emplacement of the vein, respectively (Frei et al., 1999). Eoarchean results were obtained using garnet (3739 ± 21 Ma) and sphalerite-tourmaline (3741 ± 40 Ma) Pb-Pb isochrons from post-deformational veins (Frei & Rosing, 2001) located in the southwestern part of the 3.8 Ga supracrustal sequence (Fig. 5.1). Comparable 3.7 Ga ages were also obtained with other isotopic systems in garnets, as summarized below.

Blichert-Toft and Frei (2001) made the first attempt to directly date the growth of Isua garnets using Sm-Nd and Lu-Hf isotopic systems. They collected 14 garnet-bearing samples from low-strain zones mainly located in the southwestern 3.8 Ga ISB sequence with a few of them from the eastern 3.7 Ga arm (red-outlined diamonds in Fig. 5.1a). Here, garnets overgrow the main amphibolite-metamorphic fabric or appear within replacement cross-cutting veins. Notably, these garnets do not show two distinct growth phases as most of the syn-kinematic garnets do. To justify the requirement of initial isotopic equilibrium, Blichert-Toft and Frei (2001) argued that these garnets grew from a fluid that was homogenous all across the belt. Using garnet separates and mixtures from all the samples, both the Lu-Hf (2813 ± 130 Ma) and the Sm-Nd (2818 ± 247 Ma) systems yielded almost identical ages. However, the authors noted the presence of some allanite and zircon inclusions, in agreement with allanite presence interpreted by LREE-enrichment in garnets from other samples. Hence, the robustness of the obtained ages is not clear. This led the authors to construct a Sm-Nd isochron with LREE-poor garnets only to avoid potential allanite contamination. The resulting isochron returned an age of 3714 ± 24 Ma. This age was interpreted to reflect the age of garnet growth and also to be the age of the most pervasive syn-metamorphic event M_1 in Isua (Blichert-Toft and Frei, 2001). Remarkably, this interpretation is in contrast with their

garnet descriptions suggesting post-tectonic growth. For comparison, the Sm-Nd analysis yields an almost identical age compared to the Pb-Pb value (3739 ± 21 Ma) obtained from garnets of similar veins (Frei and Rosing, 2001) and it is closer to the Pb-Pb garnet age (3544 ± 110 Ma) that Blichert-Toft and Frei (2001) reported in the same work. At the same time, they concluded the Mesoarchean ages were product of partial re-equilibration of the Lu-Hf system in zircon and the Sm-Nd system in allanite due to a metamorphic event at 2337 ± 222 Ma.

Other samples have also been dated with the Sm-Nd system. For example, a 2742 ± 25 Ma age obtained from a set of carbonate banded formations (Shimizu et al., 1990) and a 2849 ± 116 Ma from a plagioclase-amphibole-whole rock isochron (Gruau et al., 1996). Although most of the Meso-Neoarchean ages are typically interpreted as dating the post-tectonic metamorphism M_2, it is important to note that Gruau et al. (1996) argued that their calculated age reflects the timing formation of the main foliation and metamorphic minerals observed in the ISB (M_1). The authors based their conclusion on hornblende grains in the rocks being aligned with the general foliation. They also suggest that this is consistent with the foliated amphibolite facies assemblages (hornblende + plagioclase + quartz + garnet) overprinting the igneous assemblages that have been described in N-S <2.7 Ga trending Ameralik dykes in the south of the belt (Nutman, 1986).

5.3. Methodology

We selected 14 samples containing any of the targeted geochronometers, i.e., rutile, titanite and garnet for potential dating. Most of the samples were collected along the eastern arm of the ISB aiming to cover north to south and east to west transects (Fig. 5.1b-d). Moreover, a couple of enclaves within the 3.7 Ga tonalite (Fig. 5.1d) were also selected for geochronology and geothermobarometry in order to compare their timing and P-T conditions with the supracrustals within the belt. The distribution of the studied samples (Fig. 5.1b-d) aims to explore systematically ages distribution in the belt and associated areas.

5.3.1 Backscattered electron imaging

The field-emission scanning electron microscope (FE-SEM) LEO 1530 at the Georg-August-Universität Göttingen was used to obtain the backscattered electron (BSE) images of the rutile and titanite grains to assess their microstructural relationships and any chemical zoning. Working conditions were 15 kV and 20 nA current.

5.3.2 Mineral chemistry and geothermobarometry

Major mineral compositions were analysed to compute geothermobarometry data using the amphibole-plagioclase system. Measurements were done on a Jeol 8230 Electron Probe Micro Analyzer (EMPA) at the University of Leeds. Analyses were performed with 15kV accelerating voltage, 20 nA current, and a 5 µm defocused beam. Standards used for included Geo2 Almandine, Geo2 Diopside, Geo2 K-feldspar. For P-T calculations the geothermometer of Holland and Blundy (1994) and the geobarometer of Molina et al. (2015) were applied to the same amphibole-plagioclase that were in contact with each other showing textural equilibrium.

5.3.2 LA-ICP-MS U-Pb geochronology in rutile and titanite

All titanite and rutile U-Pb dating was done in-situ on polished thin sections to preserve microstructural relationships. The measurements were performed using a Resonetics Resolution M50 Laser ablation system (193 nm ArF) coupled to a Thermo Scientific Element 2 Inductively Coupled Mass Spectrometer (ICP-MS) at the Georg-August-Universität Göttingen. The laser conditions for rutile and titanite were 5 and 6 Hz repetition rate and a spot diameter of 50 and 33 µm, respectively. Ablation time was 17 s for all measurements. For data reduction and age calculation, we used Iolite 4 (Paton et al., 2010, 2011) with the VizualAge UComPbine (Petrus and Kamber, 2012) data reduction scheme without applying any common lead correction.

Fifteen to seventeen analyses of unknown samples were bracketed by three analyses of the primary reference material R-10 (1090 ± 5) (Luvizotto et al., 2009) or MKED1 (1521.02 ± 0.55 Ma) (Spandler et al., 2016) for rutile and titanite measurements, respectively. Among the

unknowns, we routinely analysed secondary reference materials. These were Sugluk-4 (1719 ± 14 Ma; Bracciali et al., 2013) and PCA-S207 (1865.0 ± 7.5 Ma; Bracciali et al., 2013) for rutile, and OLT-1 (1015±5 Ma; Sun et al., 2012) and Khan (522.2±2.2 Ma; Heaman, 2009) for titanite. Zircon 91500 (1065 Ma; (Wiedenbeck et al., 2004) was used for both rutile and titanite analysis.

5.3.3 Garnet geochronology: Separation, dissolution and analysis

For garnet separation, samples were hand-crushed and then sieved to obtain grain size fractions ranging from of 160-250 µm, 250-500 µm and 500-1000 µm. A Franz magnetic separator was used to remove quartz, feldspars, and micas and facilitate garnet identification. Following this, garnet fractions were handpicked trying to avoid visible inclusions. However, grains in some samples typically showed elongated dark inclusions (probably ilmenite or biotite) and were chosen due to lack of material. For meta-granite sample 726-3b, two fractions of different colour and size were separated (e.g., Fig. APP-D5.1a)

5.3.3.1 Sm-Nd (University of Göttingen - UGoe)

For Sm-Nd garnet preparation, a slightly modified methodology to that presented in (Anczkiewicz and Thirlwall, 2003; Hegner et al., 2010) was performed. After garnet picking, the grains were washed three times with ultrapure water and once with acetone. For the last wash, the samples were left in the ultrasonic bath for 10-15 min and then dried. Each garnet fraction was hand-crushed in a small agate mortar until a fine powder was obtained. The powders were carefully transferred to glass vials and then to 15 ml Teflon beakers to be weighed.

The garnets powders were leached with 1 ml of concentrated HNO_3 for 30 min at 140 °C. Then 4 ml of MQ water were added to the beaker to wash out the HNO_3. Both, the solution and the garnet powder were transferred to a centrifuge 50 ml tube and centrifuged for 15 min. After that, the solution was pipetted out and it was discarded. The sample was transferred back to the Teflon beaker and dried on the hot plate. Once the sample was dry, 3 ml of H_2SO_4

were added and the closed beaker was then left on the hot plate at 140 °C for 24 hours. The H$_2$SO$_4$ leachate was pipetted out and discarded. The garnet residue was washed five times with MQ water, discarding the water every time. The leached garnet and whole rock powders were decomposed for 48 hrs at 140 °C in a mixture of 1 or 0.5 HNO$_3$ and 3 or 1.5 ml of concentrated HF, respectively. The solution was evaporated at 120 °C and 5 ml of 6 M HCl were added. The beaker was put in the ultrasonic bath for 15 min and then transferred to the hot plate and left overnight. The solution was evaporated at 120 °C and the 6 M HCl step repeated. After evaporation, the samples were dissolved in 5 ml of 2.5 M HCl for column chemistry.

The light rare-earth-elements (LREE) were separated using glass columns with a bed of 5 ml AG50x8 (200–400 mesh) resin at the ultraclean laboratory, Department of Geochemistry and Isotope Geology, University of Göttingen. The secondary columns for Nd and Sm separation were packed with 2 ml LN-spec resin (100–150µm). Samples were spiked with the JLB-2 internal solution.

Measurements of the Sm and Nd isotope ratios were done with a ThermoFisher Scientific Neptune Plus MC-ICP-MS at the University of Göttingen following the methodology described in Hegner et al. (2020).

5.3.3.2 Lu-Hf and Sm-Nd isotope analysis of garnet (British Geological Survey - BGS)

Bulk rock samples (c. 50 mg) and separated garnet fractions (ranging from 3 to 50 mg) were weighed into pre-weighed Savillex beakers. Most garnet fractions were then leached in teflon-distilled 6M HCl overnight at 100 °C in order to remove phosphate inclusions, centrifuged, rinsed in milliQ water, dried and reweighed. One fraction each of samples 731-2A, 729-1B, 726-3b and 802-5 were processed without leaching to allow evaluation of the effects of the leaching procedure.

The dry garnet aliquots and bulk rock powders were spiked with mixed [176]Lu-[180]Hf and [149]Sm-[150]Nd tracer solutions. 2 ml of 16M HNO$_3$ and 6 ml of 29M HF were added, then the

Savillex beakers were left closed on a hotplate 48 hours at 170 °C, then evaporated to dryness. 1.5 ml of 16M HNO_3 were added to the samples to remove residual fluorides and evaporated to dryness. 5 ml of 8M HCl were added to the samples, and the beakers were left closed overnight at 110 °C.

Samples were re-dissolved in a solution of 1M HCl + 0.1M HF. Primary columns consisting of 2 ml of Eichrom AG50x8 cation exchange resin in 10 ml Biorad Poly-Prep columns were used to separate bulk high-field strength elements (HFSE: Ti, Hf, Zr), a fraction containing Sr, Ca and Rb, and a bulk rare-earth element (REE) fraction. Samples were loaded onto the columns in c. 1.5 ml of 1M HCl + 0.1M HF, and the HFSE were immediately eluted in 10 ml of 1M HCl + 0.1M HF. This fraction was evaporated to dryness in preparation for separation of Hf. Sr, Ca and Rb were eluted in 30 ml of 1.5M HCl and discarded. Finally, the REE were eluted in 10 ml of 6M HCl and evaporated to dryness in preparation for separation of Lu, Sm and Nd.

Hafnium separation followed a procedure adapted from Münker et al. (2001). HFSE concentrates from the primary columns were dissolved in c. 2 ml of 6M HCl and loaded onto 10 ml Biorad Poly-Prep columns packed with 1 ml of EICHROM LN-SPEC ion exchange resin. Matrix elements were eluted in 10-20 ml of 6M HCl, and 2 * 2 ml of milliQ water was then passed through the column to remove HCl from the columns prior to subsequent elution steps involving peroxide. The columns were then washed with several 10 ml column volumes of a solution containing citric acid, nitric acid and peroxide. In this medium, titanium citrate complexes show a distinctive bright orange colour, allowing Ti to be quantitatively removed from the column by repeated washing. Once all traces of Ti were removed from the columns, 5 ml of peroxide-free citric acid + nitric acid solution were eluted, again in order to avoid mixing of peroxide with HCl solutions. Zr was then washed from the columns using 50-80 ml of 6M HCl + 0.06M Hf. Finally, Hf was collected in 10 ml of 6M HCl + 0.2M HCl.

Lu, Sm and Nd were separated using 2 ml of EICHROM LN-SPEC ion exchange resin packed into 10 ml Biorad Poly-Prep columns. The bulk REE fraction was dissolved in 200 microlitres of 0.2M HCl and loaded onto the columns. La, Ce and Pr were eluted using a total of 14 ml of 0.2M HCl. Nd was collected in 3 ml of 0.3M HCl, then Sm in 4 ml of 0.6M HCl. The middle rare-earth elements were eluted in 50 ml of 2.5 M HCl, and finally Lu (+ some residual Yb) was collected in 10 ml of 6M HCl. Sm, Nd and Lu fractions were evaporated to dryness in preparation for mass spectrometry.

Lu fractions were dissolved in 1 ml of 2% HNO_3 and Hf fractions were dissolved in 1 ml of 2% HNO3 + 0.1M HF prior to analysis. Measurements of Lu and Hf and Sm and Nd rations were performed using a Thermo-Electron Neptune Plus mass spectrometer at the Geochronology and Tracers Facility of the British Geological Survey following methos stablished at the facilities and corrections and procedures described in Dubois et al. (1992), Nowell and Parrish (2001), Lapen et al. (2004) and, Isnard et al. (2005)

5.3.3.3 Lu-Hf and Sm-Nd isochrons

Garnet Lu-Hf and Sm-Nd isochron regressions and calculations of age were performed using the online software IsoplotR (Vermeesch, 2018) using a value of 6.524×10^{-12} yr^{-1} for the $\lambda^{147}Sm$ decay constant and a value of (Villa et al., 2020) 1.867×10^{-11} yr^{-1} $\lambda^{176}Lu$ decay constant (Söderlund et al., 2004). For isochrons with more than two points errors reported account for overdispersion and the value of the square root of the Mean Square of the Weighted Deviates (MSWD; Vermeesch, 2018).

5.4. Results

Samples in this study are divided into four groups based on the geochronometer, field relationships and location in the area. Such groups are referred to as: (1) mafic enclaves, (2) garnet bearing meta-granite, (3) rutile/titanite bearing mafic supracrustals, and (4) garnet bearing supracrustals. It is worth noting that the classification produces some overlap of samples with different characteristics. The grouping was nevertheless chosen for clarity. For

example, group 4 includes garnet bearing mafic rocks, Ca-rich metapelites and metapelites.

In the next sections, descriptions of field relationships, mineralogical and microstructural

characteristics of the different groups of rocks are provided.

5.4.1 Samples characterization: field and microstructural relationships
5.4.1.1 Mafic enclaves

Two mafic enclaves (724-1A, 724-3A) within the 3.7 Ga TTG located in the southeastern

zone of the intrusive (Fig. 5.1d) were selected for analysis. While sample 724-1A shows a

foliation and lineation (161/52, dip direction/angle) in the field, which is parallel to the

regional lineation (c.f. Webb et al, 2020), sample 724-3A is free of these structural features at

the outcrop scale. Both enclaves are intruded by or in contact with felsic dykes, however,

none of the lithologies show clear chilled margins. In thin section view, the rocks show a

strong foliation given by large hornblende grains and the mineral assemblage observed

consists of hornblende + plagioclase + biotite + epidote + titanite + K-feldspar + albite +

quartz + apatite + ilmenite with minor calcite and rare grains of allanite and zircon. Titanite is

a relatively abundant accessory mineral occurring both in the matrix (Fig. 5.2a) and as

inclusions in hornblende (Fig. 5.2b). It is typically euhedral and varies in size from c. 30 µm
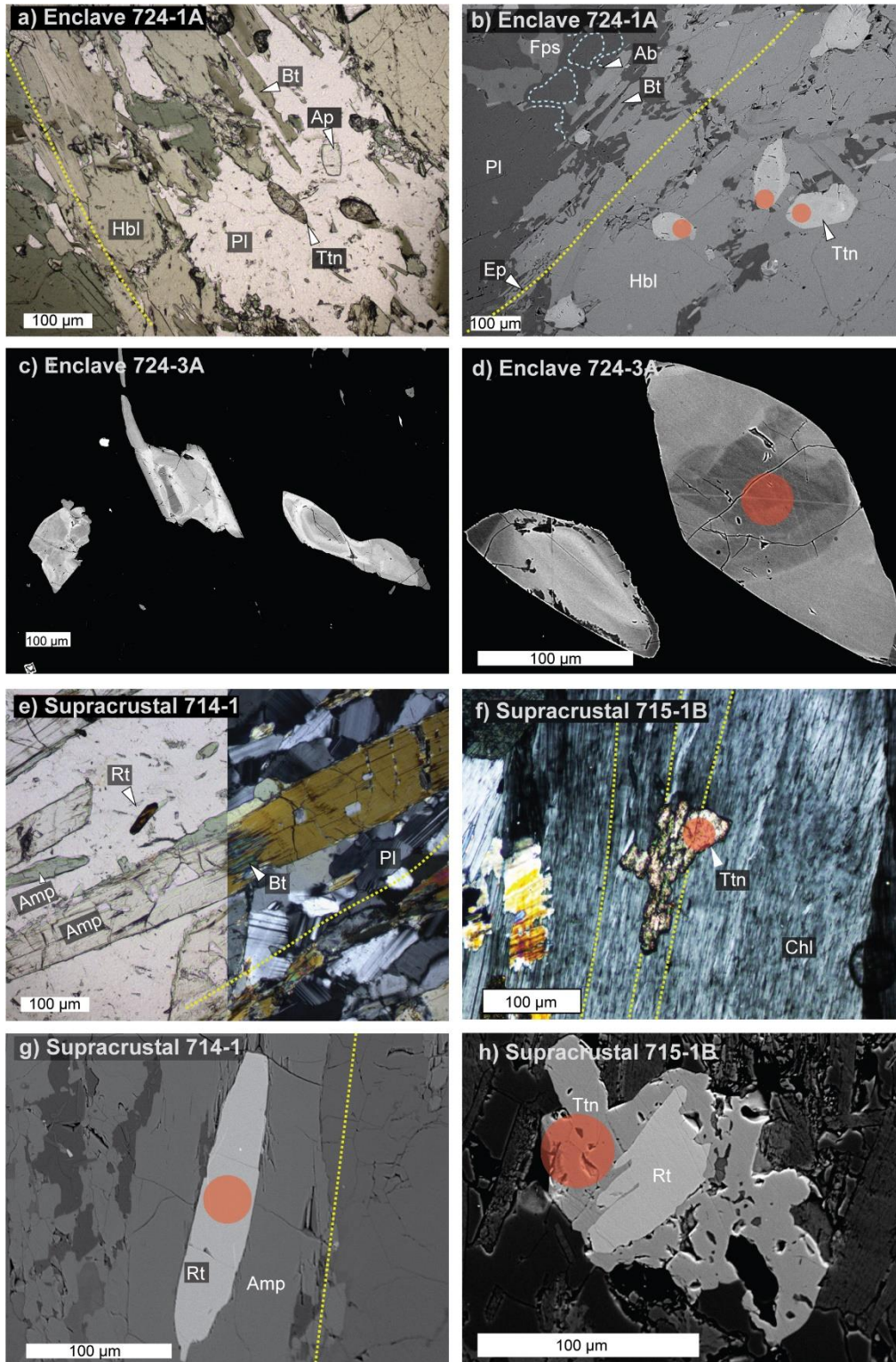
Figure 5.2 Images showing microstructural relationships and internal characteristics of rutiles and titanite in mafic enclaves (a-d) and mafic Rt/Ttn bearing supracrustals (e-h). (a) and (b) show euhedral titanite grains in the matrix following the foliation and as inclusions in hornblendes. (c) and (d) are SEM images revealing the zonation in titanite in enclave 724-3A; this zonation is also visible in the titanites of enclave 724-1A (b). (e) Typical elongated rutile grain aligned with the foliation of the Rt/Ttn bearing mafic supracrustals. (f) Titanite overgrowing the foliation in the mafic supracrustals. (g) rutile included in amphibole. (h) titanite overgrowing rutile, a common microstructural relationship in the Rt/Ttn bearing mafic supracrustals. Red spots show places were the grains were ablated for dating.

to c. 250 µm, with most of the grains showing sizes > 80 µm (Fig. 5.2a-d). The long axis of

the titanites normally follows the main foliation (e.g. Fig. 5.2a-b). BSE imaging reveals

concentric (Fig. 5.2c-d), irregular (Fig. 5.2c-d) and sector (Fig. 5.2c) zoning in the titanite

grains. Some of these changes in zoning have short wavelength (<30 µm; Fig. 5.2c-d). In

terms of microstructures, the enclaves show features that are not described in any of the other

samples. For example, they present a common association of K-feldspar + 2 plagioclases ±

biotite ± quartz, that commonly occurs as irregular intergrowths (Fig. 5.3a-c), where the K-

felspars typically appear as thin elongate finger-like microstructures (Fig. 5.3b-c). In this

association, two types of plagioclases are present: an almost pure albite and a plagioclase

enriched in anorthite component (from here on referred to as albite and plagioclase,

respectively). While albite almost only occurs when intergrowing with K-felspar and

plagioclase (Fig. 5.3a-d), the plagioclase constitutes the main feldspar phase in the rock and

even appears as inclusions within the hornblende. Reaction fronts between hornblende and

plagioclase also appear as thin films of albite and biotite (Fig. 5.3d). Epidote displays

symplectitic rims of epidote + quartz, that are commonly associated with the K-feldspars

intergrowths (e.g. Fig. 5.3e-f). In sample 724-1A, a zone of the rock poorer in hornblende, is

where K-felspar is the most abundant (Fig. 5.4)

5.4.1. Garnet bearing meta-granite

Only one sample (726-3b) is part of this "group". It is a granitic dyke intruding a mafic unit

in the southern part of the 3.7 Ga sequence and it is located close (<100 m) to the 3.7 Ga

tonalitic body (Fig. 5.1d). The meta-granite presents a weak foliation that is parallel to the

foliation of country rock. It is a SiO_2 (78.05 wt. %) and Al_2O_3 (15.62 wt. %) -rich granite

with low contents of CaO (2.01 wt. %) and Na_2O (2.44 wt. %) and almost no K_2O (0.02 wt.

%) and has a mol. $Al2O3/(Na2O+K2O+CaO) \approx 2$. All of these chemical characteristics are

often associated with S-type granites (e.g. Clemens, 2003). This Al-rich composition is
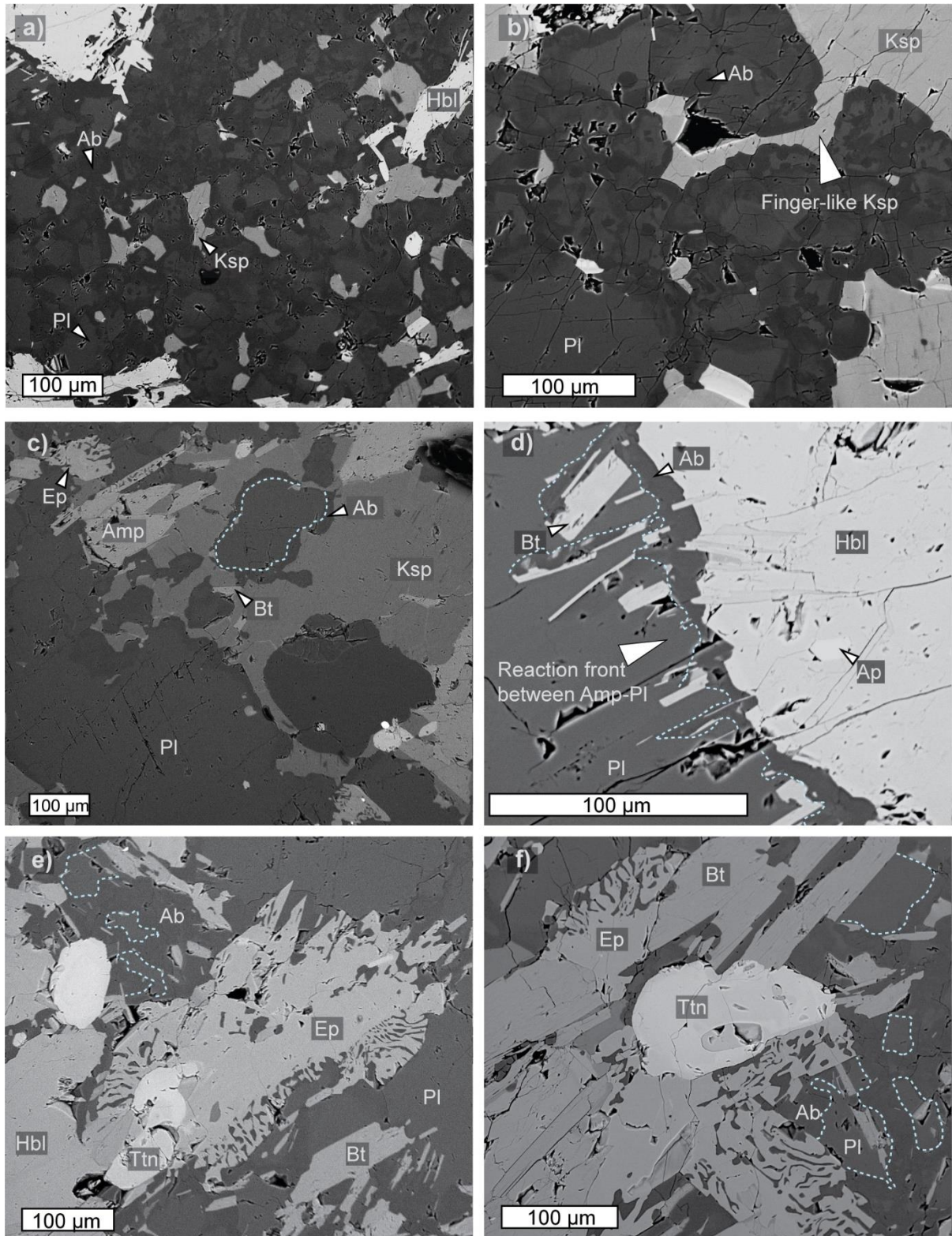
Figure 5.3 SEM images of melt microstructures in enclave 724-3A (a)-(c) irregular intergrowths of albite-Feldspar-plagioclase and some biotite. (d) Reaction rim of albite-biotite on hornblende. (e)-(f) symplectitic quartz-epidote intergrowths on epidote, the images also show that they are commonly associated to zones where the melt microstructures appear.
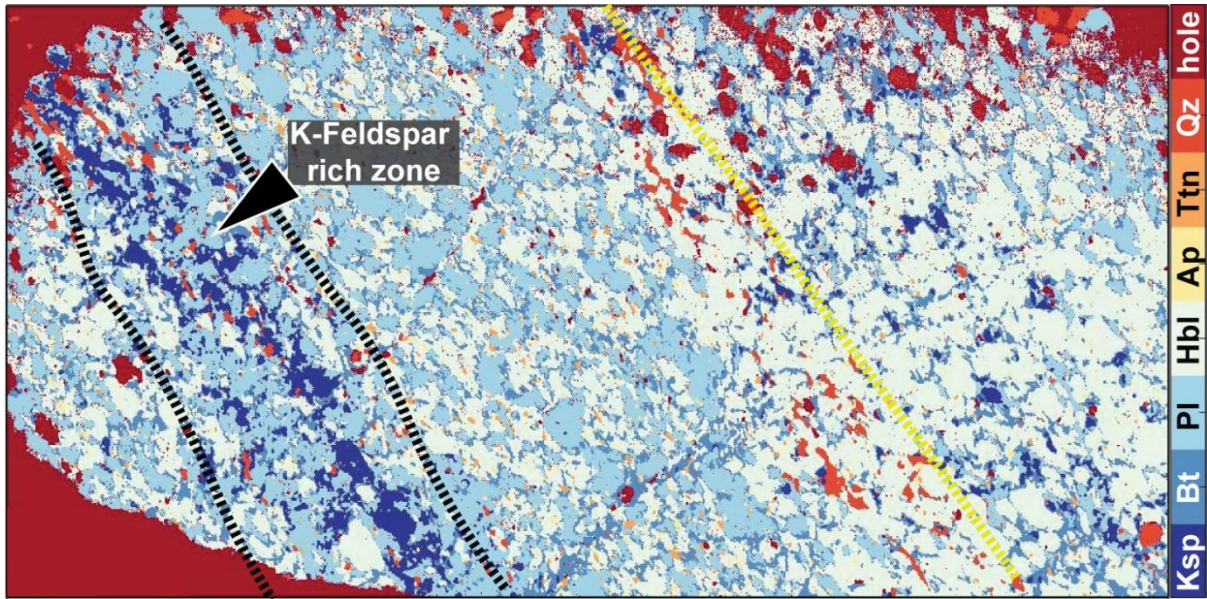
Figure 5.4 Phase map of an overview of the thin section of sample 724-1A.

reflected in the mineral assemblage comprising quartz + plagioclase + garnet + sillimanite + kyanite + staurolite with rare relics of muscovite associated to kyanite (Fig. 5.5a). Moreover, tourmaline locally appears close to the contact with the country rock. Kyanite grains are typically elongated and aligned with the foliation. As typical for kyanite, grains exhibit clear fractures perpendicular to its longest axis (Fig. 5.5a). At the same time, sillimanite occurs as prismatic (Fig. 5.5b) and fibrolitic grains (Fig. 5a) that generally follow the foliation. Some prismatic sillimanites wrap around garnets (Fig. 5a) and a few fibrolite grains grow on the edges of plagioclase (Fig. 5.5c-d). Staurolite grains display irregular borders (Fig. 5.5c). Garnets in this sample are generally different from the rest of the garnets described for the supracrustals. The grains are subhedral, nearly equant and almost inclusion-free (Fig. 5.5b, e-h). The few inclusions visible in the porphyroblasts are mainly quartz with minor small inclusions of calcite that are associated to fractures and secondary fluid inclusions. Garnets present concentric zoning for all endmembers (e.g. Fig. 5.5e, g), albeit the grossular component displays an oscillatory zoning close to the rim and some radiant zoning associated to fractures is also described for the Ca-endmember (Fig. 5.5e). The cores of the grains have
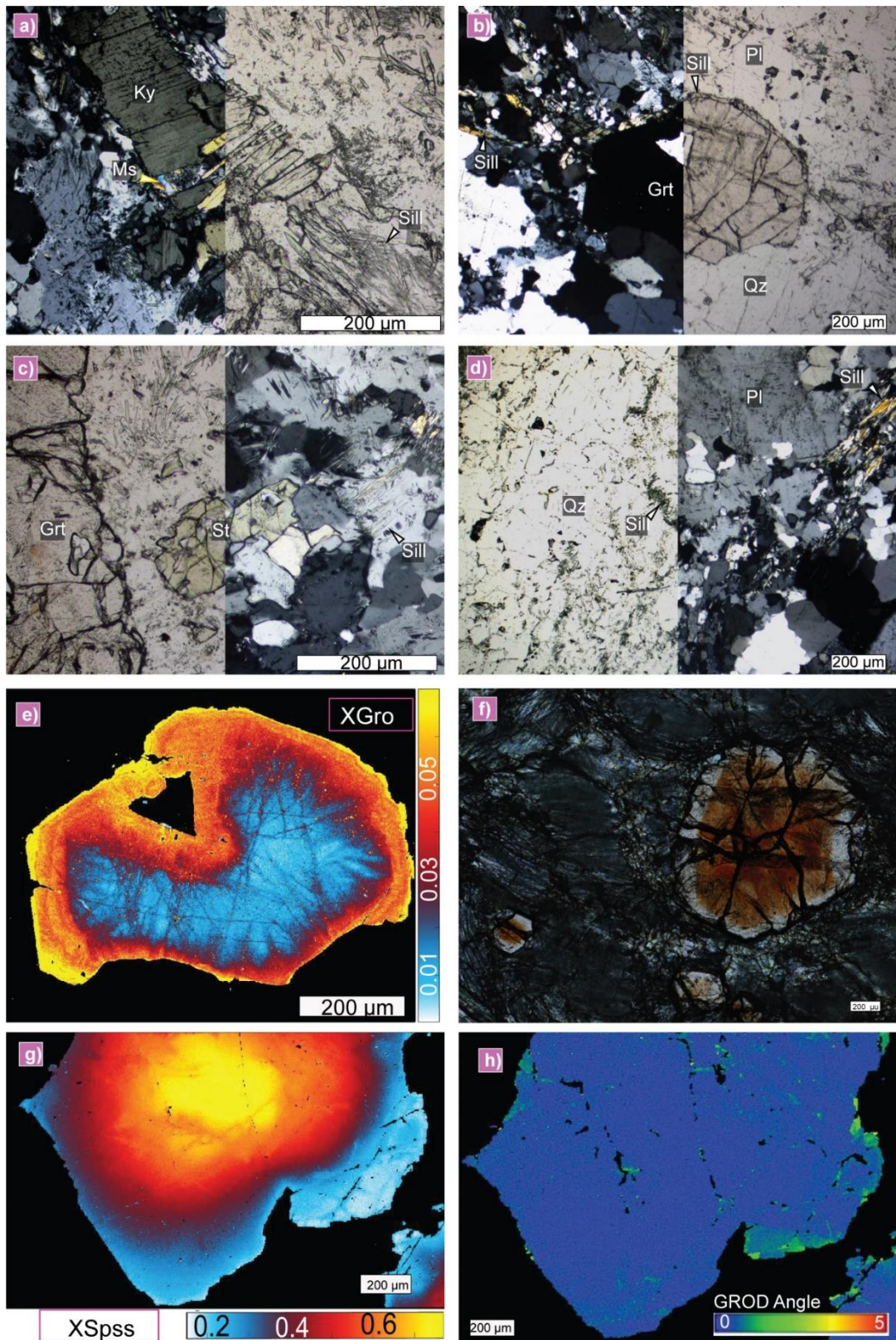
Figure 5.5 Microphotographs of meta-granite 726-3b. (a) Kyanite with relics of muscovite and associated fibrolitic sillimanite. (b) garnet with prismatic sillimanite apparently wrapping around the grain. (c) anhedral staurolite. (d) Fibrolitic sillimanite growing on the edges of plagioclase (centre of the figure) and weakly foliated prismatic sillimanite (left of the image). (e) Grossular compositional mapping of garnet in figure (b). (f) Thick section image of garnet showing a dark-coloured core. (g) X_{Spss} quantitative map and (h) GROD map of the same grain

a reddish colour, which is more obvious in thick section (Fig. 5.5f) and they are associated to a decrease in spessartine. No clear microstructural change is seen for the cores and rims of the garnets in this sample. Moreover, no significant changes in crystallographic orientation are revealed (Fig 5.5h) by Electron Backscatter Diffraction analysis (EBSD; for details of technique the reader is referred to Section 3.3.6).

5.4.1.3 Rutile/titanite bearing mafic supracrustals

Four rutile/titanite bearing mafic rocks (806-2, 806-3, 714-1, 715-1B) were selected for dating. They are located in the northeastern section of the belt (Fig.5.1b) and apart from sample 715-1B, the rest of the samples are close to the contact with the 3.7 Ga TTG (Fig. 5.1a). These rocks are part of the typical volcanosedimentary sequences of the belt and show a strong foliation and SE-dipping lineation in concordance with the rest of the units. Their main mineral assemblage consists of amphibole + plagioclase + rutile ± chlorite ± epidote ± titanite. Some samples display two types of amphiboles (e.g., Fig. 5.2e) and their optical properties suggest they are of actinolitic and tremolitic compositions. Rocks 714-1 and 806-2 exhibit localized chloritization (Fig. 5.2f). In sample 806-3, however, most of the rock show presence of late chlorite and carbonates as well as many pseudomorphs after amphiboles. Amphibolite 715-1B presents a chlorite-rich band with no clear cross-cutting relation with the aligned amphiboles; the foliation marked by the chlorite (Fig. 25.f) is parallel to that of the amphiboles. All these rocks present rutile grains that are typically small (<100 µm long) and occur both, in the matrix (Fig. 5.2e), where they are aligned with the foliation, and as inclusions in the amphiboles (e.g. Fig. 5.2g). Moreover, in sample 715-1b, post-kinematic titanite occurs in the chlorite-rich zone of the sample and appears as single irregular grains that overgrowth the foliation (Fig. 5.2f) or as irregular small rims on rutile (Fig. 5.2h).

5.4.1.4 Garnet bearing supracrustals

A detailed description for most of the garnet-bearing samples has already been given in Chapters 2 and 3. Here, a summary focused on the garnet microstructures and inclusions is

provided for the context of the dated grains. This group is comprised of samples of different garnet bearing lithologies: two meta-felsic rocks (717-5, 802-5), two Ca-rich metapelites (730-2A, 729-1B), one metapelite (714-5E) and two amphibolites (725-3A and 731-2A). Samples 717-5, 802-5 and 730-2A (Fig. 5.1c) were collected in the 3.8 Ga part of the supracrustal sequence, while the rest were collected from the 3.7 Ga section (Fig. 5.1b-d). All rocks show a strong foliation and lineation dipping towards the SE. Phase equilibria modelling applied to these samples returned peak conditions of 550-600 °C and 0.5-0.7 GPa (Chapter 2).

Ca-rich metapelites bear garnets with relatively high proportion of inclusions (41-49%; i.e. Type I garnets) aligned sub-parallel to the foliation creating inclusion patterns of type C (Fig. 5.6i.iii). They exhibit a concentric and patchy zoning with the latter being mainly observed along the boundaries with the inclusions (Fig. 3.6d,f). Patchy zoning in these grains is often coupled with changes in crystallographic orientation (Fig. 3.8e). Quartz constitutes the main inclusion in these grains, with calcite, ilmenite, biotite occurring as minor inclusions (Fig. 5.6c-d) and rare appearance of epidote, chlorite, and muscovite. Post-tectonic inclusion-poor overgrowths in these garnets is minimal.

Garnets in the meta-felsic samples are among the most skeletal grains, showing inclusion proportions from 48-63% (Type I garnet in Chapter 3). The inclusions form arc-like patterns that converge towards the pressure shadows and continue towards the external foliations (pattern A, Fig. 5.6i.i). Inclusions are dominated by quartz, but biotite and muscovite and minor inclusions of calcite, ilmenite and apatite also occur (Fig. 5.6a-b); rare inclusions of epidote, allanite and zircon were also found in some grains. The garnets display patchy zoning coupled with changes in crystallographic orientation (Fig. 3.8a-b) interpreted as consequence of growth controlled by local compositions (Chapter 3). Garnets in sample 717-5 do not exhibit the usual inclusion-poor overgrowths (Fig. 3.6c), but the overgrowths appear
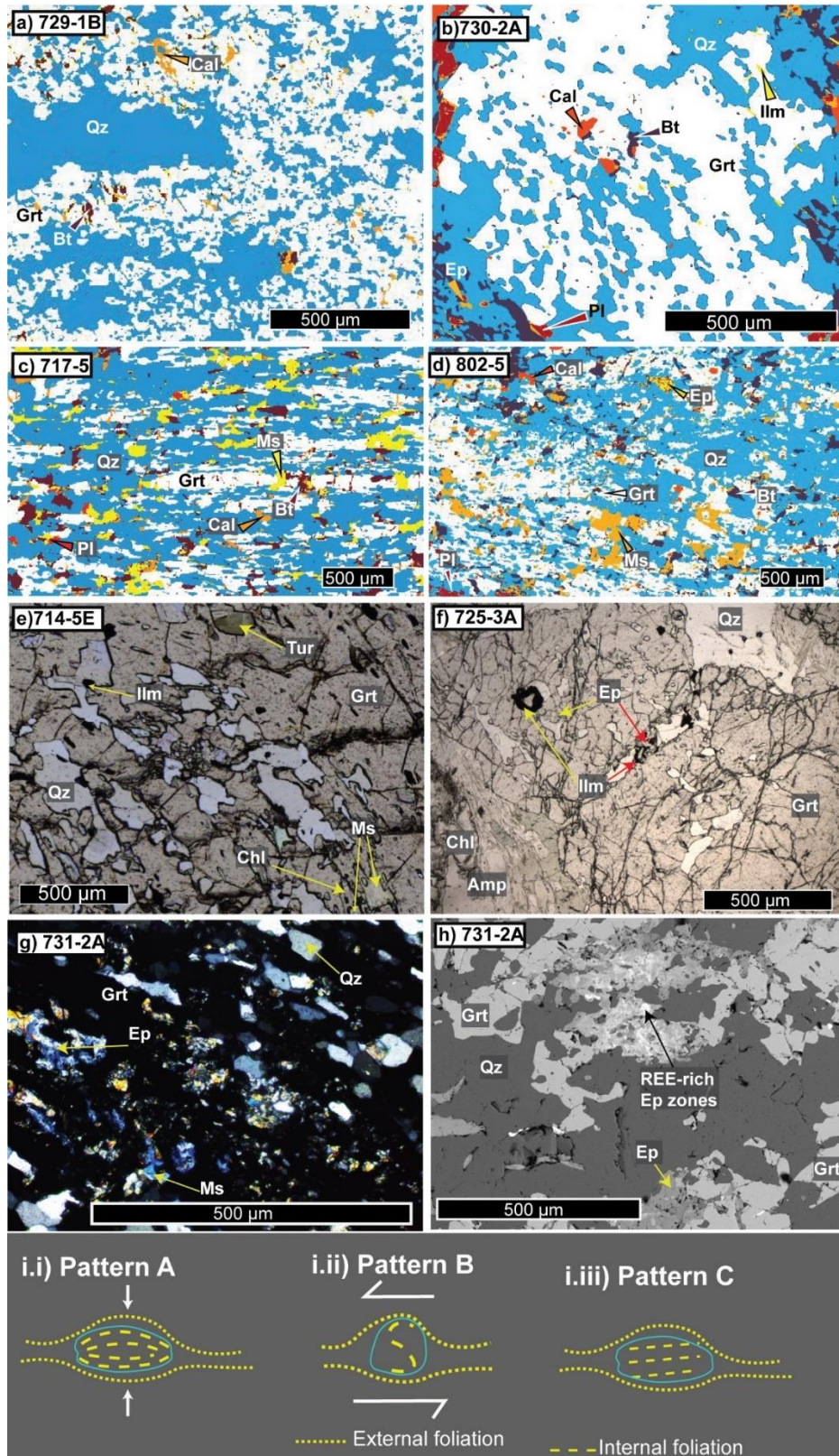
Figure 5.6 Images showing inclusions and internal microstructures of the dated garnets in the garnet-bearing supracrustals. Phase maps of garnets from (a) 729-1B and (b) 730-2A Ca-rich metapelites and from (c) 802-5 and (d) 717-5 meta-felsic rocks. (e) Petrographic photo of garnet in metapelite 714-5E. (f) Petrographic photo of garnet in amphibolite 725-3A. (g) Petrographic and (h) SEM image of garnets in epidote-amphibolite 731-2A. Schematic representation of (i.i) Pattern A, (i.ii) Pattern B and (i.iii) Pattern C of garnet internal foliations

as faceted garnets in sample 802-5 (Fig. 3.6a).

Garnets in the metapelite sample 714-5E are typically large (>1 cm) with relatively low content of inclusions (c. 28%, i.e. Type II garnets) that arrange in a spiral-like internal foliation (Type B, Fig. 5.6i.ii). They present concentric zoning with up to four compositional zones that are coupled to changes in the observed orientation of inclusions and the inclusion-poor overgrowths (e.g. Fig. 3.8f). Apart from quartz, the inclusion assemblage consists of intergrowths of chloritoid and muscovite, ilmenite, and a few tourmaline grains (Fig. 5.6e). The garnet amphibolites also contain Type II garnets with inclusions proportions of 24-31%, forming inclusion trails with patterns A (731-2A) and C (725-3A). The grains present the typical inclusion-rich cores and inclusion-poor overgrowths and show concentric zoning (Fig. 3.9c-d) altered in some zones by late fractures (Fig.3.9d). Quartz is again the dominant inclusion, although both samples also contain ilmenite and epidote (Fig. 5.6f-h). In garnets from sample 725-3A, late epidote grows in late fractures (3.6f) and in 731-2A. SEM inspection reveals irregular cores in some epidote grains that have relative high contents of REE based on their bright BSE grey colour and qualitative SEM data (Fig. 3.6h). Calcite and rare muscovite (Fig. 3.6g) are also found as inclusions in garnets from sample 731-2A.

5.4.2 Mineral chemistry and geothermobarometry
Here, we focus on the mafic enclaves for geothermobarometry and garnet compositions of the meta-granite as the metamorphic conditions and mineral compositional data of the other samples have already been covered in Chapters 2-4.

5.4.2.1 Mafic enclaves
In the mafic enclave sample 724-1A hornblende-plagioclase pairs were analysed to apply the hornblende-plagioclase thermobarometer (Holland and Blundy, 1994; Molina et al., 2015). Plagioclase occurring as inclusions and within the matrix in direct contact with amphiboles were analysed. Both groups of plagioclase yield negligible contents of orthoclase ($X_{Or} < 0.1$,
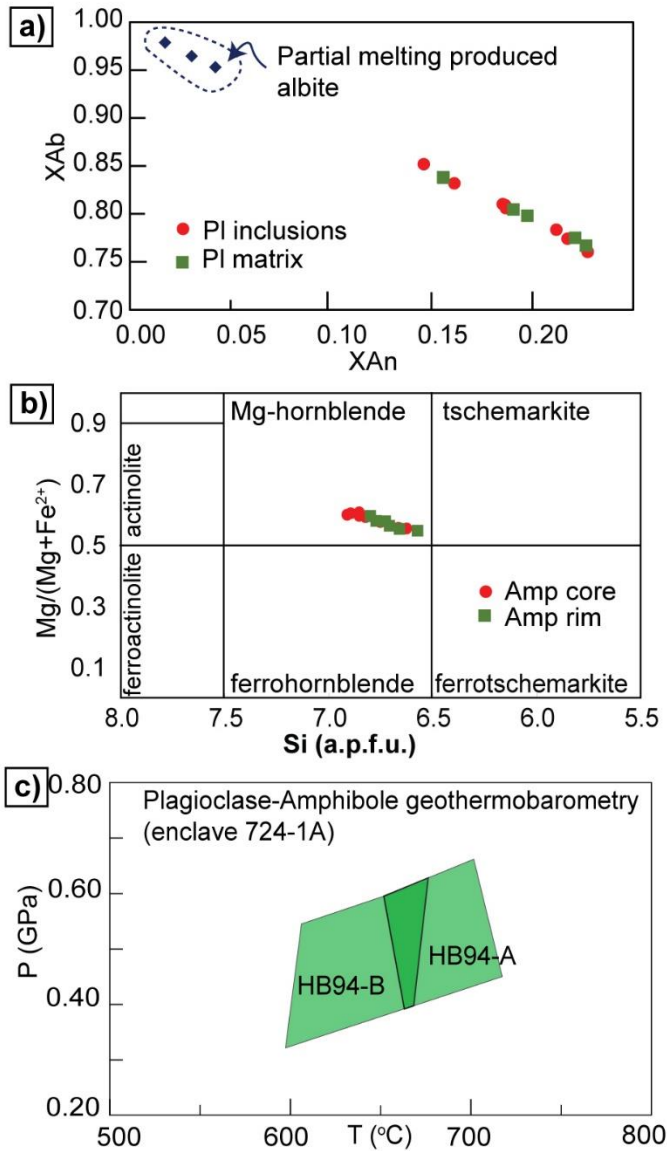
Figure 5.7 Composition of the (a)plagioclase and (b) amphiboles used for the (c) geothermobarometry of the enclave 724-1A. For the hornblende-plagioclase geothermobarometry (c) the dark green field represents the interpreted peak conditions.

Table D1) and their anorthite content varies from $X_{An} = 0.15$-0.23 (Table D1, Fig. 5.7a). Inclusion and matrix plagioclase compositions largely overlap, showing no significant variations in compositions between the two groups (Fig. 5.7a). Cores and rims of the analysed amphibole grains equally display similar compositions (Table D2, Fig. 5.7b). Because of this similarity in composition among amphiboles and plagioclases of different microstructural domains, P-T calculations for core and rim pairs reveal no clear distinction. Therefore, results are presented together. Calibration curves A and B of the Holland and Blundy (1994) geothermometer were plotted together with curves obtained by the Molina et al., (2015) geobarometer (Fig. 5.7c). The interception of calibration A with the barometer returned a P-T range from

650-725 °C and 0.40-0.65 GPa (Fig. 5.6c), while the intersection with calibration B ranges from 600-675 °C and ≈0.30-0.60 GPa (Fig. 5.6c). Both fields overlap at 650-675 °C and 0.40-0.60 GPa (Fig. 5.7c), which is considered the best estimate for the peak conditions of this sample. No data was obtained for enclave 724-3A. In addition to the plagioclase measurements, three grains of the albite and three grains of K-felspars were analysed to have

quantitative data of the intergrowths that only appear in the enclaves (Table 1). The albite

grains form a distinct compositional group compared to the other plagioclase grains (Fig.

5.7a), with contents of albite $> X_{Ab} = 0.95$ and the K-felspars are almost free of the albitic

and anorthitic components (Table D1).

5.4.2.2 Meta-granite

Composition of the garnets in meta-granite 726-3b were also obtained. They show a very

distinct composition to the grains reported in all the supracrustals (Fig. APP-D5.1b). This is

especially evident in the spessartine content that reaches X_{Spss} values of up to 0.70 in the core

of the largest grains (Fig. 5.5h, APP-D5.1b)

5.4.3 U-Pb spatially resolved titanite and rutile geochronology

5.4.3.1 Geochronology of the mafic enclaves: in-situ analysis of titanite

In-situ dating was performed on titanite grains of the amphibolite enclaves (724-1A and 724-

3A) in the ca. 3.7 Ga tonalite (cf. Fig. 5.2a-d– examples of titanites). Grains chosen were

those large enough to fit a laser spot. Thus, titanites with concentric (Fig. 5.2c-d), irregular

(Fig. 5.2c-d) and sector (Fig. 5.2c) zoning were chosen. All the grains are interpreted to have

grown during the main metamorphism of the sample (650-675 °C and 0.40-0.60 GPa; Fig.

5.7c). Laser spot for the analyses of the titanites was 33 µm but some of the zoning the

titanites display have wavelengths of <30 µm (Fig. 5.2c-d), thus measurements probably

represent a mixture of some of the zones.

For sample 724-3a, 19 titanite grains were selected. Grains yield similar $^{207}Pb/^{206}Pb$ ratios at

varying $^{238}U/^{206}Pb$ ratios, creating a horizontal array in the resulting concordia plot (Fig.

5.8a). One concordant $^{207}Pb/^{206}Pb$ age returned a value of 3800.7 ± 6.67 Ma, other three

slightly concordant $^{207}Pb/^{206}Pb$ ages (1.8-4.1 % of discordia) have similar ages of $3664.99 \pm$

4.01 Ma, 3635.44 ± 3.41 Ma, and 3646.66 ± 7.04 Ma, with a weighted mean age of 3635.31

±3.94 Ma. For sample 724-1A 64, individual grains were dated and most of them cluster at

0.3-0.4 $^{207}Pb/^{206}Pb$ ratios and 1-1.4 $^{238}U/^{206}Pb$ in the concordia plot (Fig. 5.8b). Of those

grains, 18 reveal a discordance between -1 and 1 % resulting in $^{207}Pb/^{206}Pb$ ages ranging from 3795-3568 Ma with a weighted mean age of 3680.5 ± 23.14 Ma.
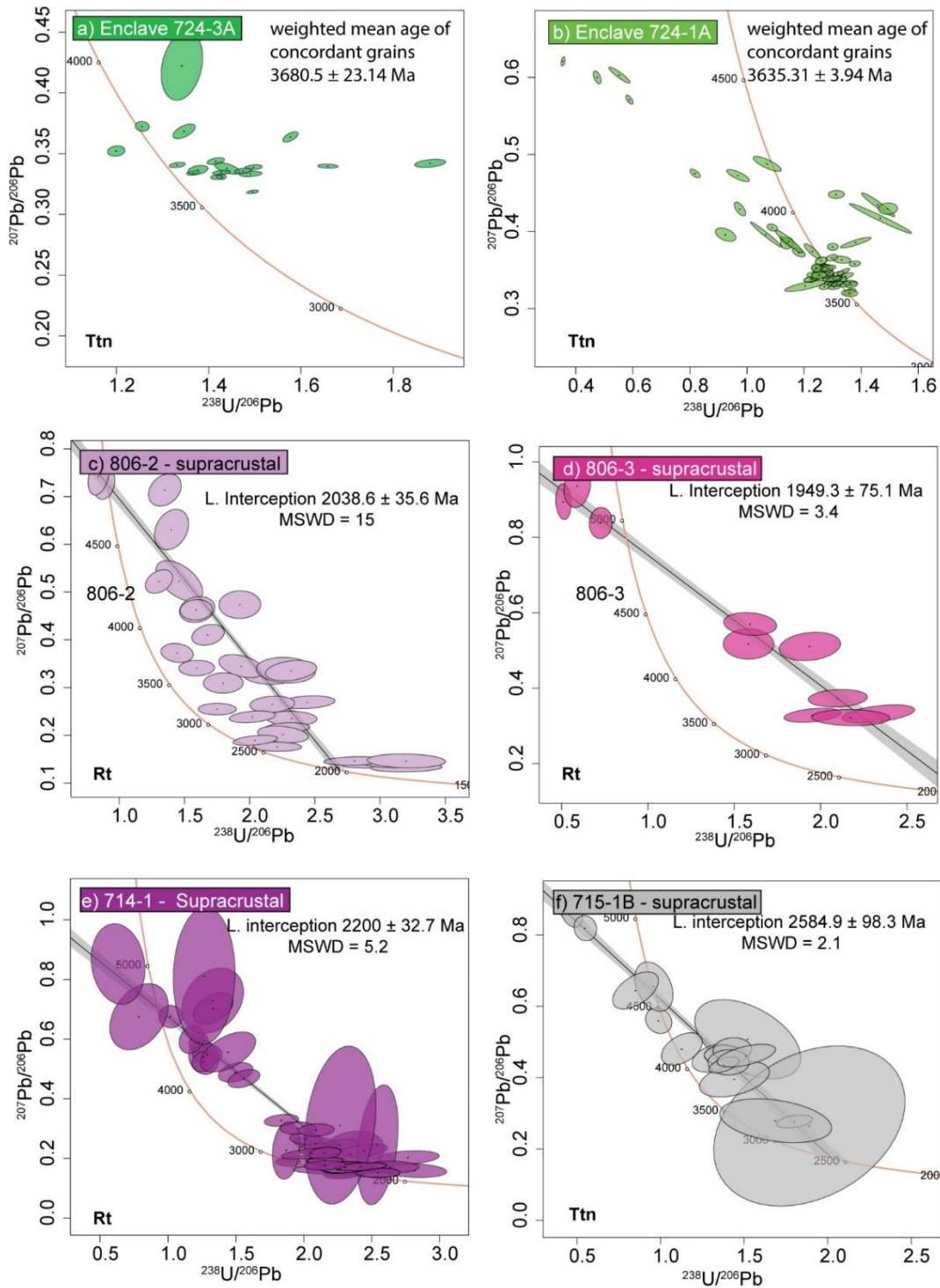
Figure 5.8 U-Pb rutile and titanite concordia diagrams for the enclaves (a) 724-1A and (b) 724-3A and the (c)-(f) rutile/titanite bearing supracrustals

5.4.3.1 Geochronology of the mafic supracrustals: In situ analysis of rutile and titanite

Thin section in-situ dating of foliation parallel, aligned rutiles (Fig. 5.2e,g) and rutiles

included in amphiboles in samples 806-2, 806-3 and 714-1 generally returned discordant U-

Pb ages (Fig. 5.8c-e), with contrasting values compared to the titanite data obtained in the

enclaves. Each sample form isochrons that intercept the concordia at similar Neoarchean

values: 2038.6 ± 35.6 Ma (for 806-2, Fig. 5.8c), 1949.3 ± 75.1 Ma (for 806-3, Fig. 5.8d) and

2200 ± 32.7 Ma (for 714-1, Fig. 5.8e). The youngest interception age is from the most altered

samples (806-3), but it overlaps within error with the close-by sample 806-2. Three rutiles in

sample 714-1 show slightly concordant $^{207}Pb/^{206}Pb$ ages (2.6-3.3 % discordance) of 2735.9 ±

65.4 Ma, 2377 ± 102 Ma, and 2461 ± 62.6.

For the amphibolite 715-1b, rutile U concentrations were found to be below detection levels.

Thus, no ages were obtained from those grains. However, 17 titanite grains overgrowing

rutile (5.2h) or overgrowing the foliation (Fig. 5.2f) were ablated. These titanite grains

typically show inclusions (e.g. 5.2h), thus some of the material dated contained impurities of

quartz and chlorite. The grains are discordant and returned $^{207}Pb/^{206}Pb$ ratio values up to ca.

0.8 (Fig. 5.8g). All the grains form an isochron with lower interception at 2584.9 ± 106.9 Ma

(Fig. 5.8g).

5.4.4 Garnet Sm-Nd and Lu-Hf geochronology

The obtained Sm- and Lu-Hf ages in the different garnet-bearing samples display dissimilar

values (Table 3, Table 4). The oldest ages were obtained in fraction 1 of the meta-granite

726-3b, which is interpreted to represent the dark red, Mn-rich garnet cores (Fig. 5.9a; APP-

D5.1). A Sm-Nd isochron obtained with four measurements returned an age of 3554.1 ± 49.3

Ma with a low MSWD (0.019, Fig. 5.9a). A slightly younger age was calculated for the Lu-

Hf system (3533.4 ± 71.1, Fig. 5.10a) excluding a slightly off value. The lighter coloured

garnet fraction of the meta-granite, interpreted to represent late magmatic growth, returned an

almost identical Lu-Hf value (3524.4 ± 74.8 Ma), but a relatively younger Sm-Nd age

(3427.5 ± 81.9 Ma).
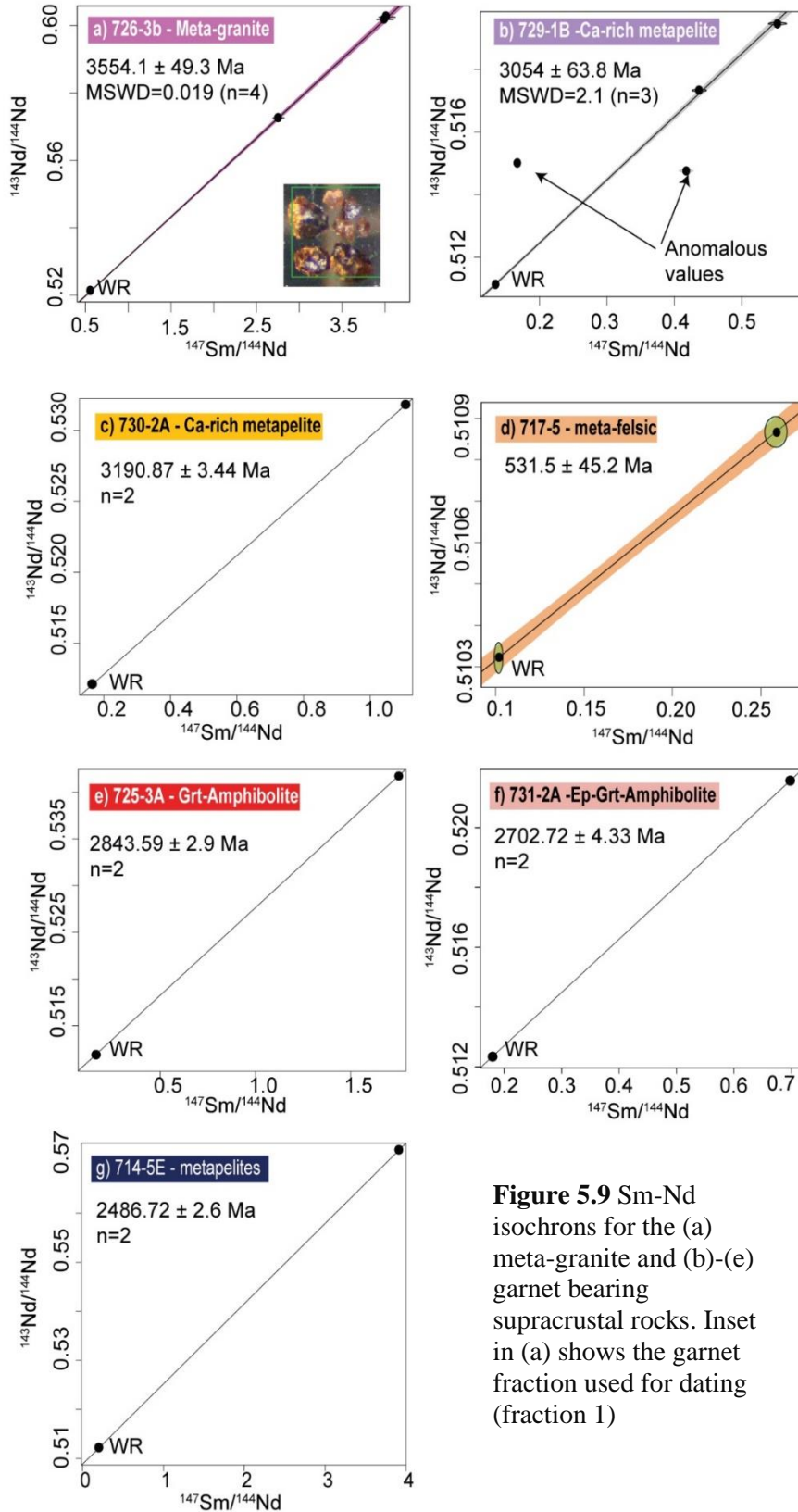
Figure 5.9 Sm-Nd isochrons for the (a) meta-granite and (b)-(e) garnet bearing supracrustal rocks. Inset in (a) shows the garnet fraction used for dating (fraction 1)

Sm-Nd and Lu-Hf ages in the supracrustal rocks are not as consistent within a single sample as for the garnets of the meta-granite. The Ca-rich metapelites (730-2A and 729-1B) with inclusion pattern C (Fig. 5.6i.iii) returned the oldest ages within the supracrustal group. The geochronology of sample 729-1B (Fig. 5.1b) reveals Sm-Nd and Lu-Hf values of 3054.5 ± 63.8 (Fig. 5.9b) and 3376 ± 52 (Fig. 5.10b), respectively with low MSWD (≤2.1). Measurements with odd values were excluded from the isochrones as these values might suggest non-systematic contamination by inclusions such as calcite and ilmenite (Fig. 5.6a-b). In contrast, calculated isochrons for the Ca-rich metapelite 730-2A (Fig. 5.1b) yield a Lu-Hf age of 2920.2 ± 33 (Fig. 5.10c) and a Sm-Nd age of 3190.87 ± 3.44 Ma (Fig 5.9c). Note that garnets from sample 730-2A are slightly poorer in inclusions compared to those from sample 729-1B (49% vs 41 %).

Garnets in the meta-felsic samples show inclusion patterns A (Fig. 5.6i.i), are very skeletal (Fig. 5.6c-d) and show a patchy zoning a high variability in crystallographic orientations (c.f. Fig. 3.8a-b). For both, samples 802-5 (2793.8 ± 628.6; Fig. 5.10d) and 717-5 (2825.8 ± 56.4 Ma; Fig. 5.10e), the Lu-Hf isochron provided near Neoarchean values. However, the Sm-Nd calculations returned no satisfactory results for 802-5 and values obtained for 717-5 are considerably low (531.5 ± 45.2 Ma; Fig. 5.9d).

Garnets from the amphibolite samples contain epidote and, in sample 731-2A, also high-REE minerals (Fig. 5.6f-h). Garnets in sample 731-2A show a clear inclusion pattern A (Fig. 5.6i.i), while the pattern in 725-3A garnets seems to be the type D, but it is not clear. The analysed garnets separated from the amphibolites revealed Meso-Neoarchean ages (Table 3, 4). For sample 725-3A (Fig. 5.1d), only Sm-Nd isotope ratio were measured, obtaining an age of 2843.59 ± 3.3 Ma (Fig. 5.9f). However, for amphibolite sample 731-2A, both isotope systems were applied, returning similar values (Sm-Nd = 2689.60 ± 36 Ma, Fig. 4.9f and Lu-Hf= 2702.72 ± 4.33 Ma, Fig. 4.10f).
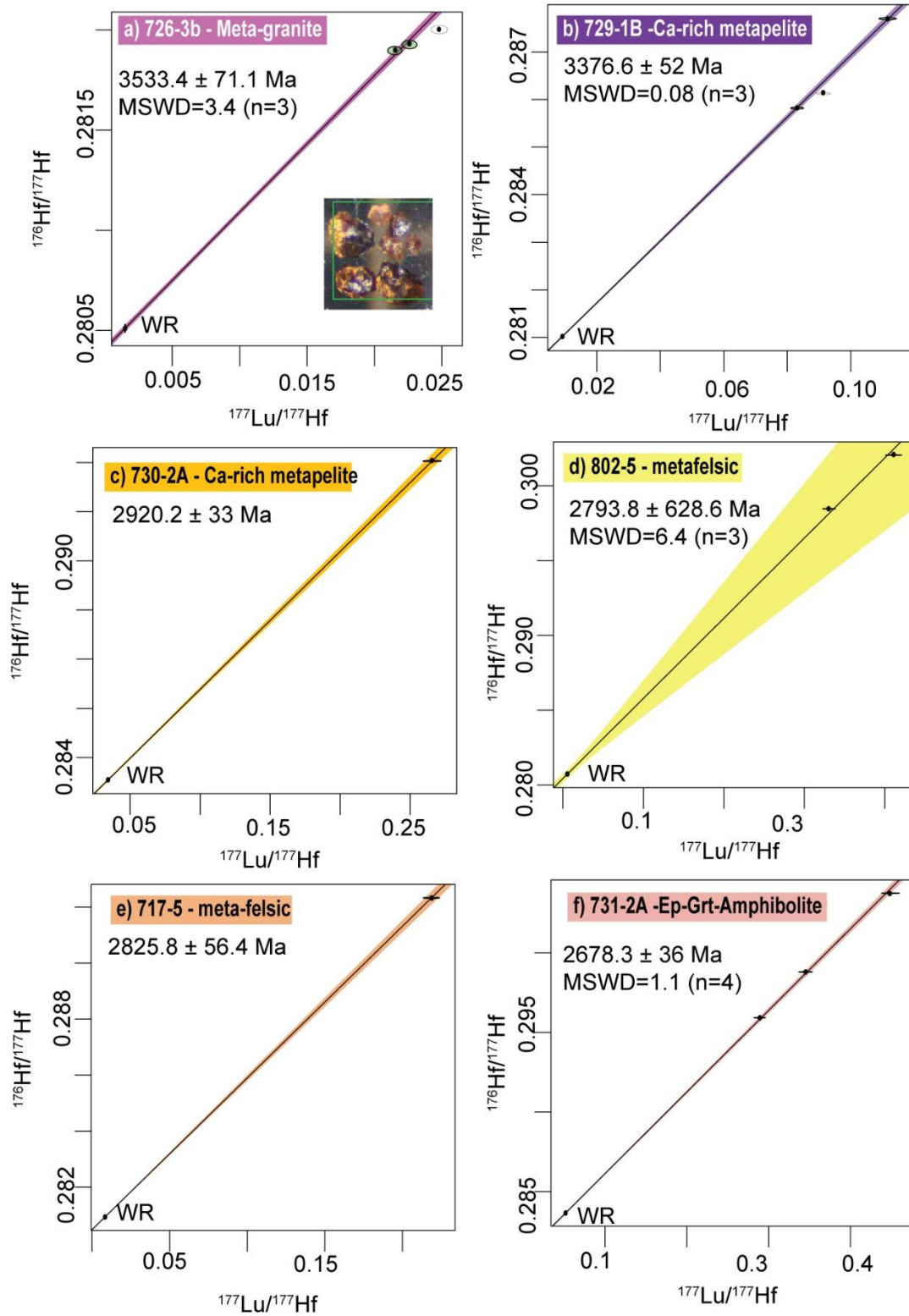
Figure 5.10 Lu-Hf isochrons for the (a) meta-granite and (b)-(e) garnet bearing supracrustal rocks. Inset in (a) shows the garnet fraction used for dating (fraction 1)

In the metapelite sample 714-5E (Fig. 5.1b), that shows large garnets (>1 cm) with a well-developed post-tectonic overgrowth (Fig. 4.3), grains have a Sm-Nd calculated age of 2486.72 ± 2.4 Ma (Fig. 5.9g)

5.5 Discussion
5.5.1 Preliminary interpretations of the geochronological data

The data presented in this work reveals a wide spread of ages ranging from the Eoarchean to the Paleoproterozoic (Fig. 5.10), similar to what has already been presented in other works (c.f. Fig. 5.1a,e). This spread might be consequence of multiple (metamorphic) events or differential retrogression affecting the geochronometers. In the following sections the geochronological data interpretation previously reported is reviewed. Then, a preliminary discussion of the new data is presented, which provides a few possible interpretations of the obtained ages based on field, mineralogical and microstructural relationships described for the rocks. In-depth analysis of the geological processes and analytical procedures that might have affected the ages will be incorporated in further work; details of what such future work would entail are provided as an outlook.

5.5.2 Previous metamorphic ages: Some remarks

Metamorphic ages reported for the ISB have been previously interpreted to record at least two major metamorphic events. However, the spread of the values has made the task of dating them almost impossible. It has been discussed that such a variation might be a consequence of multiple metamorphic events (e.g. Nutman et al., 2020) or differential retrogression of the minerals and rocks (Webb et al, 2020; Zuo et al., 2021). Hence, the discussions on the geological meaning of some of the values still continues and warrants some remarks.

The oldest previously reported metamorphic ages (c. 3700 Ma, Fig. 5.1a, e) are at odds with the crosscutting relationships of the area. These ages were obtained mainly from minerals in quartz-carbonate veins that are commonly described as following planes along the main

foliation and/or crosscutting the foliation and fabrics of the rocks (Frei et al., 1999; Blichert-Toft and Frei, 2001; Frei and Rosing, 2001). Quartz-carbonate veins crosscutting the main petrofabrics of the ISB are common in the field and are also recognized in thin sections (e.g., Webb et al., 2020; Fig. APP-C5.2). Moreover, dating of minerals like garnet that were recovered from this type of veins also included inclusions-free garnets that overgrew the main foliations of the ISB (Blichert-Toft and Frei, 2001). These (micro)structural descriptions indicate that the vein emplacement event(s) and the inclusion-free garnets growth was most likely static. Consequently, it must have happened after the main and more pervasive syn-tectono-metamorphic episode recorded in Isua (M_1). Several authors agree that M_1 must be 3660-3600 Ma or younger (Nutman and Friend, 2009; Arai et al., 2015; Webb et al., 2020), with recent analysis suggesting it could even be Neoarchean in age (Ramírez-Salazar et al., 2022), the c. 3.7 Ga ages of post-deformational veins are thus difficult to reconcile with the geological evidence in the ISB.

Moreover, fluids from which the veins were derived show a complex chemistry. Although they are typically assumed to be magmatic-derived fluids from the emplacement of the tonalites or granites in the belt (Frei et al., 1999; Blichert-Toft and Frei, 2001; Frei and Rosing, 2001), their history might be more complex. For example, Frei and Roising (2001) pointed out that the Pb chemistry of some of the veins cannot be described by a simple two-endmembers mixture. Additionally, Blichert-Toft and Frei (2001) argued that the -14 initial ε_{Nd} value they calculated was representative of the original composition of the fluid from which the garnets precipitated from. Webb et al. (2020), however, discussed that this value is at odds with the fact that the meta-igneous rocks in Isua are mainly derived from primary melts not older than 3.9 Ga (Hoffmann et al., 2014; Gardiner et al., 2019), such that fluids derived from the tonalites should not have such evolved initial ε_{Nd} values. Thus, both the chemistry and the cross-cutting relationships indicate that the c. 3.7 Ga ages (Fig. 5.1a, e) of

the veins and the garnets might not have an accurate geological meaning and therefore they are excluded from the following discussions.

5.5.3 Is the early metamorphic signature related to the tonalite emplacement?

The titanite grains found in the mafic enclaves in the c. 3.75 Ga tonalite returned the oldest ages (c. 3640-3680 Ma) of the dataset presented here (Fig. 5.11). Samples analysed show a strong foliation (e.g. Fig. 5.4) and a SE-dipping lineation that is subparallel to general lineations reported for the belt (Webb et al., 2020; Zuo et al., 2021). Hence, the metamorphic assemblages of the enclaves are typically interpreted as being the product of the same major regional syn-tectonometamorphic event (M_1) as the supracrustal rocks within the ISB (e.g. Nutman et al., 2013, 2020). However, an alternative interpretation is that they recorded local contact metamorphic in response to the emplacement of the big tonalitic bodies according to the microstructures, geothermobarometry and geochronology of the enclaves.

The mafic enclaves, both in the field and on at thin section scale, display (micro)structures that have not been reported for any rock within the ISB. For example, they present irregular intergrowths of K-feldspar + albite + plagioclase ± quartz ± biotite (Fig. 5.3a-c). This microstructural association, along with the biotite-albite reaction products on hornblendes (Fig. 5.3d), a typical indicator of partially melted rocks (Holness et al., 2011; Vernon, 2011). In sample 724-1A, these melt microstructures dominate in a section of the rock that is parallel to the foliation (Fig. 5.4a). The partial-melting origin of the albite in the intergrowths is supported by its chemistry. Albite grains that only appear in the intergrowths show compositions that have $< X_{An}= 0.05$ (Fig. 5.7a) and form a different compositional group to the main plagioclase grains (Fig. 5.7a) appearing in the matrix (Fig. 5.2a, 5.4) or as inclusion in the intergrowths (Fig. 5.3a-c). The recognition of partial melting within the enclaves points to higher metamorphic conditions than those inferred from the regional M_1 event within the ISB (550-600 °C and 0.6-0.7 GPa, see Chapters 2 and 4). The quantitative

geothermobarometric data retrieved form the hornblende-plagioclase pairs in sample 724-1A

confirm the higher-grade conditions (650-675 °C and 0.40-0.60 GPa, Fig. 5.7c).
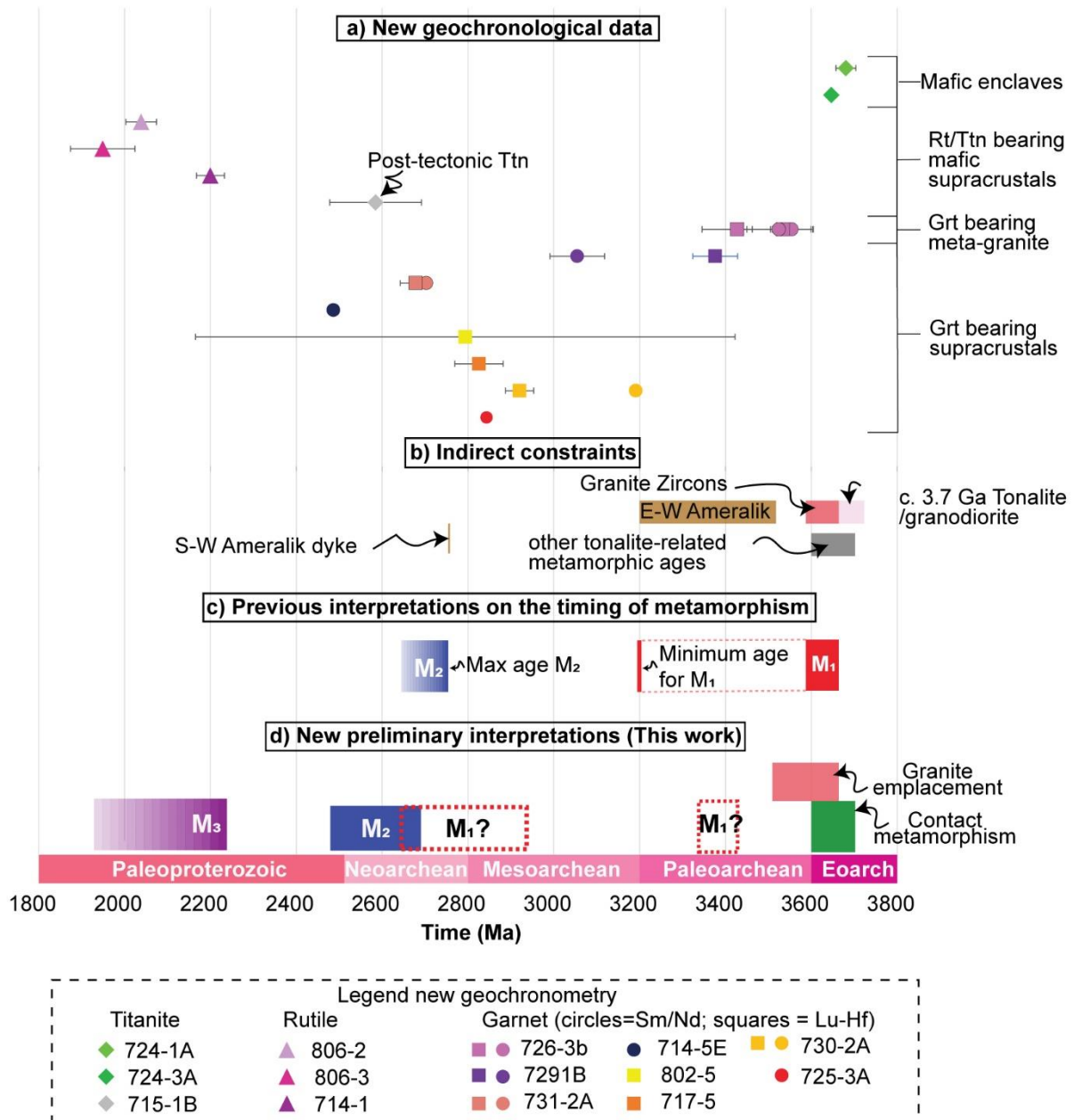
Figure 5.11 Graphic summary of the metamorphic geochronological data of the ISB. (a) New data presented in this work. (b) Indirect constraints. (c) Previous interpretations of the different metamorphic events and their ages. (d) New interpretations based in the new geochronological data and analysis of the geology of the ISB.

A classic contact metamorphism scenario would demand an increase in metamorphic grade

towards the 3.7 Ga tonalite. In this scenario, a steep temperature gradient towards the igneous

body would be expected which so far has not been reported explicitly for the area. However, some thermal increase could be explained with the proposed tectonic models for the ISB. For instance, the collision model (Model B, Nutman et al., 2013, 2020; see Fig. 4.2b) argues that during the major tectonometamorphic event (M_1), the collision of the 3.7 and 3.8 Ga terranes produced an increasing metamorphic gradient towards the centre of the 3.7 Ga tonalite due to effective crustal thickening. However, in this case, an increase in pressure should be accompanied by a rise in temperature (cf. model B, Fig. 4.2b.i). Such behaviour is not visible in our dataset. Instead, amphibolite sample 724-1A shows an increase in > 50 °C in temperature (650-675 °C in the enclave *vs.* 550-600 °C in the belt) within less than 500 m from the belt (Fig. 1c), while pressure is just within the range of the peak pressure in the belt (0.40-0.60 GPa vs 0.6-0.7 GPa, Chapter 2, 4). Consequently, it is readily possible that the metamorphism of the enclaves is a related to the tonalite emplacement itself and associated local metamorphism that is not recorded within the rest of the belt. In fact, the age obtained for enclave 724-1A (3680.5 ± 23.14 Ma) overlaps with the last reported tonalite emplacement pulses (Fig. 5.11), i.e, being in full agreement with this interpretation.

The data reported in the literature also supports the hypothesis of an intrusion-related contact metamorphism creating the signatures of the enclaves. Firstly, at present partially molten rocks have only been reported within the tonalities. Examples are a garnet-pyroxene enclave in the 3.7 Ga tonalite (Nutman et al., 2013) and a garnet-amphibolite rock in the 3.8 Ga tonalite (Hoffmann et al., 2014) south to the ISB exhibiting partial melting structures observed in the field. The lack of melt-related (micro)structures within the rest of the ISB, even in more felsic lithologies is consistent with local higher temperatures to be only recorded in the enclaves. Secondly, >3.6 Ga ages reported as being metamorphic (Fig. 5.11) have only been reported for the garnet-pyroxene enclave (3658 ± 3 Ma, Nutman et al., 2013) and titanites in granodiorites and tonalites (e.g. Crowley et al., 2002, Crowley, 2003).

Therefore, the data suggests that a >3.6 Ga high-grade local contact metamorphic was only recorded (or preserved) in the enclaves and that the main M_1 might be younger.

5.5.4 Magmatic garnet in the meta-granite?

Garnets in the meta-granite stand out compared to the rest of the garnets reported in the supracrustal rocks of the ISB. While garnets in the supracrustal rocks growing in quartz-rich environment are highly skeletal (e.g. meta-felsic, Fig. 5.6c-d), the garnets in the quartz-rich meta-granite are euhedral to subhedral with little to no inclusions (Fig. 5.5b, e-h). Thus, we interpret that their growth seems to be controlled by different factors/mechanisms to that of garnets in the supracrustals (compare Chapter 3). Moreover, changes in colour, with darker cores surrounded by clearer rims (Fig. 5.5a) coincide with high spessartine content in the centre and lower in the rim (Fig.5.5g, APP-D5.1b), with no clear microstructural or crystallographic orientations changes (Fig. 5.5h). Thus, Rayleigh fractionation (Hollister, 1966) as garnet continuously grows is most likely the responsible mechanism producing the observed chemical and colour zoning (Fig. 5.5e,g) in the grains instead of two different events. The colour variation is also evident in the picked garnets, with smaller grains displaying lighter shades than larger ones (Fig. D5.1a). The two fractions were dated to test a continuous growth hypothesis. The Lu-Hf (Fig. 5.10a) and Sm-Nd (Fig. 5.9a) ages of the larger grains are almost identical with the Sm-Nd age of the smaller grains (Table 3, Fig. 5.11), and thus it is interpreted that both fractions grew around 3.55 Ga within a single event. Within error, this value overlaps with the last pulses of granite intrusion recorded in the belt (Fig. 5.10; (Baadsgaard et al., 1986; Nutman et al., 1996; Crowley et al., 2002; Crowley, 2003) and therefore, it is interpreted that these garnets crystallized from the granitic melt. This interpretation is in agreement with high-Mn garnets that are common in magmatic paragenesis (Abbott, 1981, Jung et al. 2001).

The meta-granite, however, also experienced metamorphism. The microstructural relationships suggest sillimanite occurred after kyanite (e.g. Fig. 5.5a), pointing to elevated

pressure conditions followed by a decrease in pressure and/or rise in temperature. This inferred evolution is similar for the path obtained for M_1 (Fig. 4.8a) and therefore the metamorphic assemblage of the meta-granite could be contemporaneous or being overprinted by the main metamorphic event in the belt, but further quantitative P-T data are needed to relate them.

5.5.5 Regional syn-tectonic metamorphism (M_1): preliminary constraints from garnet geochronology of the supracrustal rocks

The ages obtained from garnets of the supracrustal rocks within the belt cover a timespan of c. 1000 Ma (Fig. 5.11). Garnet cores are considered to have grown during M_1, because their inclusion trails continue towards the foliation (e.g., samples 717-5 or 802-5, i.e., pattern A) or have spiral-like internal foliations (e.g., sample 714-5E, i.e., pattern B). Some grains have straight or slightly curved internal foliations (e.g., 730-2A, 725-3A, 729-1A, i.e., pattern C) and might be intertectonic. Microstructural evidence suggests, however, that the majority of garnets grew during M_1, and their ages, if they reflect the time of growing, should date this event. Indirect constraints (Fig. 5.1e) suggested that M_1 occurred at c. 3.66-3.60 Ga during the emplacement of the intrusions of the granites (Nutman and Friend, 2009) and that it might not be younger than the 3.2-3.5 Ga interpreted crystallization age of the E-W intruding Ameralik dykes (Nutman et al., 2004; White et al., 2000). Notwithstanding, apart for one Lu-Hf age in sample 729-1B (Fig. 5.10b), all the calculated garnet ages are younger than any of these two ranges (Fig. 5.11). Additionally, it is worth noting that three out of four of the samples with both Lu-Hf and Sm-Nd ages show large dissimilar values (from c. 250 m.y. for 730-2A to c. 2300 m.y. for 717-5) within the two systems (Fig. 5.11). The difference in ages does not show a clear pattern, i.e., the oldest age in some samples is the value obtained with the Lu-Hf system (i.e. 729-1B and 717-5), while in other is the Sm-Nd value (730-2A). Only for sample 731-2A both the obtained Lu-Hf (2678.3 ± 36 Ma) and Sm-Nd (2702.72 ± 4.33

Ma) ages are similar (Fig. 5.11). These Neoarchean ages are, relatively seen, closer to the c.

2.8 Ga values obtained for most of the garnet-bearing supracrustals (Fig. 5.11).

The diversity and discrepancies of ages within the same sample and among the large dataset

can be explained by two different approaches. Either the diversity is an effect of geological

processes including prolonged metamorphism with heterogeneous record, several

metamorphic events recorded heterogeneously throughout the area or the actual analyses and

procedures introduced artifacts.

Potential analytical artifacts may stem from mineral contamination. For example, inherited

zircon can affect the constructed whole rock – leached garnet Lu-Hf isochrons depending on

its presence within the rock. If the inherited older zircon only occurs in the matrix, it might

drag the $^{176}Hf/^{177}Hf$ of the whole rock to lower values, thus creating a steeper isochron with

apparent older ages (Scherer et al., 2000). On the contrary, if the inherited zircon is only

included in the garnet fraction, but not present in the matrix, the isochron slope could be

shallower and then produced younger apparent ages (Scherer et al., 2000). Something similar

occurs with the Sm-Nd system (Bowtell et al., 1994; Scherer et al., 2000; Anczkiewicz and

Thirlwall, 2003). Minerals rich in Nd, such as monazite, epidote and apatite, if included in

garnet, will create apparent isochrons with shallower slopes that will produces younger ages

(c.f Cheng, 2018). On the contrary, inherited old inclusions with high Sm/Nd will produce

higher $^{143}Nd/^{144}Nd$ ratios that will create steeper isochrons and then older ages (Baxter and

Scherer, 2011; Cheng, 2018). Thus, a leaching out (e.g. apatite) or not dissolving (e.g. zircon)

inclusions during chemistry preparation might have affected the ages.

Other effects like later retrogression can also affect the ages (An et al., 2018). For example,

retrograde fluids might interact with garnet and change their major and trace element

compositions, which can change the ratios of elements like Sm and Nd (An et al., 2018). This

will ultimately affect the calculated ages to probably younger values (An et al., 2018).

Additionally, mixed picked garnet domains with probably different ages also impact in the measured ratios in a non-systematic manner. If, for example, two fractions with contrasting ages are dissolved then the resulting isochron will be a mixing age (Cheng and Cao, 2015). Two clear distinct domains (inclusion-rich vs inclusion-poor) are common in the garnets of Isua. The rims are typically small, and might have not contributed to the bulk chemistry, but distinction between both domains was not always possible during picking. Bearing these possible processes and technical issues of garnet dating in mind, some preliminary interpretations to this dataset are provided in the next paragraphs.

One possible interpretation is that the oldest age obtained for the garnets in Ca-rich sample 729-1B (Lu-Hf 3376.6 ± 52, Fig. 5.10b) is the only one recording the timing of M_1, while the rest represent poor cleaning of the inclusions, differential retrogression and/or mixed core (syn-tectonic) and rim (post-tectonic) fractions. The Lu-Hf age of sample 729-1B has a low MSWD (0.08) number and relatively low errors, pointing to accuracy. This value is within the timespan of intrusion of the E-W Ameralik dykes (Fig. 4.1e, 4.11) and therefore agrees with the interpreted cross cutting relationships (White et al.; 2000; Nutman et al., 2004). Inclusions of zircon (e.g. 717-5), apatite (e.g. 717-5) and epidote (e.g. 731-2A) are documented in the garnets of the ISB, and their presence would be expected to have affected the values to too young ages.

The oldest ages obtained for the supracrustals (>2900 Ga, c.f. Fig. 5.11), however, might not reflect the actual age of M_1 itself. Garnets in Ca-rich metapelites 729-1B and 730-2A show the oldest garnet ages in the supracrustals and they display apparently intertectonic inclusions patterns (pattern C; Fig. 5.6i.iii). Therefore, it might be possible that they record an earlier metamorphism than the regional M_1, assuming the oldest age dates the first growth and not the second growth. However, their Lu-Hf (Fig. 5.10b-c) and Sm-Nd (Fig. 5.9b-c) ages have differences of c. 250-350 m.y. This points to either possible re-equilibration or disequilibrium

between the isotopic systems or problems with the distribution of the accessory minerals within the samples. Inspection of the thin section did not reveal substantial zircon in the matrix, that might shift the Lu-Hf age in 729-1B to older values. But zircon grains are typically <50 µm and a more in depth search might be needed to find them. Alternatively, the oldest age is a signature of a pre-M1 event, while the youngest ages (c. 2.7-2.9 Ga) would represent the regional M_1.

If the >2900 Ma found in the garnets from Isua do not reflect the timing of M_1, then the metamorphism might be substantially younger than currently interpreted (e.g. Crowley et al, 2002; Nutman and Friend, 2009; Nutman et al., 2020; Webb et al., 2020, Zuo et al., 2021; Chapter 2). Garnets (samples 731-2A, 717-5, 802-5) with clear syn-tectonic inclusion trails (e.g. patter A and B; Fig. 5.6i) returned ages with values c. 2.7-2.8 Ga (Fig. 5.11). For one of these samples, amphibolite 731-2A, a c. 2.7 Ga age was retrieved with both systems (Fig. 5.9f; 5.10f; 5.11). Thus, if this age reflects re-equilibration or was affected by methodological procedures, they must have impacted the Lu-Hf and Sm-Nd systems in an equitable way in order to get similar isochrons values, which is unlikely. Therefore, M_1 might be Neoarchean-Mesoarchean in age (c. 2.7 Ga; Fig. 5.11), substantially younger than the typical 3.66-3.60 Ga age interpreted for the main metamorphic event in the ISB (e.g. Crowley et al, 2002; Nutman and Friend, 2009; Nutman et al., 2020; Webb et al., 2020, Zuo et al., 2021b; Chapter 2). Ramírez-Salazar et al., (2022) already discussed the possibility that M_1 might be younger than 2.7 Ga, based on the observations of Nutman et al. (2022) that the <2.7 Ga S-W Ameralik dykes have post-crystallization magmatic fabrics dipping to the southeast, as most of the lineations in the belt. For this hypothesis to stand, the 3.5-3.2 Ga interpreted crystallization ages in the E-W Ameralik dykes would have to be inherited and the younger 2.6 Ga ages obtained in the rims of the zircons (Nutman et al., 2004) would then represent the true crystallization age, i.e., constraining the M1 regional event to >2.6 Ga. A Neoarchean-

Mesoarchean age for the syn-tectonic metamorphism of the ISB was already proposed by

Gruau et al. (1996) with a Sm-Nd age of 2849 ± 116 Ma obtained with a plagioclase-

amphibole-whole rock isochron (Gruau et al., 1996) from a foliated rock.

5.5.6 Post-tectonic (M_2) and retrograde (M_3) metamorphism

Dating of rutile and titanite in the Rt/Ttn-bearing mafic supracrustals was performed directly

on the thin sections. Therefore, microstructural relationships can inform the interpretations of

the ages. In the case of the dated titanites in sample 715-1B, their microstructural

relationships allow to associate the titanites to the post-tectonic growth, since they overgrow

both the foliation (Fig 5.2f) and aligned rutile grains (Fig. 5.2h). Based on this

microstructural occurrence of titanite, these grains can confidently be linked to the post-

tectonic the medium-temperature event (M_2) for which a lower U-Pb interception age of

2584.9 ± 98.3 Ma was obtained (Fig. 5.8f). This value is younger than the 2750 Ma age of the

N-S trending Ameralik dykes interpreted by Nutman et al. (2015) as the maximum age of this

metamorphic event (M_2, Fig. 5.11), and it is younger than most of the garnet ages obtained

here (Fig. 5.11). Therefore, we conclude that this Neoarchean age (2584.9 ± 98.3 Ma)

provides a minimum estimation for M_2.

The rutiles commonly follow the foliation of the rock (e.g. Fig. 5.2e) or occur as inclusions of

aligned amphiboles (e.g. Fig. 5.2g) and thus are interpreted as syn-tectonic. Textural

relationships of these grains show that they are overgrown by titanite (e.g. Fig. 5.2h),

meaning rutiles should be relatively older. However, the lower intercept values of c. 2200-

1949 Ma (Fig. Fig. 5.8c-e) retrieved from the rutiles are considerably younger than the age

obtained for the overgrowing titanites (Fig. 5.8f). Deformation and fluid-mineral interactions

can affect the distribution of trace elements and U-Pb ages in minerals (Piazolo et al., 2016;

Moore et al., 2020; Gordon et al., 2021; Walters et al., 2022). No clear internal deformational

features were observed in the rutiles of the Isua rocks, but fluids have been shown to have

intensively affected the rocks (e.g. sample 806-3) and titanite overgrowth might have also

affected the rutile chemistry. Therefore, we interpret the ages obtained from the rutile to most likely reflect isotopic re-equilibration due to the retrogression event(s) M_3.

5.6. Preliminary conclusions and further work

This study provides new geochronological and geothermobarometric data for the ISB and associated rocks. Description of microstructural relationships and comparison with data previously reported allowed for new preliminary interpretations that expand the tectonometamorphic understanding of the ISB. However, further work is needed to have a more complete comprehension of the rather complicated nature of the timing of the metamorphism of the belt. Some remarks are highlighted here:

Contact metamorphism: New U-Pb titanite geochronology and geothermobarometry, along with data previously reported, showed that a local c.3.6-3.7 Ga contact metamorphism is recorded in the enclaves within the 3.7 Ga tonalite. (Micro)structural observations and quantitative data allow to interpret this metamorphic signature as independent of the main regional syntectonic metamorphism (M_1) that affected the ISB. However, lineations measured in the studied samples plunge to the SE as most of the lineations recorded in the belt, suggesting that they are related, possibly by a later deformational overprint at the same or lower P-T conditions leaving the mineral assemblage unmodified. Lineations in Neoarchean Ameralik dykes (Nutman et al., 2015) also show SE-dipping lineations, showing rocks with different ages and deformational histories have a systematic lineation pattern that need to be investigated. Here, linking minerals to date to the deformation fabrics will be pivotal.

Magmatic garnet: Magmatic garnets in meta-granite were accurately dated at c. 3.55 Ga, overlapping with the last pulses of granite emplacement already dated with zircons (Crowley et al., 2002; Crowley, 2003; Nutman and Friend, 2009). Further in depth study of the protolith genesis of the meta-granite along with its metamorphic assemblage should be able to provide more insights into magmatic and metamorphic processes of the ISB.

Timing of M_1: Irrespective of potential analytical artifacts, our data shows that there is no geochronological evidence for any regional metamorphic event (M_1) at 3.66-3.60 Ga as it has been interpreted so far. The large spread in values obtained for different garnets in supracrustals from the ISB show a potentially complex geological history. While the age range could be interpreted as the signature of a number of individual events with a heterogeneous record due to lithological and fluid related diversity, field relationships do not support such a complicated picture. Alternatively, analytical artifacts may be responsible for the complex nature of the age dataset. If true, i.e. in the case of a single major regional syn-tectonic metamorphic event, two alternative interpretations of the actual date of this M1 are proposed: (1) M_1 occurred at c. 3.3 Ga or (2) at c. 2.8 Ga with earlier ages in intertectonic garnets recording local events or being affected by the presence of accessory minerals. For (1) local effects and accessory minerals resulted in too young ages, while for (2) the older ages are due to zircon presence in the bulk rock. A more in-depth analysis of the different processes and/or analytical procedures is needed to fully interpret the garnet ages obtained in this work. For example, quantify the effect of accessory inclusions according to their isotopic characteristics.

Timing constraints for M_2 and M_3: U-Pb dating of titanite and rutile directly on the thin section of mafic supracrustals within the belt provided constraints for the late metamorphism in the belt. While M_2 is late Neoarchean (2584.9 ± 98.3 Ma), the lower grade retrogression event(s) M_3 is Paleoproterozoic (<2200 Ma).

Chapter 6: The metamorphic record and evolution of the Isua supracrustal belt and its tectonic implications – an integrated discussion

The core chapters of this thesis (2-5) offer individual discussions on different aspects of the metamorphic record of the ISB that build on each other as the thesis progressed. For this conclusive chapter, an integrated discussion of the data and the tectonometamorphic record is presented highlighting the main contributions of this thesis, alongside with limitations and possible biases and other aspects briefly discussed in previous chapters. Then, the tectonic implications for the belt and the Archean geodynamics are analysed. Finally, open questions and future avenues for research are presented.

6.1 An integrated approach to reconstruct the metamorphic history of the ISB: advances and limitations

6.1.1 The syn-metamorphic record of the supracrustal rocks and other rocks within the belt

Understanding and quantifying the detailed evolution of the ISB is pivotal to discern between the different tectonic models that have been proposed for the belt (e.g. Fig. 2.3 and 4.2). Each scenario predicts different metamorphic signatures and numbers of syn- and pre-tectonic metamorphic events (Fig. 1.5, 2.1; e.g. Komiya et al., 1999; Nutman et al., 2013; 2020; Webb et al, 2020). Most of the discrepancies have been addressed and resolved in the previous chapters using a combination of different approaches and techniques.

Model A and B (Fig. 2.3 and 4.2) predict the juxtaposition of rocks with different peak metamorphic conditions and metamorphic histories (Komiya et al., 1999; Nutman et al., 2013; 2020), while model C predicts peak homogenous conditions and similar metamorphic evolutions (Webb et al., 2020). Peak metamorphic conditions should be reflected in the peak metamorphic paragenesis. Their description and quantification in Chapter 2 showed that they equilibrated at similar conditions across the ISB (550-600 °C and 0.5-0.7 GPa, Fig. 2.10). Then, previous interpretations of the existence of metamorphic gradients might be

consequence of the lack of recognition of certain microstructures and the limited P-T data.

On one hand, the apparent N-S increase in metamorphic grade in the easter arm of the belt (c.f. Komiya et al., 2002; Hayashi et al., 2005; Arai et al., 2015) might be the consequence of late chloritization of Fe-Mg bearing prograde minerals (Fig. 2.5e,h, 2.10c). These retrograde processes preserved prograde microstructures, while overprinting the prograde minerals, potentially leading to misinterpretations (section 2.4.2.1). On the other hand, the proposed increase in P-T conditions from the outer part of the belt towards the centre of the 3.7 Ga tonalite (e.g. Nutman et al., 2013) might reflect two separate metamorphic events (Chapter 5). Quantification of the P-T peak conditions (Fig. 5.7c) and descriptions of the microstructural features (Fig. 5.3), along with U-Pb titanite geochronology (3.68-3.60; Fig. 5.8a-b, 5.11), of mafic enclaves within the 3.7 Ga tonalite show that their higher metamorphic conditions (650-675 °C and 0.40-0.60 GPa) are most likely the product of contact metamorphism associated with the tonalite emplacement (Fig. 5.11). Rocks within the belt do not show any signs of this contact metamorphism, suggesting M_1 is probably younger than 3.6 Ga (section 5.5.3).

It has also been interpreted that some supracrustal rocks recorded pre-M_1 metamorphism, such that the main fabrics of the rocks do not only reflect one major syn-tectonic event (e.g. Gauthiez-Putallaz et al., 202). Different metamorphic histories are expected to be recorded in the garnet microstructures and chemical zoning and local pre-M_1 metamorphic events are interpreted from the garnet inner cores (Rollinson, 2002, 2003; Gauthiez-Putallaz et al., 2020; Nutman et al., 2022). Notwithstanding, two core chapters of this thesis offer an alternative perspective. First, the diversity in microstructures, chemical zoning, and crystallographic orientations in the garnets across the ISB does not allow to distinguish any systematic geographical variation. Hence, they do not reflect different metamorphic histories. Instead, the garnet characteristics mainly depend on the microstructures of the rocks and their

mineralogical association and/or bulk composition (section 3.5). Second, the garnet

microstructures (e.g., spiral-like internal foliations, Fig. 2.6, 3.8f, 4.3), crystallographic

orientations (e.g., Fig. 3.8f) and chemical zoning (Fig. 2.6, 3.8f, 4.3) demonstrate a

continuous garnet growth, rather than the previously interpreted hiatus in metamorphic

growth from core to annuli in the garnets (c.f. Gauthiez-Putallaz et al., 2020). Lastly, this

continuous syn-tectonic growth of the garnet can be linked to an initial near isothermal

evolution, followed by a decrease in pressure and increase in temperature (Fig. 4.11). In

summary, the analysis presented in the chapters of this thesis shows that the evolution

described for M_1 (M_1, Fig. 4.11) and its peak conditions (Fig. 2.10) seem to be common for

rocks across the ISB and points to a similar evolution of the entire supracrustal sequence

(section 4.5).

As a result, the data obtained from the meta-volcanosedimentary rocks from the ISB is

incompatible with models A and B (Fig. 2.3, 4.2) as presented by their corresponding authors

(Komiya et al., 1999; Nutman et al., 2013, 2020). However, some authors argue that rocks

(e.g. meta-dunites and serpentintes) within the ISB have magmatic and metamorphic histories

that significantly differ from the evolution of the supracrustal rocks (Friend and Nutman,

2011; Nutman et al., 2020; Guotana et al., 2021). Then their occurrence within the belt must

be evidence that the metamorphic history across the belt is not homogenous as proposed here.

In this regard the ultramafic rocks have a central role in the discussion. One of the first

interpretations regarding their chemistry suggested that they were mantle slices (Friend and

Nutman, 2011). Since mantle peridotite are typically emplaced along tectonic breaks in

former convergence zones (Coleman, 1971), then their occurrence within the ISB suggest a

more complex geological history and points to the existence of a former subduction zone (e.g.

Model B, Nutman et al., 2013; 2020). On the contrary, other authors have provided evidence

to show that these rocks are the cumulitic counterparts of the mafic rocks of the belt (Szilas et

al., 2015; Waterton et al., 2022), questioning their evidence of plate tectonics-like movements. Additionally, with regard to the nature of the protolith, the metamorphic record of the ultramafic rocks is not well understood either. Nutman et al. (2020) and Guotana et al., (2021) argue that the presence of Ti-clinohumite and Ti-chondrodite proves that the ultramafic rocks within the belt experienced (ultra)-high pressure (UHP) metamorphism (1.3->2.6 GPa). Their presence within the belt would show that rocks with contrasting metamorphic grades and histories are in direct contact, and thus, they must be evidence of the operation of plate tectonic processes (Nutman et al., 2020; Guotana et al., 2021). But this is not the only possible interpretation regarding the presence of Ti-humites. Ramírez-Salazar et al. (2022) and Waterton et al. (2022) contended that the presence of Ti-humites alone shouldn't be used to argue for (U)HP metamorphism. Ramírez-Salazar et al. (2022) argue that the characteristics of the ultramafic rocks of Isua and the microstructural association of the Ti-humite suggest they cannot be directly compared to the experiments where these minerals have been found to be stable at (U)HP conditions (Shen et al., 2015). First, the composition of the rocks is not identical to those used in the experiments (serpentinized wehrlite and harzburgite vs dunite). Second, microstructural relationships show the Ti-humites grew in the presence of carbonates (Fig. 3a in Ramírez-Salazar et al., 2022). CO_2 seems to have a role in stabilizing the Ti-humites to lower pressures, down to amphibolite conditions in marbles (Ehlers and Hoinkes, 1987). Therefore, the qualitative conditions proposed for the metamorphism of the ultramafic rocks might be overestimated (Ramírez-Salazar et al., 2022, Waterton et al., 2022), and they might have experienced similar conditions to the rest of the supracrustal rocks. The data presented here, however, does not provide a concise explanation to this problem. Further work on the ultramafics directly relating their mineralogical records and microstructural characteristics to quantitative P-T data will provide insights in their evolution and their relationship with the volcano-

sedimentary sequence. The data provided so far, however, is not conclusive to contradict a homogenous M_1 evolution for the entire supracrustal belt.

6.1.2 Putting the t into the P-T-*X*-D syn-tectonic path: implications for the tectonic evolution of the ISB

The integrated approach used in this work resulted in the reconstruction of the P-T-*X*-D syn-tectonic path that the ISB most likely experienced (Fig. 4.11). However, preliminary analysis of the new geochronological data suggests two possibilities for the timing (t) of metamorphism. Both possibilities have contrasting implications for the tectonic evolution of the ISB.

As discussed in section 5.5.5, M_1 might have occurred at c. 3370 Ma (Fig. 5.11) according to the oldest Lu-Hf age calculated in the dataset for Ca-rich metapelite 729-1B (5.10b). This interpretation is in agreement with the interpreted range (3.2-3.5 Ga) estimated for the emplacement of the E-W Ameralik dykes (White et al., 2000; Nutman et al., 2004) that is, by some authors, regarded as the minimum age for M_1 (Fig., 5.1e, 5.11; Nutman and Friend, 2009; Nutman et al., 2020; Webb et al., 2020, Zuo et al., 2021b). This P-T-*X*-D-t then would allow for Isua to have evolved in a heat pipe Earth (Fig. 4.2c), or a modified model of a subduction zone (Fig. 4.2a), albeit the former interpretation is favoured by all metamorphic records reported in this thesis. Thus, the ISB might have evolved as follows: (1) deposition of the 3.8 Ga supracrustal sequence, (2) emplacement of the 3.8 Ga tonalite as product of supracrustal rocks partial melting (c.f. Hoffmann et all., 2014, 2019; Gardiner et al., 2019). This was followed by a 100 m.y. hiatus in the deposition that stopped when (3) the 3.7 Ga supracrustal sequence was deposited and the (4) 3.7 Ga tonalite was intruded, causing the contact metamorphism of the enclaves (3.6-3.68 Ga, Fig. 5.11) that submerged into the intrusive. Then, (5) the tonalites experienced partial melting that produced the granititc dykes (Crowley et al., 2002; Crowley, 2003) with magmatic garnet (Fig. 5.5) forming at 3.66-3.55 (Fig. 5.11). Finally, (6) syn-metamorphic (M_1) sheath folding (Webb et al., 2020) at c. 3370

Ma created the peak metamorphic assemblages (550-600 °C and 0.5-0.7 GPa) and the penetrative foliations and lineations observed in the ISB. Subsequently, lower amphibolite facies metamorphism (M_2) at c. 2584.9 ± 98.3 Ma (Fig. 5.8f) produced the garnet rims and post-tectonic titanites (Fig. 5.2h,f) observed in the supracrustals. Proterozoic (<2200 Ma) fluid infiltration (M_3) created post-tectonic veins, influenced the chloritization of aligned minerals and most likely affected the prograde minerals isotopic systems (e.g., rutile) Alternatively, M_1 might have occurred later in the Meso-Neoarchean (c. 2.7-2.9, Fig. 5.11). Ramírez-Salazar et al. (2022) and Gruau et al. (1996) have already suggested the possibility that the main metamorphic event recorded in the ISB is essentially younger. Meso-Neoarchean events appear to have affected the Itsaq Gneiss Complex (Fig. 1.2). Nutman et al. (2015) proposed a collision between the Kapisilik (3070 Ma) and the Isukasia terrane (from which the ISB is part of; Fig. 1.4) at 2980-2950 Ma. The timing of this proposed event is mainly based in U-Pb zircon ages retrieved from granites that are interpreted to be metamorphic (Nutman et al., 2015). The authors suggest that this event attained high-pressure conditions, interpreted with the presence of garnet and clinopyroxene occurring in mafic rocks from the Isukasia area. However, none of the metamorphic minerals has been dated yet. In their compilation, Nutman et al. (2015), argued that this collision episode did not affect the rocks of the Isua area. Nutman et al. (2015) also proposed that during the Neoarchean ($\approx$ 2690 Ma) crustal reworking along intra-crustal shear zones was accompanied by amphibolite facies metamorphism that affected both, the Kapisilik and Isukasia terranes (Fig. 1.4), including the Isua area. This event is argued to be represented in Isua by metamorphic minerals in the Ameralik dykes (epidote and garnet, e.g. Nutman et al., 2015) and the post-tectonic rims in the supracrustal rocks (e.g. Gauthiez-Putallaz et al. 2020) and should thus represent M_2. The Meso-Neoarchean age (2.7-2.9 Ma; Fig. 5.11) obtained here for the majority of the M_1 garnets might then represent one of these plate tectonics-related events, or

the transition episodes from heat-pipe geodynamics modelled by Beall et al. (2018) (Fig. 4.2c). The hairpin-like shape of the P-T-X-D path obtained for the ISB (Fig.4.11) must be accommodated within the model of Nutman et al. (2015).

6.1.3 Constraints in M_2 and M_3

Although a majority of the discussions and data of this work concentrate on the metamorphic record of M_1, mineralogical and microstructural descriptions, along with quantitative chemical and geothermometric data on the metamorphic signatures of M_2 and M_3 have been reported.

In this work, M_2 is mainly associated with the inclusion-poor garnet rims (e.g. Fig. 1.4, 1.5, 1.6, 3.2, 3.4). As previously reported (e.g., Boak and Dymek, 1982; Rollinson, 2002, 2003; Gauthiez-Putallaz et al., 2020), their timing relative to deformation is interpreted to be post-tectonic, reflected by the clear overgrowth of the foliated fabrics (e.g. Fig. 1.4, 1.5, 1.6, 3.2, 3.4). Garnet-biotite thermometry presented in this (Fig. 2.7b) and earlier works (Fig. 2.1; Boak and Dymek, 1982; Rollinson, 2002, 2003) suggest garnet rim growth at lower temperatures compared to M_1 (<540 vs 550-600 °C). The timing of the post-tectonic metamorphism M_2 is, however, constraint with the U-Pb dating of post-tectonic titanite (5.2f,h). The Neoarchean age (2584.9 ± 98.3 Ma, Fig. 5.8f) is also consistent with previous interpretations that argue that the M_2 must be younger than 2.7 Ga, due to cross-cutting relationships (Fig. 5.11; Nutman et al., 2015). Therefore, the characterization of M_2 presented here confirms earlier reports, but the descriptions provided here shed some additional light on metamorphic processes related to M_2 that have, until now, been poorly explored. For example, post-tectonic garnet growth processes are most likely different to those documented for the inclusion-rich cores (c.f. Chapter 3). Although both seem to be controlled by former microstructures and local chemistry, growth of the inclusion-rich core is facilitated by the availability of reactants and growth along non-reactant phases like quartz of calcite (c.f. Chapter 3). On the contrary, rim growth is almost inhibited in zones where quartz is present

and enhance close to foliated Fe-Mg minerals (e.g. Fig. 3.2, 3.4), creating asymmetric microstructures in the garnet grains. Composition of the fluids and/or the different P-T conditions during garnet growth might be responsible for the change in the garnet growth mechanisms. Garnet growth related to the presence of fluids has already been reported by Blichert-Toft and Frei (2001), who found garnets growing within carbonate veins. Additionally, a garnet-carbonate vein, where garnet facets are growing towards the centre of the vein (Fig. 2.5a), is reported in this thesis (Chapter 2). This observation suggests that not all the carbonate fluids within the ISB are related to low-temperature retrogression events.

Fluid-present low temperature retrogression episodes indeed affected the ISB. In this thesis, they are summarized and referred to as M_3. For simplicity, they are commonly addressed as a single event throughout the text, although they most likely reflect different pulses of fluid infiltration. Evidence of fluid infiltration is common in the field, appearing as calcite-quartz veins that are also visible in the thin section scale (Webb et al., 2020). They affected the prograde fabrics and mineral assemblages, creating quartz-calcite pseudomorphs after garnet (Fig. 1.5c), chloritization of prograde minerals like biotite (Fig. 1.5e,g,h) and retrogression of samples leaving few relics of the former minerals. They are <2200 Ma (Fig. 5.11), as interpreted by the re-equilibrated U-Pb rutile ages reported in chapter 5 (Fig. 5.8c-e). The literature lacks a structural characterization of the different vein families, as well as a detailed description of their chemistry and mineralogy. A better understanding of these geological features will enhance our understanding of the retrograde and exhumation history of the ISB.

6.1.4 Potential limitation and bias: Can we extrapolate the results to underrepresented areas of the ISB?

The ISB is comprised of two volcanosedimentary sequences of 3.7 and 3.8 Ga (Fig. 2.1, 3.1, 4.1, 5.1). Interpretations of the geological record of the belt rely on the data retrieved from both sequences. However, most of the data used for this thesis stem from samples within the 3.7 Ga section. This is mainly because most of the geology outcropping in Isua belongs to the

younger sequence, while outcrops of the 3.8 Ga sequence are rather scarce (see and Outcrop

geology map in Nutman and Friend, 2009). This bias is even more evident in the

metamorphic data provided so far (Boak and Dymek, 1982; Dymek et al., 1998; Dymek and

Klein, 1998; Hayashi et al., 2000; Komiya et al., 2002; Rollinson, 2002, 2003; Arai et al.,

2015; Gauthiez-Putallaz et al., 2020; Nutman et al., 2020; Waterton et al., 2022). The

metamorphic data, especially the quantitative data, is (1) concentrated in the 3.7 sequence and

(2) in the eastern arm of the belt (e.g., see summaries of data in Fig. 2.1 and 5.1). Then of the

P-T conditions obtained might not be valid for western arm and the 3.8 Ga sequence

This work is not an exception to this bias problem. All the rocks analysed in this thesis were

collected along the eastern arm of the belt (Fig. 2.1, 3.1, 4.1, 5.1), with only a couple of them

sampled within the 3.7 Ga tonalite (Fig. 5.1). Nevertheless, the methodology followed here

tried to account for changes in the eastern arm from north to south and from east to west in

both sequences. Moreover, a relative larger number of rocks from the 3.8 Ga sequence was

reported (i.e., 7 samples) compared to other works (e.g. 2 in Rollinson 2002, 2003). Thus, a

more comprehensive picture of the easter arm was obtained. The previous chapters showed a

homogeneity in the P-T conditions (Chapter 2), garnet formation processes (Chapter 3) and

P-T-X-D prograde evolution (Chapter 4) of the rocks across the eastern section. All of this

pointed to a similar metamorphic history of the rocks, that was previously clouded by

retrograde processes (e.g., chloritization of foliated prograde assemblages, section 2.4.2.1.,

Fig. 1.10c) or the diversity in garnet microstructures and zoning (see Chapter 3). Moreover,

Zuo et al. (2021b), using a twin sample set, showed that the strain was also homogenous

along eastern Isua. Nevertheless, the question remains: is it possible to extrapolate the results

obtained here to the western arm? The scarce data from that region suggest that it is.

Garnet-biotite thermometry applied to three metapelites in the western 3.8 and 3.7 Ga

sequences, revealed 550-610 °C M_1 peak temperatures (Fig. 2.1; Rollinson, 2002).

Moreover, calculated Ti-in-Biotite temperatures in another sample in the western section returned a peak temperature of 578 °C (Fig. 2.1; Boak and Dymek, 1982). These values are within the range of the peak conditions obtained for M_1 in this thesis (550-600 °C, Chapter 2, 4), suggesting that all the belt indeed experienced the same metamorphic history. However, direct comparison of the pressure conditions to affirm this is not possible because quantitative data needed for pressure estimates for the western sections is still lacking. Some observations, however, might point to similarities in pressures as well. Both (Nutman et al., 1997) and Frei et al. (2002) reported the occurrence of aligned kyanite in rocks from the eastern 3.8 Ga section, that at 550-600 °C suggest minimum pressures of 0.5 GPa, again within the range obtained for rocks in the eastern arm (0.5-0.7 GPa, Chapter 2). Mineralogical descriptions of banded iron formations (Dymek and Klein, 1988) and metapelites (Rollinson, 2002) in both arms also reported similarities in the mineral assemblages that point to similar P-T conditions. But the petrological characteristics are not the only evidence of similarities between the two sections of Isua. Compilation of the measured lineations of the rocks across all the belt show that most of them have a similar dipping direction towards the SE (see Webb et al., 2020), suggesting they were deformed in the same tectonometamorphic event. Therefore, the metamorphic and structural data reported allows to confidently extrapolate the conclusions drawn from the eastern arm of the belt in this thesis: that all the ISB experienced a similar metamorphic evolution.

6.2 The nature of the igneous protoliths and their implications for the tectonic evolution of the ISB

The protoliths of the Isua are mainly of igneous origin. For instance, the ISB is mainly composed of meta-mafic rocks with boninitic and enriched tholeiitic affinities (Fig. 2.1, 3.1, 4.1; Polat et al., 2002; Jenner et al., 2009). They are most likely the source of the TTGs melts (Hoffmann et al., 2014, 2019; Gardiner et al., 2019) and thus they are genetically related to the majority of the rocks that outcrop in the Isua area. Therefore, an understanding of the

petrogenesis of their protoliths is pivotal to trace the tectonic evolution of the ISB. The meta-mafic rocks of the ISB display geochemical signatures typically found in arc-like settings such as negative Ta-Nb anomalies and enrichment in incompatible elements (Table 1.1; Gill, 2011). These signatures are commonly derived by fluids released from the subducting slab interacting with the mantle wedge (Gill, 2011). The recognition of rocks with arc-like geochemistry has been used to argue for the operation of subduction-style tectonics in Isua to produce the bulk of the supracrustal rocks (Polat et al., 2002; Jenner et al., 2009). However, a recent re-analysis of the trace elements and isotopic composition of the meta-mafic rocks of Isua argues that their chemistry can be explained by mixing of different Archean mantle reservoirs (Rollinson, 2021). Rollinson (2021) analysis centres around the geochemical signatures produced by different petrological processes such as fractionation of Hf and Nd in deep seated minerals. With this in mind, it is important to mention that although crustal recycling and fluid transport into the mantle is more efficient along subduction zones, these processes equally occur in non-uniformitarian tectonic models (e.g. Table 1.1; Fig. 1.3b-e). Consequently, the analyses provided for Isua so far, both uniformitarian and non-uniformitarian tectonics can explain the geochemistry of the meta-mafic rocks.

The chemistry of the meta-mafic rocks is directly linked to the generation of TTGs. Thermodynamic modelling has shown that the enriched tholeiites of Isua most likely represent the sources for the big intrusive bodies (Nagel et al., 2012, Hoffmann et al., 2014, 2019; Gardiner et al., 2019), However, there is still some debate on the geodynamic setting (see Nutman et al., 2022 and Ramírez-Salazar, Zuo et al., 2022). Some authors argue that they were produced at convergent margins due to the eclogitization of the subducting slab (Nutman et al., 1993, 1996, 2020). They also contend that the chemistry of zircons records the presence of paired metamorphism (Nutman et al. 2020), and therefore they should be an evidence of plate tectonics processes (Table 1.1., Fig. 1.3a). However, these assumptions are

made based on interpretations of a N-MORB source which is unlikely to be the parent to the TTGs in Isua (c.f. Hoffmann et al., 2019). Other authors agree than the TTGs were generated in an overthickened mafic crust (Hoffmann et al., 2014; Gardiner et al., 2019) that might suggest non-uniformitarian tectonics (Gardiner et al., 2019). Studying the meta-mafic rocks showing signs of partial melting will provide insights into the TTGs petrogenesis that will inform this controversy.

6.3 The larger picture: implications for Archean tectonics

The long-standing paradigm of the ISB argues that its geological record reflects the operation of subduction-driven processes (e.g. Boak and Dymek, 1982; Nutman et al., 1993; 1996, 2002, 2013, 2015a, 2015b, 2020, 2021; Komiya et al., 1999; Rollinson, 2002, 2003; Polat et al., 2002; Jenner et al., 2009; Nutman and Friend, 2009; Friend and Nutman, 2019; Guotana et al., 2021) and that, by extension, it is an evidence of the operation of plate tectonics (Fig. 1.3a) as early as the Eoarchean. Two of the main tectonic models discussed throughout these pages (Model A and B, Fig. 2.3, 4.2) proposed scenarios that agree with this interpretation. They are in line with the hypothesis that plate tectonics started in the early stages of the Earth's evolution (Korenaga, 2013, 2018; Maruyama et al., 2018; Nutman et al., 2021; Windley et al., 2021) and argue that Isua recorded some of the defining features of this type of geodynamics (see Table 1.1, Fig 1.3a).

As shown throughout this work, evidences of subduction are not indisputable and some of the features might be explained with alternative interpretations. For the case of the accretionary prism model (Model A, Fig. 4.2a), the supporting interpretation of the presence of duplex structures (Komiya et al., 1999) or an increasing metamorphic gradient (e.g., Arai et al., 2015) are incompatible with quantitative (e.g. Zuo et al., 2021b) and geochronological (c.f. Nutman et al., 2021) data retrieved from the belt. However, even if this model can explain the local geology of Isua, it should be used with caution when stating that it represents the onset of plate tectonics. It relies in the formation of a single subduction zone, and for plate tectonics

to be fully stablished in a planet, a global interconnected network of subduction zones must be operating (Table 1.1; Cawood et al., 2018, Lenardic, 2018, Stern, 2018). Moreover, numerical models have shown that local subduction zones can be developed within a sluggish lid environment (e.g. Fig. 1.3e; Fischer and Gerya, 2016; Sizova et al., 2015) or stagnant lid scenarios (Table 1.1.; Moore and Webb et al., 2013). Sluggish lid geodynamics later in the Paleoarchean have already been suggested to explain the evolution of Pilbara (e.g. Van Kranendonk, 2010, 2011) and Barberton (e.g. Brown, 2015, Sizova et al., 2015; Francois et al., 2018), thus they might have operated during the Eoarchean. In summary, if the ISB is the record of a single subduction zone where an accretionary prism is formed, it most likely represents a local event, rather than the evidence of a planet dominated by horizontal tectonics.

The orogeny model (Model B, Fig. 4.2b) is supported by the interpreted coexistence of different features that are characteristic of plate tectonic environments (c.f. Table 1.1, Fig. 1.3a). It invokes multiple subduction events affecting the rocks of Isua at different times (e.g. Nutman et al., 2013; 2015; 2020) and thus it might prove that a long-lived subduction network might have already been stablished during the early Archean. However, the arc-like chemistry of the protoliths (e.g. Polat et al., 2002), the apparent tectonic origin of the ultramafics (e.g. Friend and Nutman, 2011) and their interpreted (U)HP metamorphism (e.g. Nutman et al., 2020) can all be alternatively explained by other processes and therefore cannot be uniquely linked to plate tectonic processes. Furthermore, the geological record of the ISB is not in agreement with other plate tectonic signatures (table 1.1) that were predicted by the model such as the juxtaposition of rocks with different metamorphic history and grades (c.f. Chapter 2-4), instead all the belt shows the same P-T conditions, or the presence of tectonic breaks (c.f. Zuo et al., 2021b).

The metamorphic and structural predictions of the heat pipe model (Fig. 1.3b, 2.3c, 4.2c;)

seem to be fulfilled with the quantitative analysis provided here as well as in Webb et al.,

2020 and Zuo et al., 2021b, where the same set of samples and sites were analysed. The

conditions of the early Earth are thought to be similar to those of Io (O'Reilly and Davies,

1981). The heat-pipe model is thus theoretically possible (Moore and Webb, 2013) and it

does have real life examples, despite this being subject of controversial views by other

authors (e.g. Windley et al., 2021). The data of the ISB is then in agreement with non-

uniformitarian models. However, a source of justified critique is that many of the

observations supporting a heat-pipe mode are indirect. For example, yet we do not have direct

compositional measurements of the major, trace and isotopic compositions of rocks forming

within a heat-pipe scenario. Moreover, if M_1 occurred during the Meso-Neoarchean (c. 2.7-

2.9 Ga; Fig. 5.11), the deformational phase directly attributed to the heat pipe evolution as

proposed by Webb et al. (2020) might be difficult to accommodate, since the simulations of

the end and/or period of transition of the heat pipe model end at c. 3.0 Ga (e.g. Beall et al.

2021).

I would argue, however, that the characteristics of the ISB point to an evolution in a non-

uniformitarian scenario, where local development of subduction zones might be possible. The

ISB shows no important tectonic breaks (Zuo et al., 2021b), its structural features show that it

was folded contemporaneous to the metamorphism in a km-scale sheath fold (Webb et al.

2020) and all the rocks seem to have followed the same metamorphic history (c.f. Fig. 4.11)

as it was a single coherent unit. The Meso-Neoarchean period seems to be a stage of

transition in the geodynamic regime of the Earth (e.g. (Condie, 2018), as suggested by

multiple lines of evidences pointing to the onset of plate tectonics between 3.0-2.5 Ga (e.g.

Brown, 2006; Van Kranendonk, 2011; Gerya, 2014; Sizova et al., 2015; Brown and Johnson,

2018; Cawood et al., 2018; Holder et al., 2019; Hawkesworth et al., 2020; Palin and Santosh,

2020; Palin et al., 2020b), where vertical and horizontal dominated geodynamics might have coexisted or dominated episodically. The ISB then provides a window to non-uniformitarian processes and/or an Earth in transition. Models testing vertical tectonic processes such as sagduction or local subduction might expand the possibilities to explain the characteristics of the ISB.

6.4 Final conclusions

This thesis represents a comprehensive study on the metamorphic evolution of the Isua supracrustal belt. It provides a large new dataset retrieved from the combination of multiple techniques and approaches suggesting that the ISB evolved in a non-uniformitarian tectonic regime. These data will inform and, hopefully, encourage further discussion and interpretation of the tectonic and geological record of the ISB. Moreover, this work also discussed important aspects on the different interpretations of the ISB that were largely missing in the literature. In summary, the data and observations show that:

- The rocks across the ISB experienced a nearly homogenous syn-tectonic amphibolite facies metamorphism (M_1) at 550-600 °C and 0.5-0.7 GPa (Fig. 2.10). Quantitative and qualitative inspection of the syn-tectonic record of the garnets of the ISB show that it experienced an initial near isothermal path from 0.46 GPa to 0.7 GPa at c. 550 °C followed by a pressure decrease to 0.61 GPa while temperatures increased to up to 580 °C, falling within the peak range (Fig. 4.11). This P-T-X-D characterization shows that prograde metamorphism was accompanied contemporaneous to the development of opposite shear senses along the belt (Fig. 4.11), which are inferred to represent a syn-metamorphic sheath folding event (Webb et al., 2020; Zuo et al., 2021). Preliminary geochronological results suggest M_1 occurred either in the Paleoarchean (c. 3300 Ma, Fig. 5.11) or in the Meso-Neoarchean (2700-2900 Ma, Fig. 5.11). If the metamorphism occurred in the Paleoarchean, the metamorphic record favours the heat-pipe evolution (Fig. 1.3b) and then supports the hypothesis of an

early Earth with non-uniformitarian geodynamics. If M_1, however, occurred later in the Archean the metamorphic record of Isua might reflect an evolution in a planet in a transitional regimen of geodynamics.

- Previous contrasting metamorphic histories interpreted based on the garnet microstructural and chemical record (Rollinson, 2002, 2003; Gauthiez-Putallaz et al., 2020) are not compatible with data and observations presented in this thesis. Instead, the detailed analysis of the porphyroblasts shows that their characteristics are controlled by the (local) chemistry and microstructures of the rocks, which ultimately affect the availability of garnet forming reactants. Thus, the garnet record cannot be used to distinguish different zones within the belt as being the result of distinct metamorphic histories.

- The syn-tectonic metamorphism (M_1) was followed by a post-tectonic (lower) amphibolite facies (≤ 540 °C and ≤ 0.5 GPa; Fig. 2.10) tectonothermal event (M_2). It is recorded by the presence of inclusion-poor rims of garnets and the appearance of titanite overgrowing the foliation. In-situ U-Pb titanite dating provides a minimum growth age of 2584.9 ± 98.3 Ma (Fig. 5.11), with a maximum age (c. 2.7 Ga) provided by the crosscutting N-S Ameralik dykes (Fig. 5.11). The interpretations on M_2 are consistent with findings of previous works regarding the post-tectonic interpretation and the timing of metamorphism (e.g. Gauthiez-Putallaz et al., 2020).

- Low-grade retrogression (M_3) was distinguished in late quartz-calcite veins, garnet pseudomorphs and chloritization (Fig. 2.10c). Fluid infiltration most likely occur <2220 Ma (Fig. 5.11) and affected the entire belt, probably at a larger scale in the northeastern part. The extend of this fluid influx and associated retrogressive features is based on the dataset of this thesis heterogeneous. Retrograde features like the

chloritization could explain the misinterpretations of metamorphic gradients from north to south.

- Igneous-metamorphic processes were also reported. For the first time, the analysis of microstructures and the metamorphic record of the enclaves within the 3.7 Ga tonalite show that they experienced local contact metamorphism contemporaneous to partial melting. Contact metamorphism in the enclaves occurred at 3.60-3.68 Ga (Fig. 5.11) at it seems to not be recorded in the supracrustal rocks. Moreover, characterization of a garnet-bearing meta-granite shows that the magmatic garnet crystallized at c. 3.55 Ga (Fig. 5.11), which extends the time of extends the time of granite emplacement to younger ages.

This thesis thus provides a robust characterization of the metamorphic record of the ISB in its tectonic and geochronological context that can be used to refine the tectonic models proposed for the belt. However, some questions remain open and further work is needed to answer gaps in our knowledge of the ISB and in extension of early Earth tectonics which are highlighted below

6.5 Open Questions and future work.

Some questions and avenues of research that are needed to resolve the question of early earth geodynamics of Isua as an example for Early Earth as a whole are summarized below:

What are the petrological and tectonic processes controlling the geochemical signatures in the Archean meta-igneous rocks? Arc-like chemistry in the Archean meta-igneous rocks is typically associated to subduction processes (e.g. Polat et al. 2002). This is because in the present Earth, fluids are mainly transported to the mantle through subduction and are released to the mantle wedge to create the typical arc chemistry (Gill, 2011). However, differences in geochemical signatures of samples from different domains blur when considering older samples (Condie and Kröner, 2008; Moyen and Laurent, 2018). Moreover, in the Archean

Earth, other vertical processes like sagduction, dripping and delamination could have transported fluids and recycled crust to the mantle to account for the arc-like chemistry. Petrological processes like element fractionation might explain some of these features (e.g. Rollinson, 2021). To fully compare the impact of the possible Archean tectonic processes and the petrological processes to those occurring in the present, quantification and experiments must be conducted. This information will clarify important aspects of the geochemical record debated on the Archean geodynamics.

Can we run numerical models to understand the evolution of Archean terranes? General numerical models have been reported to describe the characteristics of the Archean Earth (e.g. Sizova et al., 2015; Francois et al. 2018). Specific models for the characteristics of the terranes might provide additional insights. Rheological, compositional, temporal, and structural directly from the field to run models closer to reality.

Can we obtain data from future space exploration missions? The lack of real-life rock examples weakens the interpretations and predictions of the non-uniformitarian models. Remote or in-situ chemical, mineralogical and structural analysis of rocks from rocky bodies like Io will provide valuable insights to advance non-uniformitarian models.

When did M_1 occur? A detailed inspection and quantification of the accessory minerals in the garnets and the matrix is needed to clarify the spread in Lu-Hf and Sm-Nd ages obtained with the garnet supracrustals (Fig 5.11). It is pivotal to fully comprehend the implications of the tectonic evolution of the ISB for the Archean geodynamics.

Does the western arm of the ISB experienced the same metamorphic evolution described here? Qualitative data points to an affirmative answer (see section 6.1.4), but a larger quantitative dataset set is needed to confirm it.

What is the role of the supracrustal rocks in the genesis of the TTGs and what can we learn from the in-situ melting of the enclaves? Thermodynamic modelling has shown that

the enriched tholeiites of the ISB are most likely the sources of the TTGs (e.g. Hoffmann et al., 2019), but no direct measurements have been performed to relate the two lithologies. Fortunately, enclaves within the tonalites show partial melting (micro)structures that could shed light on the TTG petrogenesis of the Isua area. The enclaves reported so far are garnet amphibolites (within the 3.8 Ga intrusive, Hoffmann et al., 2014), garnet-pyroxene rocks (within the 3.7 Ga intrusive, Nutman et al., 2013) and titanite-bearing amphibolites (within the 3.7 Ga intrusive, this work). These rocks have minerals (e,g. garnet, titanite, amphibole, clinopyroxene) that partition the bulk trace elements content in the TTGs. Their characterization might provide quantitative data to understand the processes and conditions of formation of the TTGs. Moreover, garnet growing contemporaneous to melting is a good reservoir for primary melts in melt inclusions (Cesare et al., 2009). A detailed inspection of garnets in partially melted rocks might reveal invaluable data to understand early TTGs genesis processes.

Why didn't the supracrustal rock record the contact metamorphism? No record of contact metamorphism has been documented so far in the supracrustal rocks despite their relatively small size when compared to the intrusive TTG bodies. The mechanisms of emplacement of the TTGs might shed some light on this. Further in-depth study of the contact between the supracrustal belt and the TTGs may help answering this question. For example, are the TTGs emplaced in small batches or sheets over a long time which would result in low regional metamorphic grades? Could thermal modelling assess this possibility?

What is the magmatic, metamorphic, and structural history of the Ameralik dykes? The Ameralik dykes are important indirect constraints to interpret the geochronological data retrieved from the supracrustal rocks. The classic interpretation argues that the E-W dykes have a crystallization age of 3.2-3.5 Ga (White et al., 2000, Nutman et al., 2004). However, based on the structural observations pointed out by Nutman et al. (2022), Ramírez-Salazar et

al. (2022) suggested their emplacement might have occurred in the Neoarchean. To fully test this hypothesis, a detailed characterization of the Ameralyk dykes is needed. Zircon geochronological data of a larger suite should be obtained. Additionally, structural information on the field and detailed microstructural work of the igneous and metamorphic mineral assemblages and fabrics will provide information on the deformation and its relative time to the deformation in the belt. The dykes are reported to have metamorphic minerals such as epidote and garnet (e.g. Nutman, 1986). Thus, P-T conditions can be retrieved from them using phase equilibria and geothermobarometry along with other independent methods like quartz-in-garnet (Kohn, 2014) or quartz-in-epidote elastic barometry (Cisneros et al., 2020). Understanding the history of the Ameralik dykes from their crystallization to their metamorphism will provide valuable insights into the geological evolution of the ISB and will facilitate the interpretations of the metamorphic record.

What is the magmatic, metamorphic, and structural history of the granites in the Isua area? The granites in the Isua area have been commonly used to constrain the timing of M_1 to 3.66-3.60 (e.g. Nutman and Friend, 2009). However, no evidence of M_1 older to 3.3 Ga was found in this work and the geochronology of magmatic garnet expands the emplacement of the granites to 3.55 Ga (Fig. 5.11). Moreover, a compilation by Zuo et al. (2021) (in their supplementary material) shows that most of the dykes are concentrated along the 3.7 Ga tonalite and 3.7 Ga supracrustal sequence. Hence, larger extrapolations of the crosscutting relationships to the bulk of Isua should be taken with a pinch of salt. Finally, no reports of metamorphic assemblages have been presented before this thesis. The Al-rich association in this S-type granites would allow to obtain a detail P-T history that could be compared to the rest of Isua. Can we draw parallels to the S-type granites of the New England belt in Eastern Australia (Pankhurst et al., 2000; Craven and Dackzo, 2018; Zhu et al., 2020)

What is the metamorphic record of the ultramafic rocks of the ISB? The presence of Ti-humites in the ultramafic rocks of the ISB might point to (U)HP conditions and therefore might suggest tectonic breaks associated with plate tectonic movements (e.g. Nutman et al., 2020; Goutana et al., 2021). However, the presence of carbonates associated with the Ti-humites (Ramírez-Salazar, Zuo et al., 2022) might suggest lower P conditions. A combination of experimental work and P-T calculations will clarify the metamorphic evolution of the ultramafics and thus help discern between a mantle origin (UHP) or a cumulitic origin sharing a similar metamorphic evolution with the rest of the belt.

What is the role of fluids in the different metamorphic events recorded in the ISB and in the general geological record of the belt? The observations presented here and in other works (e.g. Blichert-Toft and Frei, 2001) show that different generations of fluids affected the ISB. They are correlated with M_2 (e.g. Fig. 1.5a) and M_3, and they also seem to have affected structures at the outcrop scale (Allwood et al., 2018) previously interpreted as the earliest stromatolite relics (Nutman et al., 2016). A systematic field study on the different generations of veins and sampling to study their mineralogy and geochemistry is worth pursuing. The characterization of the fluids, their time of infiltration and the pathways the follow could help us understand how they affected the characteristics of the rocks in the ISB. Moreover, quantification of the distribution of the veins and fluid-related features can test the hypothesis that retrogression is more pervasive in the northeastern area (c.f. Webb et al., 2020, Chapter 2).

What are the petrological processes that controlled the growth of minerals and microstructures of M_2 and M_3? Fluids probably enhanced the growth of minerals associated with M_2 and M_3. Understanding the petrological processes behind this growth can shed light on the metamorphic evolution of Isua and larger problems in metamorphic petrology. For example, the garnet-calcite vein (Fig. 1.5a) could help us understand fluid-related garnet

growth. Moreover, the common presence of chloritization of biotite in the belt (Fig. 1.5e) to the point that some rocks are completely chloritized (e.g. Fig. 1.5h) could shed some light on the crystallographic processes of replace minerals while preserving the microstructures, and might provide some insights in the metamorphic preservation problem.

The Isua supracrustal belt is a great example to explore metamorphic processes and understand the early Earth. Its metamorphic record should be further study in more detail to clarify important questions in the Earth Sciences.

APPENDIX A – Supporting information for Chapter 2

A1 Introduction

This document contains details on the methodology used to obtain the data for Chapter 2, as well as a description of the chemical data and supporting figures.

Samples used for this study were collected in a fieldwork campaign in the Isua supracrustal belt area during the summer of 2017. During this campaign four different sets of samples were collected with different general objectives: "TM" samples were collected for metamorphic studies and make most of the samples used in this study; "JZ" samples were collected for (micro)-structural research, and are the samples used in the companion studied (Zuo et al., 2021b); "AW" samples were collected to target the protolith and origin of the ultramafic rocks; and "PH" samples represent some sites in the supracrustal rocks and the TTGs. The four set of samples share rocks collected from the same outcrop. Such samples share the same name and differ only in the prefixes. For example, samples TM17714-5A and JZ17714-5A were collected from the same lithology and outcrop, in close proximity to each other (typically within a meter), such that they can be considered twin samples. Most of the petrographic, bulk-rock composition and mineral chemistry data presented in this study are part of the TM dataset, however, we also present mineral and geothermometry data from the JZ data set

(JZ17729-1A, JZ17801-4, JZ17715-5F, JZ17715-9, JZ17715-16A, JZ17717-5, JZ17726-4, JZ17725-2c). This chapter 2 and Zuo et al. (2021b) provide both structural and metamorphic information on similar rocks sets.

We conducted a detailed study on twenty-three, mostly garnet-bearing samples of three different lithologies, including felsic, mafic, and (mafic)-metapelites collected along several east-west transects across the eastern arm of the Isua Supracrustal Belt (ISB) (Fig. 2.1). All samples were cut parallel to the lineation and perpendicular to the foliation. After detailed petrographic characterization, we selected seventeen samples for mineral compositional characterization and eight samples were processed for bulk rock major chemistry.

A2 Methodology.

A2.1 Mineral chemistry

Backscattered electron (BSE) images and the energy-dispersive X-ray spectroscopy (EDS) compositional maps were acquired with the Tescan VEGA 3 XM Scanning Electron Microscope (SEM) at the University of Leeds. The EDS maps were acquired with an accelerating voltage of 20kV and 20 nA current.

We processed the EDS compositional maps using the software XMapTools version 3.3.1 (Lanari et al., 2014). Using eleven randomly-selected points to calibrate the quantitative compositional map (Figs. 2.6) for garnet in samples 714-5E. To generate the compositional profiles along the transects in both garnets, we employed the tool "integrated lines (stripe)" which uses a central line as a reference and a given width to generate a rectangle, calculates the mean composition of all the points perpendicular to the central transect, and returns a plot showing the mean composition and the standard deviation for each point along the transect (Figs. 2.6b).

Major mineral compositions were measured by Jeol 8230 Electron Probe Micro Analyzer (EMPA) at the University of Leeds and by Jeol JXA8200 EMPA at the University of Graz. Analyses were performed under 15kV accelerating voltage, 20 nA current, and a 1 µm beam size for garnet and amphiboles, and a 5 µm defocused beam for micas and feldspars.

A2.2 Methodology. Bulk rock chemistry and phase equilibria modelling

Eight samples were dried overnight at 100 °C and a separate 1-2 g of sample was left overnight 1025 °C in order to calculate loss of ignitions (LOI). A mix 0.4 g of dried sample and 4.0 g of 66% Li tetraborate-34% metaborate flux in platinum +5% gold alloy crucible was prepared to carry the fusion of each sample; before fusion 1-2 drops of lithium Iodide solution were added to the mix. The mixtures were fused in the furnace at 1150 °C for 20 minutes, taken out and swirled gently after 10 and 15 minutes and at the end of the procedure to ensure a proper mixing before cooling. The fused glass beads were used to obtained major bulk rock chemistry, acquired by X-ray fluorescence analysis using a Rigaku ZSX Primus II spectrometer. Major elements bulk chemistry is shown in table

We assume that the bulk rock composition obtained with XRF analysis represents the reactive bulk rock composition that generated the minerals described in the thin sections. Following this logic, a total of eight isochemical phase diagrams (Fig. 8 & S6) were calculated using Perple-X software version 6.8.6 (Connolly, 2005) that contains the database of (Holland & Powell, 2011). The calculations for mafic samples (725-3a and 731-2a) were performed in the NCKFMASHTO system. For the rest of the samples, Mn was added to the modelling using the following a-x models: chlorite, garnet, orthopyroxene, mica, biotite, chlorite, staurolite, chloritoid, cordierite (White et al., 2014), epidote (Holland & Powell, 1998; 2011) , clinopyroxene (Green et al., 2007), ilmenite (White et al., 2000), plagioclase (Newton et al., 1980) and amphibole (Diener & Powell, 2012). The calculations were made assuming saturated H_2O conditions for all samples and a 5% content of Fe_2O_3 to calculate O_2 (Table A2).

A3 Results. Mineral chemistry

Garnets in all the rocks are typically almandine-rich crystals ($X_{Alm>55}$) with varying content in grossular ($X_{30}^{Gro}_{-2}$) and spessartine ($X_{25}^{Sps}_{-0}$) and a relatively narrow range of pyrope ($X_{15}^{Sps}_{-2}$) (Fig. A3a). For the meta-volcanic rocks, the content of almandine is higher in the southernmost samples (725-2c and 726-76A) when compared to their counterparts in the centre and northern part of the ISB (Fig. A3a). Biotite compositions of samples across the belt yield Ti-contents ranging from 0.15 to 0.30 (apfu) with no systematic correlation to their spatial location (Fig. S3b; Data set 2). The observed variation in Ti-content in each individual sample is typically small (c. 0.05), except for ilmenite-poor samples (717-5, 724-5A and 801-9A) that display a larger spread (Fig. A3b). Amphibole compositions in three samples (725-3a, -2b) from the southernmost part of the ISB and two from the northern part of the ISB (729-1B and 720-8) were measured. (Ramírez-Salazar et al., 2020a). All amphiboles are classified as members of the Ca-rich group plotting mainly in the hornblendetschermakite fields (Fig. APP-C3c) with no clear systematic geochemical difference associated with their geographic location. Amphibole formula calculations were made using the spreadsheet from Locock, (2014). Plagioclase compositions measured in samples 17729-1B, and 801-9A have albite-rich contents ($X_{Ab} > 0.65$) and samples 717-5 and 725-3A are rich in anorthite ($X_{An} > 0.85$; Ramírez-Salazar et al. 2020a). Mineral chemistry data can be found in Ramírez-Salazar et al. (2020a)
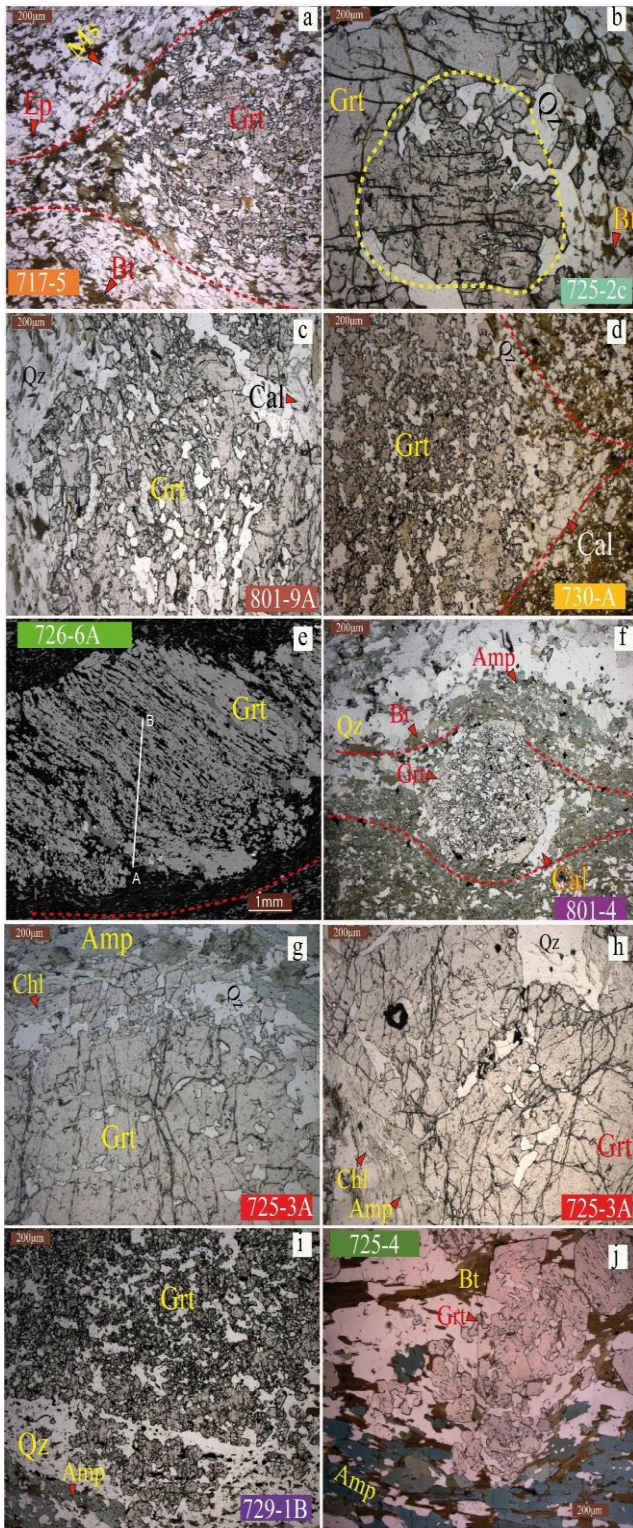
Figure. APP-A1 Photomicrographs of various garnet microstructures described in the Chapter 2. (a) Skeletal garnet showing a development of arc-like inclusion trails. (b) Garnet showing inclusion-rich core and inclusion-poor rim. (c) garnet showing curved inclusion trails. (d) skeletal garnet. (e) sheared garnet. (f) garnet showing randomly oriented inclusions and a small inclusion-poor rim. (g) and (h) big garnet porphyroblasts in mafic amphibolite. (i) Skeletal garnet. (j) garnet with curved inclusion trails, slightly resembling spiral-like shapes. Scale in all images is the same, except in (e). Red dotted lines indicate external foliation
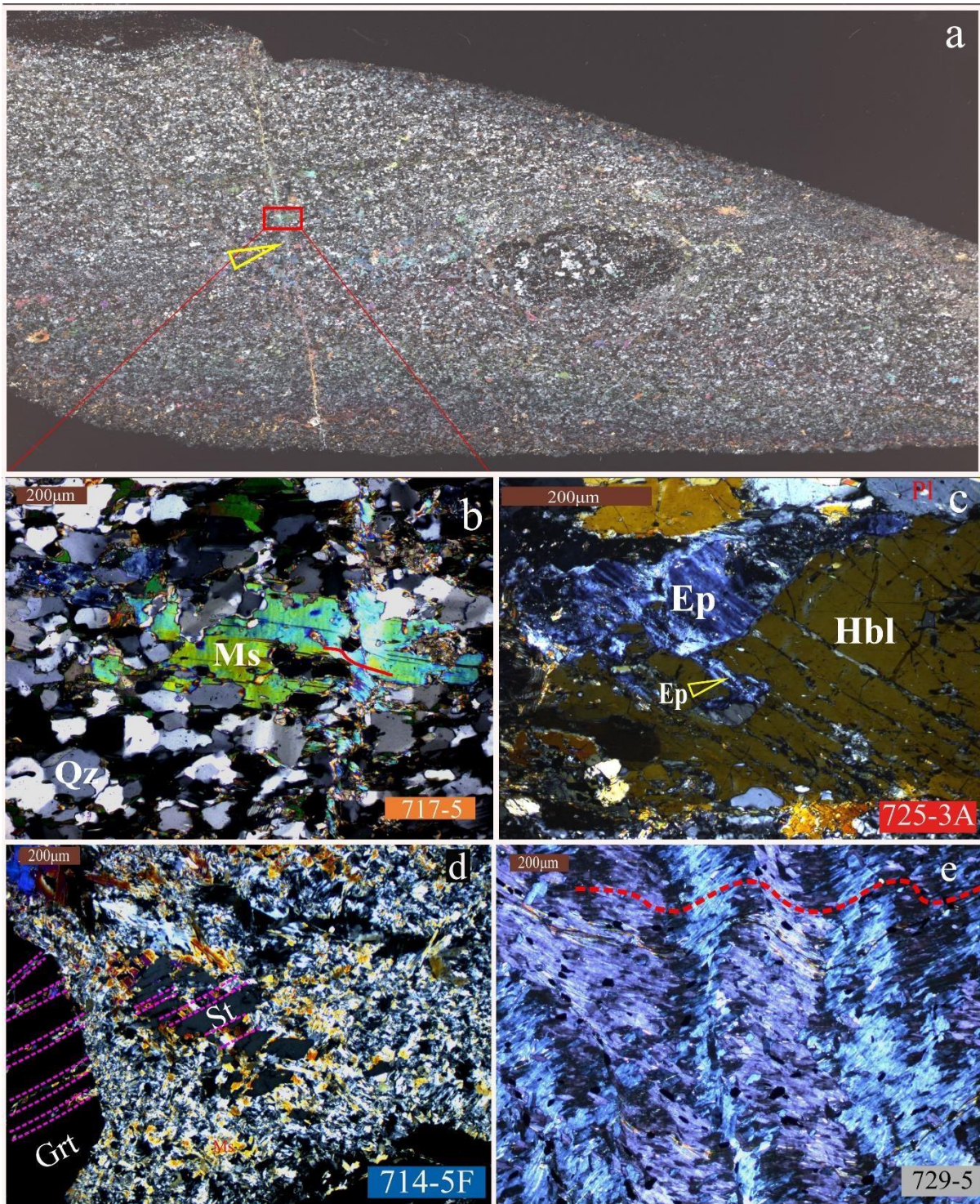
Figure. APP-A2 Photomicrographs of (a-b) sheared vein of muscovite cross-cutting the foliation; (c) Epidote/clinozoisite overgrowing amphibole, (d) muscovite replacing staurolite, and (e) crenulation cleavage in an extremely chloritized sample. Scale in all images is the same, except in (a). Red dotted lines indicate external foliation, dark pink dotted lines late fractures/veins.
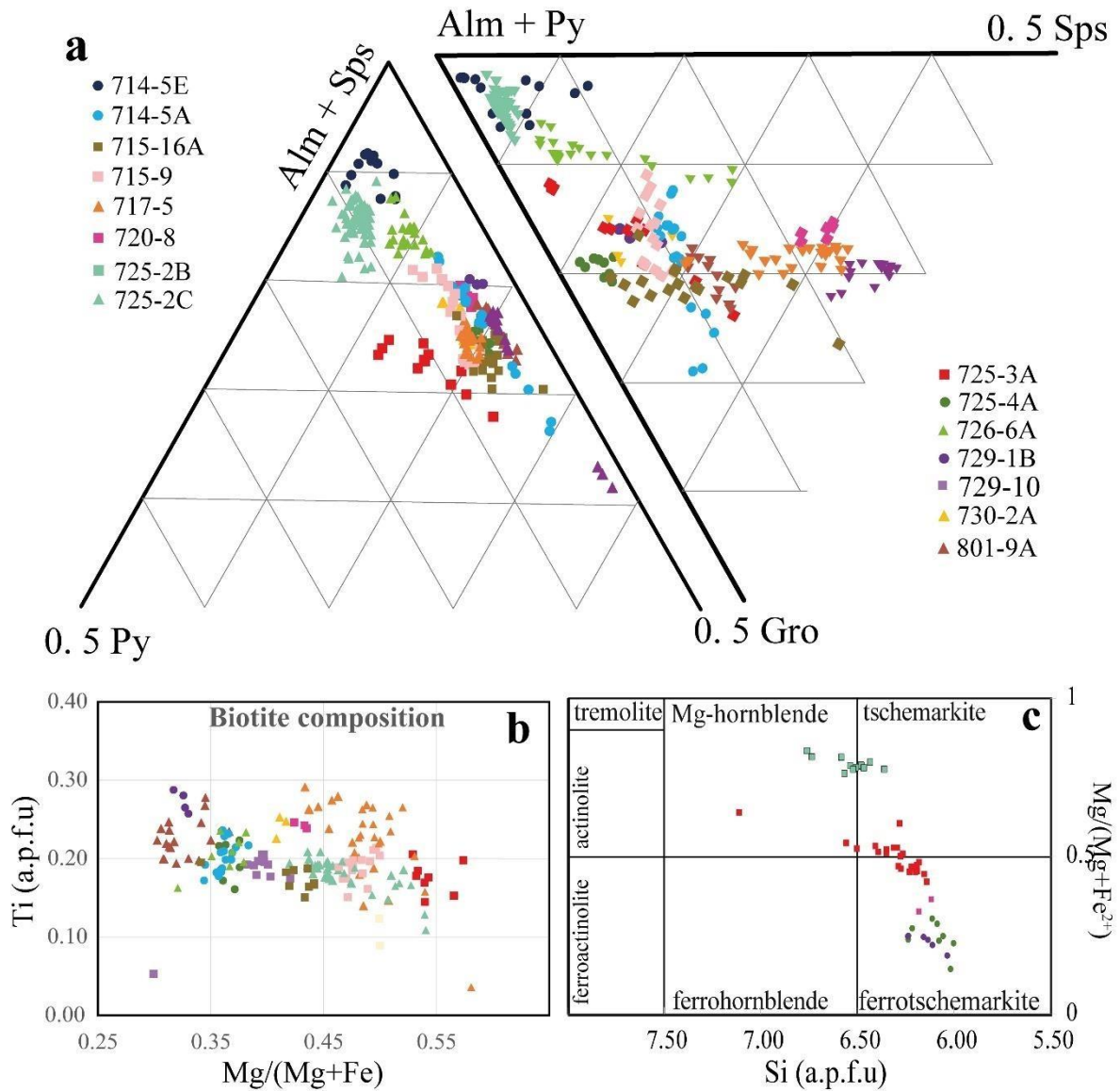
Figure APP-A3 Plots depicting the compositional variation of minerals from the ISB samples including (a) garnet ternary diagrams; and (b) biotite; and (c) Ca-amphibole classification (after Leake et al., 1997)
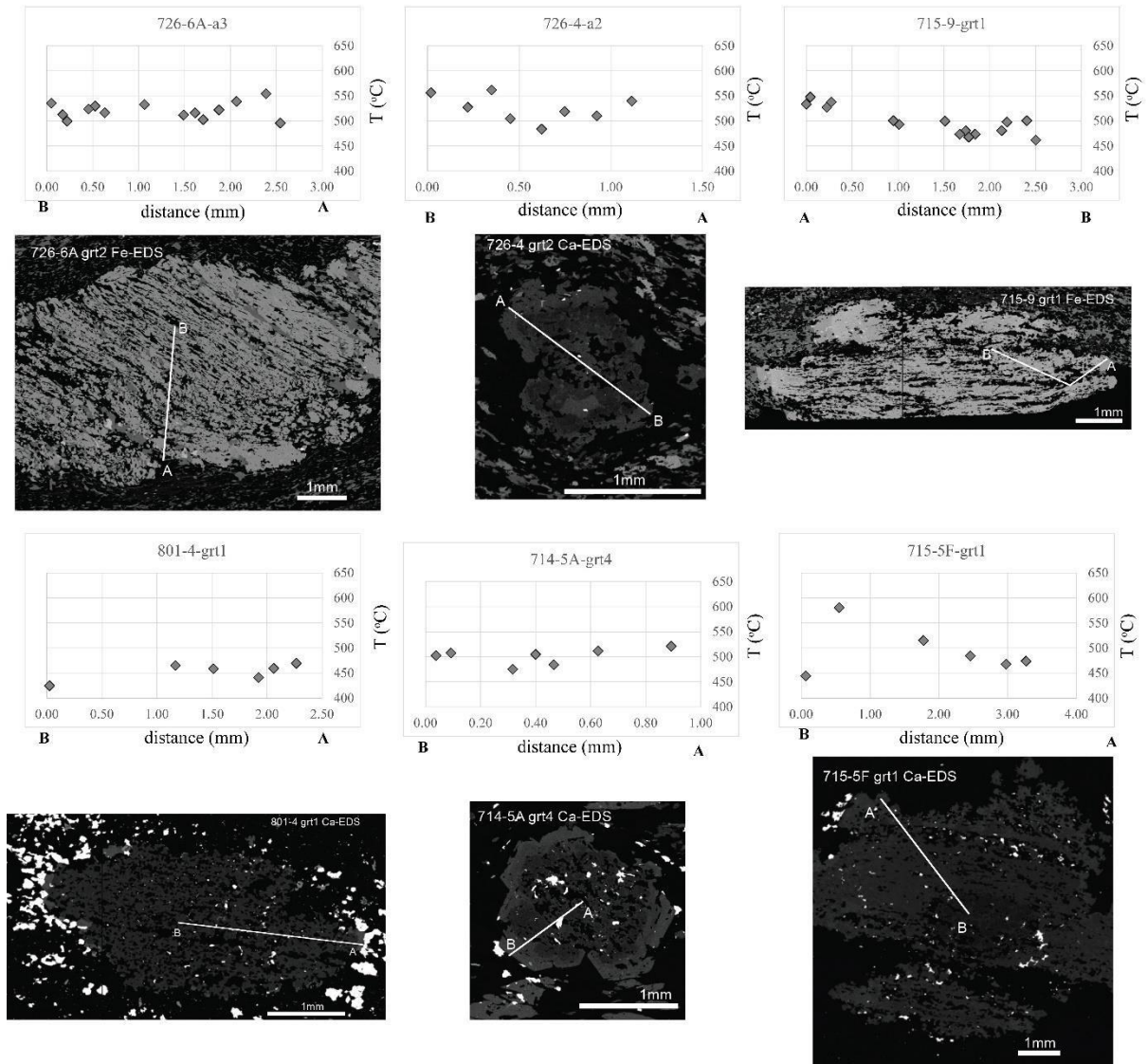
Figure APP-A4 Backscatter electron images and plots of garnet-biotite pair temperatures (Perchuk & Lavrent'eva, 1983) along transects.
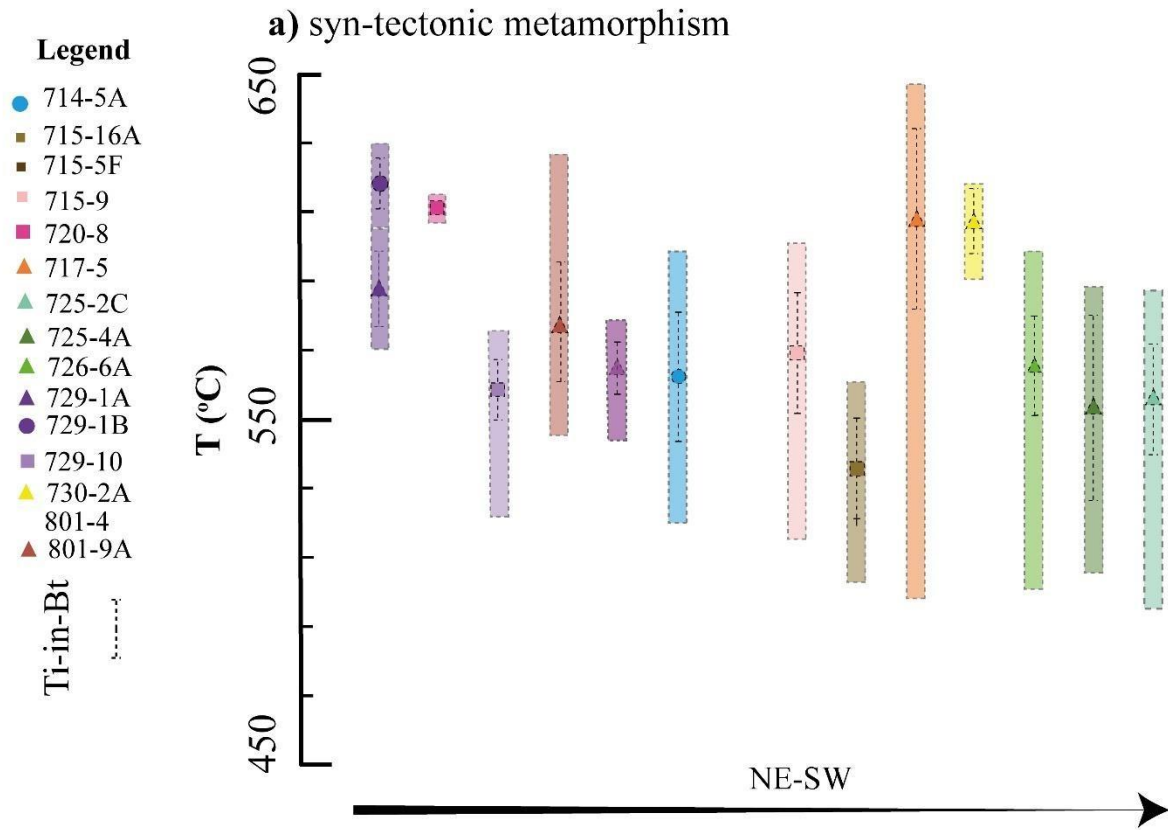
Figure APP-A5 Ti-in-Bt (Henry et al., 2005) temperature ranges (boxes) and mean temperature values (motifs with error bars).
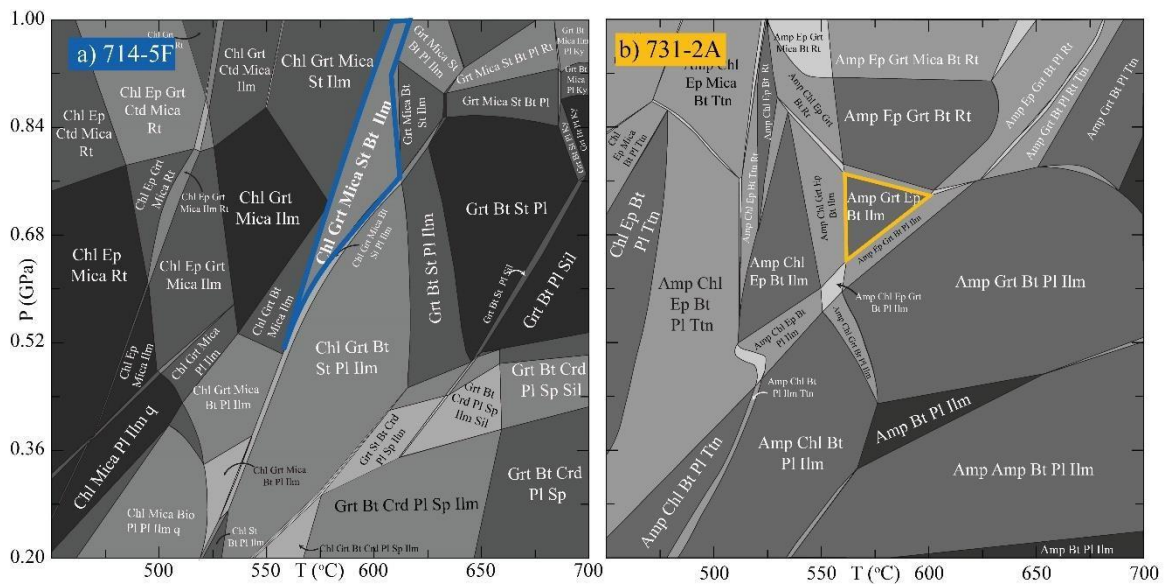
Figure A6 Isochemical phase diagrams calculated using Perple_X (Connolly, 2005) in the MnNCKFMASHTO system. All diagrams were calculated assuming a water saturated system and Fe2O3 = 5%. All fields contain quartz. Mineral abbreviations are after Whitney & Evans (2010)
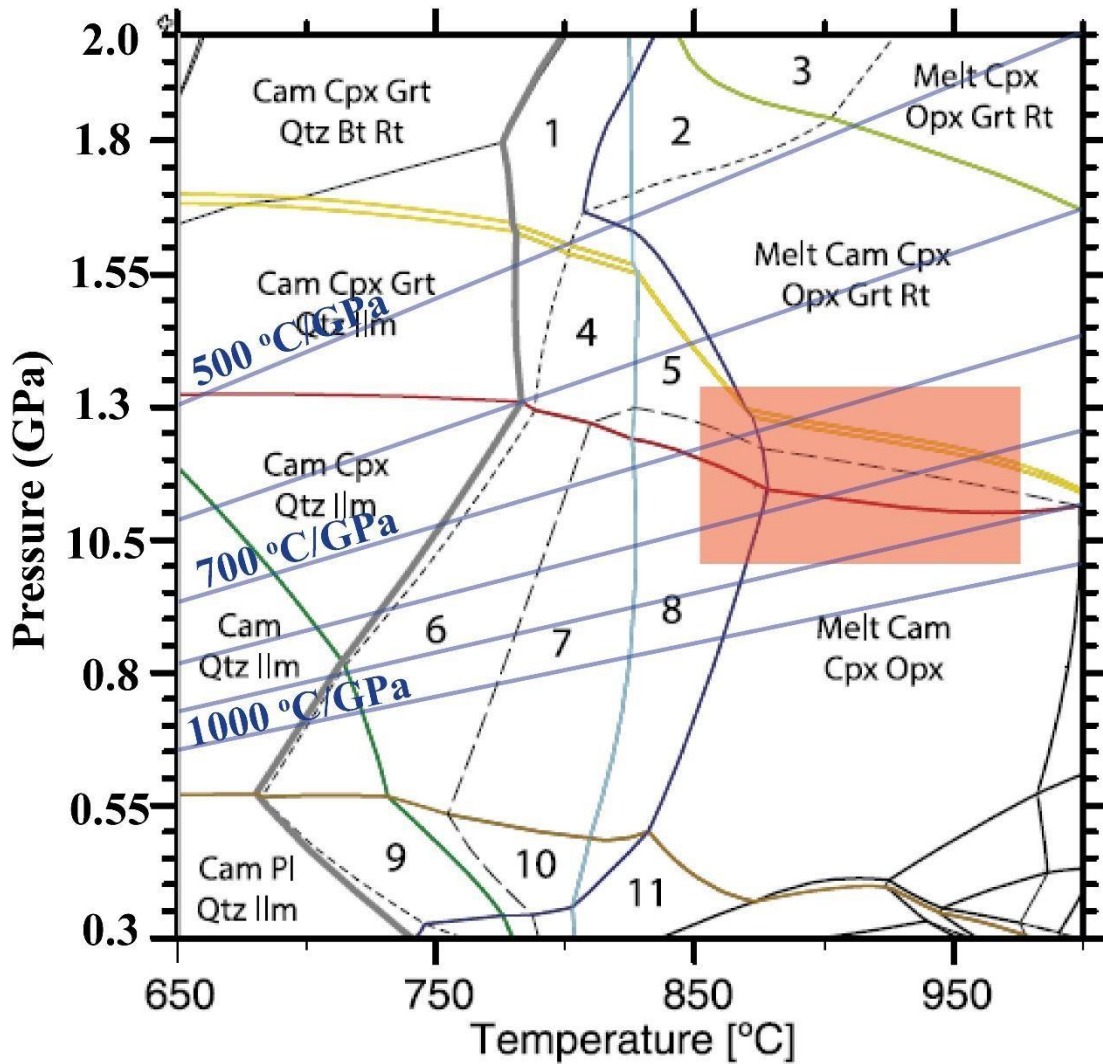
Figure APP-A7. Modified figure from Hoffmann et al. (2019) showing a calculated pseudosection for tholeiitic basalts from the Isua Supracrustal Belt. The red box highlights the conditions where tonalitic melts with and without garnet-rutile can be produced, as well as garnet-granulite assemblages (Field 5=Melt+Cam+Cpx+Grt+Qz+Ilm). The figure displays a range of T/P gradients and shows that the granulites and chemical composition of the TTG's of the ISB can be explained within a narrow range of T/P gradients (700-900 °C/GPa) contrary to the contrasting gradients (<500 vs >1000 C/GPa) interpreted by Nutman et al., (2020) (see main text for discussion). Abbrevations: Cam=Clinoamphibole; Qtz=Quartz; Pl=Plagioclase; Ilm=Ilmenite; Cpx=Clinopyroxene; Opx=Orthopyroxene; Bt=Biotite Rt= Rutile; Grt=Garnet. Colored assemblage boundaries (toward higher temperatures or pressures, respectively) indicate brown, Pl in; dark blue, Qtz out; dark green, Cpx in; dashed, Ilm out; fine dashed, upper boundary of water-saturation (H2O out); light blue, Opx in; light green, Cam out; red, Grt in; yellow, Ilm-Rt transition.

Table A1. XRF Bulk-rock composition. All samples ID are TM17- (e.g . 714-5A = TM17714-5A)

Oxide (wt %)	714-5A	714-5E	714-5F	717-5	725-2C	725-3A	729-1B	731-2A
SiO$_2$	62.24	61.92	56.77	63.87	67.11	51.75	60.72	55.52
TiO$_2$	0.442	0.374	0.343	0.52	0.444	0.19	1.39	0.95
Al$_2$O$_3$	11.5	16.09	16.85	14.56	15.25	13.42	13.78	13.22
Fe2O3total	15.65	15.62	17.91	6.11	7.55	15.66	12.67	17.17
MnO	0.52	0.18	0.166	0.21	0.082	0.60	0.24	0.454
MgO	3.02	2.8	4.02	2.81	2.22	7.62	2.08	5.21
CaO	3.65	0.39	0.36	5.56	2.18	9.74	3.83	5.22
Na$_2$O	0.52	0.424	0.239	0.17	4.026	0.73	3.28	0.338
K$_2$O	2.877	2.147	1.923	3.63	1.982	0.44	1.72	3.262
P2O5	0.081	0.021	0.014	0.17	0.077	<0.01	0.23	0.062
Cr$_2$O$_3$	0.037	0.083	0.124	<0.01	<0.010	0.02	<0.01	0.062
LOI	1.19	1.91	2.8	1.66	0.4	0.69	0.28	0.79
Total	101.727	101.959	101.519	99.27	101.321	100.86	100.22	102.258

Table A2. Recalculated bulk-rock composition used for the thermodynamic modelling. All samples ID are TM17- (e.g . 714-5A = TM17714-5A

Oxide (wt %)	714-5A	714-5E	714-5F	717-5	725-2C	725-3A	729-1B	731-2A
SiO_2	62.91	62.89	58.60	64.62	67.03	52.45	61.64	55.68
TiO_2	0.45	0.38	0.35	0.53	0.44	0.19	1.41	0.95
Al_2O_3	11.62	16.34	17.39	14.73	15.23	13.60	13.99	13.26
FeO	14.23	14.28	16.64	5.56	6.79	14.28	11.57	15.49
MnO	0.53	0.18	0.17	0.21	0.08	0.61	0.24	0.46
MgO	3.05	2.84	4.15	2.84	2.22	7.72	2.11	5.23
CaO	3.69	0.40	0.37	5.63	2.18	9.87	3.89	5.24
Na_2O	0.53	0.43	0.25	0.17	4.02	0.74	3.33	0.34
K_2O	2.91	2.18	1.99	3.67	1.98	0.45	1.75	3.27
O_2	0.08	0.08	0.09	0.03	0.04	0.08	0.06	0.09
Total	100	100	100	100	100	100	100	100

APENNDIX B-Supporting information for Chapter 3
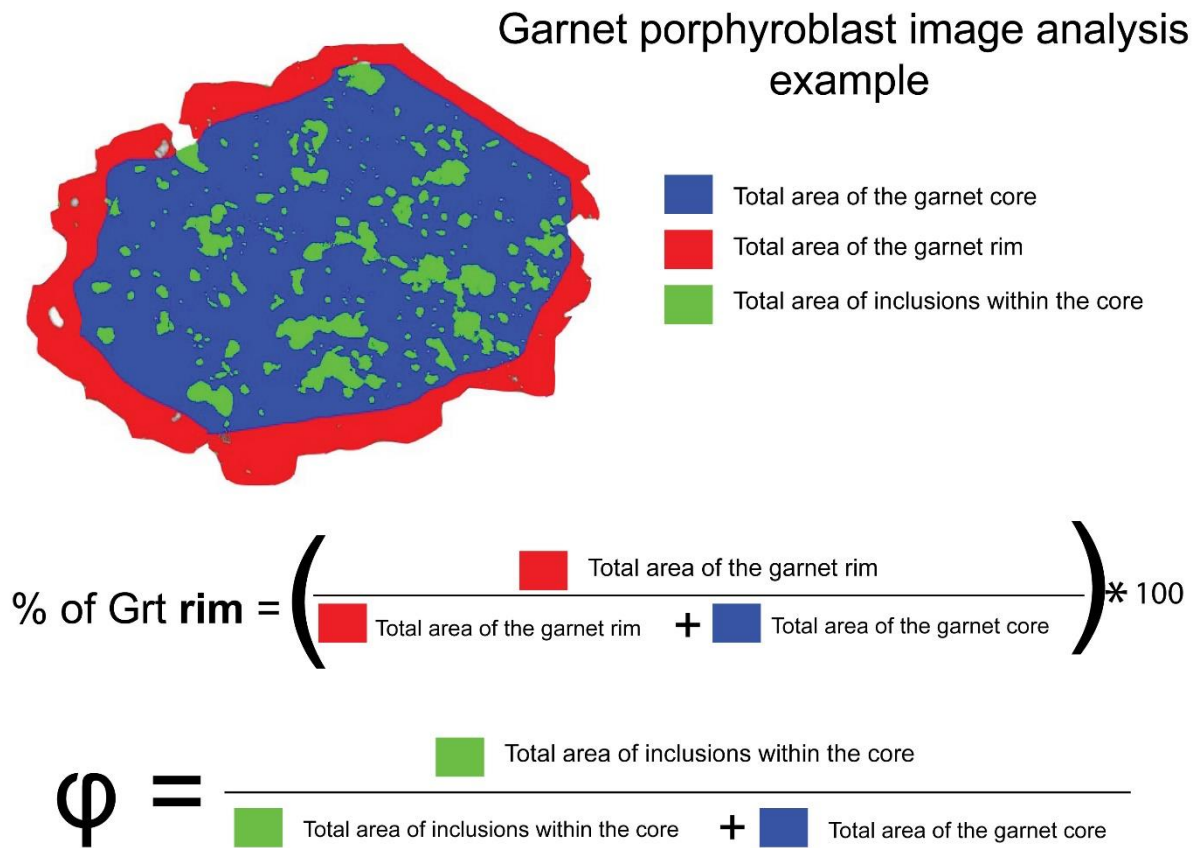
Figure APP-B1 Graphic example of the image analysis used for the quantification of the garnet microstructures and inclusion proportions.
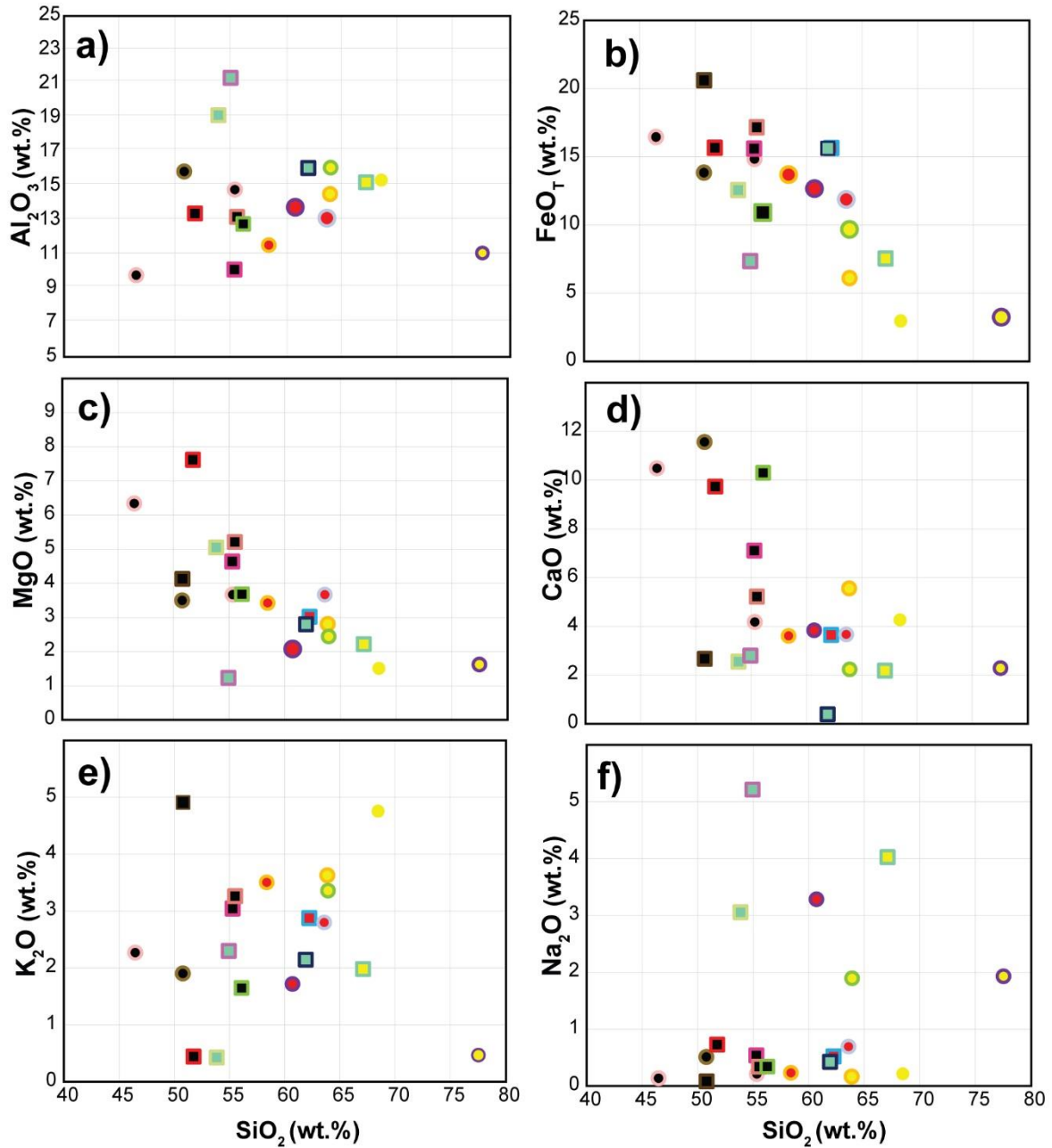
Figure APP-B2. Chemical plots. a)-f) Harker diagrams for bulk rock chemistry, SiO2 vs a) Al_2O_3; b) FeO_{Tot}; c) MgO; d) CaO; e) K_2O; f) Na_2O. *Chemistry for layered sample 717-3 is a mix of the different layers.

**Comparasion of the total volume of the main constituent phases in the rock
and in representative cores of the porphyroblasts**

Figure APP-B3 Comparison of phase percentage in the matrix and representative garnet cores. Abbreviations after Whitney and Evans (2010)
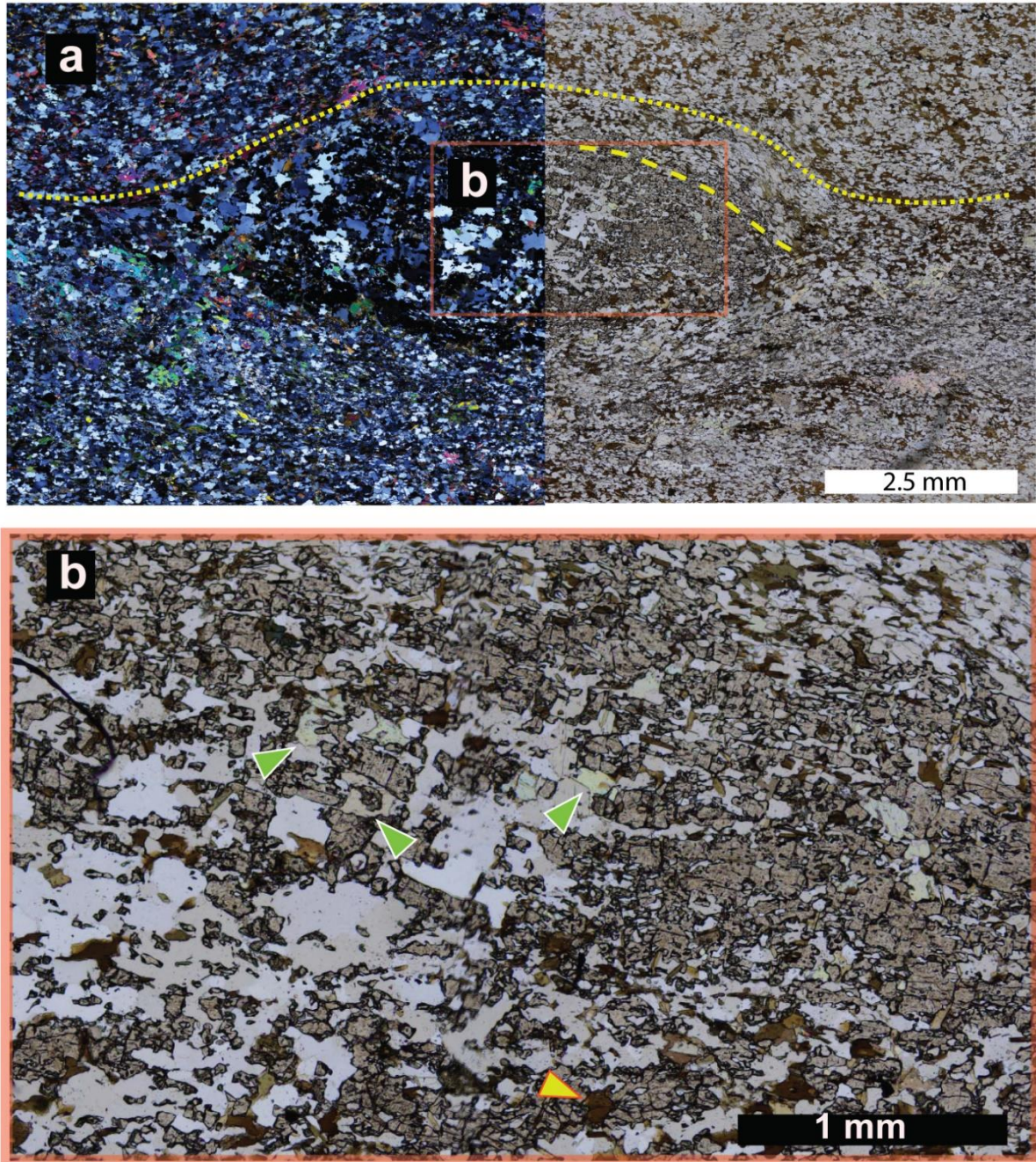
Figure APP-B4 Petrographic photographs of garnet microstructures in Type-I garnet in sample 717-5. a) Garnet and surrounding matrix showing internal and external foliations. b) typical irregular apparently interconnected internal microstructures in garnet showing have some of the garnet branches grow on biotites (yellow arrows) or muscovite (green arrows).

Figure APP-B5. Chemical maps of type-I garnets. a) meta-felsic volcanic 717-5; pattern A. b) meta-felsic volcanic 726-6A; pattern B. c) meta-felsic volcanic 726-4; pattern C. d) amphibolite 715-16A; pattern D. (a) and (b) quantitative compositional mapsand (c)-(f) qualitatative elemental maps.

Figure APP-B6 Comparison of compositional zoning and GROD mapping in Type II spiral-like garnet from metapelite 714-5E.

Figure APP-B7. Image with important features of garnet microstructure. a) Processed high-resolution optical microscope images of two garnet grains from sample 725-2C, showing that in more skeletal cores, post-tectonic grains tend to appear as small euhedral grains (left) and in less skeletal grains post-tectonic garnet appears as a continuous grain mantling the core (right). b) Phase map of a sections of JZ717-3-P-rich layer showing how post-tectonic rims grow bigger on top or close to foliated minerals like biotite (red arrows) but their growth is limited or inhibited next to quartz-rich zones (yellow arrows).
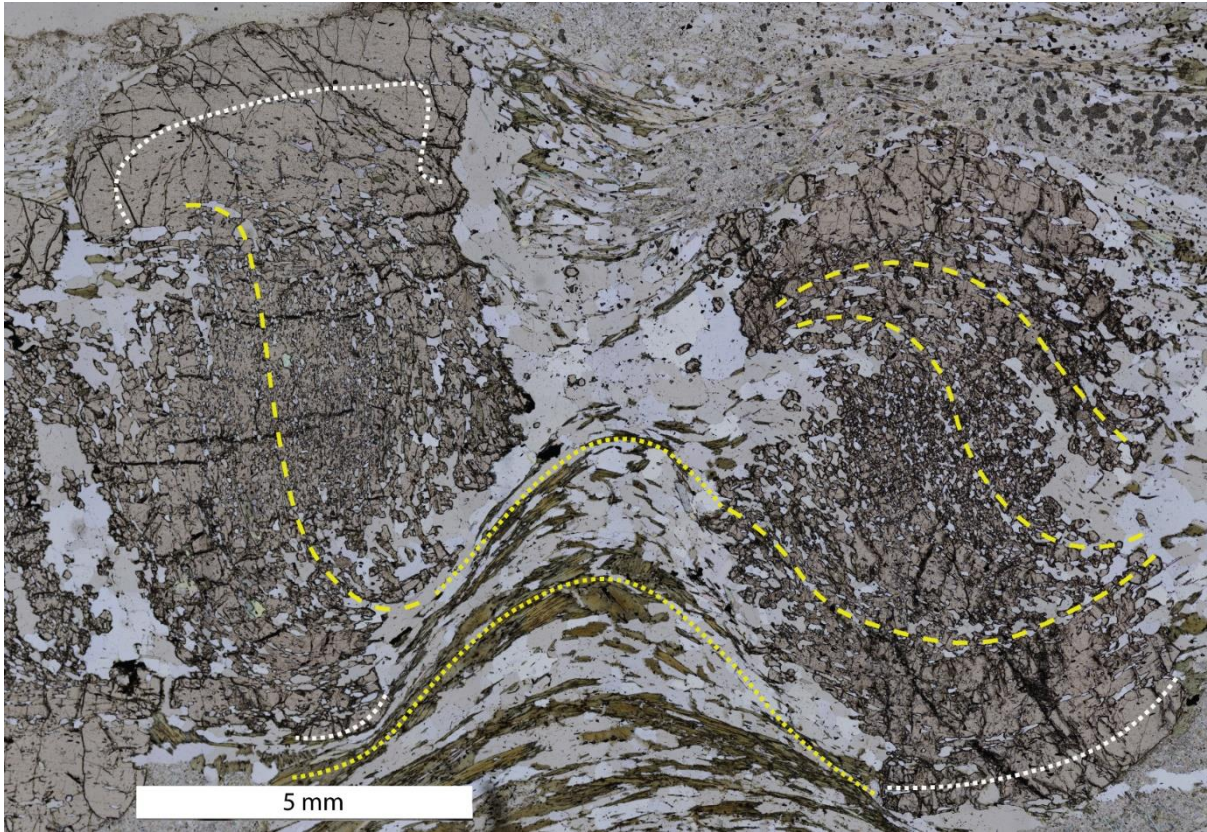
Figure APP-B8. Microscope images of garnet microstructures of spiral-like garnets in metapelite 714-5E, right garnet is the one in Fig. 8f and left garnet the one in figure B6
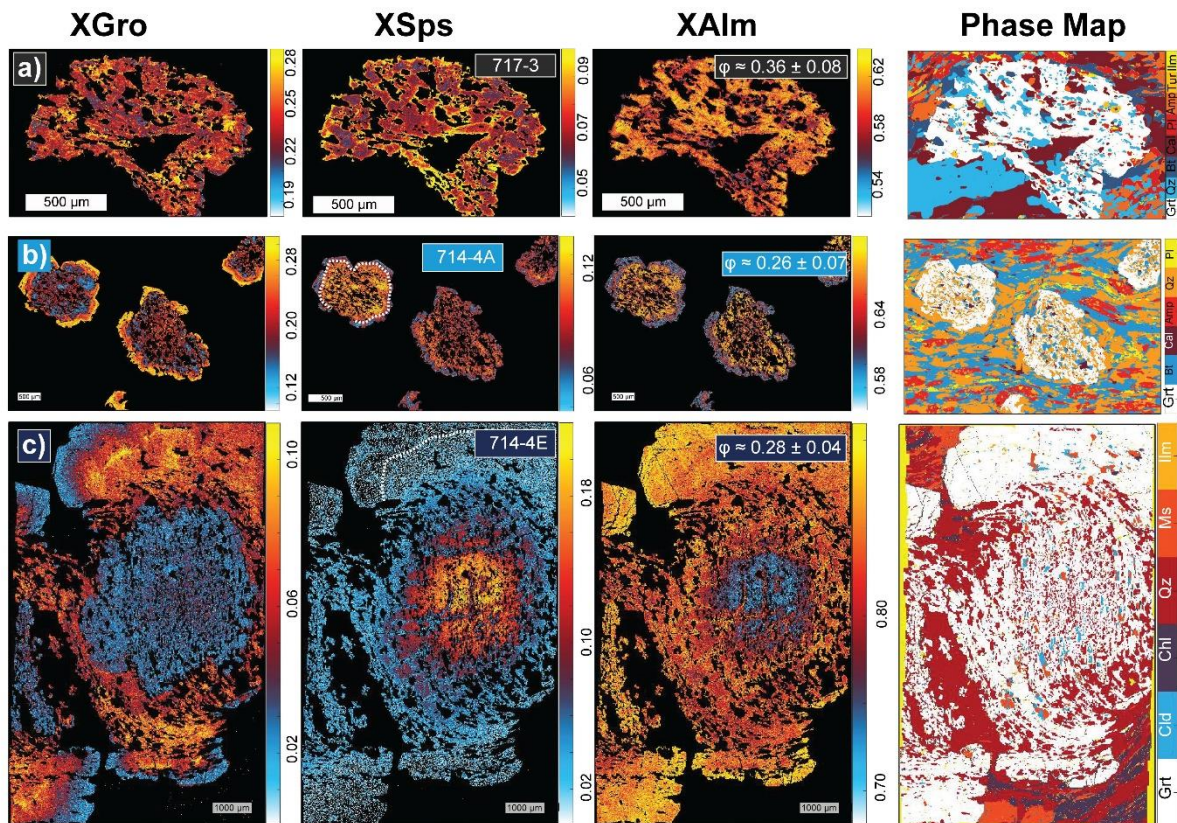
Figure APP-B9. Quantitative compositional maps for non-skeletal garnets.
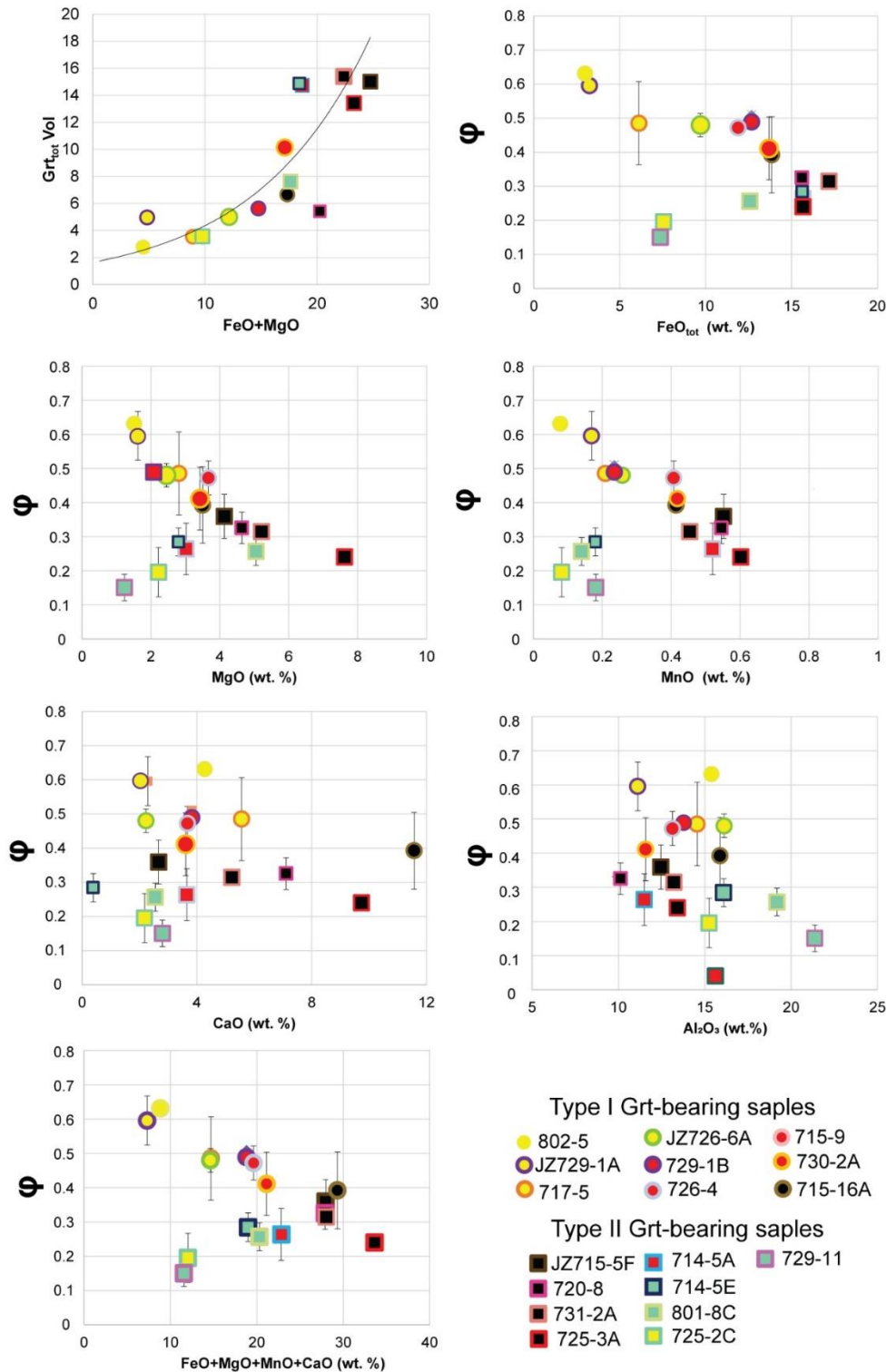
Figure APP-B10. Diagrams showing changes in the proportion of garnet in the porphyroblasts with respect to bulk rock chemistry. a) shows total modal abundance of garnet in the sample vs content of FeO and MgO, trend suggest that higher contents of MgO and FeO will allow more production of garnet; b-f) major elements of garnet vs φ.

Table B1. XRF bulk rock composition. Data for samples 714-5A, 714-5E, 725-3A, 729-1B, 731-2ª, 717-5 and 725-2C taken from Chapter 2. All oxides in weight percentage.

"TM17" samples	Age (Ga)	SiO_2	TiO_2	$Al2O_3$	FeO_{tot}	MnO	MgO	CaO	Na_2O	K_2O	P_2O_5	Cr_2O_3	LOI	Total	Al_2O_3/TiO_2	Longitude	Latitude
714-5A	3.7	62.24	0.442	11.5	15.65	0.52	3.02	3.65	0.52	2.877	0.081	0.037	1.19	101.73		65.171295	-49.833468
714-5E	3.7	61.92	0.374	16.09	15.62	0.18	2.8	0.39	0.424	2.147	0.021	0.083	1.91	101.96		65.171295	-49.833468
JZ715-5F	3.7	50.8	0.201	12.46	20.61	0.552	4.13	2.67	0.08	4.91	0.009	0	2.76	99.18	61.99	65.169422	-49.823217
720-8	3.7	55.29	0.73	10.13	15.60	0.55	4.64	7.11	0.54	3.05	0.08	0.04	3.39	101.14	13.83	65.197303	-49.770205
725-2c	3.7	67.11	0.444	15.25	7.55	0.082	2.22	2.18	4.026	1.982	0.077	<0.010	0.4	101.32		65.098302	-50.00803
725-3A	3.7	51.75	0.19	13.42	15.66	0.60	7.62	9.74	0.73	0.44	<0.01	0.02	0.69	100.86	69.89	65.098261	-49.998603
JZ729-1A	3.7	77.55	0.121	11.12	3.24	0.169	1.62	2.29	1.93	0.47	0.02		1.4			65.111243	-50.017674
729-1B	3.7	60.72	1.39	13.78	12.67	0.24	2.08	3.83	3.28	1.72	0.23	<0.01	0.28	100.22		65.20005	-49.798507
801-8C	3.7	53.85	0.33	19.18	12.57	0.14	5.05	2.55	3.06	0.43	<0.01	0.19	3.38	100.72		65.18258	-49.80878
729-11	3.7	54.94	0.79	21.37	7.36	0.18	1.23	2.80	5.21	2.30	0.11	<0.01	1.30	97.59			
731-2A	3.7	55.52	0.95	13.22	17.17	0.454	5.21	5.22	0.338	3.262	0.062	0.062	0.79	102.26	13.91	65.18258	-49.80878

APPENDIX C – Supporting information for Chapter 4
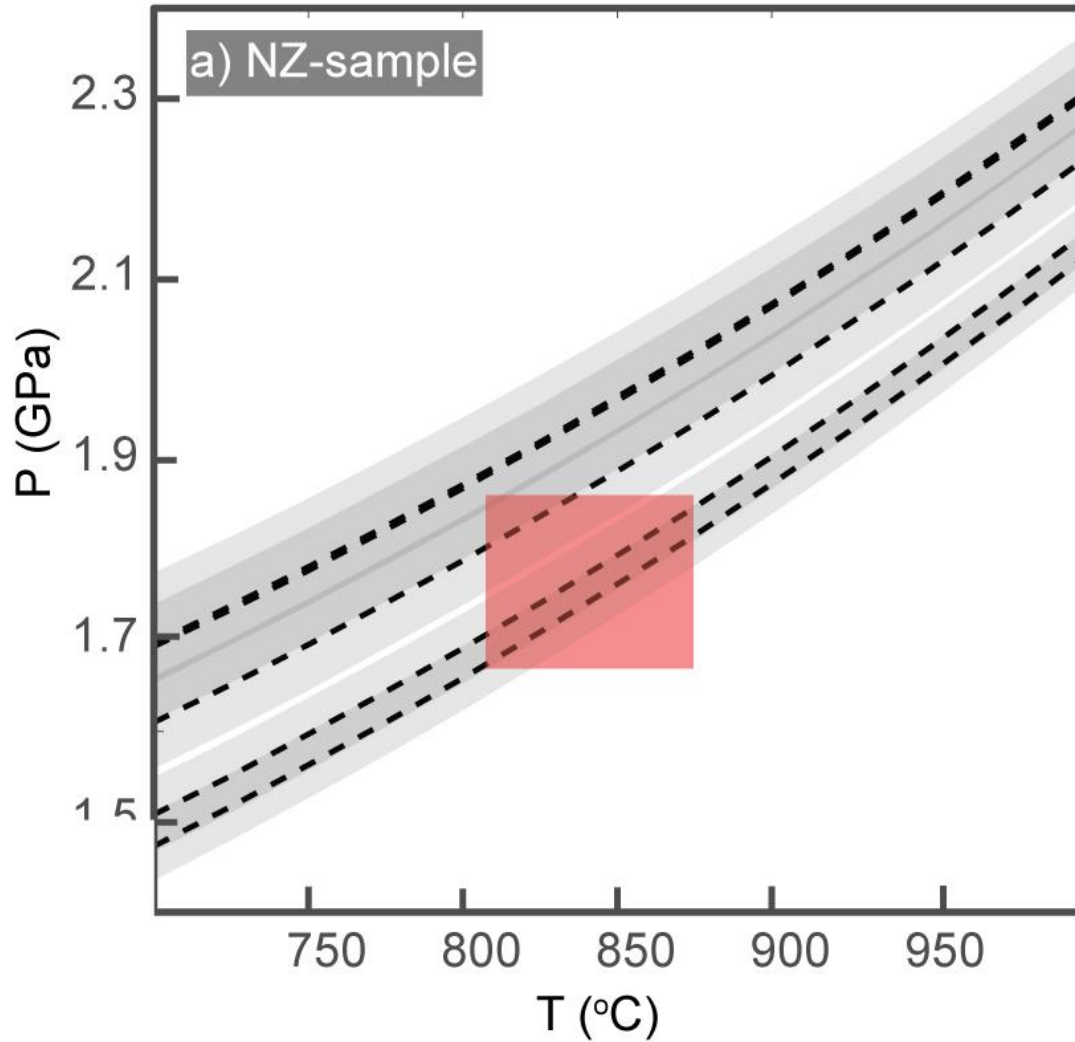
Figure APP-C4.1 Comparison of the QuiG barometry (dotted lines and grey fields) with the conventional and phase equilibria thermobarometry (red square) for the sample Breaksea Orthogneiss, New Zealand.
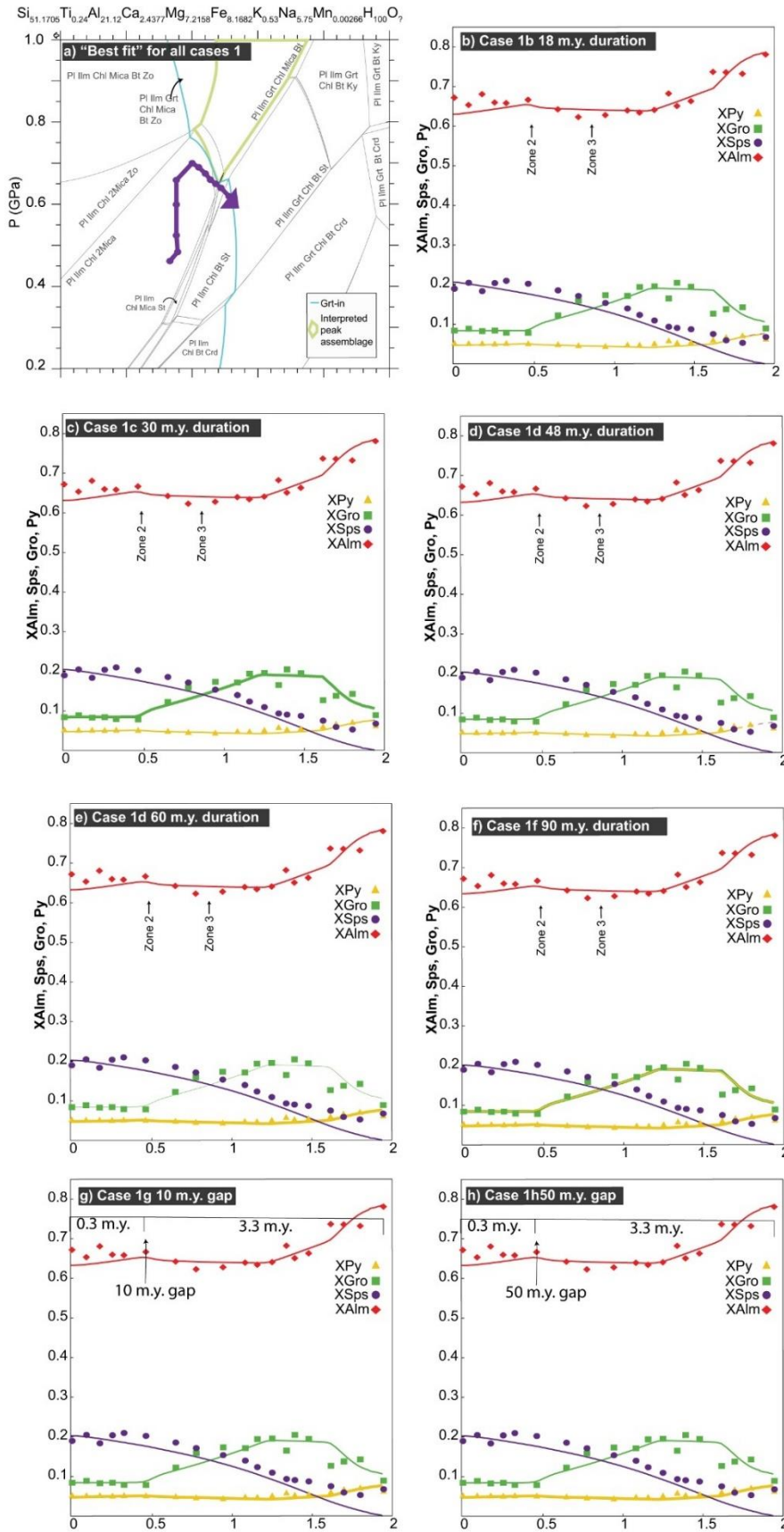
Figure APP-C4.2. (a) P-T path for the different cases 1 testing different timing (b-f) and time gaps (g-h) in the garnet growth. None of the changes in time affected significantly the profile.
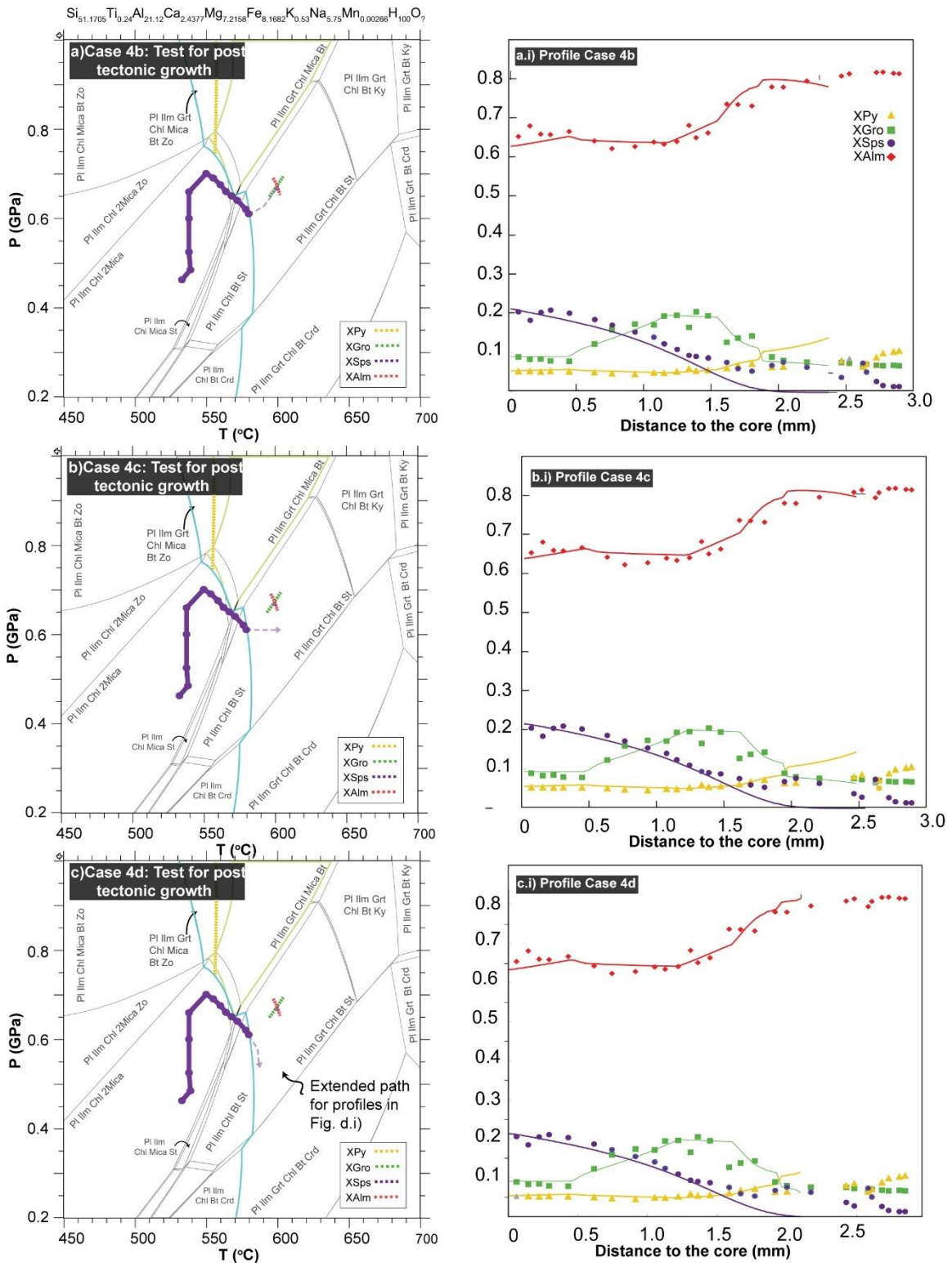
Figure APP-C4.3 Test for different extended P-T trying to model the composition of the post-tectonic rims.

Table C4.1 Composition of the metapelites

"TM17" samples	714-5E	801-8C
SiO_2	61.92	53.85
TiO_2	0.374	0.33
$Al2O_3$	16.09	19.18
FeO_{tot}	15.62	12.57
MnO	0.18	0.14
MgO	2.8	5.05
CaO	0.39	2.55
Na_2O	0.424	3.06
K_2O	2.147	0.43
P_2O_5	0.021	<0.01
Cr_2O_3	0.083	0.19
LOI	1.91	3.38
Total	101.96	100.72
Longitude	65.1713	65.18258
Latitude	-49.83347	-49.80878

Table C4.2 Composition of the garnet transects with distance to the core

	SiO2 (wt.%)	TiO2 (wt.%)	Al2O3 (wt.%)	FeO (wt.%)	MnO (wt.%)	MgO (wt.%)	CaO (wt.%)	Total	Distance to the core (mm)	Alm	Py	Sps	Gro
7145E -Grt1	37.28	0.03	21.06	35.05	5.21	1.34	1.20	101.16	0.00	79.17	5.38	11.92	3.48
7145E -Grt2	37.03	0.33	20.87	34.75	5.09	1.37	1.24	100.68	0.08	78.55	5.54	11.65	3.59
7145E -Grt3	37.19	0.02	21.06	35.31	5.16	1.37	1.12	101.23	0.17	79.46	5.50	11.76	3.23
7145E -Grt4	37.11	0.03	21.01	35.06	5.18	1.33	1.21	100.93	0.32	79.22	5.35	11.85	3.51
7145E -Grt5	37.10	0.03	21.09	35.08	5.23	1.36	1.19	101.08	0.40	79.08	5.48	11.94	3.44
7145E -Grt6	37.16	0.05	20.94	35.00	5.12	1.32	1.13	100.72	0.51	79.48	5.35	11.78	3.30
7145E -Grt7	37.01	0.02	20.95	35.42	5.15	1.39	1.07	101.01	0.60	79.60	5.56	11.72	3.07
7145E -Grt8	37.10	0.02	20.94	35.63	5.04	1.36	1.22	101.32	0.66	79.62	5.42	11.41	3.50
7145E -Grt9	37.01	0.02	20.95	35.31	4.96	1.39	1.10	100.74	0.79	79.82	5.59	11.36	3.19

7145E-Grt10	36.93	0.37	21.19	34.78	4.86	1.42	1.10	100.64	0.85	79.10	5.75	11.19	3.21
7145E-Grt11	36.99	0.02	21.00	35.67	4.70	1.43	1.10	100.91	0.99	80.33	5.73	10.72	3.17
7145E-Grt12	36.86	0.02	21.08	35.50	4.33	1.44	1.16	100.39	1.07	80.76	5.83	9.98	3.38
7145E-Grt13	36.90	0.02	20.99	36.32	4.09	1.44	1.15	100.91	1.15	81.58	5.77	9.30	3.30
7145E-Grt14	41.45	0.02	19.58	35.97	1.79	1.24	1.56	101.61	1.25	85.62	5.26	4.32	4.76
7145E-Grt15	36.99	0.02	20.87	38.30	1.85	1.49	1.06	100.59	1.31	86.63	6.00	4.24	3.08
7145E-Grt16	36.98	0.02	20.98	38.07	2.27	1.51	1.07	100.90	1.42	85.65	6.06	5.17	3.07
7145E-Grt17	37.14	0.03	20.91	36.81	3.53	1.49	1.00	100.91	1.55	83.00	5.99	8.06	2.88
7145E-Grt18	37.28	0.02	20.82	36.93	3.20	1.51	1.07	100.83	1.70	83.45	6.09	7.32	3.09
7145E-Grt19	37.17	0.04	20.98	37.22	2.99	1.50	0.96	100.86	1.81	84.23	6.06	6.85	2.77
7145E-Grt20	36.93	0.02	20.93	37.60	2.66	1.54	1.00	100.69	2.00	84.79	6.21	6.08	2.88
7145E-Grt21	37.06	0.02	21.04	38.10	2.42	1.56	1.05	101.26	2.04	85.23	6.23	5.48	3.01
7145E-Grt22	37.09	0.04	20.96	37.79	2.36	1.54	1.03	100.81	2.10	85.35	6.20	5.40	2.98
7145E-Grt23	36.92	0.02	21.08	37.72	2.08	1.53	0.99	100.35	2.20	86.02	6.23	4.80	2.89
									2.32				
7145E-Grt25	37.15	0.02	21.05	38.03	2.21	1.66	0.97	101.08	2.39	85.50	6.63	5.03	2.78
7145E-Grt26	36.81	0.03	21.03	37.86	2.10	1.63	0.98	100.44	2.52	85.72	6.57	4.82	2.83
	37.07	0.02	21.14	38.13	1.85	1.74	1.05	101.01	2.56	85.73	6.97	4.21	3.03
7145E-Grt28	37.21	0.03	20.93	37.78	1.68	1.57	1.87	101.07	2.68	84.50	6.28	3.81	5.36
7145E-Grt29	37.23	0.04	21.07	37.54	1.72	1.59	1.92	101.11	2.77	84.16	6.34	3.91	5.51
7145E-Grt30	37.17	0.02	20.99	37.90	1.63	1.53	1.64	100.88	2.83	85.37	6.13	3.72	4.73
7145E-Grt31	37.25	0.02	20.99	37.07	1.67	1.47	2.65	101.12	2.89	82.75	5.85	3.78	7.58
7145E-Grt32	37.32	0.03	21.12	37.00	1.63	1.41	2.65	101.16	2.94	83.00	5.62	3.70	7.62
7145E-Grt33	37.08	0.02	20.90	37.70	1.48	1.45	1.94	100.57	3.08	85.13	5.82	3.38	5.61

7145E -Grt34	37.32	0.02	21.22	37.57	1.39	1.43	2.19	101.14	3.14	84.70	5.75	3.17	6.33
7145E -Grt35	37.25	0.03	20.97	37.57	1.26	1.44	2.50	101.02	3.24	84.16	5.74	2.87	7.18
7145E -Grt36	37.32	0.14	20.90	37.70	1.07	1.34	2.49	100.97	3.36	84.72	5.39	2.44	7.17
7145E -Grt37	37.27	0.05	20.92	38.46	0.87	1.42	2.25	101.24	3.43	85.84	5.67	1.96	6.43
7145E -Grt38	36.97	0.02	21.07	38.68	0.68	1.37	2.06	100.85	3.52	86.98	5.49	1.55	5.93
7145E -Grt39	37.22	0.03	20.90	38.50	0.72	1.42	2.20	100.99	3.66	86.32	5.67	1.62	6.32
7145E -Grt40	37.41	0.02	20.91	38.85	0.69	1.42	1.98	101.29	3.71	87.02	5.68	1.56	5.68
7145E -Grt41	37.22	0.03	20.98	39.14	0.56	1.38	1.75	101.06	3.80	88.08	5.52	1.28	5.05
7145E -Grt42	37.14	0.04	21.01	38.65	0.74	1.42	1.97	100.97	3.89	86.87	5.68	1.69	5.67
7145E -Grt43	37.08	0.05	20.99	38.67	0.57	1.40	2.11	100.87	4.01	86.90	5.63	1.30	6.08
7145E -Grt44	37.13	0.03	21.06	38.95	0.49	1.42	1.91	100.98	4.10	87.64	5.68	1.11	5.51
7145E -Grt45	37.22	0.04	20.95	38.93	0.47	1.41	2.21	101.23	4.21	86.92	5.63	1.06	6.32
7145E -Grt46	37.37	0.03	20.99	38.83	0.48	1.43	2.16	101.30	4.31	86.93	5.71	1.09	6.20
7145E -Grt47	37.42	0.03	21.07	38.18	0.45	1.34	2.61	101.09	4.41	86.01	5.39	1.02	7.53
7145E -Grt48	37.32	0.02	21.10	38.06	0.46	1.35	2.82	101.13	4.46	85.42	5.38	1.04	8.11
7145E -Grt49	36.92	0.03	21.03	39.01	0.48	1.40	1.99	100.86	4.54	87.52	5.60	1.09	5.72
7145E -Grt50	37.09	0.03	20.99	38.87	0.47	1.47	1.89	100.81	4.63	87.50	5.91	1.08	5.45
7145E -Grt51	37.05	0.02	20.96	38.52	0.72	1.43	2.06	100.76	4.76	86.65	5.72	1.64	5.94
7145E -Grt52	36.98	0.02	21.20	38.11	0.31	1.54	2.14	100.31	4.85	86.74	6.25	0.72	6.24
7145E -Grt53	37.13	0.03	20.83	38.27	0.24	1.60	2.07	100.17	4.94	86.89	6.47	0.55	6.02
7145E -Grt54	37.44	0.02	21.08	38.83	0.27	1.66	1.87	101.17	5.04	87.30	6.65	0.61	5.39
7145E -Grt55	37.32	0.02	21.12	38.97	0.42	1.59	1.76	101.20	5.13	87.58	6.35	0.95	5.07
7145E -Grt56	37.11	0.06	21.01	38.99	0.40	1.62	1.65	100.83	5.22	87.75	6.48	0.90	4.76
7145E -Grt57	37.28	0.02	21.07	38.95	0.73	1.53	1.37	100.96	5.31	88.13	6.17	1.68	3.97

Sample													
7145E-Grt58	37.38	0.02	21.05	39.08	0.40	1.79	1.29	101.01	5.42	88.13	7.20	0.90	3.72
7145E-Grt59	37.06	0.03	21.02	38.79	0.22	2.42	1.02	100.57	5.55	86.84	9.66	0.49	2.94
7145E-Grt60	37.38	0.03	21.30	38.10	0.35	2.32	0.93	100.41	5.69	86.97	9.44	0.81	2.72
7312A-Grt1	37.09	0.28	20.99	25.58	8.17	0.99	7.41	100.52	0.00	56.37	3.91	18.24	20.92
7312A-Grt2	37.12	0.36	20.81	25.81	8.42	1.04	6.68	100.24	0.06	57.27	4.11	18.92	18.99
7312A-Grt3	37.34	0.23	21.01	26.32	8.48	1.06	6.59	101.02	0.17	57.92	4.16	18.90	18.58
7312A-Grt4	37.00	0.41	20.79	25.75	8.33	0.99	7.18	100.45	0.27	56.57	3.87	18.54	20.21
7312A-Grt5	37.17	0.37	20.86	25.48	8.50	1.00	7.24	100.62	0.34	56.02	3.94	18.93	20.39
7312A-Grt6	37.00	0.06	20.59	25.24	8.37	1.02	6.14	98.42	0.44	58.08	4.18	19.51	18.10
7312A-Grt7	37.02	0.21	20.78	26.24	8.56	0.97	6.66	100.44	0.53	57.85	3.81	19.11	18.81
7312A-Grt8	36.96	0.37	20.78	25.74	8.20	0.91	7.35	100.30	0.69	56.69	3.56	18.29	20.74
7312A-Grt9	37.43	0.29	20.95	25.87	8.62	0.95	6.71	100.82	0.91	57.30	3.75	19.34	19.04
7312A-Grt10	37.52	0.22	20.92	25.37	7.87	1.06	7.82	100.77	1.25	55.83	4.15	17.54	22.05
7312A-Grt11	37.27	0.23	20.96	26.30	8.12	1.23	6.61	100.72	1.32	57.94	4.82	18.12	18.66
7312A-Grt12	37.31	0.24	21.02	25.59	7.88	1.28	7.29	100.61	1.45	56.36	5.03	17.58	20.57
7312A-Grt13	37.30	0.05	21.15	26.72	8.32	1.03	6.09	100.66	2.97	59.61	4.10	18.80	17.41
7312A-Grt14	37.37	0.06	21.08	26.56	8.40	0.95	6.47	100.88	3.02	58.90	3.75	18.87	18.38
7312A-Grt15	37.39	0.09	21.31	26.41	8.11	0.95	6.78	101.03	3.14	58.59	3.74	18.22	19.27
7312A-Grt16	37.39	0.06	20.93	26.56	8.10	0.99	6.41	100.44	3.23	59.29	3.94	18.31	18.33
7312A-Grt17	37.35	0.11	21.20	26.99	7.96	1.03	6.23	100.86	3.34	60.03	4.07	17.93	17.75
7312A-Grt18	37.15	0.10	21.22	26.12	7.93	0.98	7.16	100.66	3.48	57.84	3.86	17.79	20.31
7312A-Grt19	37.14	0.05	21.16	26.06	7.98	1.02	6.92	100.32	3.51	58.08	4.05	18.01	19.76
7312A-Grt20	37.55	0.06	21.05	26.20	8.30	0.88	6.50	100.54	3.62	58.81	3.51	18.87	18.69

7312A-Grt21	36.58	0.11	21.91	25.76	8.14	0.85	6.57	99.91	3.70	58.51	3.43	18.73	19.12
7312A-Grt22	37.41	0.08	21.15	26.55	8.38	0.88	6.73	101.19	3.78	58.59	3.48	18.73	19.03
7312A-Grt23	37.14	0.10	21.02	26.55	8.58	0.92	6.22	100.53	3.89	59.09	3.63	19.34	17.74
7312A-Grt24	37.31	0.04	21.08	26.58	8.64	0.92	6.18	100.75	4.00	59.16	3.65	19.48	17.62
7312A-Grt25	37.21	0.08	21.06	26.21	8.16	0.90	6.85	100.48	4.08	58.33	3.58	18.39	19.53
7312A-Grt26	37.11	0.10	20.92	26.24	8.00	0.93	7.04	100.33	4.14	58.18	3.67	17.97	20.00
7312A-Grt27	37.39	0.15	20.93	26.50	7.63	0.93	7.21	100.74	4.25	58.56	3.65	17.08	20.41
7312A-Grt28	37.36	0.17	20.87	26.39	7.63	0.96	7.26	100.64	4.33	58.28	3.77	17.07	20.54
7312A-Grt29	37.35	0.21	20.86	26.38	7.50	0.94	7.07	100.31	4.41	58.75	3.74	16.92	20.17
7312A-Grt30	37.52	0.18	21.08	26.59	7.15	1.00	7.58	101.10	4.53	58.45	3.92	15.92	21.35
7312A-Grt31	37.70	0.15	21.06	26.43	7.21	1.02	7.37	100.94	4.59	58.56	4.03	16.18	20.92
7312A-Grt32	37.34	0.17	21.11	27.03	6.88	1.07	7.14	100.74	4.68	59.79	4.22	15.41	20.23
7312A-Grt33	37.37	0.24	20.94	27.69	6.45	1.13	6.80	100.62	4.79	61.31	4.46	14.46	19.29
7312A-Grt34	37.61	0.20	21.13	28.12	6.00	1.18	6.90	101.14	4.92	62.06	4.63	13.41	19.51
7312A-Grt35	37.57	0.21	21.17	28.19	5.94	1.18	6.70	100.96	4.98	62.52	4.69	13.34	19.04
7312A-Grt36	37.25	0.14	20.96	27.97	5.55	1.16	7.35	100.39	5.11	61.86	4.59	12.43	20.83
7312A-Grt37	37.25	0.19	21.06	27.99	5.83	1.17	6.87	100.36	5.13	62.27	4.63	13.14	19.58
7312A-Grt38	37.17	0.17	21.07	29.52	4.91	1.31	6.27	100.42	5.30	65.59	5.18	11.05	17.85
7312A-Grt39	37.33	0.14	21.10	29.35	5.07	1.26	6.38	100.63	5.35	65.17	4.99	11.40	18.15
7312A-Grt40	37.43	0.16	21.18	29.38	4.75	1.26	6.71	100.88	5.44	65.01	4.99	10.65	19.02
7312A-Grt41	37.19	0.18	20.95	29.76	4.41	1.31	6.52	100.32	5.56	66.02	5.19	9.91	18.53
7312A-Grt42	37.47	0.14	21.06	29.70	4.59	1.31	6.48	100.75	5.62	65.83	5.19	10.30	18.40
7312A-Grt43	37.34	0.15	21.09	30.00	4.17	1.33	6.86	100.94	5.72	65.91	5.21	9.28	19.31
7312A-Grt44	37.20	0.15	21.01	29.82	4.36	1.37	6.34	100.25	5.80	66.37	5.42	9.83	18.08

7312A-Grt45	37.52	0.19	21.10	30.54	3.93	1.45	6.12	100.85	5.89	67.69	5.73	8.82	17.38
7312A-Grt46	37.46	0.13	20.97	30.98	3.68	1.46	6.14	100.83	6.00	68.38	5.76	8.23	17.36
7312A-Grt47	37.26	0.12	21.07	30.43	3.51	1.46	6.48	100.33	6.07	67.63	5.78	7.90	18.45
7312A-Grt48	37.47	0.22	20.99	30.59	3.29	1.47	6.78	100.81	6.17	67.33	5.78	7.33	19.12
7312A-Grt49	37.46	0.46	21.07	30.04	3.47	1.53	6.73	100.76	6.27	66.29	6.03	7.76	19.03
7312A-Grt50	37.37	0.16	21.14	29.82	3.55	1.55	6.63	100.22	6.36	66.53	6.17	8.02	18.95
7312A-Grt51	37.33	0.17	20.96	30.02	3.16	1.51	7.14	100.29	6.46	66.39	5.96	7.08	20.23
7312A-Grt52	37.42	0.12	21.28	30.88	2.42	1.62	7.12	100.87	6.57	67.93	6.36	5.39	20.07
7312A-Grt53	37.37	0.16	21.12	29.98	2.28	1.62	7.88	100.41	6.64	66.01	6.35	5.08	22.23
7312A-Grt54	37.43	0.13	21.10	31.11	2.53	1.65	6.46	100.42	6.74	69.11	6.54	5.69	18.39
7312A-Grt55	37.43	0.14	20.93	31.89	2.22	1.79	5.90	100.30	6.81	70.85	7.09	5.00	16.79
7312A-Grt56	37.35	0.06	21.13	31.72	2.09	1.90	6.25	100.50	6.91	70.05	7.48	4.67	17.68
7312A-Grt57	37.49	0.08	21.24	31.23	2.53	1.89	6.11	100.57	6.99	69.31	7.48	5.69	17.37
7312A-Grt58	37.55	0.09	21.16	27.27	6.22	1.41	6.90	100.60	7.06	60.60	5.59	14.00	19.64
7312A-Grt59	37.37	0.03	21.40	27.88	5.79	1.41	7.01	100.89	7.09	61.58	5.57	12.95	19.84
7312A-Grt60	37.38	0.07	21.12	28.03	5.40	1.36	7.18	100.54	7.18	62.04	5.35	12.10	20.36
7312A-Grt61	37.26	0.08	21.28	28.08	4.68	1.48	7.73	100.59	7.27	61.80	5.81	10.43	21.80
7312A-Grt62	37.53	0.05	21.27	27.77	4.58	1.53	7.83	100.55	7.37	61.43	6.03	10.26	22.19
7312A-Grt63	37.23	0.05	21.25	27.84	4.60	1.55	7.66	100.18	7.41	61.71	6.11	10.33	21.75
7312A-Grt64	37.68	0.06	21.35	24.46	8.21	0.91	8.05	100.72	7.43	54.63	3.64	18.57	23.04
7312A-Grt65	36.15	0.05	20.94	24.42	7.77	0.95	7.45	97.73	7.43	56.05	3.88	18.06	21.91
8018C-Grt9	36.99	0.04	21.03	29.55	8.24	1.31	2.89	100.05	0.00	67.20	5.32	18.98	8.42
8018C-Grt10	37.03	0.03	21.21	28.88	8.93	1.29	3.07	100.45	0.09	65.35	5.22	20.47	8.90

8018C-Grt11	37.06	0.01	21.29	30.27	8.06	1.31	2.88	100.88	0.17	68.08	5.24	18.36	8.30
8018C-Grt12	37.35	0.04	21.20	29.11	8.88	1.28	2.90	100.75	0.25	65.97	5.15	20.38	8.42
8018C-Grt13	37.22	0.02	21.19	29.02	9.13	1.30	2.72	100.60	0.32	65.83	5.25	20.98	7.91
8018C-Grt14	37.28	0.06	21.13	29.45	8.82	1.28	2.70	100.72	0.46	66.65	5.18	20.22	7.83
8018C-Grt15	37.14	0.00	21.29	28.53	8.14	1.24	4.25	100.59	0.65	64.22	4.96	18.56	12.26
8018C-Grt16	37.71	0.03	21.27	28.01	7.61	1.18	5.57	101.38	0.78	62.27	4.67	17.14	15.87
8018C-Grt17	37.56	0.02	21.26	27.89	6.74	1.12	6.01	100.60	0.94	62.78	4.49	15.37	17.33
8018C-Grt18	37.42	0.04	21.03	28.45	6.14	1.21	5.95	100.24	1.08	63.95	4.86	13.98	17.13
8018C-Grt19	37.60	0.05	21.26	28.39	5.45	1.21	6.77	100.73	1.16	63.40	4.81	12.33	19.37
8018C-Grt20	37.67	0.15	21.11	28.73	4.84	1.30	6.84	100.64	1.25	64.06	5.17	10.93	19.54
8018C-Grt21	37.43	0.04	21.21	30.64	4.14	1.48	5.78	100.72	1.34	68.21	5.89	9.34	16.49
8018C-Grt22	37.74	0.05	21.09	29.18	4.00	1.34	7.16	100.57	1.39	65.07	5.34	9.03	20.46
8018C-Grt23	37.53	0.02	21.22	29.55	3.83	1.38	6.77	100.30	1.48	66.28	5.52	8.70	19.46
8018C-Grt24	37.47	0.05	20.82	32.56	3.28	1.50	4.37	100.06	1.62	73.65	6.06	7.51	12.66
8018C-Grt25	37.59	0.01	21.30	32.87	2.61	1.69	4.80	100.87	1.70	73.56	6.74	5.92	13.76
8018C-Grt26	37.49	0.06	21.49	32.79	2.33	1.80	4.99	100.95	1.80	73.18	7.16	5.27	14.27
8018C-Grt27	37.03	0.01	21.07	34.62	2.95	1.57	3.08	100.33	1.95	78.04	6.31	6.74	8.90
8018C-Grt28	37.34	0.01	21.15	34.57	3.31	1.60	2.76	100.74	2.03	78.00	6.44	7.56	7.98
8018C-Grt29	37.33	0.03	21.05	35.13	2.74	1.61	2.61	100.50	2.20	79.57	6.50	6.29	7.57
8018C-Grt30	37.16	0.00	21.17	35.94	1.61	1.99	2.61	100.48	2.46	80.83	7.98	3.67	7.52
8018C-Grt31	37.59	0.02	21.02	36.20	1.21	2.12	2.52	100.68	2.51	81.43	8.50	2.76	7.26
8018C-Grt32	37.15	0.02	21.09	35.02	3.19	1.58	2.34	100.39	2.61	79.42	6.41	7.33	6.80
8018C-Grt33	37.16	0.03	21.05	35.53	2.19	1.77	2.40	100.13	2.64	80.73	7.17	5.04	6.99
8018C-Grt34	37.30	0.01	21.07	36.29	1.15	2.19	2.35	100.36	2.71	81.77	8.80	2.63	6.78

8018C -Grt35	37.42	0.04	21.01	36.37	0.70	2.45	2.31	100.29	2.76	81.85	9.83	1.58	6.66
8018C -Grt36	37.23	0.07	21.10	36.49	0.58	2.57	2.36	100.40	2.84	81.54	10.24	1.31	6.76
8018C -Grt37	37.30	0.03	20.97	36.21	0.58	2.62	2.31	100.02	2.88	81.45	10.51	1.32	6.66
8018C -Grt38	37.12	0.05	21.05	35.79	2.13	1.95	2.13	100.22	3.00	80.98	7.87	4.88	6.18

APPENDIX D – Supporting information for Chapter 5
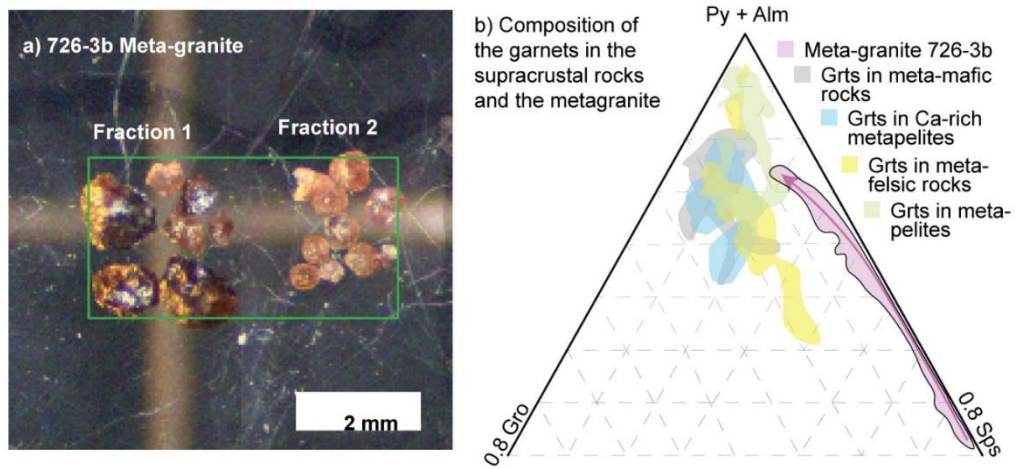
Figure APP-D5.1 a) Garnet fractions separated from the 726b meta-granite. (b) Composition of the meta-granite compared to the composition of the garnets from the supracrustal rocks.
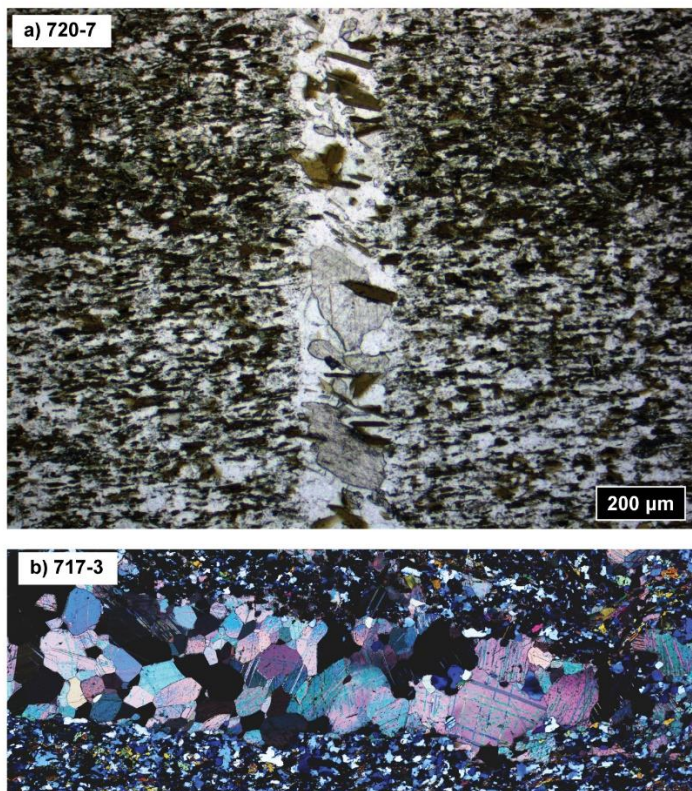
Figure APP-D5.2 Quartz-calcite veins. (a) Quartz-Calcite vein crosscutting main foliation. (b) Granoblastic post-tectonic calcite vein emplaced concordantly with the foliation.

Table D1. Composition of plagioclase and feldspars in enclave 724-1A. An=anorthite; Ab=Albite and Or=Orthoclase. c=included plagioclase; r=plagioclase in matrix. Numbers of Pl correspond to their pair amphibole (Table 2) used for geothermobarometry

	SiO$_2$	Al2O$_3$	FeO	MnO	MgO	CaO	Na$_2$O	K$_2$O	Total	An	Ab	Or
Pl1c	64.70	21.99	0.16	0.01	-0.01	3.36	9.58	0.12	99.90	0.16	0.83	0.01
Pl2c	64.10	22.16	0.23	-0.01	0.01	3.89	9.41	0.08	99.87	0.19	0.81	0.00
Pl3c	63.74	22.09	0.08	0.00	0.01	3.95	9.48	0.08	99.43	0.19	0.81	0.00
Pl4c	64.67	22.30	0.13	0.00	0.00	3.93	9.38	0.13	100.55	0.19	0.81	0.01
pl5c	65.60	21.78	0.10	-0.01	0.01	3.10	9.98	0.04	100.60	0.15	0.85	0.00
Pl6c	63.50	22.63	0.20	-0.01	0.01	4.46	9.11	0.08	99.99	0.21	0.78	0.00
Pl7c	62.92	23.02	0.13	0.01	0.00	4.62	9.10	0.15	99.95	0.22	0.77	0.01
Pl8c	62.91	22.69	0.10	0.00	0.01	4.74	8.77	0.22	99.42	0.23	0.76	0.01
Pl9r	62.86	22.98	0.07	0.00	-0.01	4.79	8.97	0.12	99.78	0.23	0.77	0.01
Pl10r	63.34	23.00	0.08	0.00	0.00	4.62	8.94	0.06	100.05	0.22	0.78	0.00
Pl11r	63.39	22.24	0.09	0.00	-0.02	4.04	9.43	0.09	99.26	0.19	0.80	0.01
Pl12r	64.17	22.69	0.17	0.00	-0.01	4.19	9.36	0.08	100.66	0.20	0.80	0.00
Pl13r	64.72	21.72	0.13	-0.01	-0.01	3.27	9.74	0.11	99.68	0.16	0.84	0.01
Pl14r	64.74	22.02	0.17	0.00	0.00	3.32	9.87	0.12	100.24	0.16	0.84	0.01
Kfs1	65.13	18.30	0.12	0.00	-0.01	0.03	0.56	15.75	99.88	0.00	0.05	0.95
Kfs2	65.00	18.10	0.05	0.01	0.00	0.02	0.56	15.78	99.50	0.00	0.05	0.95
Kfs3	65.00	18.10	0.05	0.01	0.00	0.02	0.56	15.78	99.50	0.00	0.05	0.95
Ab1	68.45	19.57	0.12	-0.01	0.00	0.65	11.26	0.09	100.12	0.03	0.96	0.00
Ab2	68.73	19.24	0.10	0.00	-0.02	0.37	11.57	0.07	100.06	0.02	0.98	0.00
Ab3	67.91	19.92	0.13	-0.02	0.00	0.91	11.29	0.08	100.22	0.04	0.95	0.00

Table D2. Composition of amphiboles in enclave 724-1A. c=amphibole core; r=amphibole rim. Numbers of Amp corresond to their pair plagioclase (Table 1) used for geothermobarometry

	SiO$_2$	TiO$_2$	Al2O$_3$	FeO	MgO	MnO	CaO	Na$_2$O	K$_2$O	Total
Amp1c	46.11	0.40	8.44	16.64	11.55	0.32	11.94	1.21	0.90	97.51
Amp2c	45.94	0.46	7.93	16.77	11.70	0.35	11.97	1.18	0.80	97.10
Amp3c	44.76	0.51	8.72	17.31	10.93	0.35	11.75	1.33	1.03	96.69
Amp4c	45.91	0.36	8.07	15.84	11.61	0.33	12.05	1.14	0.78	96.10
Amp5c	45.18	0.39	8.49	16.42	11.28	0.33	11.88	1.20	0.95	96.12
Amp6c	45.91	0.37	8.10	16.12	11.57	0.34	12.05	1.02	0.79	96.27
Amp7c	43.84	0.41	9.72	18.13	10.23	0.33	11.79	1.32	1.08	96.84
Amp8c	43.91	0.75	9.14	17.60	10.47	0.35	11.86	1.37	1.06	96.50
Amp9r	44.45	0.71	8.92	16.71	10.98	0.34	11.86	1.31	1.03	96.32
Amp10r	43.26	0.39	10.05	18.35	9.96	0.32	11.65	1.39	1.16	96.52
Amp11r	44.25	0.48	9.11	17.56	10.48	0.34	11.92	1.19	1.00	96.33
Amp12r	43.86	0.65	9.14	17.89	10.37	0.33	11.88	1.40	1.01	96.54
Amp13r	44.69	0.37	8.72	17.10	10.84	0.34	11.87	1.15	0.93	96.01
Amp14r	45.23	0.36	8.36	17.05	11.29	0.37	11.84	1.21	0.92	96.63

Table D3. **Sm**-Nd data for the garnet-rock isochrons. G=garnet, R=rock, analysis with * denote measurements made at the University of Gottingen

Sample	Nd (ppm)	Sm (ppm)	147Sm/144Nd	± 2s	143Nd/144Nd	± 2s	Age	± 2s	MSWD
714-5E-G*	0.14	0.91	3.8469	0.003587	0.571854	0.0000110	2486.72	2.4	n/a
714-5E-R*	5.14	1.15	0.1359	0.000127	0.511158	0.0000080			
725-3A-G*	0.08	0.22	1.7247	0.001608	0.541208	0.0000160	2843.59	3.3	n/a
725-32AR*	2.88	0.81	0.1697	0.000158	0.512091	0.0000080			
730-2A-G*	0.15	0.27	1.0888	0.001015	0.531445	0.0000100	3190.87	3.44	n/a
730-2A-R*	7.44	2.18	0.1771	0.000165	0.512267	0.0000080			
731-2A-G*	0.26	0.3	0.6984	0.000651	0.521561	0.0000110	2702.72	2.63	n/a
731-2A-R*	9.53	2.84	0.1801	0.000168	0.512341	0.0000080			
717-5-R	32.9582	5.5429	0.1016	0.0010162	0.510322	0.0000153	531.5	45.2	n/a
717-5-R	0.3079	0.1317	0.2585	0.002585033	0.510867	0.0000153			
726-3B-R	1.5564	1.4557	0.5666	0.00566618	0.521284	0.0000156	3554.1	49.3	0.019
726-3B-G	4.4951	29.1264	3.9997	0.039996598	0.601783	0.0000181			
726-3B-G	4.5947	29.9471	4.0239	0.040238864	0.602524	0.0000181			
726-3B-G	7.4920	33.6821	2.7563	0.027563494	0.572568	0.0000172			
726-3B-F2-G	1.0873	5.7072	3.2248	0.032247641	0.581394	0.0000174	3524.4	74.8	n/a
729-1B-R	26.1128	5.7887	0.1340	0.001339701	0.511128	0.0000153	3054.5	63.8	2.1
729-1B-G	2.7762	0.7643	0.1665	0.001665278	0.515013	0.0000155			
729-1B-G	1.3395	0.9673	0.4370	0.004370416	0.517323	0.0000155			
729-1B-G	2.1345	1.4730	0.4174	0.004174125	0.514757	0.0000154			
729-1B-G	0.9749	0.8904	0.5530	0.005530319	0.519454	0.0000156			
802-5-R	25.3279	4.4548	0.1063	0.001062768	0.510443	0.0000153		n/a	
802-5-G	0.1831	0.1480	0.4870	0.004869924	0.496978	0.0000149			
802-5-R	0.21281	0.2407	0.6837	0.006837233	0.511517	0.0000153			
730-2A-R	10.4881	3.1281	0.1803	0.001802984	0.512289	0.0000154			
730-2A	0.1238	0.131697	0.6467	0.006467165	0.536339	0.0000161			

Table D4. Lu-Hf data for the garnet-rock isochrons. G=garnet, R=rock.

Sample	Hf (ppm)	Lu (ppm)	176Lu/177Hf	± 2s (1%)	176Hf/177Hf	± 2s (0.003%)	Age (Ma)	± 2s	MSWD
717-5-R	2.8881	0.1712	0.0084	0.0000840	0.280938	0.0000084	2825.8	56.4	n/a
717-5-R	2.9332	4.5184	0.2187	0.0021874	0.292331	0.0000088			
726-3B-R	3.9281	0.0413	0.0015	0.0000149	0.280511	0.0000084			
726-3B-G	17.5731	2.7968	0.0226	0.0002256	0.281927	0.0000085			
726-3B-G	19.0893	2.8958	0.0215	0.0002150	0.281897	0.0000085	3533.4	71.1	3.4
726-3B-G	18.8669	3.3076	0.0248	0.0002485	0.282002	0.0000085			
726-3B-F2-G	9.2268	2.8161	0.0433	0.0004327	0.283354	0.0000085	3524.4	74.8	n/a
729-1B-R	5.2634	0.3373	0.0091	0.0000908	0.281016	0.0000084			
729-1B-G	5.0356	2.9491	0.0831	0.0008306	0.285820	0.0000086			
729-1B-G	4.7277	3.1933	0.0959	0.0009589	0.291361	0.0000087	3376	52	0.08
729-1B-G	6.5742	5.1707	0.1116	0.0011159	0.287700	0.0000086			
729-1B-G	5.1942	3.3463	0.0914	0.0009138	0.286124	0.0000086			
802-5-R	2.8466	0.1053	0.0052	0.0000524	0.280715	0.0000084			
802-5-G	2.5887	6.0248	0.3308	0.0033084	0.298461	0.0000090	2793.8	628.6	6.4
802-5-R	2.3718	6.8525	0.4110	0.0041097	0.302044	0.0000091			
730-2A-R	2.1533	0.5170	0.0340	0.0003404	0.283077	0.0000085	2920.2	33	n/a
730-2A	2.203105	4.11922	0.2657	0.0026568	0.29606	0.0000089			
731-2A-R	0.7947	0.2911	0.0519	0.0005194	0.283666	0.0000085			
731-2A-G	1.1178	2.2738	0.2890	0.0028904	0.295925	0.0000089			
731-2A-G	0.9828	2.3855	0.3451	0.0034505	0.298803	0.0000090	2678.3	36	1.1
731-2A-G	0.9564	3.0171	0.4489	0.0044888	0.303749	0.0000091			
731-2A-G	0.9989	2.2097	0.3145	0.0031445	0.298340	0.0000090			

REFERENCES

- Abbott, D., Drury, R., and Smith, W.H.F., 1994, Flat to steep transition in subduction style: Geology, v. 22, p. 937–940, doi:10.1130/0091-7613(1994)022<0937:FTSTIS>2.3.CO;2.
- Abbott, R.N., 1981, The role of manganese in the paragenesis of magmatic garnet: an example from the Old Women-Piute Range, California: a discussion.: Journal of Geology, v. 89, p. 767–769, doi:10.1086/628644.
- Ague, J.J., Carlson, W.D., 2013. Metamorphism as garnet sees it: The kinetics of nucleation and growth, equilibration, and diffusional relaxation. Elements 9, 439–445. https://doi.org/10.2113/gselements.9.6.439
- Allwood, A. C., Rosing, M. T., Flannery, D. T., Hurowitz, J. A., & Heirwegh, C. M. (2018). Reassessing evidence of life in 3,700-million-year-old rocks of Greenland. Nature, 563(7730), 241–244. https://doi.org/10.1038/s41586-018-0610-4
- An, S.C., Li, S.G., and Liu, Z., 2018, Modification of the Sm–Nd isotopic system in garnet induced by retrogressive fluids: Journal of Metamorphic Geology, v. 36, p. 1039–1048, doi:10.1111/jmg.12426.
- Anczkiewicz, R., and Thirlwall, M.F., 2003, Improving precision of Sm-Nd garnet dating by H 2SO 4 leaching: A simple solution to the phosphate inclusion problem: Geological Society Special Publication, v. 220, p. 83–91, doi:10.1144/GSL.SP.2003.220.01.05.
- Angel, R.J., Murri, M., Mihailova, B., and Alvaro, M., 2019, Stress, strain and Raman shifts: Zeitschrift fur Kristallographie - Crystalline Materials, v. 234, p. 129–140, doi:10.1515/zkri-2018-2112.
- Appel, P. W. U., Rollinson, H. R., & Touret, J. L. R., 2001,. Remnants of an early Archaean (> 3.75 Ga) sea-floor, hydrothermal system in the Isua Greenstone Belt. Precambrian Research, 112(1–2), 27–49. https://doi.org/10.1016/S0301-9268(01)00169-3
- Arai, T., Omori, S., Komiya, T., and Maruyama, S., 2015, Intermediate P/T-type regional metamorphism of the Isua Supracrustal Belt, southern west Greenland: The oldest Pacific-type orogenic belt? Tectonophysics, v. 662, p. 22–39, doi:10.1016/j.tecto.2015.05.020.
- Baadsgaard, H., Nutman, A.P., and Bridgwater, D., 1986, Geochronology and isotopic variation of the early Archaean Amitsoq gneisses of the Isukasia area, southern West Greenland: Geochimica et Cosmochimica Acta, v. 50, p. 2173–2183, doi:10.1016/0016-7037(86)90072-4.
- Baxter, E.F., and Scherer, E.E., 2013, Garnet geochronology: Timekeeper of tectonometamorphic processes: Elements, v. 9, p. 433–438, doi:10.2113/gselements.9.6.433.
- Baxter, E.F., Caddick, M.J., and Dragovic, B., 2017, Garnet: A Rock-Forming Mineral Petrochronometer: Reviews in Mineralogy and Geochemistry, v. 83, p. 469–533, doi:10.2138/rmg.2017.83.15.
- Beall, A.P., Moresi, L., and Cooper, C.M., 2018, Formation of cratonic lithosphere during the initiation of plate tectonics: Geology, v. 46, p. 487–490, doi:10.1130/G39943.1.
- Bédard, J.H., 2018, Stagnant lids and mantle overturns: Implications for Archaean tectonics, magmagenesis, crustal growth, mantle evolution, and the start of plate tectonics: Geoscience Frontiers, v. 9, p. 19–49, doi:10.1016/j.gsf.2017.01.005.
- Black, L.P., Gale, N.H., Moorbath, S., Pankhurst, R.J., and McGregor, V.R., 1971, Isotopic Dating of Very Early Precambrian Amphibolite Facies Gneisses from the

Godthaab District, West Greenland: Earth and Planetary Science Letters, v. 12, p. 245–259.

- Bland, M.T., and Mckinnon, W.B., 2016, Mountain building on Io driven by deep faulting: Nature Geoscience, v. 9, p. 429–432, doi:10.1038/ngeo2711.

- Blichert-Toft, J., and Frei, R., 2001, Complex Sm-Nd and Lu-Hf isotope systematics in metamorphic garnets from the Isua supracrustal belt, West Greenland: Geochimica et Cosmochimica Acta, v. 65, p. 3177–3189, doi:10.1016/S0016-7037(01)00680-9.

- Boak, J.L., and Dymek, R.F., 1982, Metamorphism of the ca. 3800 Ma supracrustal rocks at Isua, West Greenland: implications for early Archaean crustal evolution: Earth and Planetary Science Letters, v. 59, p. 155–176, doi:10.1016/0012-821X(82)90123-6.

- Bohlen, S.R., and Mezger, K., 1989, Origin of Granulite Terranes and the Formation of the Lowermost Continental Crust: Science, v. 244, p. 326–329.

- Bons, P.D., Elburg, M.A., and Gomez-Rivas, E., 2012, A review of the formation of tectonic veins and their microstructures: Journal of Structural Geology, v. 43, p. 33–62, doi:10.1016/j.jsg.2012.07.005.

- Borinski, S.A., Hoppe, U., Chakraborty, S., Ganguly, J., and Bhowmik, S.K., 2012, Multicomponent diffusion in garnets I: General theoretical considerations and experimental data for Fe-Mg systems: Contributions to Mineralogy and Petrology, v. 164, p. 571–586, doi:10.1007/s00410-012-0758-0.

- Bowtell, S.A., Cliff, R.A., and Barnicoat, A.C., 1994, Sm-Nd isotopic evidence on the age of eclogitization in the Zermatt-Saas ophiolite: Journal of Metamorphic Geology, v. 12, p. 187–196, doi:10.1111/j.1525-1314.1994.tb00013.x.

- Bracciali, L., Parrish, R.R., Horstwood, M.S.A., Condon, D.J., and Najman, Y., 2013, UPb LA-(MC)-ICP-MS dating of rutile: New reference materials and applications to sedimentary provenance: Chemical Geology, v. 347, p. 82–101, doi:10.1016/j.chemgeo.2013.03.013.

- Bridgwater, D., Watson, J., & Windley, B. F. (1973). The Archaean craton of the North Atlantic region. Philosophical Transactions of the Royal Society A: Mathematical, Physical and Engineering Sciences, 512, 493–512.

- Brouwer, F.M., Burri, T., Engi, M., and Berger, A., 2005, Eclogite relics in the Central Alps: PT - evolution, Lu-Hf ages and implications for formation of tectonic mélange zones: Schweizerische Mineralogische und Petrographische Mitteilungen, v. 85, p. 147–174.

- Brown, M., 1993, P - T - t evolution of orogenic belts and the causes of regional metamorphism: Journal of the Geological Society, v. 150, p. 227–241.

- Brown, M., 2001, From microscope to moutain belt: 150 years of petrology and its contribution to understanding geodynamics, particularly the tectonics of orogens: Journal of Geodynamics, v. 32, p. 115–164, doi:10.1016/S0264-3707(01)00018-7.

- Brown, M., 2006, Duality of thermal regimes is the distinctive characteristic of plate tectonics since the Neoarchean: Geology, v. 34, p. 961–964, doi:10.1130/G22853A.1.

- Brown, M., 2010, Paired metamorphic belts revisited: Gondwana Research, v. 18, p. 46–59, doi:10.1016/j.gr.2009.11.004.

- Brown, M., 2010, Paired metamorphic belts revisited: Gondwana Research, v. 18, p. 46–59, doi:10.1016/j.gr.2009.11.004.

- Brown, M., 2015, Paleo- to Mesoarchean polymetamorphism in the Barberton Granite-Greenstone Belt, South Africa: Constraints from U-Pb monazite and Lu-Hf garnet geochronology on the tectonic processes that shaped the belt: Discussion:

Bulletin of the Geological Society of America, v. 127, p. 1550–1557, doi:10.1130/B31198.1.

- Brown, M., and Johnson, T., 2018, Secular change in metamorphism and the onset of global plate tectonics: American Mineralogist, v. 103, p. 181–196, doi:10.2138/am-2018-6166.
- Bucher, K., and Frey, M., 2002, Petrogenesis of Metamorphic Rocks. 7th edition. Springer.
- Buick, I.S., Hermann, J., Williams, I.S., Gibson, R.L., and Rubatto, D., 2006, A SHRIMP U-Pb and LA-ICP-MS trace element study of the petrogenesis of garnet-cordierite-orthoamphibole gneisses from the Central Zone of the Limpopo Belt, South Africa: Lithos, v. 88, p. 150–172, doi:10.1016/j.lithos.2005.09.001.
- Burov, E., and Yamato, P., 2008, Continental plate collision, P-T-t-z conditions and unstable vs. stable plate dynamics: Insights from thermo-mechanical modelling: Lithos, v. 103, p. 178–204, doi:10.1016/j.lithos.2007.09.014.
- Caddick, M.J., Konopásek, J., and Thompson, A.B., 2010, Preservation of garnet growth zoning and the duration of prograde metamorphism: Journal of Petrology, v. 51, p. 2327–2347, doi:10.1093/petrology/egq059.
- Carlson, W.D., 1989, The significance of intergranular diffusion to the mechanisms and kinetics of porphyroblast crystallization: Contributions to Mineralogy and Petrology, v. 103, p. 1–24, doi:10.1007/BF00371361.
- Carlson, W.D., 2011. Porphyroblast crystallization: Linking processes, kinetics, and microstructures. Int. Geol. Rev. 53, 406–445. https://doi.org/10.1080/00206814.2010.496184
- Carlson, W.D., Hixon, J.D., Garber, J.M., Bodnar, R.J., 2015. Controls on metamorphic equilibration: The importance of intergranular solubilities mediated by fluid composition. J. Metamorph. Geol. 33, 123–146. https://doi.org/10.1111/jmg.12113
- Cawood, P., and Pisarevsky, S.A., 2006, Precambrian Plate Tectonics : Criteria and Evidence Precambrian Plate Precambrian plate tectonics : Criteria and evidence:, doi:10.1130/GSAT01607.1.
- Cawood, P.A., Hawkesworth, C.J., Pisarevsky, S.A., Dhuime, B., Capitanio, F.A., and Nebel, O., 2018, Geological archive of the onset of plate tectonics: Philosophical Transactions of the Royal Society A: Mathematical, Physical and Engineering Sciences, v. 376, doi:10.1098/rsta.2017.0405.
- Cesare, B., Ferrero, S., Salvioli-Mariani, E., Pedron, D., and Cavallo, A., 2009, "Nanogranite" and glassy inclusions: The anatectic melt in migmatites and granulites: Geology, v. 37, p. 627–630, doi:10.1130/G25759A.1.
- Chapman, T., Clarke, G.L., Piazolo, S., and Daczko, N.R., 2017, Evaluating the importance of metamorphism in the foundering of continental crust: Scientific Reports, v. 7, p. 1–12, doi:10.1038/s41598-017-13221-6.
- Cheng, H., and Cao, D., 2015, Protracted garnet growth in high-P eclogite: Constraints from multiple geochronology and P-T pseudosection: Journal of Metamorphic Geology, v. 33, p. 613–632, doi:10.1111/jmg.12136.
- Cheng, H.A.O., 2018, Garnet Lu–Hf and Sm–Nd geochronology: A time capsule of the metamorphic evolution of orogenic belts: Geological Society Special Publication, v. 474, p. 47–67, doi:10.1144/SP474.7.
- Chernoff, C.B., and Carlson, W.D., 1997, Disequilibrium for Ca during growth of pelitic garnet: Journal of Metamorphic Geology, v. 15, p. 421–438, doi:10.1111/j.1525-1314.1997.00026.x.

- Cisneros, M., Ashley, K.T., and Bodnar, R.J., 2020, Evaluation and application of the quartz-inclusions-in-epidote mineral barometer: American Mineralogist, v. 105, p. 1140–1151, doi:10.2138/am-2020-7379.
- Clarke, G.L., Daczko, N.R., and Miescher, D., 2013, Identifying relic igneous garnet and clinopyroxene in eclogite and granulite, Breaksea orthogneiss, New Zealand: Journal of Petrology, v. 54, p. 1921–1938, doi:10.1093/petrology/egt036.
- Clemens, J.D., 2003, S-type granitic magmas - petrogenetic issues, models and evidence: Earth-Science Reviews, v. 61, p. 1–18, doi:10.1016/S0012-8252(02)00107-1.
- Coggon, R., Holland, T.J.B., and Street, D., 2002, Mixing properties of phengitic micas and revised garnet-phengite thermobarometers: , p. 683–696.
- Coleman, R.G., 1971, Tectonic Eraplacement Upper Mantle Peridotires along Continental Edges: Journal of Geophysical Research, v. 76, p. 1212–1222.
- Collins, W. J., 1989, Polydiapirism of the Archean Mount Edgar Batholith, Pilbara Block, Western Australia. Precambrian Research, 43(1–2), 41–62. https://doi.org/10.1016/0301-9268(89)90004-1
- Condie, K.C., 2018, A planet in transition: The onset of plate tectonics on Earth between 3 and 2 Ga? Geoscience Frontiers, v. 9, p. 51–60, doi:10.1016/j.gsf.2016.09.001.
- Condie, K.C., and Kröner, A., 2008, When did plate tectonics begin? evidence from the orogenic record (K. C. Condie & V. Pease, Eds.): v. 440, 281–294 p., doi:10.1130/2008.2440(14).
- Connolly, J.A.D., 2005. Computation of phase equilibria by linear programming: A tool for geodynamic modeling and its application to subduction zone decarbonation. Earth Planet. Sci. Lett. 236, 524–541. https://doi.org/10.1016/j.epsl.2005.04.033
- Craven, S. J., & Daczko, N. R. (2018). High-temperature–low-pressure metamorphism and the production of S-type granites of the Hillgrove Supersuite, southern New England Orogen, NSW, Australia. Australian Journal of Earth Sciences, 65(2), 191-207.
- Crowley, J.L., 2003, U-Pb geochronology of 3810-3630 Ma granitoid rocks south of the Isua greenstone belt, southern West Greenland: Precambrian Research, v. 126, p. 235–257, doi:10.1016/S0301-9268(03)00097-4.
- Crowley, J.L., Myers, J.S., and Dunning, G.R., 2002, Timing and nature of multiple 3700-3600 Ma tectonic events in intrusive rocks North of the Isua greenstone belt, southern West Greenland: Bulletin of the Geological Society of America, v. 114, p. 1311–1325, doi:10.1130/0016-7606(2002)114<1311:TANOMM>2.0.CO;2.
- Cutts, K.A., Stevens, G., and Kisters, A., 2015, Reply to "paleo- to mesoarchean polymetamorphism in the barberton granite-greenstone belt, South Africa: Constraints from U-Pb monazite and Lu-Hf garnet geochronology on the tectonic processes that shaped the belt: Discussion" by M. Brown: Bulletin of the Geological Society of America, v. 127, p. 1558–1563, doi:10.1130/B31304.1.
- Cutts, K.A., Stevens, G., Hoffmann, J.E., Buick, I.S., Frei, D., and Münker, C., 2014, Paleo- to Mesoarchean polymetamorphism in the Barberton Granite- Greenstone Belt , South Africa : Constraints from U-Pb monazite and Lu- Hf garnet geochronology on the tectonic processes that shaped the belt: , p. 251–270, doi:10.1130/B30807.1.
- Daniel, C.G., and Spear, F.S., 1999, The clustered nucleation and growth processes of garnet in regional metamorphic rocks from north-west Connecticut, USA: Journal of Metamorphic Geology, v. 17, p. 503–520, doi:10.1046/j.1525-1314.1999.00200.x.

- de Capitani, C., and Brown, T.H., 1987, The computation of chemical equilibrium in complex systems containing non-ideal solutions: Geochimica et Cosmochimica Acta, v. 51, p. 2639–2652, doi:10.1016/0016-7037(87)90145-1.
- De Capitani, C., and Petrakakis, K., 2010, The computation of equilibrium assemblage diagrams with Theriak/Domino software: American Mineralogist, v. 95, p. 1006–1016, doi:10.2138/am.2010.3354.
- de Paoli, M.C., Clarke, G.L., Klepeis, K.A., Allibone, A.H., and Turnbull, I.M., 2009, The eclogite-granulite transition: Mafic and intermediate assemblages at Breaksea sound, New Zealand: Journal of Petrology, v. 50, p. 2307–2343, doi:10.1093/petrology/egp078.
- Dempster, T.J., Coleman, S., Kennedy, R., Chung, P., Brown, R.W., 2020. Growth zoning of garnet porphyroblasts: Grain boundary and microtopographic controls. J. Metamorph. Geol. 1–17. https://doi.org/10.1111/jmg.12558
- Dempster, T.J., La Piazza, J., Taylor, A.G., Beaudoin, N., and Chung, P., 2017, Chemical and textural equilibration of garnet during amphibolite facies metamorphism: The influence of coupled dissolution–reprecipitation: Journal of Metamorphic Geology, v. 35, p. 1111–1130, doi:10.1111/jmg.12278.
- Dempster, T.J., Symon, S., Chung, P., 2017. Intergranular diffusion rates from the analysis of garnet surfaces: Implications for metamorphic equilibration. J. Metamorph. Geol. 35, 585–600. https://doi.org/10.1111/jmg.12247
- De Wit, M. J., Hart, R. A., & Hart, R. J. (1987). The Jamestown Ophiolite Complex, Barberton mountain belt: a section through 3.5 Ga oceanic crust. Journal of African Earth Sciences (1983), 6(5), 681-730.
- Dhuime, B., Hawkesworth, C.J., Cawood, P.A., and Storey, C.D., 2012, A change in the geodynamics of continental growth 3 billion years ago: Science, v. 335, p. 1334–1336, doi:10.1126/science.1216066.
- Diener, J. F. A., & Powell, R. ,2012, Revised activity-composition models for clinopyroxene and amphibole. Journal of Metamorphic Geology, 30(2), 131–142. https://doi.org/10.1111/j.1525-1314.2011.00959.x
- Dymek, R.F., and Klein, C., 1988, Chemistry, petrology and origin of banded iron-formation lithologies from the 3800 MA isua supracrustal belt, West Greenland: Precambrian Research, v. 39, p. 247–302, doi:10.1016/0301-9268(88)90022-8.
- Dymek, R.F., Brothers, S.C., Craig, M., 1988. Petrogenesis of Ultramafic Metamorphic Rocks from. J. Petrol. 29, 1353–1397.
- Ehlers, K., and Hoinkes, G., 1987, Titanian chondrodite and clinohumite in marbles from the Ötztal crystalline basement: Mineralogy and Petrology, v. 36, p. 13–25, doi:10.1007/BF01164366.
- Engi, M., Lanari, P., and Kohn, M.J., 2017, Significant Ages — An Introduction to Petrochronology: v. 83, p. 1–12.
- Evans, T.P., 2004, A method for calculating effective bulk composition modification due to crystal fractionation in garnet-bearing schist: Implications for isopleth thermobarometry: Journal of Metamorphic Geology, v. 22, p. 547–557, doi:10.1111/j.1525-1314.2004.00532.x.
- Faleiros, F.M., Campanha, G.A. da C., Bello, R.M. da S., Fuzikawa, K., 2010. Quartz recrystallization regimes, c-axis texture transitions and fluid inclusion reequilibration in a prograde greenschist to amphibolite facies mylonite zone (Ribeira Shear Zone, SE Brazil). Tectonophysics 485, 193–214. https://doi.org/10.1016/j.tecto.2009.12.014
- Faryad, S.W., and Ježek, J., 2019, Compositional zoning in garnet and its modification by diffusion during pressure and temperature changes in metamorphic

rocks; an approach and software: Lithos, v. 332–333, p. 287–295, doi:10.1016/j.lithos.2019.03.002.

- Faryad, S.W., Baldwin, S.L., Jedlicka, R., and Ježek, J., 2019, Two-stage garnet growth in coesite eclogite from the southeastern Papua New Guinea (U)HP terrane and its geodynamic significance: Contributions to Mineralogy and Petrology, v. 174, p. 1–16, doi:10.1007/s00410-019-1612-4.

- Fischer, R., and Gerya, T., 2016, Early Earth plume-lid tectonics: A high-resolution 3D numerical modelling approach: Journal of Geodynamics, v. 100, p. 198–214, doi:10.1016/j.jog.2016.03.004.

- François, C., Philippot, P., Rey, P., and Rubatto, D., 2014, Burial and exhumation during Archean sagduction in the East Pilbara Granite-Greenstone Terrane: Earth and Planetary Science Letters, v. 396, p. 235–251, doi:10.1016/j.epsl.2014.04.025.

- Frei, R., and Rosing, M.T., 2001, The least radiogenic terrestrial leads; implications for the early Archean crustal evolution and hydrothermal-metasomatic processes in the Isua Supracrustal Belt (West Greenland): Chemical Geology, v. 181, p. 47–66, doi:10.1016/S0009-2541(01)00263-7.

- Frei, R., Bridgwater, D., Rosing, M., and Stecher, O., 1999, Controversial Pb-Pb and Sm-Nd isotope results in the early Archean Isua (West Greenland) oxide iron formation: Preservation of primary signatures versus secondary disturbances: Geochimica et Cosmochimica Acta, v. 63, p. 473–488, doi:10.1016/S0016-7037(98)00290-7.

- Frei, R., Rosing, M. T., Waight, T. E., & Ulfbeck, D. G., 2002, Hydrothermal-metasomatic and tectono-metamorphic processes in the Isua supracrustal belt (West Greenland): A multi-isotopic investigation of their effects on the Earth's oldest oceanic crustal sequence. Geochimica et Cosmochimica Acta, 66(3), 467–486. https://doi.org/10.1016/S0016-7037(01)00781-5

- Friend, C.R.L., and Nutman, A.P., 2005, New pieces to the Archaean terrane jigsaw puzzle in the Nuuk region, southern West Greenland: Steps in transforming a simple insight into a complex regional tectonothermal model: Journal of the Geological Society, v. 162, p. 147–162, doi:10.1144/0016-764903-161.

- Friend, C.R.L., and Nutman, A.P., 2011, Dunites from Isua, Greenland: A ca. 3720 Ma window into subcrustal metasomatism of depleted mantle: Geology, v. 39, p. 663–666, doi:10.1130/G31904.1.

- Friend, C.R.L., and Nutman, A.P., 2019, Tectono-stratigraphic terranes in Archaean gneiss complexes as evidence for plate tectonics: The Nuuk region, southern West Greenland: Gondwana Research, v. 72, p. 213–237, doi:10.1016/j.gr.2019.03.004.

- Furnes, H., de Wit, M., Staudigel, H., Rosing, M., & Muehlenbachs, K. (2007). A vestige of Earth's oldest ophiolite. science, 315(5819), 1704-1707.

- Gaidies, F., Capitani, C., and Abart, R., 2008, THERIA_G: A software program to numerically model prograde garnet growth: Contributions to Mineralogy and Petrology, v. 155, p. 657–671, doi:10.1007/s00410-007-0263-z.

- Gaidies, F., Petley-Ragan, A., Chakraborty, S., Dasgupta, S., and Jones, P., 2015, Constraining the conditions of Barrovian metamorphism in Sikkim, India: P-T-t paths of garnet crystallization in the Lesser Himalayan Belt: Journal of Metamorphic Geology, v. 33, p. 23–44, doi:10.1111/jmg.12108.

- Gardiner, N.J., Johnson, T.E., Kirkland, C.L., and Szilas, K., 2019, Modelling the Hafnium-Neodymium Evolution of Early Earth: A Study from West Greenland: Journal of Petrology, v. 60, p. 177–197, doi:10.1093/petrology/egy110.

- Gauthiez-Putallaz, L., Nutman, A., Bennett, V., Rubatto, D., 2020. Origins of high δ18O in 3.7–3.6 Ga crust: A zircon and garnet record in Isua clastic metasedimentary rocks. Chem. Geol. 119474. https://doi.org/10.1016/J.CHEMGEO.2020.119474
- George, F.R., and Gaidies, F., 2017, Characterisation of a garnet population from the Sikkim Himalaya: insights into the rates and mechanisms of porphyroblast crystallisation: Contributions to Mineralogy and Petrology, v. 172, p. 1–22, doi:10.1007/s00410-017-1372-y.
- George, F.R., and Gaidies, F., 2020, Simultaneous operation of opposing reaction mechanisms: The influence of matrix heterogeneity on post-kinematic garnet crystallization in an inverted metamorphic sequence: Journal of Metamorphic Geology, v. 38, p. 743–769, doi:10.1111/jmg.12539.
- Gerya, T. V., Stern, R.J., Baes, M., Sobolev, S. V., and Whattam, S.A., 2015, Plate tectonics on the Earth triggered by plume-induced subduction initiation: Nature, v. 527, p. 221–225, doi:10.1038/nature15752.
- Gerya, T. V., Yuen, D.A., and Sevre, E.O.D., 2004, Dynamical causes for incipient magma chambers above slabs: Geology, v. 32, p. 89–92, doi:10.1130/G20018.1.
- Gerya, T., 2014, Precambrian geodynamics: Concepts and models: Gondwana Research, v. 25, p. 442–463, doi:10.1016/j.gr.2012.11.008.
- Gill, R., 2011, Igneous rocks and processes: a practical guide. John Wiley & Sons.
- Göğüş, O.H., and Pysklywec, R.N., 2008, Near-surface diagnostics of dripping or delaminating lithosphere: Journal of Geophysical Research: Solid Earth, v. 113, p. 1–11, doi:10.1029/2007JB005123.
- Gonzalez, J.P., Thomas, J.B., Baldwin, S.L., and Alvaro, M., 2019, Quartz-in-garnet and Ti-in-quartz thermobarometry: Methodology and first application to a quartzofeldspathic gneiss from eastern Papua New Guinea: Journal of Metamorphic Geology, p. 1–16, doi:10.1111/jmg.12508.
- Gordon, S.M., Kirkland, C.L., Reddy, S.M., Blatchford, H.J., Whitney, D.L., Teyssier, C., Evans, N.J., and McDonald, B.J., 2021, Deformation-enhanced recrystallization of titanite drives decoupling between U-Pb and trace elements: Earth and Planetary Science Letters, v. 560, p. 116810, doi:10.1016/j.epsl.2021.116810.
- Goscombe, B., Foster, D.A., Gray, D., and Wade, B., 2017, Metamorphic response and crustal architecture in a classic collisional orogen: The Damara Belt, Namibia: Gondwana Research, v. 52, p. 80–124, doi:10.1016/j.gr.2017.07.006.
- Green, E., Holland, T., & Powell, R. (2007). An order-disorder model for omphacitic pyroxenes in the system jadeite-diopside-hedenbergite-acmite, with applications to eclogitic rocks. American Mineralogist, 92(7), 1181–1189. https://doi.org/10.2138/am.2007.2401
- Gruau, G., Rosing, M., Bridgwater, D., and Gill, R.C.O., 1996, Resetting of Sm-Nd systematics during metamorphism of > 3.7-Ga rocks: Implications for isotopic models of early Earth differentiation: Chemical Geology, v. 133, p. 225–240, doi:10.1016/S0009-2541(96)00092-7.
- Guotana, J.M., Morishita, T., Nishio, I., Tamura, A., Mizukami, T., Tani, K., Harigane, Y., Szilas, K., and Pearson, D.G., 2021, Deserpentinization and high-pressure (eclogite-facies) metamorphic features in the Eoarchean ultramafic body from Isua, Greenland: Geoscience Frontiers, p. 101298, doi:10.1016/j.gsf.2021.101298.
- Hacker, B.R., Kelemen, P.B., and Behn, M.D., 2011, Differentiation of the continental crust by relamination: Earth and Planetary Science Letters, v. 307, p. 501–516, doi:10.1016/j.epsl.2011.05.024.

- Hawkesworth, C.J., and Brown, M., 2018, Earth dynamics and the development of plate tectonics: Philosophical Transactions of the Royal Society A: Mathematical, Physical and Engineering Sciences, v. 376, p. 1–5, doi:10.1098/rsta.2018.0228.
- Hayashi, M., Komiya, T., Nakamura, Y., Maruyama, S., 2000. Archean regional metamorphism of the isua supracrustal belt, Southern West Greenland: Implications for a driving force for archean plate tectonics, International Geology Review. https://doi.org/10.1080/00206810009465128
- Heaman, L.M., 2009, The application of U-Pb geochronology to mafic, ultramafic and alkaline rocks: An evaluation of three mineral standards: Chemical Geology, v. 261, p. 43–52, doi:10.1016/j.chemgeo.2008.10.021.
- Hegner, E., Rajesh, S., Willbold, M., Müller, D., Joachimski, M., Hofmann, M., Linnemann, U., Zieger, J., and Pradeepkumar, A.P., 2020, Sediment-derived origin of the putative Munnar carbonatite, South India: Journal of Asian Earth Sciences, v. 200, p. 104432, doi:10.1016/j.jseaes.2020.104432.
- Heijlen, W., Appel, P. W. U., Frezzotti, M. L., Horsewell, A., & Touret, J. L. R. (2006). Metamorphic fluid flow in the northeastern part of the 3.8-3.7 Ga Isua Greenstone Belt (SW Greenland): A re-evalution of fluid inclusion evidence for early Archean seafloor-hydrothermal systems. Geochimica et Cosmochimica Acta, 70(12), 3075–3095. https://doi.org/10.1016/j.gca.2006.04.005
- Henry, D. J., Guidotti, C. V., & Thomson, J. A., 2005, . The Ti-saturation surface for low-to-medium pressure metapelitic biotites: Implications for geothermometry and Ti-substitution mechanisms. American Mineralogist, 90(2–3), 316–328. https://doi.org/10.2138/am.2005.1498
- Hermann, J., and Rubatto, D., 2003, Relating zircon and monazite domains to garnet growth zones: Age and duration of granulite facies metamorphism in the Val Malenco lower crust: Journal of Metamorphic Geology, v. 21, p. 833–852, doi:10.1046/j.1525-1314.2003.00484.x.
- Herzberg, C., Asimow, P.D., Arndt, N., Niu, Y., Lesher, C.M., Fitton, J.G., Cheadle, M.J., and Saunders, A.D., 2007, Temperatures in ambient mantle and plumes: Constraints from basalts, picrites, and komatiites: Geochemistry, Geophysics, Geosystems, v. 8, doi:10.1029/2006GC001390.
- Herzberg, C., Condie, K., and Korenaga, J., 2010, Thermal history of the Earth and its petrological expression: Earth and Planetary Science Letters, v. 292, p. 79–88, doi:10.1016/j.epsl.2010.01.022.
- Hickmott, D.D., Shimizu, N., Spear, F.S., and Selverstone, J., 1987, Trace-element zoning in a metamorphic garnet: Geology, v. 15, p. 573–576, doi:10.1130/0091-7613(1987)15<573:TZIAMG>2.0.CO;2.
- Hiess, J., Bennett, V.C., Nutman, A.P., Williams, I.S., 2009. In situ U-Pb, O and Hf isotopic compositions of zircon and olivine from Eoarchaean rocks, West Greenland: New insights to making old crust. Geochim. Cosmochim. Acta 73, 4489–4516. https://doi.org/10.1016/j.gca.2009.04.019
- Hiess, J., Bennett, V.C., Nutman, A.P., Williams, I.S., 2011. Archaean fluid-assisted crustal cannibalism recorded by low δ 18 O and negative ε Hf(T) isotopic signatures of West Greenland granite zircon. Mineral. Petrol. 101, 1027–1050. https://doi.org/10.1007/s00410-010-0578-z
- Hirsch, D.M., Prior, D.J., Carlson, W.D., 2003. An overgrowth model to explain multiple, dispersed high-Mn regions in the cores of garnet porphyroblasts. Am. Mineral. 88, 131–141. https://doi.org/10.2138/am-2003-0116

- Hoffmann, J. E., Zhang, C., Moyen, J.-F., & Nagel, T. J. ,2019, The Formation of Tonalites–Trondjhemite–Granodiorites in Early Continental Crust. In Earth's Oldest Rocks (Issue Chapter 11). https://doi.org/10.1016/b978-0-444-63901-1.00007-1
- Hoffmann, J.E., Nagel, T.J., Münker, C., Næraa, T., and Rosing, M.T., 2014, Constraining the process of Eoarchean TTG formation in the Itsaq Gneiss Complex, southern West Greenland: Earth and Planetary Science Letters, v. 388, p. 374–386, doi:10.1016/j.epsl.2013.11.050.
- Holder, R.M., Viete, D.R., Brown, M., and Johnson, T.E., 2019, Metamorphism and the evolution of plate tectonics: Nature, v. 572, p. 378–381, doi:10.1038/s41586-019-1462-2.
- Holland, T. J. B., & Powell, R., 1998, An internally consistent thermodynamic data set for phases of petrological interest. Journal of Metamorphic Geology, 16(3), 309–343. https://doi.org/10.1111/j.1525-1314.1998.00140.x
- Holland, T. J. B., & Powell, R., 2011, An improved and extended internally consistent thermodynamic dataset for phases of petrological interest, involving a new equation of state for solids. Journal of Metamorphic Geology, 29(3), 333–383. https://doi.org/10.1111/j.1525-1314.2010.00923.x
- Holland, T., and Blundy, J., 1994, Non-ideal interactions in calcic amphiboles and their bearing on amphibole-plagioclase thermometry: Contributions to Mineralogy and Petrology, v. 116, p. 433–447, doi:10.1007/BF00310910.
- Holland, T., Baker, J., and Powell, R., 1998, Mixing properties and activity-composition relationships of chlorites in the system MgO-FeO-Al2O3-SiO2-H2O: European Journal of Mineralogy, v. 10, p. 395–406, doi:10.1127/ejm/10/3/0395.
- Hollister, L. S., 1966, Garnet zoning: an interpretation based on the Rayleigh fractionation model. Science, 154(3757), 1647-1651.
- Holness, M.B., Cesare, B., and Sawyer, E.W., 2011, Melted rocks under the microscope: Microstructures and their interpretation: Elements, v. 7, p. 247–252, doi:10.2113/gselements.7.4.247.
- Hopkins, M., Harrison, T.M., and Manning, C.E., 2008, Low heat flow inferred from >4 Gyr zircons suggests Hadean plate boundary interactions: Nature, v. 456, p. 493–496, doi:10.1038/nature07465.
- Inui, M., and Toriumi, M., 2004, A theoretical study on the formation of growth zoning in garnet consuming chlorite: Journal of Petrology, v. 45, p. 1369–1392, doi:10.1093/petrology/egh016.
- Jenner, F.E., Bennett, V.C., Nutman, A.P., Friend, C.R.L., Norman, M.D., and Yaxley, G., 2009, Evidence for subduction at 3.8 Ga: Geochemistry of arc-like metabasalts from the southern edge of the Isua Supracrustal Belt: Chemical Geology, v. 261, p. 83–98, doi:10.1016/j.chemgeo.2008.09.016.
- Jin, X., Zhang, Y.X., Whitney, D.L., Zhang, K.J., Raia, N.H., Hamelin, C., Hu, J.C., Lu, L., Zhou, X.Y., and Khalid, S. Bin, 2021, Crustal Material Recycling Induced by Subduction Erosion and Subduction channel Exhumation: A Case Study of Central Tibet (western China) Based on P-T-t Paths of the Eclogite-Bearing Baqing Metamorphic Complex: Bulletin of the Geological Society of America, v. 133, p. 1575–1599, doi:10.1130/B35638.1.
- Johnson, T. E., Brown, M., Gardiner, N. J., Kirkland, C. L., & Smithies, R. H., 2017, Earth's first stable continents did not form by subduction. Nature, 543(7644), 239–242. https://doi.org/10.1038/nature21383
- Kahl, M., Chakraborty, S., Pompilio, M., & Costa, F., 2015, Constraints on the nature and evolution of the magma plumbing system of Mt. Etna volcano (1991-2008) from

a combined thermodynamic and kinetic modelling of the compositional record of minerals. Journal of Petrology, 56(10), 2025–2068. https://doi.org/10.1093/petrology/egv063

- Kelemen, P.B., and Behn, M.D., 2016, Formation of lower continental crust by relamination of buoyant arc lavas and plutons: Nature Geoscience, v. 9, p. 197–205, doi:10.1038/ngeo2662.
- Kemp, A.I.S., 2018, Early earth geodynamics: Cross examining the geological testimony: Philosophical Transactions of the Royal Society A: Mathematical, Physical and Engineering Sciences, v. 376, doi:10.1098/rsta.2018.0169.
- Kohn, M.J., 2014, "Thermoba-Raman-try": Calibration of spectroscopic barometers and thermometers for mineral inclusions: Earth and Planetary Science Letters, v. 388, p. 187–196, doi:10.1016/j.epsl.2013.11.054.
- Kohn, M.J., 2017, Titanite Petrochronology: Reviews in Mineralogy and Geochemistry, v. 83, p. 419–441, doi:10.2138/rmg.2017.83.13.
- Komiya, T., Hayashi, M., Maruyama, S., & Yurimoto, H., 2002, Intermediate-P/T type Archean metamorphism of the Isua supracrustal belt: Implications for secular change of geothermal gradients at subduction zones and for Archean plate tectonics. American Journal of Science, 302(9), 806–826. https://doi.org/10.2475/ajs.302.9.806
- Komiya, T., Maruyama, S., Masuda, T., Nohda, S., Hayashi, M., and Okamoto, K., 1999, Plate tectonics at 3.8-3.7 Ga: Field evidence from the Isua Accretionary Complex, southern West Greenland: Journal of Geology, v. 107, p. 515–554, doi:10.1086/314371.
- Konrad-Schmolke, M., Zack, T., O'Brien, P.J., and Jacob, D.E., 2008, Combined thermodynamic and rare earth element modelling of garnet growth during subduction: Examples from ultrahigh-pressure eclogite of the Western Gneiss Region, Norway: Earth and Planetary Science Letters, v. 272, p. 488–498, doi:10.1016/j.epsl.2008.05.018.
- Korenaga, J., 2013, Initiation and Evolution of Plate Tectonics on Earth: Theories and Observations: Annual Review of Earth and Planetary Sciences, v. 41, p. 117–151, doi:10.1146/annurev-earth-050212-124208.
- Korenaga, J., 2018, Crustal evolution and mantle dynamics through Earth history: Philosophical Transactions of the Royal Society A: Mathematical, Physical and Engineering Sciences, v. 376, doi:10.1098/rsta.2017.0408.
- Kretz, R., 1966. Grain-Size Distribution for Certain Metamorphic Minerals in Relation to Nucleation and Growth. J. Geol. 74, 147–173. https://doi.org/10.1086/627152
- Kretz, R., 1969. On the spatial distribution of crystals in rocks. Lithos 2, 39–65. https://doi.org/10.1016/S0024-4937(69)80005-8
- Kretz, R., 1974. Some models for the rate of crystallization of garnet in metamorphic rocks. Lithos 7, 123–131. https://doi.org/10.1016/0024-4937(74)90025-5
- Kretz, R., 1993. A garnet population in Yellowknife schist, Canada. J. Metamorph. Geol. 11, 101–120. https://doi.org/10.1111/j.1525-1314.1993.tb00134.x
- Krogh, E.J., Oh, C.W., and Liou, J.C., 1994, Polyphase and anticlockwise P-T evolution for Franciscan eclogites and blueschists from Jenner, California, USA: Journal of Metamorphic Geology, v. 12, p. 121–134, doi:10.1111/j.1525-1314.1994.tb00008.x.
- Lanari, P., Vho, A., Bovay, T., Airaghi, L., Centrella, S., 2019. Quantitative compositional mapping of mineral phases by electron probe micro-analyser. Geol. Soc. Spec. Publ. 478, 39–63. https://doi.org/10.1144/SP478.4

- Lanari, P., Vidal, O., De Andrade, V., Dubacq, B., Lewin, E., Grosch, E.G., Schwartz, S., 2014. XMapTools: A MATLAB©-based program for electron microprobe X-ray image processing and geothermobarometry. Comput. Geosci. 62, 227–240. https://doi.org/10.1016/j.cageo.2013.08.010
- Lang, H.M., Rice, J.M., 1985. Regression modelling of metamorphic reactions in metapelites, snow peak, Northern Idaho. J. Petrol. 26, 857–887. https://doi.org/10.1093/petrology/26.4.857
- Leake, B. E., Woolley, A. R., Arps, C. E. S., Birch, W. D., Gilbert, M. C., Grice, J. D., Hawthorne, F. C., Kato, A., Kisch, H. J., Krivovichev, V. G., Linthout, K., Laird, J., Mandarino, J. A., Maresch, W. V., Nickel, E. H., Rock, N. M. S., Schumacher, J. C., Smith, D. C., Stephenson, N. C. N., Youzhi, G. (1997). Nomenclature of amphiboles: Report of the subcommittee on amphiboles of the international mineralogical association, commission on new minerals and mineral names. American Mineralogist, 82(9–10), 1019–1037. https://doi.org/10.1180/minmag.1997.061.405.13
- Lenardic, A., 2018, The diversity of tectonic modes and thoughts about transitions between them: Philosophical Transactions of the Royal Society A: Mathematical, Physical and Engineering Sciences, v. 376, doi:10.1098/rsta.2017.0416.
- Li, Z.H., Gerya, T. V., and Burg, J.P., 2010, Influence of tectonic overpressure on P-T paths of HP-UHP rocks in continental collision zones: Thermomechanical modelling: Journal of Metamorphic Geology, v. 28, p. 227–247, doi:10.1111/j.1525-1314.2009.00864.x.
- Locock, A. J., 2014, An Excel spreadsheet to classify chemical analyses of amphiboles following the IMA 2012 recommendations. Computers and Geosciences, 62, 1–11. https://doi.org/10.1016/j.cageo.2013.09.011
- Loomis, T.P., 1983. Compositional zoning of crystals: a record of growth and reaction history. Kinet. Equilib. Miner. React. 1–60. https://doi.org/10.1007/978-1-4612-5587-1_1
- Lourenço, D.L., Rozel, A.B., Ballmer, M.D., and Tackley, P.J., 2020, Plutonic-Squishy Lid: A New Global Tectonic Regime Generated by Intrusive Magmatism on Earth-Like Planets: Geochemistry, Geophysics, Geosystems, v. 21, doi:10.1029/2019GC008756.
- Luvizotto, G.L. et al., 2009, Rutile crystals as potential trace element and isotope mineral standards for microanalysis: Chemical Geology, v. 261, p. 346–369, doi:10.1016/j.chemgeo.2008.04.012.
- Maldonado, R., Weber, B., Ortega-Gutiérrez, F., and Solari, L.A., 2018, High-pressure metamorphic evolution of eclogite and associated metapelite from the Chuacús complex (Guatemala Suture Zone): Constraints from phase equilibria modelling coupled with Lu-Hf and U-Pb geochronology: Journal of Metamorphic Geology, v. 36, p. 95–124, doi:10.1111/jmg.12285.
- Manea, V.C., Manea, M., Kostoglodov, V., Currie, C.A., and Sewell, G., 2004, Thermal structure, coupling and metamorphism in the Mexican subduction zone beneath Guerrero: Geophysical Journal International, v. 158, p. 775–784, doi:10.1111/j.1365-246X.2004.02325.x.
- Maruyama, S., Santosh, M., and Azuma, S., 2018, Initiation of plate tectonics in the Hadean: Eclogitization triggered by the ABEL Bombardment: Geoscience Frontiers, v. 9, p. 1033–1048, doi:10.1016/j.gsf.2016.11.009.

- Mazzucchelli, M.L., Angel, R.J., and Alvaro, M., 2021, EntraPT: An online platform for elastic geothermobarometry: American Mineralogist, v. 106, p. 830–837, doi:10.2138/am-2021-7693CCBYNCND.
- Mazzucchelli, M.L., Burnley, P., Angel, R.J., Morganti, S., Domeneghetti, M.C., Nestola, F., and Alvaro, M., 2018, Elastic geothermobarometry: Corrections for the geometry of the host-inclusion system: Geology, v. 46, p. 231–234, doi:10.1130/G39807.1.
- McKinnon, W.B., Schenk, P.M., and Dombard, A.J., 2001, Chaos on Io: A model for formation of mountain blocks by crustal heating, melting, and tilting: Geology, v. 29, p. 103–106, doi:10.1130/0091-7613(2001)029<0103:COIAMF>2.0.CO;2.
- Miyashiro, A., 1961, Evolution of metamorphic belts: Journal of Petrology, v. 2, p. 277–311, doi:10.1093/petrology/2.3.277.
- Miyashiro, A., 1973, Paired and unpaired metamorphic belts: Tectonophysics, v. 17, p. 241–254, doi:10.1016/0040-1951(73)90005-X.
- Miyazaki, K., 2015, Diffusion-controlled growth and degree of disequilibrium of garnet porphyroblasts: is diffusion-controlled growth of porphyroblasts common? Progress in Earth and Planetary Science, v. 2, doi:10.1186/s40645-015-0055-4.
- Molina, J.F., Moreno, J.A., Castro, A., Rodríguez, C., and Fershtater, G.B., 2015, Calcic amphibole thermobarometry in metamorphic and igneous rocks: New calibrations based on plagioclase/amphibole Al-Si partitioning and amphibole/liquid Mg partitioning: Lithos, v. 232, p. 286–305, doi:10.1016/j.lithos.2015.06.027.
- Moorbath, S., O'Nions, R.K., Pankhurst, R.J., 1973. Early Archaean age for the Isua iron formation, West Greenland. Nature 245, 138–139.
- Moorbath, S., O'Nions, R.K., Pankhurst, R.J., Gale, N.H., and McGregor, V.R., 1972, Further Rubidium-Strontium Age Determinations on the Very Early Precambrian Rocks of the Godthaab District, West Greenland: Nature Physical Science, v. 240, p. 78–82.
- Moore, J., Beinlich, A., Porter, J.K., Talavera, C., Berndt, J., Piazolo, S., Austrheim, H., and Putnis, A., 2020, Microstructurally controlled trace element (Zr, U–Pb) concentrations in metamorphic rutile: An example from the amphibolites of the Bergen Arcs: Journal of Metamorphic Geology, v. 38, p. 103–127, doi:10.1111/jmg.12514.
- Moore, W.B., and Webb, A.A.G., 2013, Heat-pipe earth: Nature, v. 501, p. 501–505, doi:10.1038/nature12473.
- Moyen, J.F., and Laurent, O., 2018, Archaean tectonic systems: A view from igneous rocks: Lithos, v. 302–303, p. 99–125, doi:10.1016/j.lithos.2017.11.038.
- Mueller, T., Watson, E.B., Harrison, T.M., 2010. Applications of diffusion data to high-temperature earth systems. Rev. Mineral. Geochemistry 72, 997–1038. https://doi.org/10.2138/rmg.2010.72.23
- Müller, T., Dohmen, R., Becker, H.W., ter Heege, J.H., and Chakraborty, S., 2013, Fe-Mg interdiffusion rates in clinopyroxene: Experimental data and implications for Fe-Mg exchange geothermometers: Contributions to Mineralogy and Petrology, v. 166, p. 1563–1576, doi:10.1007/s00410-013-0941-y.
- Mulligan, S.R., Wells, M.L., Hoisch, T.D., Salamat, A., Childs, C., Tschauner, O., Affinati, S.C., Wills, M.A., and Smith, G.A., 2022, Deviation between quartz-in-garnet elastic geobarometry and equilibrium-based pressure-temperature modeling in Barrovian metamorphic rocks: Journal of Metamorphic Geology, p. 1–61, doi:10.1111/jmg.12658.

- Murri, M., Mazzucchelli, M.L., Campomenosi, N., Korsakov, A. V., Prencipe, M., Mihailova, B.D., Scambelluri, M., Angel, R.J., and Alvaro, M., 2018, Raman elastic geobarometry for anisotropic mineral inclusions: American Mineralogist, v. 103, p. 1869–1872, doi:10.2138/am-2018-6625CCBY.
- Myers, J.S., 2001. Protoliths of the 3.8-3.7 Ga Isua greenstone belt, West Greenland. Precambrian Res. 105, 129–141. https://doi.org/10.1016/S0301-9268(00)00108-X
- Nagel, T. J., Hoffmann, J. E., & Münker, C., 2012, Generation of Eoarchean tonalite-trondhjemite-granodiorite series from ahickened mafic arc crust. Geology, 40(4), 375–378. https://doi.org/10.1130/G32729.1
- Nagurney, A.B., Caddick, M.J., Pattison, D.R.M., Michel, F.M., 2021. Preferred orientations of garnet porphyroblasts reveal previously cryptic templating during nucleation. Sci. Rep. 1–9. https://doi.org/10.1038/s41598-021-85525-7
- Negulescu, E., Săbău, G., and Massonne, H.J., 2018, Growth of chloritoid and garnet along a nearly isothermal burial path to 70 km depth: an example from the Bughea Metamorphic Complex, Leaota Massif, South Carpathians: Mineralogy and Petrology, v. 112, p. 535–553, doi:10.1007/s00710-017-0552-9.
- Newton, R.C., Charlu, T. V., and Kleppa, O.J., 1980, Thermochemistry of the high structural state plagioclases: Geochimica et Cosmochimica Acta, v. 44, p. 933–941, doi:10.1016/0016-7037(80)90283-5.
- Nicoli, G., Moyen, J.F., and Stevens, G., 2016, Diversity of burial rates in convergent settings decreased as Earth aged: Scientific Reports, v. 6, p. 1–10, doi:10.1038/srep26359.
- Nutman, A. P., Bennett, V. C., Friend, C. R. L., & Chivas, A. R. (2017). The Isua Supracrustal Belt of the North Atlantic Craton (Greenland): Spotlight on Sedimentary Systems With the Oldest Preserved Sedimentary Structures (~3.7, w3.75, and ~3.8 Ga). In Sediment Provenance. Elsevier Inc. https://doi.org/10.1016/B978-0-12-803386-9.00020-4
- Nutman, A. P., Bennett, V. C., Friend, C. R. L., & Yi, K. (2020). Eoarchean contrasting ultra-high-pressure to low-pressure metamorphisms (< 250 to > 1000 ° C / GPa) explained by tectonic plate convergence in deep time. Precambrian Research, 344(March), 105770. https://doi.org/10.1016/j.precamres.2020.105770
- Nutman, A. P., Bennett, V. C., Friend, C. R. L., Kranendonk, M. J. Van, & Chivas, A. R. (2016). Rapid emergence of life shown by discovery of 3,700-million-year-old microbial structures. Nature, 537(7621), 535–538. https://doi.org/10.1038/nature19355
- Nutman, A.P., 1986. The early Archaean to Proterozoic history of the Isukasia area, southern West Greenland. Gronlands Geol. Undersogelse Bull. 154, 80. https://doi.org/10.34194/bullggu.v154.6696
- Nutman, A.P., and Collerson, K.D., 1991, Very early Archean crustal-accretion complexes preserved in the North Atlantic craton: Geology, v. 19, p. 791–794, doi:10.1130/0091-7613(1991)019<0791:VEACAC>2.3.CO;2.
- Nutman, A.P., and Friend, C.R.L., 2009, New 1:20,000 scale geological maps, synthesis and history of investigation of the Isua supracrustal belt and adjacent orthogneisses, southern West Greenland: A glimpse of Eoarchaean crust formation and orogeny: Precambrian Research, v. 172, p. 189–211, doi:10.1016/j.precamres.2009.03.017.
- Nutman, A.P., Bennett, V.C., Chivas, A.R., Friend, C.R.L., Liu, X.M., and Dux, F.W., 2015, 3806Ma Isua rhyolites and dacites affected by low temperature

Eoarchaean surficial alteration: Earth's earliest weathering: Precambrian Research, v. 268, p. 323–338, doi:10.1016/j.precamres.2015.07.014.

- Nutman, A.P., Bennett, V.C., Friend, C.R.L., 2015. The emergence of the Eoarchaean proto-arc: Evolution of a c. 3700 Ma convergent plate boundary at Isua, southern West Greenland. Geol. Soc. Spec. Publ. 389, 113–133. https://doi.org/10.1144/SP389.5

- Nutman, A.P., Bennett, V.C., Friend, C.R.L., and Rosing, M.T., 1997, ~ 3710 and ≥ 3790 Ma volcanic sequences in the Isua (Greenland) supracrustal belt; structural and Nd isotope implications: Chemical Geology, v. 141, p. 271–287, doi:10.1016/S0009-2541(97)00084-3.

- Nutman, A.P., Bennett, V.C., Friend, C.R.L., and Yi, K., 2020, Eoarchean contrasting ultra-high-pressure to low-pressure metamorphisms (<250 to >1000 °C/GPa) explained by tectonic plate convergence in deep time: Precambrian Research, v. 344, p. 105770, doi:10.1016/j.precamres.2020.105770.

- Nutman, A.P., Bennett, V.C., Friend, C.R.L., Hidaka, H., Yi, K., Lee, S.R., and Kamiichi, T., 2013, The itsaq gneiss complex of greenland: Episodic 3900 to 3660 Ma juvenile crust formation and recycling in the 3660 to 3600 Ma Isukasian orogeny: American Journal of Science, v. 313, p. 877–911, doi:10.2475/09.2013.03.

- Nutman, A.P., Bennett, V.C., Friend, C.R.L., Polat, A., Hoffmann, E., and Kranendonk, M. Van, 2021, Fifty years of the Eoarchean and the case for evolving uniformitarianism: Precambrian Research, v. 367, p. 106442, doi:10.1016/j.precamres.2021.106442.

- Nutman, A.P., Friend, C.R.L., 2009. New 1:20,000 scale geological maps, synthesis and history of investigation of the Isua supracrustal belt and adjacent orthogneisses, southern West Greenland: A glimpse of Eoarchaean crust formation and orogeny. Precambrian Res. 172, 189–211. https://doi.org/10.1016/j.precamres.2009.03.017

- Nutman, A.P., Friend, C.R.L., and Bennett, V.C., 2022, Comment on "Tectonics of the Isua Supracrustal Belt 1: P-T-X-d Constraints of a Poly-Metamorphic Terrane" by A. Ramírez-Salazar et al. and "Tectonics of the Isua Supracrustal Belt 2: Microstructures Reveal Distributed Strain in the Absence of Major Fault : Tectonics, p. 1–8, doi:10.1029/2021tc007036.

- Nutman, A.P., Friend, C.R.L., Bennett, V.C., McGregor, V.R., 2004. Dating of the Ameralik dyke swarms of the Nuuk district, southern West Greenland; Mafic intrusion events starting from c. 3510 Ma. J. Geol. Soc. London. 161, 421–430. https://doi.org/10.1144/0016-764903-043

- Nutman, A.P., Friend, C.R.L., Kinny, P.D., and McGregor, V.R., 1993, Anatomy of an early Archean gneiss complex: 3900 to 3600 Ma crustal evolution in southern West Greenland: Geology, v. 21, p. 415–418, doi:10.1130/0091-7613(1993)021<0415:AOAEAG>2.3.CO;2.

- Nutman, A.P., McGregor, V.R., Friend, C.R.L., Bennett, V.C., and Kinny, P.D., 1996, The Itsaq Gneiss Complex of southern West Greenland; the world's most extensive record of early crustal evolution (3900-3600 Ma): Precambrian Research, v. 78, p. 1–39.

- Nutman, Allen P., Allaart, J. H., Bridgwater, D., Dimroth, E., & Rosing, M. (1984). Stratigraphic and geochemical evidence for the depositional environment of the early archaean isua supracrustal belt, southern west greenland. Precambrian Research, 25(4), 365–396. https://doi.org/10.1016/0301-9268(84)90010-X

- Palin, R.M., and Santosh, M., 2020, Plate tectonics: What, where, why, and when? Gondwana Research, doi:10.1016/j.gr.2020.11.001.

- Palin, R.M., Santosh, M., Cao, W., Li, S.S., Hernández-Uribe, D., and Parsons, A., 2020, Secular change and the onset of plate tectonics on Earth: Earth-Science Reviews, v. 207, p. 103172, doi:10.1016/j.earscirev.2020.103172.
- Palin, R.M., Weller, O.M., Waters, D.J., and Dyck, B., 2016, Quantifying geological uncertainty in metamorphic phase equilibria modelling; A Monte Carlo assessment and implications for tectonic interpretations: Geoscience Frontiers, v. 7, p. 591–607, doi:10.1016/j.gsf.2015.08.005.
- Pankhurst, R. J., Rapela, C. W., and Fanning, C. M., 2000, Age and origin of coeval TTG, I-and S-type granites in the Famatinian belt of NW Argentina. Earth and Environmental Science Transactions of the Royal Society of Edinburgh, 91(1-2), 151-168.
- Passchier, C. W., & Trouw, R. A., 2005, Microtectonics. Springer Science & Business Media.
- Paton, C., Hellstrom, J., Paul, B., Woodhead, J., and Hergt, J., 2011, Iolite: Freeware for the visualisation and processing of mass spectrometric data: Journal of Analytical Atomic Spectrometry, v. 26, p. 2508–2518, doi:10.1039/c1ja10172b.
- Paton, C., Woodhead, J.D., Hellstrom, J.C., Hergt, J.M., Greig, A., and Maas, R., 2010, Improved laser ablation U-Pb zircon geochronology through robust downhole fractionation correction: Geochemistry, Geophysics, Geosystems, v. 11, doi:10.1029/2009GC002618.
- Peacock, S.M., 1996, Thermal and Petrologic Structure of Subduction Zones: Geophysical Monograph, v. 96, p. 119–133.
- Perchuk, L. L., and Lavrent'eva, I. V., 1983, Experimental investigation of exchange equilibria in the system cordierite-garnet-biotite. Kinetics and Equilibrium in Mineral Reactions, 199–239. https://doi.org/10.1007/978-1-4612-5587-1_7
- Petrus, J.A., and Kamber, B.S., 2012, VizualAge: A Novel Approach to Laser Ablation ICP-MS U-Pb Geochronology Data Reduction: Geostandards and Geoanalytical Research, v. 36, p. 247–270, doi:10.1111/j.1751-908X.2012.00158.x.
- Piazolo, S., La Fontaine, A., Trimby, P., Harley, S., Yang, L., Armstrong, R., and Cairney, J.M., 2016, Deformation-induced trace element redistribution in zircon revealed using atom probe tomography: Nature Communications, v. 7, p. 1–7, doi:10.1038/ncomms10490.
- Piazolo, S., Montagnat, M., & Blackford, J. R., 2008, Sub-structure characterization of experimentally and naturally deformed ice using cryo-EBSD. Journal of Microscopy, 230(3), 509-519.
- Polat, A., and Hofmann, A.W., 2003, Alteration and geochemical patterns in the 3.7-3.8 Ga Isua greenstone belt, West Greenland: Precambrian Research, v. 126, p. 197–218, doi:10.1016/S0301-9268(03)00095-0.
- Polat, A., Hofmann, A. W., & Rosing, M. T., 2002, Boninite-like volcanic rocks in the 3.7-3.8 Ga isua greenstone belt, West Greenland: Geochemical evidence for intra-oceanic subduction zone processes in the early earth. Chemical Geology, 184(3–4), 231–254. https://doi.org/10.1016/S0009-2541(01)00363-1
- Ramírez-Salazar, A., Müller, T., Piazolo, S., Webb, A., Hauzenberger, C., Zuo, J., Haproff, P., Harvey, J., Wong, T., Charlton, C., 2020. Tectonics of the Isua supracrustal belt 1: P-T-X-d constraints of a poly-metamorphic terrane. Whole rock major elements chemistry from metamorphic rocks, Version Version 1.0. Interdisciplinary Earth Data Alliance (IEDA). https://doi.org/10.26022/IEDA/111667. Accessed 2020-09-11

- Ramírez-Salazar, A., Müller, T., Piazolo, S., Webb, G A.Hauzenberger, C., Zuo, J., Haproff, P., Harvey, J., Wong, T., Charlton, C., 2020. Tectonics of the Isua supracrustal belt 1: P-T-X-d constraints of a poly-metamorphic terrane. Garnet, biotite, plagioclase and amphibole chemistry, Version Version 1.0. Interdisciplinary Earth Data Alliance (IEDA). https://doi.org/10.26022/IEDA/111668. Accessed 2020-09-11.
- Ramírez-Salazar, A., Zuo, J., Müller, T., Webb, A.A.G., Sorger, D., Piazolo, S., Haproff, P., Harvey, J., Wang, Q., Hauzenberger, C., Wong, T. K. (2022) Reply to Comment by A.P. Nutman et al. on "Tectonics of the Isua Supracrustal Belt 1: P-T-X-d Constraints of a Poly-Metamorphic Terrane" by A. Ramírez-Salazar et al. and "Tectonics of the Isua Supracrustal Belt 2: Microstructures Reveal Distributed Strain in the Absence of Major Fault Structures" by J. Zuo et al. Tectonics, e2021TC007148 https://doi.org/10.1029/2021TC007148
- Reddy, S. M., Timms, N. E., Pantleon, W., & Trimby, P. (2007). Quantitative characterization of plastic deformation of zircon and geological implications. Contributions to Mineralogy and Petrology, 153(6), 625-645.
- Robyr, M., Vonlanthen, P., Baumgartner, L.P., and Grobety, B., 2007, Growth mechanism of snowball garnets from the Lukmanier Pass area (Central Alps, Switzerland): A combined μCT/EPMA/EBSD study: Terra Nova, v. 19, p. 240–244, doi:10.1111/j.1365-3121.2007.00741.x.
- Rollinson, H., 2002, The metamorphic history of the Isua Greenstone Belt, West Greenland: Geological Society Special Publication, v. 199, p. 329–350, doi:10.1144/GSL.SP.2002.199.01.16.
- Rollinson, H., 2003. Metamorphic history suggested by garnet-growth chronologies in the Isua Greenstone Belt, West Greenland. Precambrian Res. 126, 181–196. https://doi.org/10.1016/S0301-9268(03)00094-9
- Rollinson, H., 2007. Recognising early Archaean mantle: A reappraisal. Contrib. to Mineral. Petrol. 154, 241–252. https://doi.org/10.1007/s00410-007-0191-y
- Rollinson, H., 2021, No plate tectonics necessary to explain Eoarchean rocks at Isua: v. XX, p. 1–5, doi:10.1130/G49278.1/5434685/g49278.pdf.
- Rosing, M.T., Rose, N.M., Bridgwater, D., and Thomsen, H.S., 1996, Earliest part of Earth's stratigraphic record: A reappraisal of the >3.7 Ga Isua (Greenland) supracrustal sequence: Geology, v. 24, p. 43–46, doi:10.1130/0091-7613(1996)024<0043:EPOESS>2.3.CO;2.
- Rozel, A.B., Golabek, G.J., Jain, C., Tackley, P.J., and Gerya, T., 2017, Continental crust formation on early Earth controlled by intrusive magmatism: Nature, v. 545, p. 332–335, doi:10.1038/nature22042.
- Scherer, E.E., Cameron, K.L., and Blichert-Toft, J., 2000, Lu–Hf garnet geochronology: Closure temperature relative to the Sm–Nd system and the effects of trace mineral inclusions: Geochimica et Cosmochimica Acta, v. 64, p. 3413–3432.
- Schneider, C.A., Rasband, W.S., Eliceiri, K.W., 2012. NIH Image to ImageJ: 25 years of image analysis. Nat. Methods 9, 671–675. https://doi.org/10.1038/nmeth.2089
- Shen, T., Hermann, J., Zhang, L., Lü, Z., Padrón-Navarta, J. A., Xia, B., & Bader, T. (2015). UHP metamorphism documented in Ti-chondrodite- and Ti-clinohumite-bearing serpentinized ultramafic rocks from Chinese southwestern Tianshan. Journal of Petrology, 56(7), 1425–1458. https://doi.org/10.1093/petrology/egv042
- Shimizu, H., Umemoto, N., Masuda, A., and Appel, P.W.U., 1990, Sources of iron-formations in the archean isua and malene supracrustals, West Greenland: Evidence

from La-Ce and sm-nd isotopic data and REE abundances: Geochimica et Cosmochimica Acta, v. 54, p. 1147–1154, doi:10.1016/0016-7037(90)90445-Q.

- Sizova, E., Gerya, T., and Brown, M., 2014, Contrasting styles of Phanerozoic and Precambrian continental collision: Gondwana Research, v. 25, p. 522–545, doi:10.1016/j.gr.2012.12.011.
- Sizova, E., Gerya, T., Brown, M., and Perchuk, L.L., 2010, Subduction styles in the Precambrian: Insight from numerical experiments: Lithos, v. 116, p. 209–229, doi:10.1016/j.lithos.2009.05.028.
- Sizova, E., Gerya, T., Brown, M., and Stüwe, K., 2018, What drives metamorphism in early Archean greenstone belts? Insights from numerical modeling: Tectonophysics, v. 746, p. 587–601, doi:10.1016/j.tecto.2017.07.020.
- Sizova, E., Gerya, T., Stüwe, K., and Brown, M., 2015, Generation of felsic crust in the Archean: A geodynamic modeling perspective: Precambrian Research, v. 271, p. 198–224, doi:10.1016/j.precamres.2015.10.005.
- Smit, M. A., Scherstén, A., Næraa, T., Emo, R. B., Scherer, E. E., Sprung, P., Bleeker, W., Mezger, K., Maltese, A., Cai, Y., Rasbury, E. T., & Whitehouse, M. J. (2019). Formation of Archean continental crust constrained by boron isotopes. Geochemical Perspectives Letters, 2019, 23–26. https://doi.org/10.7185/geochemlet.1930
- Smith, J. R., Piazolo, S., Daczko, N. R., & Evans, L. (2015). The effect of pre-tectonic reaction and annealing extent on behaviour during subsequent deformation: Insights from paired shear zones in the lower crust of Fiordland, New Zealand. Journal of Metamorphic Geology, 33(6), 557-577.
- Smithies, R. H., Champion, D. C., & Van Kranendonk, M. J. (2009). Formation of Paleoarchean continental crust through infracrustal melting of enriched basalt. Earth and Planetary Science Letters, 281(3–4), 298–306. https://doi.org/10.1016/j.epsl.2009.03.003
- Söderlund, U., Patchett, P. J., Vervoort, J. D., & Isachsen, C. E. (2004). The 176Lu decay constant determined by Lu–Hf and U–Pb isotope systematics of Precambrian mafic intrusions. Earth and Planetary Science Letters, 219(3-4), 311-324.
- Spandler, C., Hammerli, J., Sha, P., Hilbert-Wolf, H., Hu, Y., Roberts, E., and Schmitz, M., 2016, MKED1: A new titanite standard for in situ analysis of Sm-Nd isotopes and U-Pb geochronology: Chemical Geology, v. 425, p. 110–126, doi:10.1016/j.chemgeo.2016.01.002.
- Spear, F.S., and Daniel, C.G., 2001, Diffusion control of garnet growth, Harpswell Neck, Maine USA: Journal of Metamorphic Geology, v. 19, p. 179–195, doi:10.1046/j.0263-4929.2000.00306.x.
- Spear, F.S., and Daniel, C.G., 2003, Three-dimensional imaging of garnet porphyroblast sizes and chemical zoning: Nucleation and growth history in the garnet zone: American Mineralogist, v. 88, p. 245.
- Spear, F.S., and Wolfe, O.M., 2019, Implications of overstepping of garnet nucleation for geothermometry, geobarometry and P–T path calculations: Chemical Geology, v. 530, p. 119323, doi:10.1016/j.chemgeo.2019.119323.
- Spear, F.S., Kohn, M.J., Florence, F.P., and Menard, T., 1991, A model for garnet and plagioclase growth in pelitic schists: implications for thermobarometry and P-T path determinations: Journal of Metamorphic Geology, v. 8, p. 683–696, doi:10.1111/j.1525-1314.1990.tb00495.x.

- Spear, F.S., Selverstone, J., Hickmott, D., Crowley, P., and Hodges, K. V., 1984, P-T paths from garnet zoning: A new technique for deciphering tectonic processes in crystalline terranes: Geology, v. 12, p. 87–90.
- Spear, F.S., Thomas, J.B., and Hallett, B.W., 2014, Overstepping the garnet isograd: a comparison of QuiG barometry and thermodynamic modeling: Contributions to Mineralogy and Petrology, v. 168, p. 1–15, doi:10.1007/s00410-014-1059-6.
- Spruzeniece, L., Piazolo, S., & Maynard-Casely, H. E. (2017). Deformation-resembling microstructure created by fluid-mediated dissolution–precipitation reactions. Nature communications, 8(1), 1-9.
- Staples, R.D., Gibson, H.D., Berman, R.G., Ryan, J.J., Colpron, M., 2013. A window into the Early to mid-Cretaceous infrastructure of the Yukon-Tanana terrane recorded in multi-stage garnet of west-central Yukon, Canada. J. Metamorph. Geol. 31, 729–753. https://doi.org/10.1111/jmg.12042
- Stern, R.J., 2005, metamorphic terranes that the modern episode of subduction tectonics began in Neoproterozoic time: Geology, v. 33, p. 557–560, doi:10.1130/G21365.1.
- Stern, R.J., 2018, The evolution of plate tectonics: Philosophical Transactions of the Royal Society A: Mathematical, Physical and Engineering Sciences, v. 376, doi:10.1098/rsta.2017.0406.
- St-Onge, M.R., 1987. Zoned poikiloblastic garnets: P-T paths and syn-metamorphic uplift through 30 km of structural depth, wopmay orogen, Canada. J. Petrol. 28, 1–21. https://doi.org/10.1093/petrology/28.1.1
- Strnad, L., Mihaljevic, M., and Sebek, O., 2005, Laser ablation and solution ICP-MS determination of rare earth elements in USGS BIR-1G, BHVO-2G and BCR-2G glass reference materials: Geostandards and Geoanalytical Research, v. 29, p. 303–314, doi:10.1111/j.1751-908x.2005.tb00902.x.
- Sun, J.F., Yang, J.H., Wu, F.Y., Xie, L.W., Yang, Y.H., Liu, Z.C., and Li, X.H., 2012, In situ U-Pb dating of titanite by LA-ICPMS: Chinese Science Bulletin, v. 57, p. 2506–2516, doi:10.1007/s11434-012-5177-0.
- Szilas, K., Kelemen, P.B., and Rosing, M.T., 2015, The petrogenesis of ultramafic rocks in the >3.7Ga Isua supracrustal belt, southern West Greenland: Geochemical evidence for two distinct magmatic cumulate trends: Gondwana Research, v. 28, p. 565–580, doi:10.1016/j.gr.2014.07.010.
- Thompson, A.B., and Ridley, J., 1987, Pressure-Temperature-Time (P-T-t) histories of orogenic belts: Philosophical Transactions of the Royal Society of London, v. 321, p. 27–45.
- Tracy, R.J., and Robinson, P., 1976, Garnet composition and zoning in the determination of temperature and pressure of metamorphism, central Massachusetts: v. 61, p. 762–775.
- Turcotte, D. L., 1989, A heat pipe mechanism for volcanism and tectonics on Venus. Journal of Geophysical Research, 94(B3), 2779–2785. https://doi.org/10.1029/JB094iB03p02779
- Turner, S., Wilde, S., Wörner, G., Schaefer, B., and Lai, Y.J., 2020, An andesitic source for Jack Hills zircon supports onset of plate tectonics in the Hadean: Nature Communications, v. 11, p. 1–5, doi:10.1038/s41467-020-14857-1.
- van Hunen, J., and van den Berg, A.P., 2008, Plate tectonics on the early Earth: Limitations imposed by strength and buoyancy of subducted lithosphere: Lithos, v. 103, p. 217–235, doi:10.1016/j.lithos.2007.09.016.

- Van Kranendonk, M.J., 2007, Tectonics of Early Earth (M. J. Van Kranendonk, R. H. Smithies, & V. C. Bennett, Eds.): v. 15, 1105–1116 p., doi:10.1016/S0166-2635(07)15086-6.
- Van Kranendonk, M.J., 2010, Two types of Archean continental crust: Plume and plate tectonics on early earth: American Journal of Science, v. 310, p. 1187–1209, doi:10.2475/10.2010.01.
- Van Kranendonk, M.J., 2011, Onset of Plate Tectonics: Science, v. 333, p. 413–415.
- Vermeesch, P., 2018, IsoplotR: A free and open toolbox for geochronology. Geoscience Frontiers, 9(5), 1479-1493.
- Vernon, R.H., 2011, Microstructures of melt-bearing regional metamorphic rocks: Memoir of the Geological Society of America, v. 207, p. 1–11, doi:10.1130/2011.1207(01).
- Villa, I. M., Holden, N. E., Possolo, A., Ickert, R. B., Hibbert, D. B., & Renne, P. R. (2020). IUPAC-IUGS recommendation on the half-lives of 147Sm and 146Sm. Geochimica et cosmochimica acta, 285, 70-77.
- von Huene, R., and Scholl, D.W., 1991, Observations at convergent margins concerning sediment subduction, subduction erosion, and the growth of continental crust: Reviews of Geophysics, v. 29, p. 279–316, doi:10.1029/91RG00969.
- Walters, J.B., Cruz-Uribe, A.M., Song, W.J., Gerbi, C., and Biela, K., 2022, Strengths and limitations of in situ U-Pb titanite petrochronology in polymetamorphic rocks: An example from western Maine, USA. : Journal of Metamorphic Geology, p. 0–2, doi:10.1111/jmg.12657.
- Waters, D.J., 2021. Metamorphism of Quartzofeldspathic Rocks, 2nd ed, Encyclopedia of Geology. Elsevier Inc. https://doi.org/10.1016/b978-0-08-102908-4.00098-9
- Waterton, P., Guotana, J.M., Nishio, I., Morishita, T., Tani, K., Woodland, S., Legros, H., Pearson, D.G., and Szilas, K., 2022, No mantle residues in the Isua Supracrustal Belt: Earth and Planetary Science Letters, v. 579, p. 117348, doi:10.1016/j.epsl.2021.117348.
- Webb, A.A.G., Müller, T., Zuo, J., Haproff, P.J., Ramírez-Salazar, A., 2020. A non-plate tectonic model for the Eoarchean Isua supracrustal belt. Lithosphere 12, 166–179. https://doi.org/10.1130/L1130.1
- Weller, O.M., Mottram, C.M., St-Onge, M.R., Möller, C., Strachan, R., Rivers, T., and Copley, A., 2021, The metamorphic and magmatic record of collisional orogens: Nature Reviews Earth and Environment, v. 2, p. 781–799, doi:10.1038/s43017-021-00218-z.
- White, Powell, Holland, and Worley, 2000, The effect of TiO2 and Fe2O3 on metapelitic assemblages at greenschist and amphibolite facies conditions: Mineral equilibria calculations in the system K2O-FeO-MgO-Al2O3-SiO2-H2O-TiO2-Fe2O3. Journal of Metamorphic Geology, 18(5), 497–511. https://doi.org/10.1046/j.1525-1314.2000.00269.x
- White, R. V., Crowley, J.L., and Myers, J.S., 2000, Earth's oldest well-preserved mafic dyke swarms in the vicinity of the Isua greenstone belt, southern West Greenland: Geology of Greenland Survey Bulletin, v. 186, p. 65–72, doi:10.34194/ggub.v186.5217.
- White, R. W., Powell, R., Holland, T. J. B., Johnson, T. E., and Green, E. C. R., 2014, New mineral activity-composition relations for thermodynamic calculations in metapelitic systems. Journal of Metamorphic Geology, 32(3), 261–286. https://doi.org/10.1111/jmg.12071

- White, R.W., Powell, R., and Holland, T.J.B., 2007, Progress relating to calculation of partial melting equilibria for metapelites: Journal of Metamorphic Geology, v. 25, p. 511–527, doi:10.1111/j.1525-1314.2007.00711.x.
- Whitney, D. L., & Evans, B. W., 2010, Abbreviations for names of rock-forming minerals. American mineralogist, 95(1), 185-187.
- Whitney, D.L., Cooke, M.L., and Du Frane, S.A., 2000, Modeling of radial microcracks at corners of inclusions in garnet using fracture mechanics: Journal of Geophysical Research: Solid Earth, v. 105, p. 2843–2853, doi:10.1029/1999jb900375.
- Whitney, D.L., Goergen, E.T., Ketcham, R.A., Kunze, K., 2008. Formation of garnet polycrystals during metamorphic crystallization. J. Metamorph. Geol. 26, 365–383. https://doi.org/10.1111/j.1525-1314.2008.00763.x
- Wiedenbeck, M. et al., 2004, Further Characterisation of the 91500 Zircon Crystal: Geostandards and Geoanalytical Research, v. 28, p. 9–39.
- Wilbur, D.E., Ague, J.J., 2006. Chemical disequilibrium during garnet growth: Monte Carlo simulations of natural crystal morphologies. Geology 34, 689–692. https://doi.org/10.1130/G22483.1
- Windley, B.F., Kusky, T., and Polat, A., 2021, Onset of plate tectonics by the Eoarchean: Precambrian Research, v. 352, p. 105980, doi:10.1016/j.precamres.2020.105980.
- Wolfe, O.M., and Spear, F.S., 2018, Determining the amount of overstepping required to nucleate garnet during Barrovian regional metamorphism, Connecticut Valley Synclinorium: Journal of Metamorphic Geology, v. 36, p. 79–94, doi:10.1111/jmg.12284.
- Yang, P., Rivers, T., 2001. Chromium and manganese zoning in pelitic garnet and kyanite: Spiral, overprint, and oscillatory (?) zoning patterns and the role of growth rate. J. Metamorph. Geol. 19, 455–474. https://doi.org/10.1046/j.0263-4929.2001.00323.x
- Zack, T., and Kooijman, E., 2017, Petrology and geochronology of rutile (M. J. Kohn, M. Engi, & P. Lanari, Eds.): Mineralogical Society of America, v. 83, 443–467 p., doi:10.2138/rmg.2017.83.14.
- Zeh, A., Holness, M.B., 2003. The effect of reaction overstep on garnet microtextures in metapelitic rocks of the Ilesha Schist Belt, SW Nigeria. J. Petrol. 44, 967–991. https://doi.org/10.1093/petrology/44.6.967
- Zhu, Z., Campbell, I. H., Allen, C. M., & Burnham, A. D. (2020). S-type granites: Their origin and distribution through time as determined from detrital zircons. Earth and Planetary Science Letters, 536, 116140.
- Zuo, J., Webb, A.A.G., Johnson, T.E., McKenzie, N.R., Kirkland, C.L., Ng, H.C., and Lo, C.Y., 2021a, Model versus measured detrital zircon age signatures of the early Earth: Earth and Planetary Science Letters, v. 575, p. 117182, doi:10.1016/j.epsl.2021.117182.
- Zuo, J., Webb, A.A.G., Piazolo, S., Wang, Q., Müller, T., Ramírez-Salazar, A., Haproff, P.J., 2021b. Tectonics of the Isua Supracrustal Belt 2: Microstructures Reveal Distributed Strain in the Absence of Major Fault Structures. Tectonics 40. https://doi.org/10.1029/2020TC006514

Anthony Ramirez Salazar

The metamorphic evolution of the Isua supracrustal belt: Implications for Archean

tectonics